Department of Engineering Science

Coherent Unsteadiness in Film Cooling

Richard Fawcett

St John's College

Hilary Term 2011

A thesis submitted in partial fulfilment of the requirements for the degree of Doctor of Philosophy

University of Oxford

Coherent Unsteadiness in Film Cooling

Richard Fawcett, St John's College

submitted for DPhil, Hilary Term 2011

Film cooling is vital for the cooling of the blades and vanes in the high temperature environment of a jet engine high pressure turbine stage. Previous research into film cooling has typically concentrated on its time-mean performance. However, results from other studies upon more simplified geometries, suggest that coherent unsteadiness is likely to also be present in film cooling flows. The research presented in this thesis, therefore, aims to characterise what coherent unsteadiness, if any, is present within film cooling flows.

Cylindrical and shaped cooling holes, located upon the pressure surface of a turbine blade within a large scale linear cascade, have been investigated. A blowing ratio range of 0.5 to 2.0 has been investigated, with either a plenum or perpendicular crossflow at the cooling hole inlet. Particle Image Velocimetry, high speed photography and Hot Wire Anemometry have been used to investigate the jet downstream of both cooling holes. The impact of crossflow at the hole inlet upon the flowfield inside both cooling holes has been investigated using Hot Wire Anemometry and a further numerical model solved by applying TBLOCK.

The results presented in the current thesis, show the existence of two coherent unsteady structures in the jet downstream of both the cylindrical and the shaped holes. These structures are called shear layer vortices and hairpin vortices, and their formation is dependent on the velocity difference across the jet shear layer. Inside the cooling hole coherent hairpin vortices also appear to occur, with their formation dependent on the direction and magnitude of the crossflow at the hole inlet. The coherent unsteadiness presented here is shown for the first time for film cooling flows, and recommendations to build on the current study, in what is potentially an interesting research area, are made at the end of this thesis.

Acknowledgements

I would like to say thank you to both my supervisors Andrew Wheeler and Li He for all their support and guidance on this project, especially in providing new ideas to help explain the results and for always having the door open when I had a question.

The Osney lab workshop are thanked for all their help with manufacturing the parts for the experimental investigation, especially Gerald who always managed to get things done for me even at a moment's notice.

Thanks are expressed to the project sponsors: the EPSRC and Rolls-Royce plc. Additionally thanks should also go to the EPSRC Engineering Instrument Loan Pool for the provision of the equipment for the High Speed Photography.

The Osney lab has been a great place to study for a DPhil, and I would like to thank all the staff and students, especially Adam, Brian, Chris, Devin, Francis, James and Salva for many great times. Thanks must also go to all my friends in St John's MCR for making the non-engineering side of my Oxford life just as enjoyable.

To my parents I want to say thank you for their support with this DPhil, but most importantly for giving me the upbringing that means I have been able to study for a DPhil in the first place.

To my girlfriend, Annika, I would really like to say a big thank you for always being there for me, especially in the last months of writing up.

Contents

Nomenclature

All nomenclature is defined in the section within which it is first used. If the same nomenclature is also used in subsequent sections it is included here.

A	Throat Area
C	Blade Chord, Coefficient
D	Hole Diameter
f	Frequency
i	Sample, Image
L	Hole Length
$\dot{m}$	Mass Flow Rate
n	Total Number of Samples or Images
Re	Reynolds number
S	Distance Upstream of Hole Exit
St	Strouhal number
p	Pressure
T	Temperature
t	Time
V	Velocity
X	Downstream/Axial Direction
Y	Normal Direction
Z	Spanwise Direction

Greek Characters

α	Hole Inclination Angle
λ	Spatial Distance between Vortices
μ	Dynamic Viscosity
ρ	Density
ω	Vorticity
Ω	Normalised Vorticity

Subscripts

0	Total
1	Cascade Inlet
∞	Cooling Hole Exit, 50% Axial Chord
c	Coolant Bulk, Cooling Hole
D	Discharge
e	Cascade Exit
i	Sample, Image
in	In
out	Out
p	Pressure
rms	Root Mean Squared
s	Relative to Hole Axis
str	Propagation of Structures

x	Downstream/Axial Direction
y	Normal Direction
z	Spanwise Direction

Superscripts

Apostrophe	Instantaneous Quantity

Abbreviations

BR	Blowing Ratio
CFR	Crossflow Ratio
CRVP	Counter-Rotating Vortex Pair
DTS	Dual Time Stepping
FFT	Fast Fourier Transform
HWA	Hot Wire Anemometry
JICF	Jet in Crossflow
LES	Large Eddy Simulation
LDV	Laser Doppler Velocimetry
NGV	Nozzle Guide Vane
PIV	Particle Image Velocimetry
(U-)RANS	(Unsteady) Reynolds Averaged Navier Stokes
TET	Turbine Entry Temperature

Chapter 1

Introduction

The concept of the jet engine was first conceived by Frank Whittle in the late 1920s, to improve upon the performance of the piston engines of the time [69]. Initially Whittle's idea was ignored by the British Air Ministry. However, the advent of World War II meant that its potential could no longer be overlooked, and by the end of the war jet powered aircraft were being used in combat operations. However, the first jet powered flight in 1939 did not use one of Whittle's engines. Instead it was made by a German Heinkel He 178 with its jet engine designed by a team headed by Hans von Ohain [70]. Von Ohain knew nothing of Whittle's jet engine design, and developed his theory for a jet engine independently whilst a PhD student at the University of Gottingen in the early 1930s.

The end of World War II saw the jet engine begin to be used to power commercial aircraft, with the first commercial jet-powered flight being that of the deHavilland Comet in 1952. The market for commercial jet powered flight has since grown to more than 4.5 million passengers a year [1]. The market is continuing to grow and Rolls-Royce (one of the leading jet engine manufacturers) predicts there to be a requirement for 65,000 new jet powered commercial aircraft, in total worth more than US$800 billion, over the next twenty years [80].

A cut-away of a modern jet engine is shown in Fig. 1.1. Ambient air enters the front of the engine and is diffused inside the inlet. The air passes through the fan, which does work upon it and raises its total pressure. Downstream of the fan the air is split into two channels, one for the 'bypass air' and the other for the 'core' air.

Downstream of the fan the core air enters into the compressor. The compressor is a series

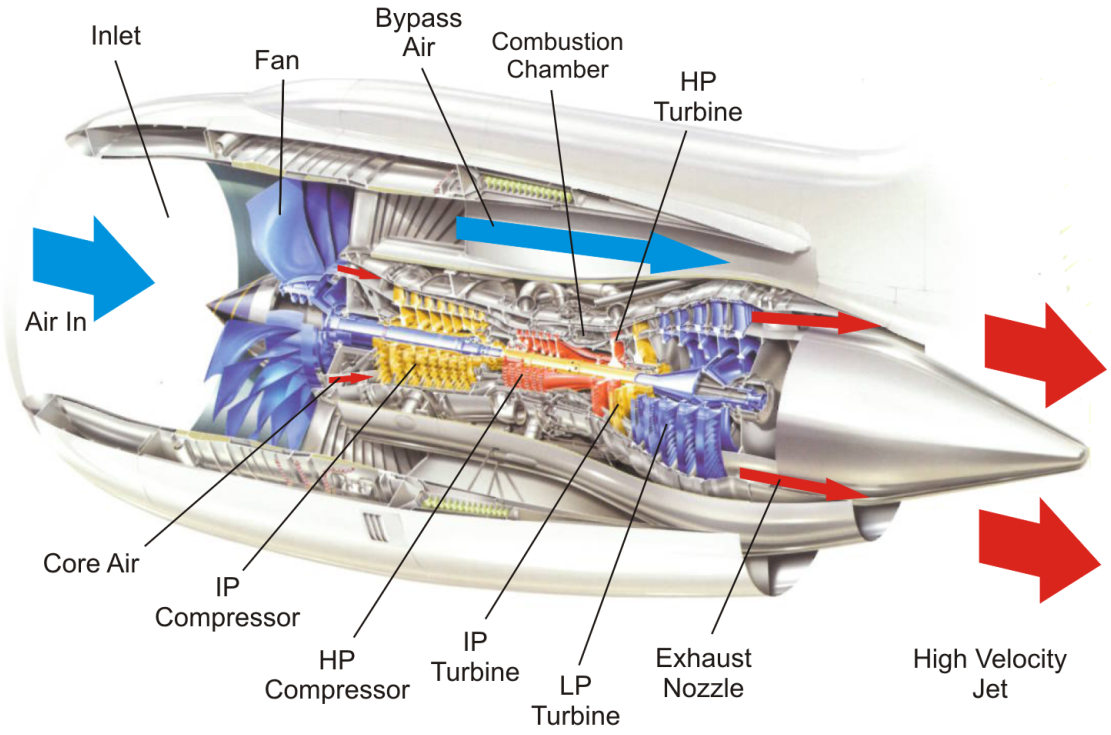

Figure 1.1: Cut-away view of a modern jet engine for civil transport aircraft, adapted from Rolls-Royce [85].

of alternate rows of rotating and stationary aerofoils, called blades and vanes respectively, that are arranged around an annulus. Compressors, like the fan, do work on the fluid and raise the pressure of the incoming air. On a modern engine, the compressor exit pressure will be about 40 times the inlet pressure. In Fig. 1.1 the compressor is split into an intermediate pressure (IP) compressor and a high pressure (HP) compressor. This is done so that the rotational speed of the blades can be better matched to the local flow conditions.

The high pressure air from the compressor enters the combustion chamber where kerosene is injected and combusted. This raises the temperature of the airstream from the compressor to over 2000K in the combustion chamber.

The high temperature and high pressure airstream now enters the turbine. The turbine, like the compressor, is formed by rows of stationary vanes and rotating blades. However, in contrast to the compressor, work is extracted from the air to rotate the turbine. Concentric shafts on the engine axis connect the turbine to the compressor, and so the rotation of the turbine is used to rotate the upstream compressor and fan. The turbine is split into

high, intermediate and low pressure sections, with each connected by a shaft to a section of the compressor or the fan as denoted by the colour codes in Fig. 1.1. Figure 1.1 is of a Rolls-Royce jet engine and it should be noted that other engine manufacturers typically split the turbine into only high and low pressure sections.

On exiting the LP turbine the pressure and temperature of the air is still larger than the ambient conditions downstream of the jet. This difference is used to accelerate the exiting air through the exhaust nozzle to form a high velocity jet. The velocity of this jet is higher than the velocity of the airstream entering the engine inlet. According to Newton's third law this change of momentum across the engine generates a reaction force, more commonly referred to as thrust, which propels the aircraft forward.

To increase the thrust generated by the engine the momentum rise across it must be increased. The propulsive efficiency decreases and noise levels increase if this rise in momentum is achieved by increasing the velocity of the exiting air. Therefore the high velocity air from the engine core is commonly mixed, downstream of the exhaust nozzle, with the lower velocity bypass air which does not pass through the engine core. Thus the momentum rise across the engine is achieved by a small acceleration of a large body of air, rather than by the acceleration of the core air alone.

Aircraft must carry all the fuel required for their flight, which means that the penalty for high fuel consumption is larger than that for land-based power generation, as additional thrust is required to carry the fuel to be burnt later in the flight. Unsurprisingly there has been a large focus on improving jet engine cycle efficiency to reduce airline operating costs. In response to this need specific fuel consumption has been reduced by 50% since the 1950s [85]. Despite this improvement, fuel currently accounts for around 20% [84] of an airline's operating costs, and so engine manufacturers are continually striving to increase the engine cycle efficiency further.

Additionally there is a growing awareness of the environmental impacts of emissions of greenhouse gases such as carbon dioxide. The proposed introduction of carbon based legislation [96], which aims to curb these emissions, adds further to the requirement upon engine manufacturers to achieve improvements in the cycle efficiency.

One method of increasing the efficiency of a non-ideal jet engine cycle is to raise the temperature of the air exiting the combustion chamber. Figure 1.2 shows the rise in the

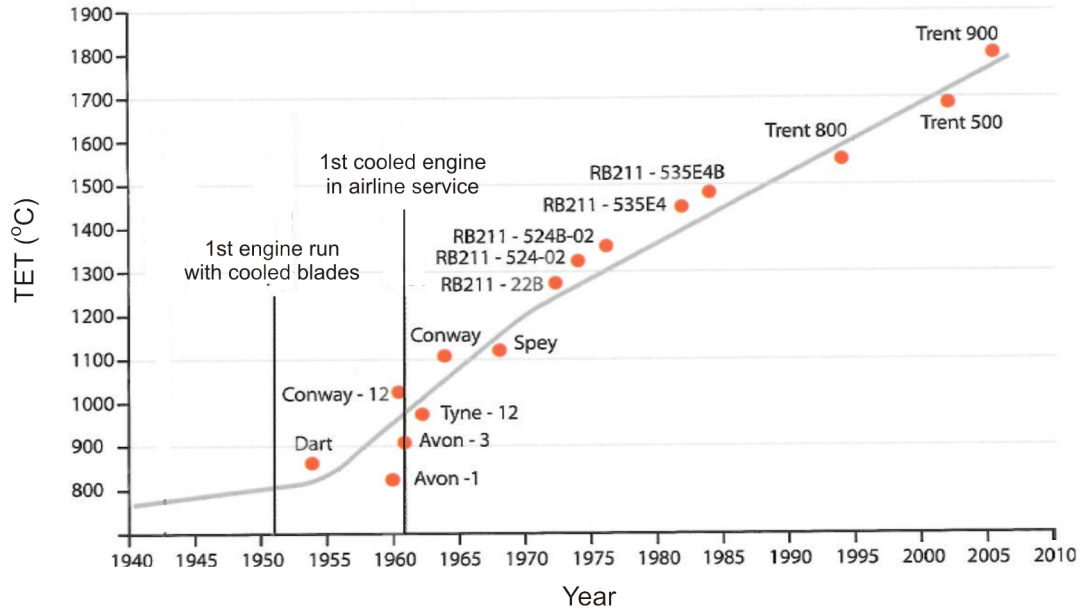

Figure 1.2: Increase in Turbine Entry Temperature (TET) with time, including different Rolls-Royce engine marks, adapted from Rolls-Royce [85].

Turbine Entry Temperature (TET) with time, and it can be seen that there has been a 1000K increase since the 1950s.

Early in the development of the jet engine, the point was reached whereby the air temperature at the inlet to the turbine was higher than the melting point of the materials used within the turbine. New materials for turbine blades have been developed since 1950s, and presently single crystal nickel alloy blades are used. However, material developments on their own would have permitted a rise in the TET of only a few hundred degrees. The largest fraction of the increase in the TET has instead been made possible by the introduction of turbine cooling.

Early blade cooling designs were typically of a single passage of cooling air running spanwise through the blade interior which ejected into the mainstream turbine flow at the blade tip. In time, developments in manufacturing techniques have allowed the single passage to be developed into the serpentine passage arrangement, shown in Fig. 1.3(a), which features multiple passages running from the blade hub to tip.

To reduce the heat transferred to the blade surface some of the cooling air in the interior passages is bled out of small holes and onto the blade surfaces, as shown in Fig. 1.3(a). The

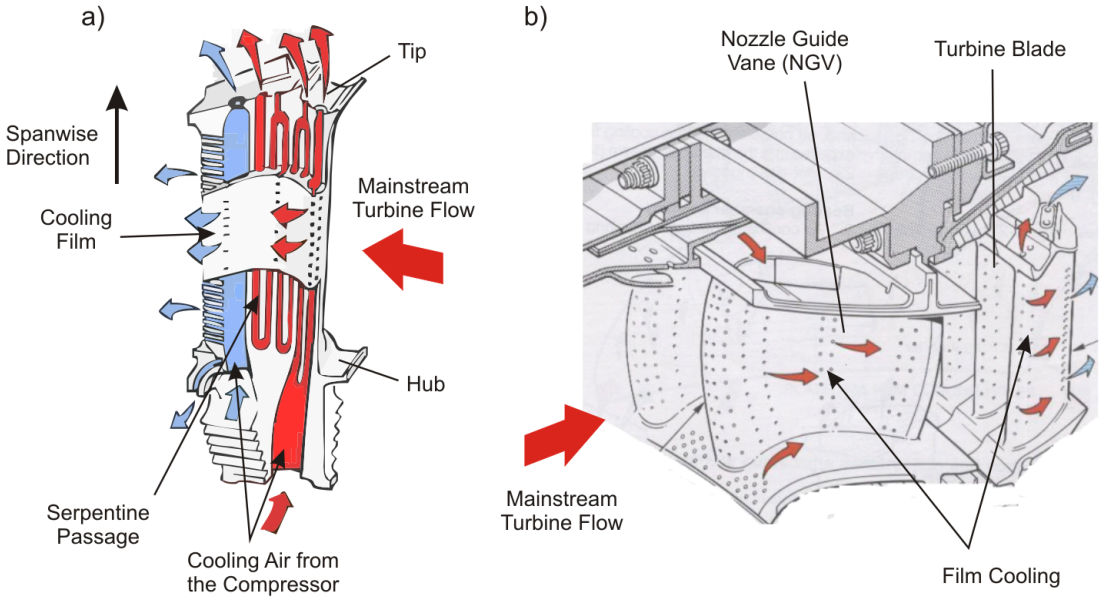

Figure 1.3: Film cooling on a high pressure turbine stage, (a) part cut-away view of a blade and (b) exterior view of an NGV and a blade, adapted from Rolls-Royce [85].

jets emerging from these holes form a film of lower temperature air on the blade surface, and so reduce the temperature difference between the blade surface and the air closest to the blade surface. This process is called film cooling, and Fig. 1.3(b) shows that rows of film cooling holes are located not just on the turbine blade, but also on the Nozzle Guide Vane (NGV) upstream of the blade.

The pressure of the cooling air is required to be larger than that of the mainstream, and so it must be bled from the compressor. This means that work is done to raise the air pressure, but as the coolant avoids the combustion chamber less work can be extracted from it once in the turbine. Consequently for a given TET, cooling will decrease the engine cycle efficiency. However, the increase in the maximum possible TET due to the use of cooling means that it is overall beneficial to the cycle efficiency, and typically around 20% of the core air is used for cooling.

The rows of film cooling holes in Fig. 1.3 have spaces between the holes, which means that the resulting film will not be uniform. Ideally, to achieve a uniform spread, the film would be produced using a continuous slot in the blade surface rather than discrete holes. Mechanical stresses imposed on the turbine blade prohibit the use of a slot, and so the

film cooling designer must instead aim to achieve the best lateral spread of coolant from discrete holes. On account of their simplicity to manufacture the earliest film cooling holes were of a cylindrical cross-section. To improve upon the poor lateral (spanwise) spread of the coolant from cylindrical holes, shaped holes, which feature an expanding hole exit, have been developed, and are now routinely used by film cooling designers.

The demand to further increase the jet engine cycle efficiency means that improved film cooling strategies are desired. These will either use less coolant to attain the same cooling performance or achieve more cooling with no increase in the amount of coolant flow.

Film cooling has been a major research topic within the jet engine community since the 1950s and continues to be today. The majority of previous research into the performance of film cooling holes, in terms of their impact on surface heat transfer and the associated changes in the aerodynamic flowfield, has concentrated on the time-mean state. However, studies of a Jet in Crossflow (widely referred to as JICF), have shown that the mixing of a jet with an external crossflow is likely to contain coherent unsteady structures.

Coherent unsteady structures are flow features that vary periodically with time, in contrast to turbulence which is described as random unsteadiness. Coherent unsteadiness, like turbulence, will impact upon the observed time-mean flowfield and could be either beneficial or detrimental to a film cooling design. The tendency towards time-mean investigations, means that there is little understanding within the film cooling community as to whether coherent unsteadinesss is firstly present within film cooling flows, and secondly whether it's effects are relevant to turbine blade design.

The research presented within this thesis represents one of the first attempts to address the issue of coherent unsteadiness within film cooling flows. The first aim of the research is to establish experimentally if coherent unsteadiness is indeed present in flows typical of film cooling. Upon establishing that coherent unsteadiness is present within film cooling flows, the research shall focus on understanding its formation mechanism.

The literature review presented in the next chapter of this thesis outlines the current state of the art in film cooling research in more depth than is possible in this introduction. Although film cooling has not been the subject of studies into coherent unsteadiness, cases with some similarities to film cooling have been investigated. Within the literature review these studies are introduced, and from these it is possible to predict what coherent unsteady

structures might be present in film cooling flows.

The majority of the present investigation has been experimental work performed upon a large scale linear cascade, which was modified to have cooling holes on a blade pressure surface. The cooling system, which featured either cylindrical or shaped holes, is described in Chapter 3. An introduction to the experimental techniques used to observe the unsteady flowfield is given in Chapter 4. Additionally a numerical model was used to help understand the flowfield within the cooling hole, and the validation of this numerical model is described in Chapter 5.

The results of the current investigation are shown in Chapters 6 to 9. Chapters 6 and 7 show the impact of both the cooling hole inlet condition and the velocity of the jet, on the coherent unsteadiness in the jet downstream of the hole exit. Coherent unsteadiness is also present inside the cooling hole, and Chapters 8 and 9 show how it varies for changes in the direction and magnitude of crossflow at the hole inlet.

The principal conclusions of the investigation are made in Chapter 9, and here it is shown that coherent unsteadiness is present for film cooling holes typical of turbine blade film cooling. The observed coherent unsteadiness being present both in the jet downstream of the hole exit and inside the cooling hole. To build on the conclusions of the current thesis a series of recommendations are made at the end of Chapter 9.

Chapter 2

Literature Review

Since its conception in the 1950s film cooling has been the subject of a large body of research, and it is quoted by Bunker [11] that this amounts to over 2700 articles. The majority of these investigations have been time-mean measurements of the heat transfer on the surface downstream of the cooling hole exit. In contrast, aerodynamic studies of film cooling, especially experimental ones, are far less numerous. The first part of this literature review combines these aerodynamic and surface measurements to describe the time-mean flowfield from the hole inlet, through the cooling hole and into the flowfield downstream of the hole exit.

It was alluded to in the introduction chapter, when justifying the current research, that the unsteady flowfield has not been a major subject for film cooling research. To gain an understanding of the likely coherent unsteady features which may be present in film cooling flows, the second part of this literature review presents investigations on the cases of the Jet in Crossflow (JICF) and the wall jet. In these cases, which have similarities to film cooling, coherent unsteadiness has been observed.

To aid the reading of the current chapter it is felt appropriate to introduce some key geometric terminology. A cylindrical cooling hole is shown in Fig. 2.1, and is defined in terms of its diameter (D), which is normal to the axis of the hole, its length (L) and the inclination angles of the inlet and exit (respectively α_{in} and α_{out}). The pitch (P) is the spanwise distance between two cooling holes. In film cooling flows the mainstream turbine flow means that an external crossflow is present at the hole exit. The edges of the hole, as shown in Fig. 2.1, are referred to in this review as the leading and trailing edges based on

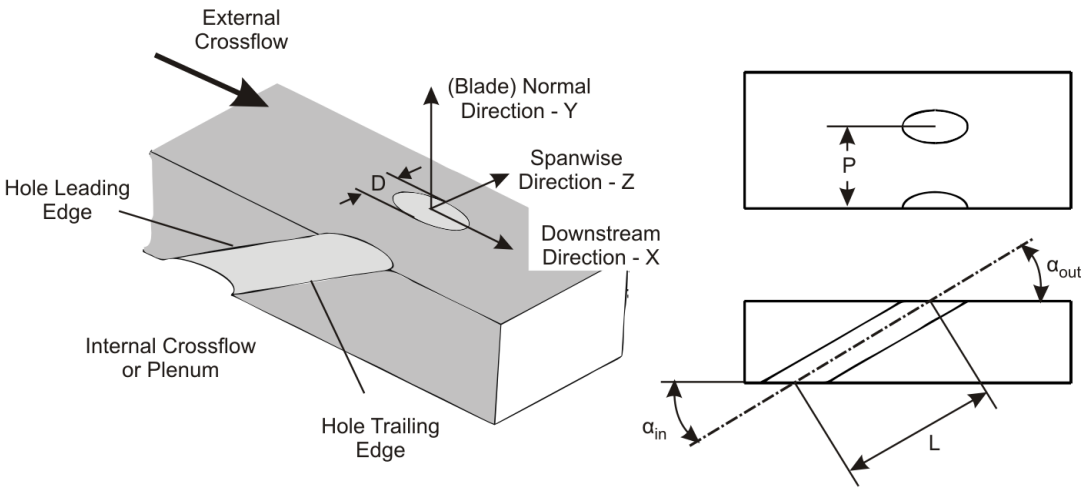

Figure 2.1: Geometry of a cylindrical film cooling hole.

the direction of the external crossflow.

Dimensions are given in Cartesian co-ordinates which have their origin at the intercept of the hole axis and the external surface. The Cartesian directions within this review are named the downstream, normal and spanwise directions respectively. The hole centreline plane, upon which results discussed in this review are regularly presented, refers to the XY plane at Z equal to 0.

2.1 Time-mean Flowfield

The opening topics of this section detail the time-mean flowfield close to the hole inlet and that within the cooling hole. The later topics show the time-mean flowfield downstream of the hole exit and how the changes seen inside the cooling hole influence the downstream flowfield. It is possible to improve film cooling performance by modifying the cooling hole from the original cylindrical hole geometry shown in Fig. 2.1, and as such the final topics of this section introduce shaped holes, compound angled holes and more recent 'novel' hole geometries.

2.1.1 Hole Inlet with a Plenum Chamber

Within the open literature the most common way to feed a film cooling hole during experimental testing has been from a plenum chamber. Figure 2.2 shows oil flow visualisations, upon a thin acrylic plate coated with oil on the hole centreline, obtained by Lee et al [56]

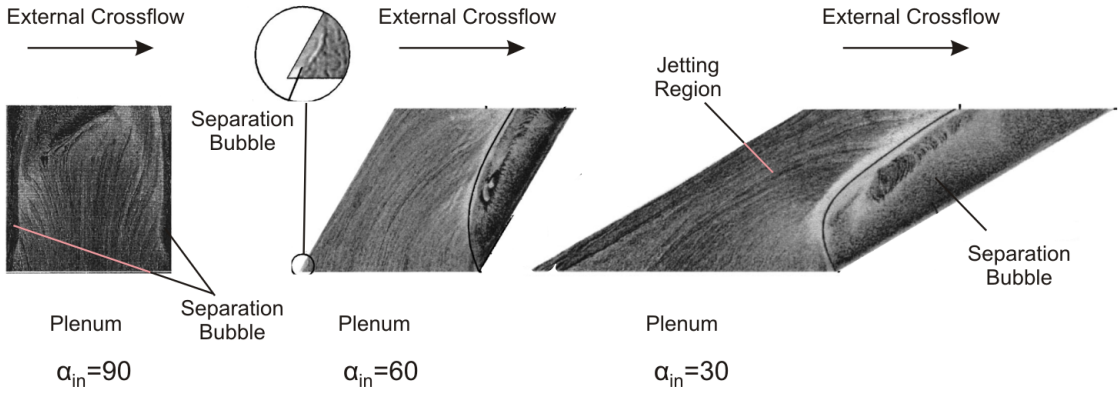

Figure 2.2: Oil flow visualisations showing the size of the separation bubble with variation in the hole inlet inclination angle (α_{in}), from Lee et al [56]. Re_D=120×10^3.

for a variation in the inlet inclination angle. For an inlet inclination angle of 90° it is shown in Fig. 2.2 that a separation bubble was formed at both the leading and trailing edges of the hole. Figure 2.2 shows that decreasing the inlet inclination angle, and increasing the flow turning angle, led to a larger separation bubble on the trailing edge and a reduction of that at the leading edge. At low inlet inclination angles the region towards the leading edge through which the flow passes is commonly called the jetting region.

Lee et al [56] did not isolate the change in the inclination angle of the hole inlet from the change in the inclination angle at the hole exit. Burd and Simon [13] compared the discharge coefficients of cooling holes with α_{in} equal to 90° and 30°, for a constant exit inclination angle of 30°.

The discharge coefficient (C_D) is a measure of the effective area of the cooling hole and is found as the ratio of the mass flow rate ($\dot{m}_c$) through the cooling hole to the ideal mass flow rate ($\dot{m}_{ideal}$) given isentropic expansion through the cooling hole. For incompressible flows, such as that in the experiment of Burd and Simon, the discharge coefficient can be found according to Eq. 2.1. Here $\dot{m}_{ideal}$ is approximated using the pressure difference across the cooling hole ($p_{0c} - p_\infty$) and the Bernoulli equation. For compressible flows, the ideal mass flow rate should be found using the equation for isentropic expansion.

$$C_D = \frac{\dot{m}_c}{\dot{m}_{ideal}} = \frac{\dot{m}_c}{A_c\sqrt{2\rho(p_{0c} - p_\infty)}} \tag{2.1}$$

Burd and Simon [13] showed that the discharge coefficient was approximately 10% smaller for a hole inclined at 30° to the plenum than that at 90°, over a Re_D range of

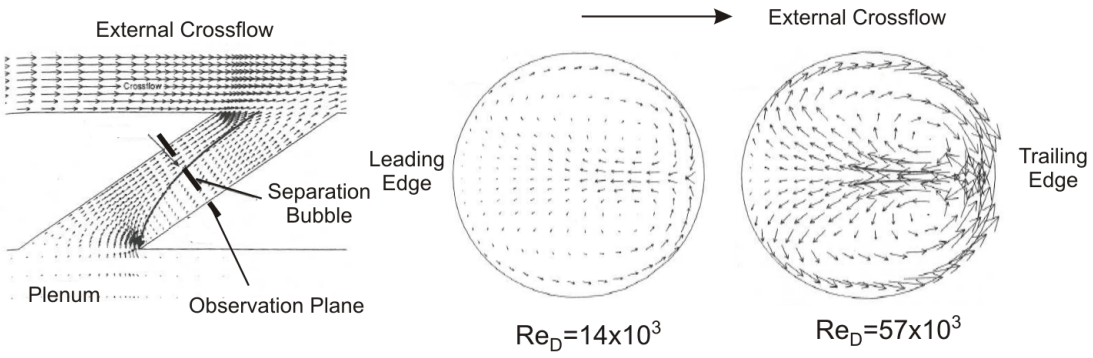

Figure 2.3: Vortices on a plane normal to the hole axis from Leylek and Zerkle [58].

$3 \times 10^3 - 20 \times 10^3$. The lower discharge coefficient, implies a decrease in the effective area and so confirms that the size of the inlet separation is increased with a reduction in the inlet inclination angle.

The bias of the coolant towards the hole leading edge due to the jetting effect was shown by Burd and Simon to be less pronounced if the hole length was increased. Velocity profiles taken at the hole exit plane showed that the exiting jet was only biased towards the leading edge for a hole length of lower than 2.3D. For holes of length 4D and larger Burd and Simon showed that the coolant passed around the inlet separation bubble to given a more uniform velocity profile at the hole exit plane.

The first computational model of a film cooling hole in open literature to include the plenum and the cooling hole was that of Leylek and Zerkle [58]. Prior to this study just the flowfield downstream of the hole exit had been modeled, with a velocity profile assumed at the hole exit. Leylek and Zerkle [58] used the PHOENICS system of codes with a standard k-ε turbulence model. The cooling hole had inlet and exit inclination angles of 35° and a length of 3.5D. This geometry was identical to the experimental study of Pietrzyk et al [78], [79] (discussed later in this review), from which the results downstream of the cooling hole exit were used for validation.

Figure 2.3 shows a pair of counter-rotating vortices on a plane normal to the hole axis. Leylek and Zerkle saw these were present for both Re_D equal to $14{\times}10^3$ and $57{\times}10^3$. The vortices were present within the inlet separation bubble and the magnitude of their circulation, as shown in Fig. 2.3, was seen to increase with hole Reynolds number. Leylek and Zerkle also presented turbulent intensity profiles within the cooling hole, and showed the dominant location for turbulence production to be the velocity gradient between the

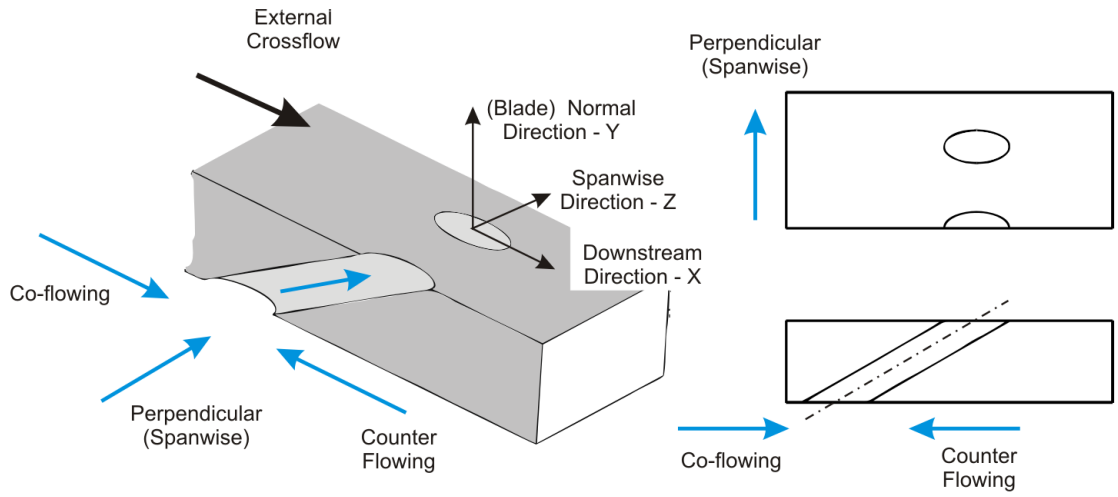

Figure 2.4: Internal crossflow directions.

jetting region and the separation bubble.

The studies discussed previously within this section had sharp edges at the inlet to the cooling hole. Hay et al [37] investigated the impact of radiusing the inlet angle on the trailing edge of cooling holes with α_{in} equal to 30°. The inclusion of a radius of 0.75D increased the discharge coefficient by up to 20%, implying a reduction in the size of the inlet separation bubble.

2.1.2 Hole Inlet with Internal Crossflow

Although most studies of film cooling have their cooling holes fed from a plenum chamber, in reality many cooling holes upon a turbine blade or NGV have a crossflow at the hole inlet. The serpentine passage inside a turbine blade interior means that many cooling holes are fed from a crossflow orientated perpendicularly to the mainstream flow at the hole exit. The case where internal crossflow is in the same direction as the mainstream is referred to as co-flowing, whilst that in the opposite direction to the mainstream is referred to as counter flowing. In theory any direction crossflow is possible, however for simplicity previous research has investigated only these three crossflow directions. The crossflow directions are shown in Fig. 2.4 for a cooling hole with a 30° inlet inclination angle.

To aid the reading of this review the internal crossflow velocity (V_{cross}) used by the respective authors has been normalised with respect to the bulk velocity through the cooling hole (V_c) to form the Crossflow Ratio (CFR), as shown in Eq. 2.2.

$$CFR = \frac{V_{cross}}{V_c} \tag{2.2}$$

Hay et al [38] were the first to investigate the impact of internal crossflow upon film cooling holes. Hay et al studied the discharge coefficients of holes inclined at 30° and 90°, at both the inlet and exit, fed by an internal crossflow orientated in either the co-flowing or perpendicular direction. The investigation had a hole Reynolds number range of 63×10^3-170×10^3 with a CFR of up to 0.6.

Within this range, co-flowing crossflow led to a decrease in the discharge coefficient through the hole inclined at 90°. In contrast co-flowing crossflow increased the discharge coefficient of the 30° inclined hole compared to the plenum fed case. Perpendicular crossflow led to a reduction in the discharge coefficient of the 30° inclined hole. The change in discharge coefficient with respect to the plenum condition was highly dependent on the Re_D, and the direction and CFR of the internal crossflow. Within the range investigated by Hay et al [38] this change was as large as ±30%. Similar trends in the discharge coefficient were seen in the later studies of Gritsch et al [33] [31].

The first study to look at the flowfield inside a cooling hole fed from a crossflow was the study of Thole et al [95], using LDV (Laser Doppler Velocimetry). Thole et al investigated a hole of Re_D equal to 52×10^3 inclined at 30° to a co-flowing crossflow of CFR equal to either 0.0, 1.2 or 2.0. The lowest CFR represented a plenum case, and the jetting effect discussed previously could be seen within the in-hole velocity profile. At a CFR equal to 1.2 the jetting effect was not apparent with the maximum velocity close to the hole axis. At CFR equal to 2.0 the highest in-hole velocity was towards the trailing edge.

Thole et al proposed that co-flowing crossflow reduces the inlet separation at the trailing edge as less coolant makes a sharp turn to enter the hole. However there appears to be an optimum CFR, as the velocity profile at CFR equal to 2.0 suggested that the inlet separation bubble on the leading edge had increased in size.

Kholi and Thole [47] compared co-flowing, counter flowing and perpendicular internal crossflows computationally. The cooling hole was inclined at 35° and the CFR were 0.4 and 0.7 for Re_D of 5×10^3 and 10×10^3 respectively. Note should be made that Kohli and Thole investigated two cooling hole exit geometries, however these will be discussed later in this chapter as it is felt that they do not impact the hole inlet characteristics. Kohli and Thole

used the FLUENT solver with the standard k-ε turbulence model and wall functions.

Comparing the velocity profiles it was apparent that the counter flowing crossflow led to the largest trailing edge separation bubble. This meant the jetting region was narrowest for the counter flowing case and consequently, on account of the high velocity gradient in the shear layer, the turbulence production was the largest of the three cases. For the perpendicular case, only one of the two vortices shown in Fig. 2.3 was present inside the hole. This asymmetric profile was seen at both the CFR investigated, and Kohli and Thole stated that the vortex centre appeared to spiral with distance along the hole.

The flowfield inside a short hole, of length 0.7D and Re_D equal to 12×10^3, inclined normal to a crossflow channel was studied experimentally by Peterson and Plesniak [76] [77], using Particle Image Velocimetry (PIV). The row in which the cooling hole was situated was fed with either co-flowing or counter flowing crossflow, in which all the coolant passed out of the holes. Interestingly Peterson and Plesniak observed two pairs of counter rotating vortices midway along the hole length. One pair was due to the trailing edge inlet separation shown previously in Fig. 2.3, but additionally, for the counter flowing case, there was also a mirroring vortex pair from the separation at the leading edge of the inlet.

2.1.3 Surface Measurements Downstream of the Hole Exit

Studies of film cooling in open literature prior to the late 1960s investigated film cooling obtained using a slot, and a detailed review of these early works is provided by Goldstein [26].

The first investigation published in open literature with film cooling from discrete holes was that of Goldstein et al [28] in 1968. Within this study the film cooling hole was inclined at 35° to the blade surface with a hole length in excess of 40D. An exit inclination angle of 35° is representative of holes on the surfaces of the turbine blade away from the leading edge region, and as such most film cooling studies have used a similar value. The hole length of 40D is typical of early film cooling studies, but as stated by Leylek and Zerkle [58], and inferred from more recent geometries in open literature, hole lengths of greater than 10D are not common for blade film cooling applications.

The Reynolds number of the cooling holes investigated by Goldstein et al [28] ranged from $8 \times 10^3 - 78 \times 10^3$. The mass flow rate ($\dot{m}_c$) through the hole was compared to the mainstream flow at the hole exit in terms of the non-dimensional blowing ratio (BR). The

BR is the ratio of the mass flux of coolant to the mass flux of the mainstream flow as expressed in Eq. 2.3. Here c subscripts denote the coolant and ∞ the mainstream flow at the hole exit. Goldstein et al investigated a BR range of 0.1 up to 2.0, a range which has been typical of most subsequent studies.

$$BR = \frac{\rho_c V_c}{\rho_\infty V_\infty} \tag{2.3}$$

Goldstein et al [28] quantified the coverage of the coolant film upon the downstream surface, as in many later studies, using the adiabatic film effectiveness, as shown in Eq. 2.4. Here T_c is the initial temperature of the coolant and T_∞ is the temperature of the mainstream. The adiabatic wall temperature (T_{aw}) is the local temperature of the insulated downstream surface with film cooling present.

$$\eta_{ad} = \frac{T_{aw} - T_\infty}{T_c - T_\infty} \tag{2.4}$$

The adiabatic wall condition means that the wall temperature (T_{aw}) is equal to the isothermal film temperature (T_f). In reality the surface of a turbine blade will not be adiabatic, and so the film effectiveness should be defined explicitly in terms of the isothermal film temperature (T_f), as shown in Eq. 2.5.

$$\eta_f = \frac{T_f - T_\infty}{T_c - T_\infty} \tag{2.5}$$

The practical difficulty of measuring the local isothermal film temperature (T_f) directly, has meant that the adiabatic film effectiveness has been used in the majority of film cooling studies. Therefore in this review the adiabatic film effectiveness will also be referred to as the film effectiveness.

Goldstein et al saw that increasing the BR from 0 to 0.5 led to a rise in the downstream film effectiveness. However increasing the BR to greater than 0.5, saw a gradual decrease in the film effectiveness compared to that at a BR equal to 0.5, even though the quantity of coolant was increasing. Goldstein et al postulated that this decrease in film effectiveness at higher BR was due to the jet penetrating further into the mainstream due to the increase in jet momentum. This meant that a wake region formed under the jet that filled with un-cooled mainstream air.

Bergeles et al [8] measured the film effectiveness downstream of a cooling hole, of similar dimensions to Goldstein et al, using Helium as a tracer and the analogy between heat and mass transfer. A similar decrease in film effectiveness was seen by Bergeles et al for a BR greater than 0.5. Centreline velocity profiles, presented in the same study, confirmed that the reduction in the film effectiveness was due to the separation of the jet at higher blowing ratios.

In a turbine stage the temperature of the mainstream is greater than that of the coolant. As both fluids are at a similar pressure the ideal gas equation means that the density of the coolant is greater than that of the mainstream. This difference in density is expressed as a density ratio (DR), as shown in Eq. 2.6. Although the value of the DR will vary depending on the engine operating condition typical values lie in the range of 1.6 to 2.0.

$$DR = \frac{\rho_c}{\rho_\infty} \tag{2.6}$$

The first study to investigate the variation in film effectiveness with change in the DR was that of Goldstein et al [27]. Here the refrigerant R-12 was used to obtain a DR of approximately 3.5. This case was compared to the centreline film effectiveness obtained using air, and it was seen that the BR at which maximum film effectiveness occurred increased for the higher DR case. Comparing the two cases using the momentum ratio (MR), as defined in Eq. 2.7, meant that the maximum film effectiveness occurred at the same MR for both DR. This observation has been subsequently presented by Sinha et al [91], and the film effectiveness profiles in that study have been widely used as a test case for computational modeling of film cooling.

$$MR = \frac{\rho_c {V_c}^2}{\rho_\infty {V_\infty}^2} \tag{2.7}$$

Eriksen and Goldstein [22] and Leiss [57] have shown that an increase in the boundary layer displacement thickness leads to a decrease in the laterally averaged film effectiveness. Eriksen and Goldstein attributed this decrease to be due to the change in the velocity profile in the boundary layer. Stating that if the displacement thickness is smaller then there is a 'fuller' velocity profile and so the jet requires a higher momentum to separate from the blade surface. Hence for blowing ratios close to that of jet separation the film effectiveness can be enhanced by a reduction in the boundary layer displacement thickness.

The change in the film effectiveness due to different combinations of laminar and turbulent flows was investigated by Goldstein and Yoshida [29]. Turbulent and laminar mainstream boundary layers of the same displacement thickness were seen to have little difference upon the downstream laterally averaged film effectiveness. In contrast, a laminar jet separated from the blade surface at a lower BR than a turbulent jet of the same Reynolds number. Consequently it appeared that turbulence within the jet assisted in keeping it attached to the blade surface.

The pressure gradient is not uniform about a turbine blade and Leiss [57], Hay et al [40] and Teekaram et al [93] have investigated the impact of different favourable and adverse pressure gradients upon film effectiveness. To do this the authors used a flat plate with a contoured wall on the opposite side of the wind tunnel. A favourable pressure gradient led to a shift in the film effectiveness to that which would have been expected at a lower blowing ratio. Whilst if the adverse pressure gradient was sufficiently high then relaminarisation of the boundary layer occurred.

Passage through the combustion chamber upstream of the turbine leads to turbulence intensity levels of greater than 10% at the inlet of the NGV. Some of this turbulence will be damped by the acceleration through the NGV, but it is likely that the turbulence level is still greater than the levels of less than 2% used in the majority of film cooling investigations.

The effects of turbulence intensity and turbulent length scale have been investigated by Kadotani and Goldstein [44] [45] and Burd et al [12]. Here the turbulence intensity in the mainstream was varied up to 12% and the length scale up to 0.3D. Analysis of the thermal flowfield showed that increasing the length scale or the turbulence intensity increased mixing between the jet and the mainstream. The film effectiveness distribution showed that this increase in mixing led to a reduction in the laterally averaged film effectiveness.

The heat flux ($\dot{q}_f$) into a turbine blade, as shown in Eq. 2.8, is dependent on the local heat transfer coefficient (h_f) as well as the temperature difference between the coolant film and the blade surface ($T_f - T_w$): where the variation in the local temperature difference can be inferred from a film effectiveness distribution.

$$\dot{q}_f = h_f(T_f - T_w) \tag{2.8}$$

Two of the earliest studies to investigate the effect of film cooling on the heat transfer

coefficient (h_f) were those of Eriksen and Goldstein [22] and Hay et al [39]. Both studies showed a rise in the h_f immediately downstream of the hole exit compared to the un-cooled case, due to the mixing of the cooling jet with the mainstream flow. The only exception to this was the case of Eriksen and Goldstein [22] with a BR of less than 0.5 were the jet remained attached to the blade surface. With increasing downstream distance the h_f reduced back to the un-cooled value. The acceleration of the mainstream around the blockage presented by the cooling jet meant that there was an additional increase in the h_f away from the centreline.

2.1.4 Aerodynamic Flowfield Downstream of the Hole Exit

There have been relatively few experimental investigations into the aerodynamic flowfield downstream of a film cooling hole. However, in the context of more general fluid dynamics research there have been a larger number of studies of the case of a jet entering normally, in contrast to the 35° typical of film cooling studies, into an external crossflow. This setup is commonly referred to as Jet in Crossflow (JICF).

The majority of JICF studies have investigated a BR in excess of those typical of film cooling. One of the earliest aerodynamic studies of a JICF to investigate a BR less than 2.0 was that of Andreopoulos and Rodi [5]. Andreopoulos and Rodi investigated holes of Reynolds number $20 \times 10^3 - 80 \times 10^3$ with a BR ranging from 0.5 to 2.0, and presented time-mean velocity, turbulence intensity and shear stress profiles obtained using a 3-wire hot wire probe. Centreline time-mean velocity profiles were similar to those shown by Bergeles et al [8] for an inclined hole, showing an attached jet at BR equal to 0.5 and a separated jet with a wake region underneath at a BR of 1.0 and 2.0.

The lateral velocity near the surface was towards the hole centreline, which showed that the wake region under the jet was formed of mainstream fluid that had passed around the jet core. The velocity vectors in the secondary flow (YZ) plane showed that the velocity component towards the hole centreline was part of a Counter-Rotating Vortex Pair (CRVP) which formed within the jet core. The CRVP in the jet of BR equal to 1.0 is shown in Fig. 2.5, and it is seen that the vortex centre moved away from the blade surface and towards the hole centreline with increasing downstream distance. This trend was also seen by Andreopoulos and Rodi for the jets of BR equal to 0.5 and 2.0.

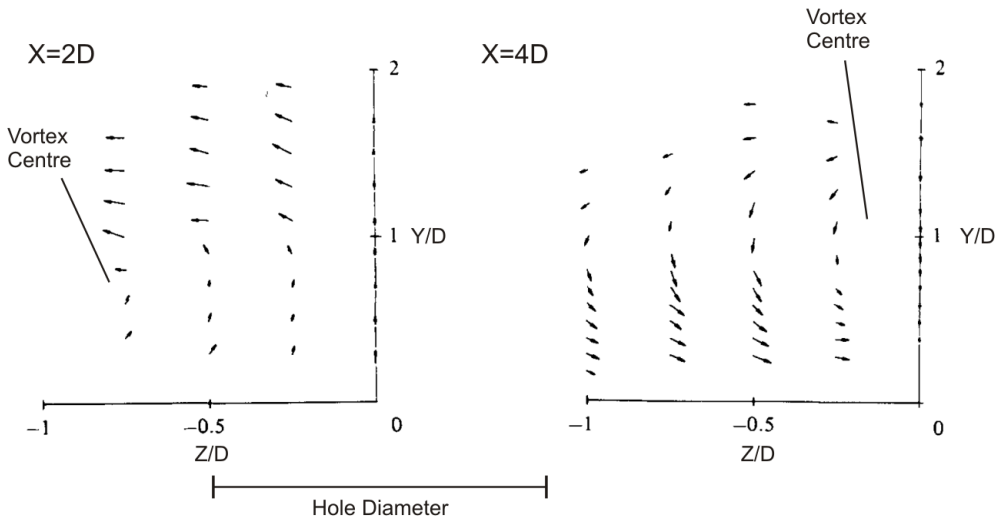

Figure 2.5: Velocity vectors in the secondary flow plane (left) 2D downstream and (right) 4D downstream for a jet of BR equal to 1.0 entering normally into crossflow. From Andreopoulos and Rodi [5].

The CRVP had been seen previously for the JICF case of BR greater than 2.0, and a review of these early studies was provided by Margason [63]. The consensus of that work was that the vorticity in the CRVP is generated due to the interaction of the jet with the mainstream fluid. However, there is some debate about the finer details of the CRVP formation, and within this review it is felt more appropriate to discuss this with regard to the instantaneous measurements presented in the section on the unsteady flowfield.

It should be highlighted here that the vortex pair present within the hole, shown in Fig. 2.3, is not the initiation of the CRVP as demonstrated by the presence of a CRVP when only a single vortex is present within the hole [47]. However, although they are not the formation mechanism, the in-hole vortices do appear to merge with those in the CRVP, as Peterson and Plesniak [77] have shown the CRVP to have a lower circulation when vortices of the opposite sense of rotation were present within the hole.

Andreopoulos and Rodi [5] show that the velocity gradient between the mainstream and the jet led to the production of shear stresses on the upper surface of the jet. The level of shear stress production depended on the magnitude of the velocity gradient in the shear layer, with an increase due to the rise in the BR from 0.5 to 2.0. In the wake region the velocity was lower than that in the jet core. The velocity gradient through this shear layer led to the production of shear stresses of opposite magnitude to those in the upper shear

layer.

The aerodynamic flowfield downstream of short holes inclined at 35° to the blade surface was investigated by Pietrzyk et al [78] using LDV. Pietrzyk et al tested short holes of length 3.5D fed from a plenum chamber, compared to the long holes (length 10D) of Andreopoulos and Rodi [5]. This meant that the in-hole jetting effect, due to the separation bubble at the hole inlet, had an influence upon the velocity profile at the hole exit.

Pietrzyk et al [78] investigated blowing ratios of 0.25, 0.5 and 1.0. The velocity profile presented by Pietrzyk et al at a BR of 1.0, shows that the jet to have separated from the blade surface. The turbulence intensity profiles also show that at a BR of 1.0, the separation bubble at the hole inlet led to a region of high turbulence intensity at the trailing edge of the hole exit. A region of high turbulence intensity was not seen at the hole exit by Pietrzyk et al for a BR of 0.25 or in the long holes of Andreopoulos and Rodi [5].

The computational study of Leylek and Zerkle [58] presented temperature contours in the downstream flowfield. These temperature contours are shown in Fig. 2.6 and showed that the presence of the CRVP within the jet core, shown in Fig. 2.5, meant that higher temperature mainstream fluid was drawn underneath the jet when it was separated from the blade surface. This phenomena contributes to the reduction in film effectiveness at higher blowing ratios observed in the previously discussed surface measurements. The temperature contours, shown in Fig. 2.6, for the separated jet form a kidney shape. Thus within the film cooling community the CRVP is widely referred to as the 'kidney vortex'. To remain consistent with wider literature though the CRVP name will be used within this study.

Leylek and Zerkle compared their computational results with those of Sinha et al [91]. This comparison showed the centreline film effectiveness predicted computationally to be greater than that seen experimentally. In contrast the film effectiveness away from the centreline was under predicted compared to the experimental case. Additionally, the separation of the jet at a blowing ratio of 1.0 was not predicted computationally. Leylek and Zerkle attributed this discrepancy as being due to use of the isotropic k-ε turbulence model, when in reality the mixing between the jet and mainstream was anisotropic.

Harrison and Bogard [35] present a comprehensive review of time-mean Reynolds Averaged Navier Stokes (RANS) computational modeling of film cooling subsequent to the study of Leylek and Zerkle [58]. Harrison and Bogard also present a comparison of the isotropic

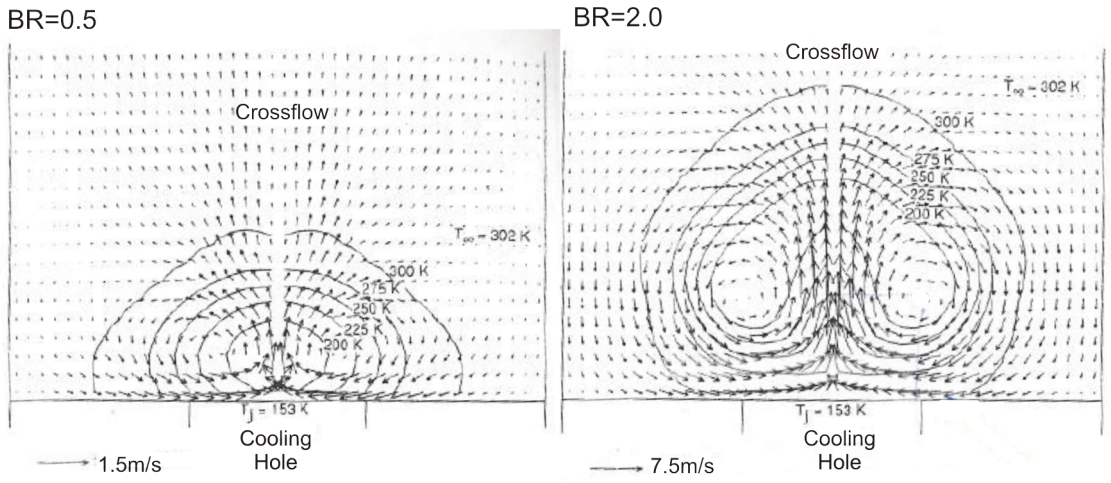

Figure 2.6: Temperature contours 5D downstream for a jet emerging from a hole inclined at 35°. From Leylek and Zerkle [58].

k-ε and k-ω turbulence models with the anisotropic Reynolds Stress model. Here the hypothesis that the mixing being anisotropic was the main reason for the poor prediction of film effectiveness was contradicted, as the Reynolds Stress turbulence model was shown to perform little better than the isotropic turbulence models.

2.1.5 Impact of Internal Crossflow on the Downstream Flowfield

The investigations introduced previously with regard to the flow downstream of the hole exit all had cooling holes either fed from a plenum or of a long hole length. Within this review it has been discussed that a crossflow at the hole inlet affects the flowfield near the exit of short holes, with a co-flowing crossflow having been shown to reduce the in-hole jetting effect. Gritsch et al [32], on the same experimental facility as Thole et al [95], showed that co-flowing crossflow led to a doubling of the centreline film effectiveness compared to that with a plenum fed hole.

The film effectiveness results of Saumweber and Schulz [89] showed the asymmetry in the in-hole vortices with perpendicular crossflow to also lead to a rise in the film effectiveness compared to the plenum fed case. Steady state computations by Saumweber and Schulz for a jet of BR equal to 1.0 and a CFR of 1.0 showed that the position of the CRVP rotated compared to the plenum fed case. The rise in the film effectiveness was attributed to this change in the flowfield, as one half of the CRVP in the separated jet was brought closer to the surface.

2.1.6 Turbine Blade Environment

The studies discussed so far in this review have all been studies of film cooling on a flat plate. In practice film cooling holes will be located upon the surface of a turbine blade (or vane), where the rotation, upstream wakes, shocks and secondary flows will impact upon the film cooling performance.

Dring et al [19] have shown, using a large scale rotating rig, that the centrifugal effect of rotation can introduce a radial component into the trajectory of film cooling jets. The radial deflection was dependent on the jet momentum, with a jet of lower momentum being deflected more than one of higher momentum.

The time-mean measurements of Mehendale et al [68] showed that the passage of wakes through a cooled turbine cascade could lead to a reduction in the blade suction surface film effectiveness. Abhari and Epstein [3] showed experimentally that with film cooling the fluctuations in the heat transfer coefficient with wake passing differed from those for an un-cooled blade. To predict this change, Abhari and Epstein developed a linear model to simulate the impact of the pressure fluctuation due to wake passing on the blowing ratio of the film cooling holes.

The interaction of the endwall boundary layer with the leading edge of the turbine blade leads to the formation of a horseshoe vortex [53]. The leg of the horseshoe vortex upon the pressure surface merges with the passage vortex. The passage vortex forms due to the pressure gradient across the blade passage, and moves towards the suction surface whilst entraining additional fluid from the mainstream passage flow. Langston [53] shows that by the exit plane of the cascade the passage vortex extends spanwise up to 0.3 times the blade pitch. The tip leakage vortex is caused by flow spilling over the rotor blade tip from the pressure to the suction surface. Yamamoto [102] shows that the spanwise height of the vortex to be less than that of the passage vortex, but its presence forces the passage vortex away from the suction surface towards the pressure surface.

Secondary flow features such as these will introduce lateral and normal velocity components on the flowfield, and so impact on the trajectory of film cooling jets in their vicinity. This has been shown to be the case in endwall film cooling by Freidrichs et al [25].

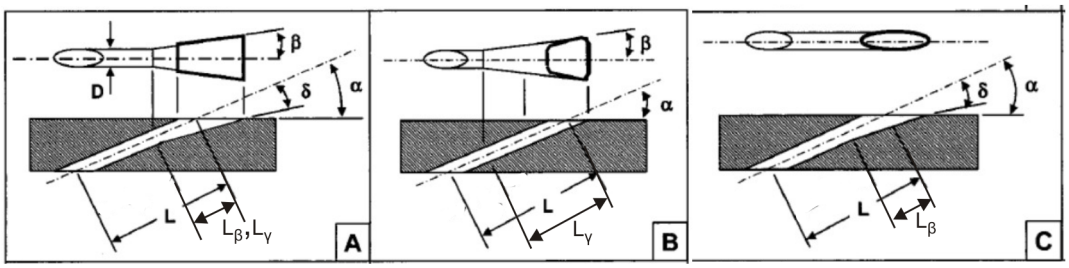

Figure 2.7: Types of shaped hole (a) lateral and laidback (b) lateral-only, and (c) laidback-only, from Bunker [11].

2.1.7 Shaped Cooling Holes

The term 'shaped hole' is normally used to refer to a cylindrical hole with an expanding exit. Shaped holes are commonly used on a turbine blade surface downstream of the leading edge region, and have been described in the review paper of Bunker [11] as the one primary advancement in film cooling technology that has been put into widespread practice.

Film cooling jets from cylindrical holes, as discussed previously in this review, have poor lateral spread downstream of the hole exit and separate from the surface at a BR of approximately 1.0. Expanding the exit means that a greater lateral spread is obtained and the reduction in jet momentum means that the jet remains attached to the blade surface.

Bunker describes shaped hole geometries as fitting into four types, namely lateral and laidback, lateral-only, laidback-only and conical. The conical shaped hole has rarely been investigated in open literature, so will not be discussed here. The three other types are shown in Fig. 2.7, where γ is the lateral expansion angle and β is the laidback angle. The starting distances for these angles are expressed as L_γ and L_β respectively.

The first experiment in open literature with shaped cooling holes was that of Goldstein et al [27], which included only a lateral expansion of the hole exit (case B in Fig. 2.7). Flow visualisation with smoke and measurements of the downstream film effectiveness confirmed that the shaped hole provided an improved lateral spread of coolant and prevented separation of the jet at higher blowing ratios.

The time-mean computation of Hyams and Leylek [42] showed that the inclusion of only a laidback angle (case C in Fig. 2.7) also improved the laterally averaged effectiveness compared to a cylindrical hole. This improvement was attributed to the reduction in the angle of the exiting jet with respect to the surface. However, the lack of a lateral expansion

meant that the lateral spread of coolant was little better than with a cylindrical hole.

Gritsch et al [32] compared the film effectiveness downstream of lateral-only and laidback and lateral shaped holes (respectively cases B and A in Fig. 2.7). Here it was shown that combining the two expansion angles resulted in the highest laterally averaged film effectiveness over the widest range of BR.

The optimal angle for the expansion of a 2-D diffuser is approximately 6° [64]. The lateral angle and laidback angles of a shaped hole are both typically greater than this, meaning that the shaped hole is an over expanding diffuser. It has been shown computationally, by Kohli and Thole [47], and experimentally, by Porter et al [81], that this over expansion can lead to a stagnant region at the centre of the expanding exit.

Gritsch et al [32] also noted that there was some asymmetry in the film effectiveness profile downstream of both the lateral-only and lateral and laidback shaped holes. This asymmetry was attributed to the over expanding nature of the diffuser, causing the jet to become biased to one edge of the diffuser. A similar effect, though not discussed in detail, has been shown by Lu et al [61] and Laveau and Abhari [54].

There have been few aerodynamic measurements of the flowfield downstream of a shaped hole. The earliest is that of Thole et al [94] which compared the downstream flowfield of lateral-only (case B in Fig. 2.7) and laidback and lateral shaped holes (case A in Fig. 2.7) with that of a cylindrical hole at a blowing ratio of 1.0. Centreline velocity profiles showed the existence of a small separation near the hole exit for the lateral-only shaped hole which was not present when a laidback angle was included.

Normal velocity profiles presented by Thole et al [94] led them to suggest that no CRVP is present in the jet downstream of a shaped hole. However, the shaped holes investigated by Thole et al were fed by a co-flowing internal crossflow, and subsequent studies by Jessen et al [43] and Laveau and Abhari [54] have shown that a CRVP can be present for a plenum fed shaped hole.

The studies of Gristch et al [34] and Saumweber and Schulz [89] both show perpendicular crossflow at the hole inlet (as defined in Fig. 2.4), to dramatically increase the asymmetry in the film effectiveness distribution. This was attributed to the single vortex inside the cooling hole tube due to the perpendicular crossflow. In contrast to the cylindrical hole, this led to a reduction in the laterally averaged film effectiveness for the shaped hole, so

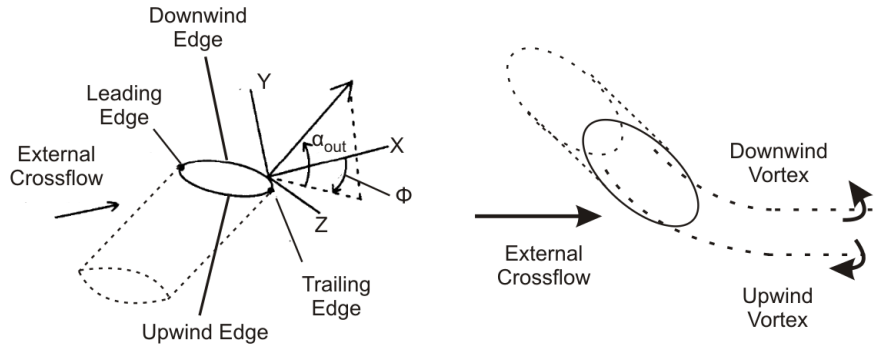

Figure 2.8: Compound angle geometry, adapted from McGovern and Leylek [66]

that it was closer to that of the equivalently fed cylindrical hole.

2.1.8 Compound Angled Cooling Holes

To improve the lateral spread of coolant downstream of cylindrical holes they are sometimes rotated relative to the direction of the mainstream. This angle of rotation is called the compound angle (Φ) and is shown in Fig. 2.8. Here the edges of the hole are referred to as the upwind and downwind edges depending on their position relative to the mainstream direction.

Detailed consideration of the most suitable compound angle did not appear in open literature until the 1990s, although holes with a compound angle had been used in turbines since the 1970s. One of the earliest was the two part study of Ekkad et al [20] [21], in which the impact of varying the compound angle from 30 to 90° was investigated. Ekkad et al showed that all compound angles increased laterally averaged film effectiveness, but the increased blockage of the mainstream led to an increase in the heat transfer coefficient at large compound angles. In combining the heat transfer coefficient and the effectiveness measurements, Ekkad et al showed that the optimum compound angle to minimise the heat flux to be around 45°.

The flowfield study of Lee et al [55] showed the jet from a hole with a compound angle in the range of 30° to 90°, to have only a single vortex in the downstream flowfield compared to the pair of vortices in the CRVP. This vortex was that leaving from the downwind edge of the hole shown in Fig. 2.8. McGovern and Leylek [66] investigated the flowfield computationally, and their velocity profiles at the hole exit showed that the cooling flow at the upwind edge was blocked by the mainstream. This suppressed the formation of the

upwind vortex and therefore only the downwind vortex was seen in the downstream jet.

2.1.9 Novel Cooling Hole Geometries

The film cooling studies discussed previously have only investigated the heat transfer characteristics of a given cooling hole, with little consideration of the associated aerodynamic losses due to mixing with the mainstream. The hypothesis of Sargison et al [87] was that tripping the boundary layer, and the associated increase in mixing and aerodynamic loss, could be avoided by ensuring the cooling jet was laminar.

The 'console' design, described by Sargison et al [87] [88], had a cross-section which expanded laterally from circular, but unlike the shaped hole the upper and lower walls converged. The overall effect was that the hole cross-sectional area reduced. This convergence meant the coolant flow was accelerated and consequently remained laminar or relaminarised if turbulent. Sargison et al showed that for a flat plate and an NGV model, that the 'console' design reduced the aerodynamic loss by more than 50% from that with a shaped hole, with a comparable level of heat transfer.

It was proposed by Bunker [10] that placing the exit of cylindrical holes in a shallow trench orientated normal to the mainstream flow, could produce an improved lateral spread of cooling. Similar reasoning also led to cratered holes, with a circular recess at the hole exit. A range of trench and crater geometries have subsequently been investigated by Waye and Bogard [99] and Lu et al [61] [62]. The downstream film effectiveness and heat transfer distributions presented, showed that although it was possible to reduce the heat flux compared to a cylindrical hole, both geometries still led to a higher heat flux than with a shaped hole. Additionally Lim et al [59] have shown a trenched hole to lead to an increase in aerodynamic loss compared to both cylindrical and shaped holes.

Kusterer et al [52] proposed that pairs of compound angled holes oriented in opposite directions could be used to create a CRVP with the opposite sense rotation to that downstream of a cylindrical hole. The intention of this design was that the normal velocity at the centre of the CRVP would be towards the blade surface, and so the separation of the jet from the blade surface would be reduced. Kusterer et al called this Double Jet Film Cooling (DJFC), and showed computationally that it was possible to create a CRVP of the opposite sense of rotation.

The idea of modifiying the vorticity in the CRVP from a cylindrical hole was also investigated by Heidmann and Ekkad [41] with their 'Anti-Vortex' hole design. Here smaller diameter side tubes branched away at compound angles from the main cylindrical hole. The sense of rotation of the vortices emerging from the side tubes was opposite to those of the CRVP in the jet exiting from the main hole. The hypothesis was that the neighbouring vortices would combine, and so reduce the strength of the CRVP. The surface effectiveness results of Dhungel et al [18] showed that it was possible to design an 'anti-vortex' hole that reduced the heat load compared to a cylindrical hole but not a shaped hole.

2.2 Unsteady Flowfield

The vast majority of film cooling studies have provided only time-mean measurements. In contrast, the case of a Jet in Crossflow (JICF) has been investigated with regard to the unsteady flowfield. The JICF differs from a typical film cooling case in that the hole length is generally long enough to develop fully developed pipe flow (L/D greater than 10) and the blowing ratio is usually larger than 2.0. Here only experimental studies that offer an explanation of the unsteady structures are discussed.

The four principal flowfield structures within a JICF that have been referred to are horseshoe vortices, wake vortices, shear layer vortices and the Counter Rotating Vortex Pair (CRVP), all of which are shown schematically in Fig. 2.9. Earlier the CRVP has been shown in Fig. 2.5 as a time-mean feature of the flowfield, but unsteady measurements, discussed here, show that it is likely to be influenced by coherent unsteady features of the jet.

The horseshoe vortices are caused by the roll-up of the boundary layer due to the adverse pressure gradient upstream of the jet leading edge, in the same way that horseshoe vortices form upstream of the leading edge of a turbine blade. Figure 2.10(a), taken from Fric and Roshko [24], shows smoke streaklines fed into the boundary layer upstream of a JICF. The horseshoe vortices are formed upstream of the jet, and are then swept around the jet to be orientated in the streamwise direction. The horseshoe vortices are subsequently broken down by the turbulence in the wake within half a hole diameter of the jet trailing edge. Morton and Ibbetson [71] make a similar statement to describe the downstream penetration, stating that they are insignificant by the side of the jet.

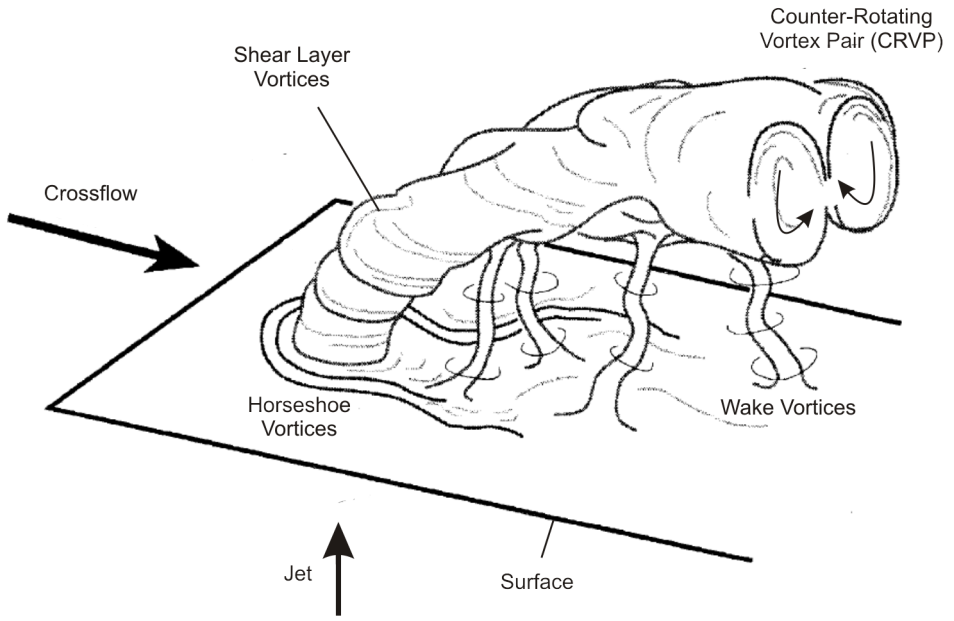

Figure 2.9: Schematic of the JICF with principal flow structures, taken from Fric and Roshko [24].

Wake vortices, shown in Fig. 2.10(b) using smoke visualisation, are vortices aligned normal to the blade surface which are observed in the wake under the jet core. The smoke in Fig. 2.10(b) was introduced into the boundary layer in the same way as in Fig. 2.10(a), and shows that the wake vortices are formed of boundary layer fluid. This mechanism was introduced by Fric and Roshko [24], who showed that wake vortices were caused by the separation of the boundary layer due to the adverse pressure gradient downstream of the hole.

Shear layer vortices have been seen to form in the shear layer between the jet and the mainstream, due to instabilities, in the same way that vortices form in the shear layer of a free jet [7] [15]. Figure 2.10(c) shows shear layer vortices in a JICF, using smoke streaklines introduced on the centreline upstream of the jet.

Ideally, film cooling jets will be attached to the downstream blade surface to provide high film effectiveness, and so wake vortices would not be able to form. Similarly the failure of horseshoe vortices to penetrate far beyond the jet trailing edge means that they would not be expected to significantly affect the downstream flowfield. Consequently this review focuses on the shear layer vortices and the CRVP which are believed to be most relevant to film cooling flows.

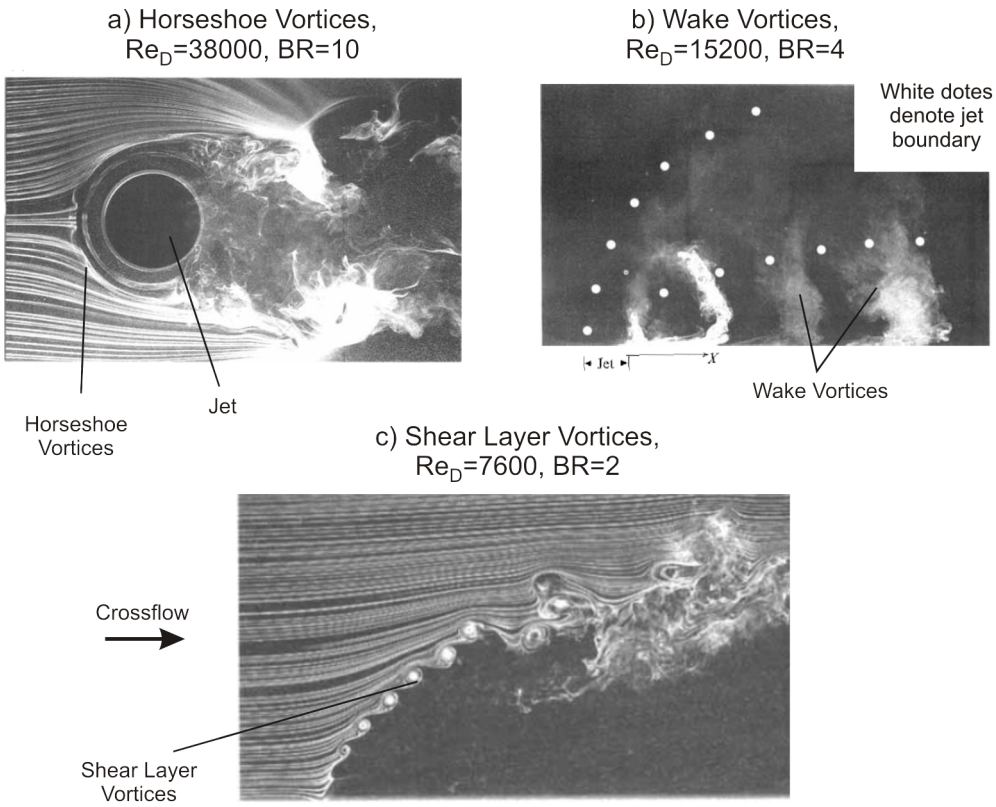

Figure 2.10: Smoke visualisation of (a) horseshoe vortices, (b) wake vortices and (c) shear layer vortices, from Fric and Roshko [24].

Limited computational evidence has also been presented by Tyagi and Acharya [97] for the existence of coherent hairpin vortices in film cooling jets. These are the same structures as seen experimentally by Matsuda et al [65] for the case of a wall jet, and are described at the end of this part of the literature review.

2.2.1 Shear Layer Vortices

Vortices in the shear layer between two fluids are the result of a Kelvin-Helmholtz instability [6] [23]. A Kelvin-Helmholtz instability is initiated by velocity perturbations normal to the shear layer. Vorticity is present in the shear layer due to the velocity difference in the shear layer. Perturbations cause the vorticity to become concentrated in discrete locations and so form the characteristic vortices shown in Fig. 2.10(c).

Kelso et al [46] have used smoke injected into the boundary layer of the jet upstream of the hole exit to visualise the shear layer vortices. Their image of a jet with a blowing ratio of 2.2 is shown in Fig. 2.11(a). The red smoke in Fig. 2.11(a) was released into the pipe boundary layer at the leading edge 0.06D before the exit plane, and forms distinct vortices

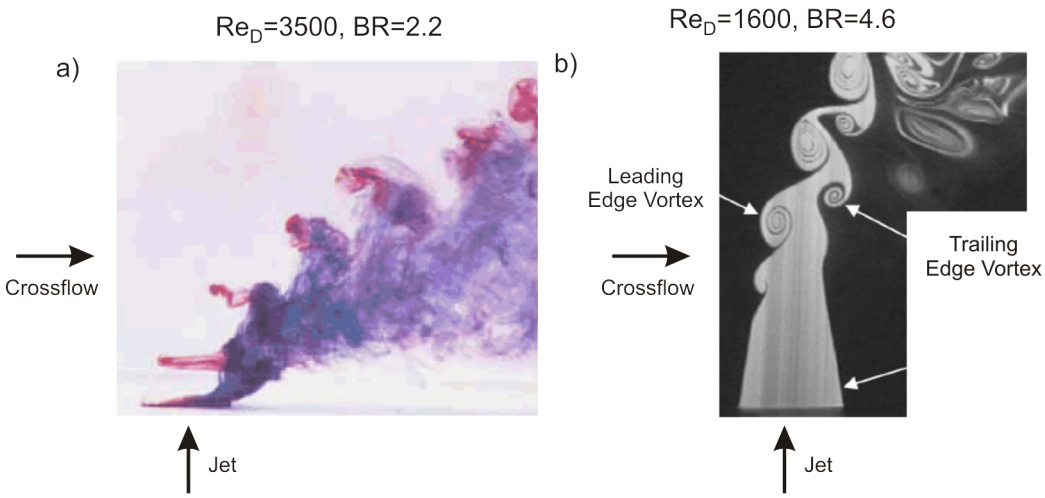

Figure 2.11: Shear layer vortices in the jet from a cylindrical hole, (a) from Kelso et al [46] and (b) from Lim et al [60].

perpendicular to the jet axis. For now the reader is asked to ignore the purple smoke, as this will be discussed later in the section in regard to the CRVP formation.

A centreline illumination of a jet of BR equal to 4.6 obtained by Lim et al [60] is shown in Fig. 2.11(b). To obtain the image Lim et al seeded the jet with fluorescein dye and illuminated it with a laser light sheet. The sheet illumination shows that shear layer vortices also form on the trailing face of the jet. However, the vortices do not appear to be symmetrical across the jet, with those on the trailing face beginning further from the hole exit than those on the leading face.

The passing frequency (f) of the shear layer vortices in Fig. 2.11 can be non-dimensionalised to form a Strouhal number, as shown in Eq. 2.9, where λ is the spatial distance between the vortices. Table 2.1 details the Strouhal number estimated for the shear layer vortices shown in Fig. 2.11 and for images presented within other studies. Visual inspection of Tab. 2.1 shows that the Strouhal number appears largely independent of BR and, although there are some outliers, there may be a rise with an increase in the jet and mainstream Reynolds number.

$$St = \frac{fD}{V} = \frac{D}{\lambda} \tag{2.9}$$

Andreopoulos [4] also investigated shear layer vortices within the shear layer of a JICF using Hot Wire Anemometry. This was conducted at a mainstream Reynolds number of $41{\times}10^3$, which is an order of magnitude higher than the studies listed in Tab. 2.1. At

Study	BR	$Re_{D,c}$	$Re_{D,\infty}$	St= $\frac{D}{\lambda}$ (est.)
Lim et al [60]	4.6	1600	350	1
Kelso et al [46]	2.2	3500	1600	1
Kelso et al [46]	4.0	6400	1600	2
Haven and Kurosaka [36]	1.6	3000	1900	1
Fric and Roshko [24]	2.0	7600	3800	2
Andreopoulos [4]	4.0	5100	1300	1

Table 2.1: Strouhal number of the passing of Shear Layer Vortices within a JICF. Estimated from images in the respective studies.

this mainstream Reynolds number, Andreopoulos showed that the Strouhal number was independent of the jet Reynolds number and had a constant value of 0.4.

Comparing the two images in Fig. 2.11 it is apparent that for the case of BR equal to 2.2 the shear layer vortices were present at the jet exit plane, however at the higher BR of 4.6 the shear layer vortices did not form until 1D from the hole exit. Kelso et al [46] and Haven and Kurosaka [36] both present evidence for a unsteady vortex at the leading edge of the hole, which they referred to as a 'hovering vortex'.

The smoke visualisation images shown in Fig. 2.12 show a hovering vortex at the exit plane of a square hole obtained by Haven and Kurosaka. The vortex was shown to form within the separated region immediately upstream of the hole exit. This separated region was only present at lower BR, and arised due to the capping effect of the crossflow upon the lower momentum jet. The hovering vortex is shown to occur inside the separated region in the first image of Fig. 2.12, whilst in the second image the vortex has been shed into the jet as a shear layer vortex.

The study of New et al [72], in which elliptical holes were investigated in addition to a cylindrical hole, showed that the aspect ratio of the hole also influenced whether vortices were formed due a hovering vortex at the leading edge. Figure 2.13 shows for an elliptical hole of low aspect ratio, where the minor axis was perpendicular to the crossflow, that shear layer vortices were observed immediately downstream of the hole exit, suggesting that a hovering vortex was present. In contrast for the same BR, for a hole of high aspect ratio, New et al show a laminar shear layer which subsequently broke down to shear layer vortices.

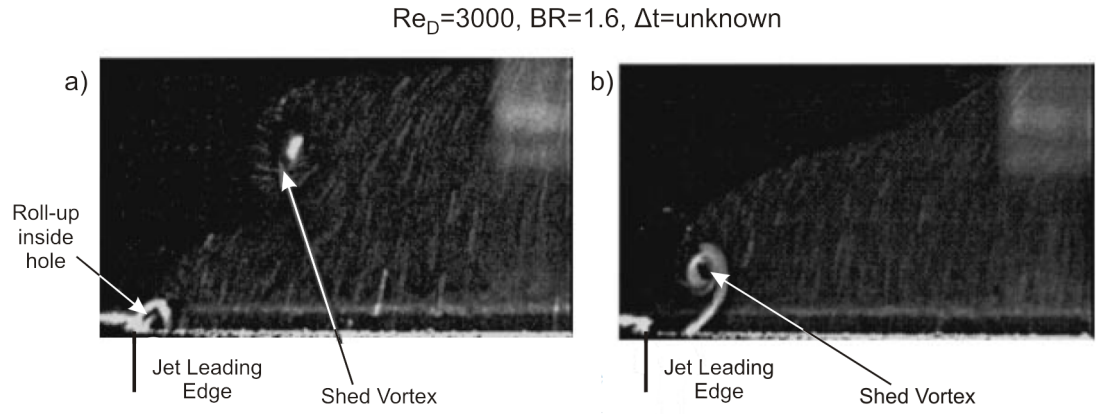

Figure 2.12: Hovering vortex at the leading edge of the exit of a square hole, from Haven and Kurosaka [36].

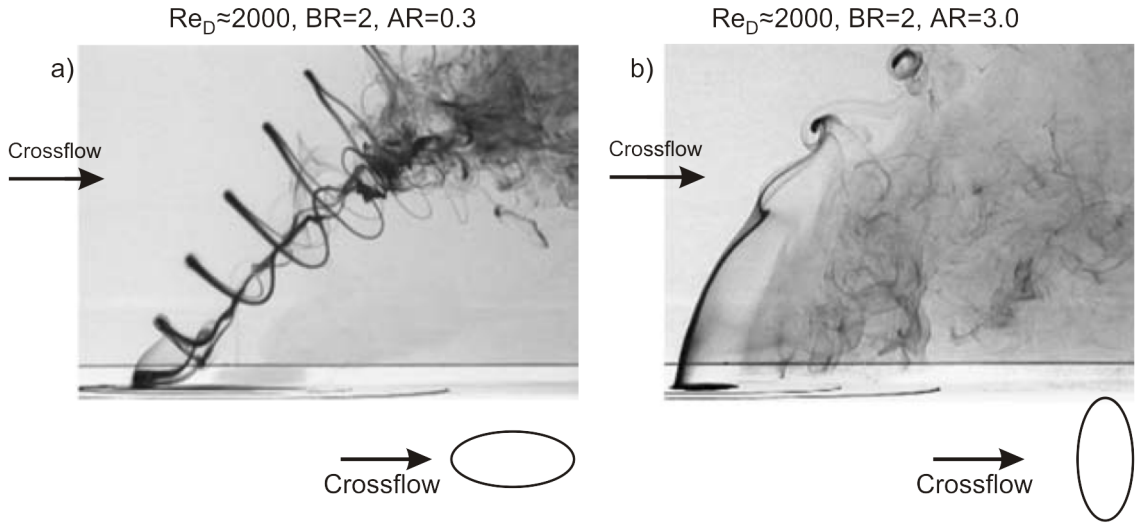

Figure 2.13: Shear layer vortices for elliptical holes of differing aspect ratio (AR), from New et al [72].

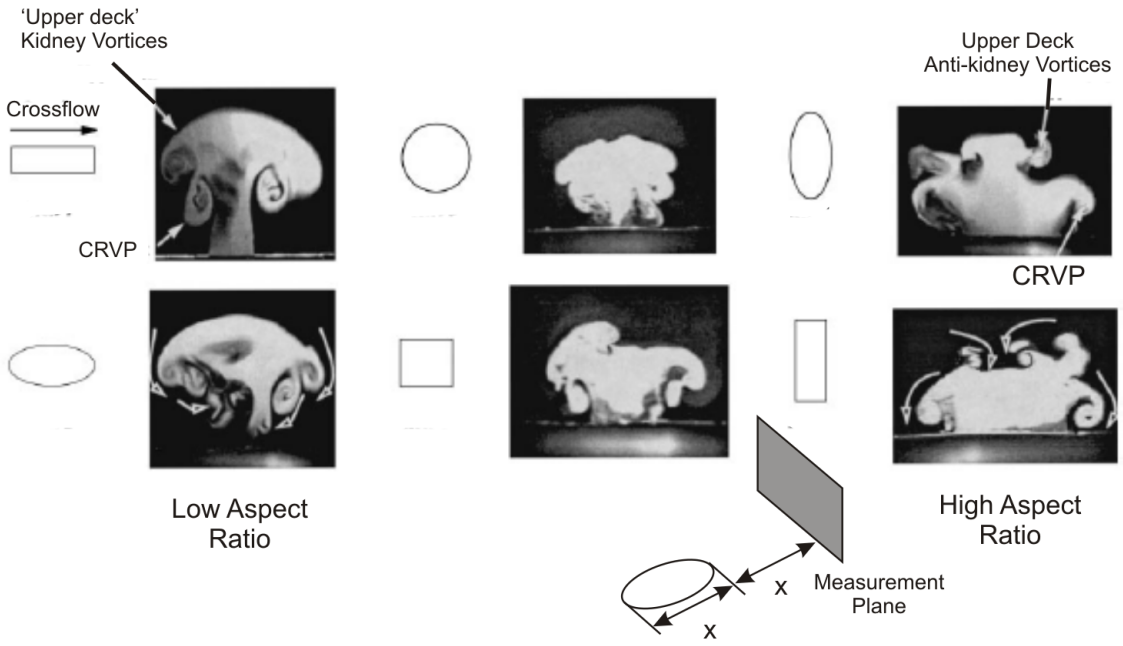

Figure 2.14: Smoke visualisation in the secondary flow plane downstream of the hole exit for changing aspect ratio at a BR equal to 1.6, from Haven and Kurosaka [36].

Haven and Kurosaka [36] first drew attention to the existence of unsteady secondary vortices orientated in the direction of the jet above the CRVP in their study of holes of differing aspect ratio. The initial intention of the authors was to investigate if, by increasing the aspect ratio of the hole, the vortices in the CRVP would be moved further apart from each other and so reduce their impact

Figure 2.14 shows smoke visualisation plots for six different hole geometries, those on the left had a low aspect ratio and those on the right had a high aspect ratio. Haven and Kurosaka highlighted a pair of vortices that appeared above the CRVP, which they named upper deck vortices. For holes of low aspect ratio the upper deck vortices had the same sense of rotation as the CRVP, but at higher aspect ratios their sense of rotation was reversed. Consequently Haven and Kurosaka, on account of the CRVP being often referred to as a kidney vortex, described them respectively as either kidney or anti-kidney vortices. Instantaneous vorticity plots obtained using Particle Image Velocimetry (PIV) showed that the upper deck vortices were unsteady. The kidney vortex (same rotation as the CRVP) had a passing frequency of 5Hz, which based on the jet velocity and hole width equalled a Strouhal number of 1.2. However, no evidence for a characteristic passing frequency was presented by Haven and Kurosaka for the anti-kidney vortex.

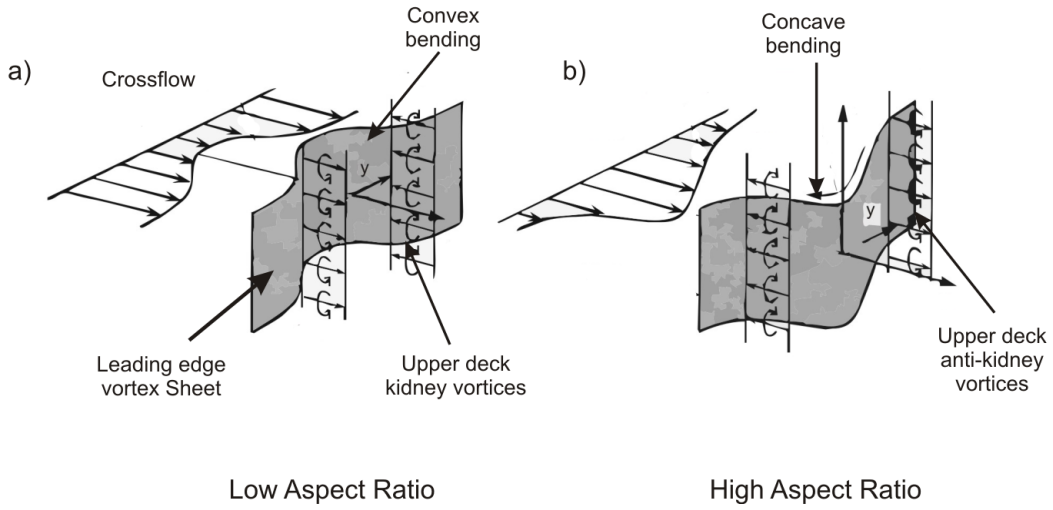

Figure 2.15: Warping of the leading edge vortex sheet with change in the hole aspect ratio, from Haven and Kurosaka [36].

Viewing the jets shown in Fig. 2.14 in the centreline plane Haven and Kurosaka saw that the jets from holes of a higher aspect ratio separated less from the surface. Haven and Kurosaka attributed this reduction in separation to the anti-kidney vortices canceling out a fraction of the vorticity within the CRVP. Haven and Kurosaka proposed that the sense of rotation of the upper deck structures depended on the bending of the vortex sheet at the leading edge of the jet. A low aspect ratio hole would have high 'resistance' to the crossflow and so would bend in the convex manor shown in Fig. 2.15(a). In contrast a high aspect ratio hole, which has a larger surface exposed to the crossflow, would offer less resistance and bend in the concave manor shown in Fig. 2.15(b). The concave bending leads to upper deck anti-kidney vortices to be seen in secondary flow plane shown in Fig. 2.14, while the upper deck kidney vortices are the result of convex bending.

2.2.2 Counter Rotating Vortex Pair (CRVP)

The formation of the CRVP has been the subject of much research and a number of formation mechanisms have been proposed. Andreopoulos [4] suggested that the CRVP is formed due to the folding of the shear layer vortex loops. Morton and Ibbetson [71] proposed a detailed mechanism to show how the boundary layer vorticity in the jet and on the surface combine to form the CRVP. In both cases insufficient experimental evidence was provided for these mechanisms to be confirmed. The studies of Lim et al [60] and New et al [72]

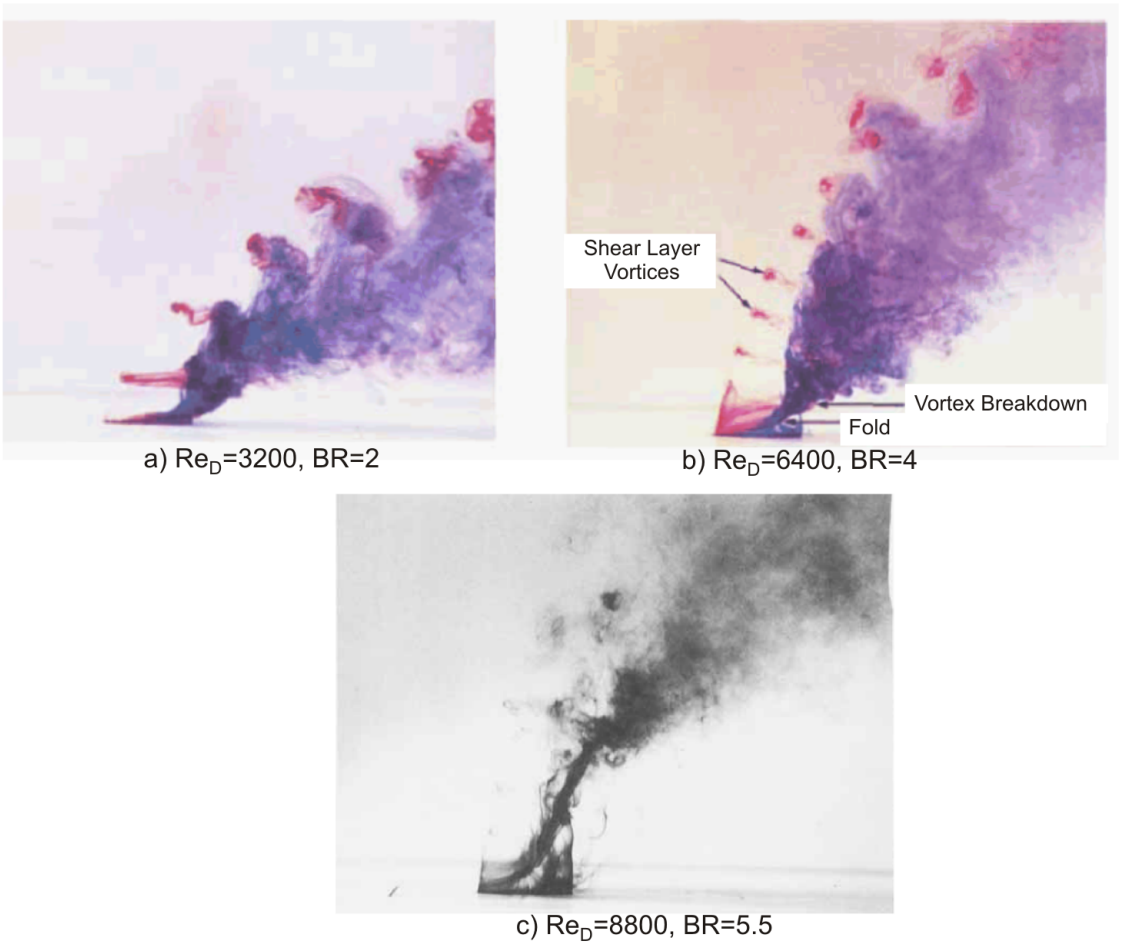

Figure 2.16: Smoke visualisation in which purple smoke is injected into the in-hole boundary layer upstream of the exit plane, from Kelso et al [46].

propose a further mechanism based on the reorientation of the shear layer vortices, and provide detailed smoke visualisation to support their ideas.

Figure 2.16 shows smoke visualisation images for jets of increasing blowing ratio from 2.2 to 5.5 presented by Kelso et al [46]. The image at BR equal to 2.2 is the same as that included in Fig. 2.11, however in this case it is the purple smoke that will be discussed. It should be noted that in the black and white image (Fig. 2.16(c)) only purple smoke was present. The purple smoke was fed into the jet boundary 1.6D upstream of the hole exit plane around the entire jet circumference. In contrast the red smoke was only injected at the leading edge.

When the BR was 2.2, Fig. 2.16 shows that all the purple smoke exited the hole close to the trailing edge of the jet, and immediately spread out to encompass the majority of the jet core. Figure 2.16 shows that increasing the BR to 4 and 5.5 moved the exit position

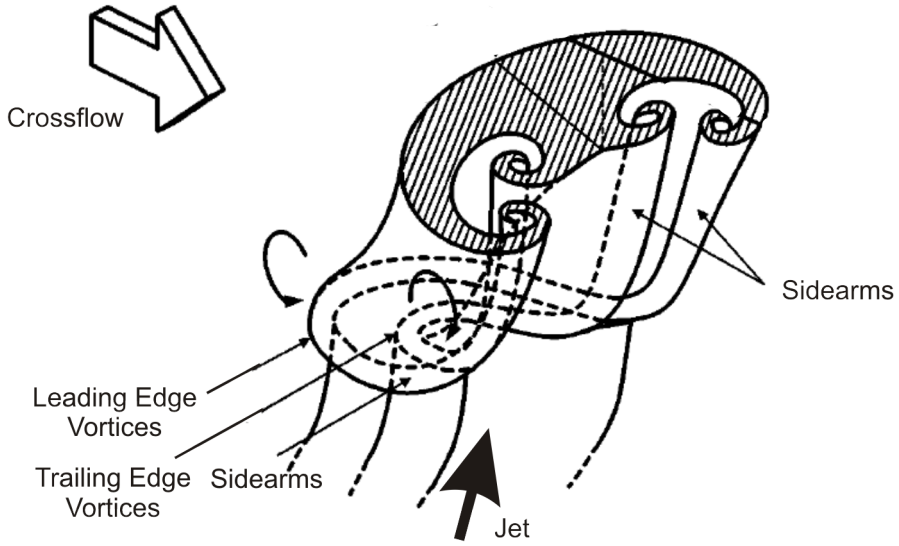

Figure 2.17: Schematic of the formation of the CRVP, based on images of a jet of BR equal to 4.6 and Re_D equal to 1600, from Lim et al [60].

of the purple smoke closer to the leading edge of the hole. In these cases a distinct column of smoke can be seen close to the hole exit. Kelso et al attributed this column of smoke to a folding of the jet vortex sheet due to the presence of the external crossflow. With increasing distance from the hole the vortex caused by the folding process suffered a vortex breakdown, beyond which the smoke spread out to cover the entire jet cross section.

In addition to the sheet illumination shown in Fig. 2.11, Lim et al [60] also seeded the jet of BR equal to 4.6 using only dye in the boundary layer upstream of the hole exit. Based on these results with smoke visualisation, Lim et al drew the schematic shown in Fig. 2.17. Figure 2.17 shows that the leading edge and trailing edge shear layer vortices, discussed previously, are not in fact one continuous vortex loop and instead both twist into sidearms which are then re-orientated in the direction of the jet. The two vortices within the side arms then merge with the CRVP which was initiated by the folding of the vortex sheet.

New et al [72], as mentioned previously continued the study of Lim et al [60] to investigate an elliptical hole of varying aspect ratio. Sheet illumination of the dye-seeded jet in the secondary flow plane showed that unsteady upper deck vortices were present as was shown by Haven and Kurosaka [36]. However, based on the images obtained, New et al suggested that the kidney and anti-kidney upper deck structures, seen by Haven and Kurosaka, were in fact different unsteady structures.

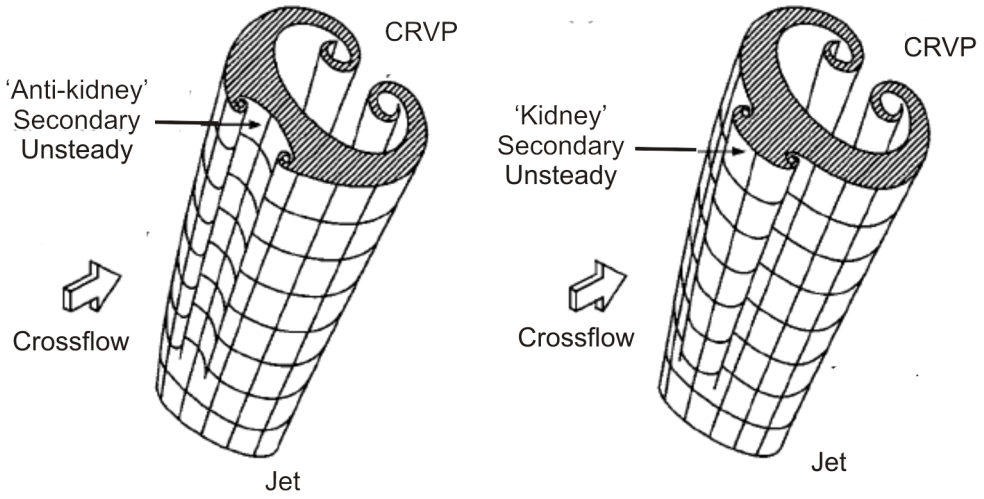

Figure 2.18: Leading edge secondary unsteady structures from New et al [72].

New et al noted that the upper deck kidney structures, which were only highlighted by Haven and Kurosaka for the low aspect ratio case, always seemed to form on the sides of the jet regardless of the aspect ratio. Based on this observation New et al attributed these as being the side arms of the leading edge vortices shown in Figure 2.17 and christened them primary unsteady structures. New et al agreed that the anti-kidney vortices, shown by Haven and Kurosaka for high aspect ratio holes, were formed by bending of the leading edge vortex sheet, but found that either sense of rotation could occur - even at the same BR. New et al named the anti-kidney vortices to be a secondary unsteady vortex pair and concluded that they could have either sense of rotation, as shown schematically in Fig. 2.18, but that they were only present for holes of high aspect ratio.

2.2.3 Computational Modelling

Steady RANS computational modeling, with both isotropic and anisotropic turbulence models, has been stated earlier in this review to be a poor predictor of the downstream film effectiveness. The possible existence of coherent unsteady structures, such as those introduced in this review, could be a contributing factor in this discrepancy.

Unsteady RANS (U-RANS) modeling, in which the computational model is solved in time but still with a turbulence model, has not been widely used in studies of film cooling. The tendency instead has been towards modeling using LES (Large Eddy Simulation). In addition to solving in time, the larger scales of turbulence are resolved explicitly in LES

with turbulence modeling used only for the smallest scales of turbulence.

Yuan et al [103] was one of the first studies to model a JICF using LES. The results presented for a blowing ratio of 3.0 showed that LES was able to match the salient features of the rms velocity profiles and the time-mean velocity profiles. Whilst the vorticity iso-surfaces were consistent with the schematic in Fig. 2.17, showing the presence of both leading and trailing edge vortices, and the sidearms.

The increase in grid density and the requirement to solve in time means that the number of computations is far larger for an LES model than a steady RANS model. However, the continual reduction in the cost of computing means that it is now considered practical to use LES for single hole film cooling studies. Tyagi and Achraya [97], Renze et al [83] and Peet and Lele [74] have all compared their LES results with the film effectiveness measurements of Sinha et al [91] for a blowing ratio of 0.5. These comparisons show their LES models to predict the film effectiveness distributions obtained by Sinha et al to within 5%. This is better than the previously introduced steady RANS model of Leylek and Zerkle [58], which had differences of up to 30%.

2.2.4 Hairpin Vortices

The LES study of Tyagi and Acharya [97] also showed the existence of a coherent unsteady structure in the jet downstream of a cylindrical hole with a blowing ratio of 1.0. The hole had a length of 6D, inlet and exit inclination angles of 35° and was fed from a plenum chamber. Figure 2.19(a), which shows iso-surfaces of vorticity, shows the vortices to emerge from the hole orientated in the spanwise direction. These vortices then became orientated in the streamwise direction as the jet flowed away from the hole. The sense of rotation of the streamwise vortices was the same as the CRVP. The passing frequency of the structures estimated from Fig. 2.19(a) was of a Strouhal number of approximately 0.8.

Matsuda et al [65] studied a wall jet in which a circular jet was ejected parallel to a surface with no external crossflow. Using Hot Wire Anemometry, Matsuda et al measured changes in the lateral velocity and built up the schematic shown here as Fig. 2.19(b). The hairpin structure, with a vortex initially in the lateral direction being re-orientated into the streamwise direction is the same as that shown computationally by Tyagi and Acharya [97]. The Strouhal number of the passing of the hairpin vortices was found by Matsuda et al to

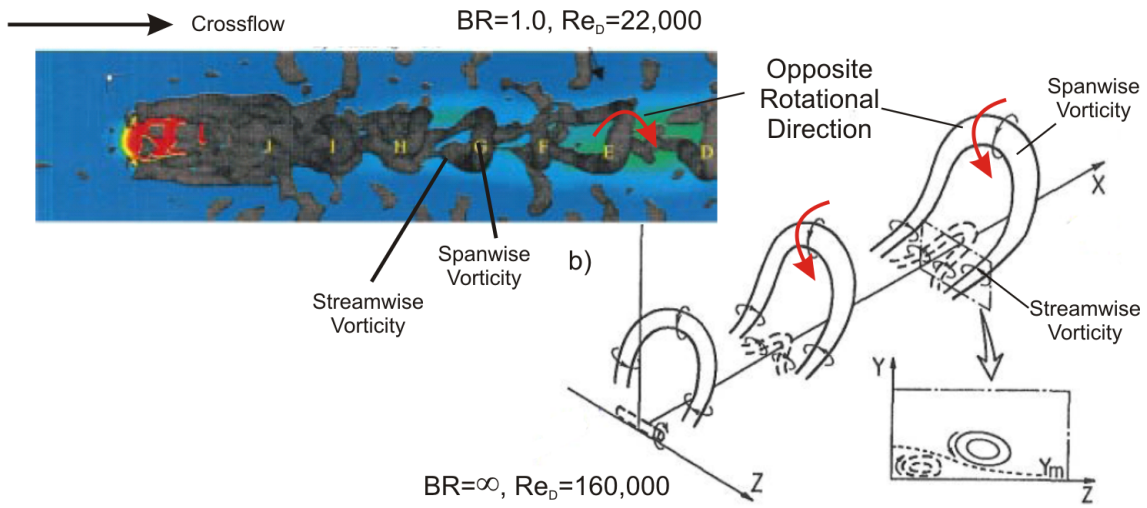

Figure 2.19: Hairpin vortices (a) in a film cooling jet from an LES computation of Tyagi and Acharya [97] and (b) in a wall jet with schematic based on Hot Wire measurements from Matsuda et al [65].

be 0.5, with the sense of rotation being the opposite of that obtained by Tyagi and Acharya. The difference in the sense of rotation can be explained by the change in the direction of the velocity gradient across the shear layer.

2.3 Summary

Within this review the datum cooling hole design in open literature has been shown to be a cylindrical cooling hole. Cylindrical holes, away from the leading edge region, are typically inclined at approximately 30° to the downstream surface, with a blowing ratio of less than 2.0. Investigations of the time-mean flowfield have shown that the jet emerging from the cooling hole will separate from the downstream surface for a blowing ratio greater than 0.5. Within the jet core two counter rotating vortices, referred to as a CRVP, draw mainstream fluid onto the surface. Separation and the CRVP both have an adverse effect on the film effectiveness downstream of the cooling hole.

Shaped holes with a diffusing exit reduce the jet momentum and so alleviate the separation of the jet seen for a cylindrical hole. Additionally the increased lateral expansion leads to a more uniform lateral spread of coolant.

The flow condition at the entry of the cooling hole impacts upon the separation bubble formed downstream of the hole inlet. These changes influence the time-mean flowfield

downstream of the hole exit. It has been shown that perpendicular internal crossflow, which is of the same orientation as the serpentine passage within a turbine blade, can have a detrimental impact on the performance of a shaped hole.

The poor performance of steady RANS calculations in predicting downstream film effectiveness compared to unsteady LES computations, suggests that there may be some coherent unsteadiness within film cooling jets. It has also been shown that hairpin vortices may be present, which have been seen experimentally for the case of a wall jet. Similarly studies on the unsteady flowfield about the Jet in Crossflow have shown coherent shear layer vortices and proposed a mechanism by which these merge with the CRVP.

The current research aims to characterise the coherent unsteadiness occurring in film cooling flows. The research discussed in this review suggests that coherent unsteadiness is present in film cooling flows. However, for geometries typical of film cooling there has so far been only one unsteady computational study, at only one flow condition, which has explicitly investigated coherent unsteadiness. To improve the understanding of film cooling flows, there is clearly a need to characterise the occurrence of coherent unsteadiness across a wider range of flow conditions.

The time-mean results in this review have shown that the flow conditions at the hole inlet have an impact on the flowfield downstream of the hole exit. Coherent unsteadiness is also likely to be affected by changes in the hole inlet condition, and thus it is important in the current study to consider the perpendicular crossflow configuration which is typically used on a turbine blade. Changes in the flow condition at the hole inlet will also vary the in-hole flowfield. No unsteady investigations of the flowfield inside a cooling hole have been performed. Therefore the aim of the current study to investigate the presence of coherent unsteadiness inside the hole is of relevance, as coherent unsteadiness arising here may impact upon that in the downstream jet.

On considering the results of previous studies there appears to be a clear justification for the current investigation, where coherent unsteadiness inside and downstream of the hole will be investigated for a range of hole inlet conditions. These results should provide a first step in establishing the importance of coherent unsteadiness to film cooling design.

Chapter 3

Experimental Facility

The experimental work conducted for this thesis was undertaken on the Oxford Super Scale Cascade at the University of Oxford's Southwell (Osney) Laboratory. Film cooling research had not been previously undertaken on this facility, and the modifications made to include film cooling are described in this chapter.

This chapter opens by introducing the Super Scale Cascade in more detail, before explaining the chosen location for the cooling holes upon the blade surface. The geometries of the two chosen cooling hole configurations are then detailed. Two types of cooling hole inlet were to be investigated, firstly that of an 'ideal' case in which the holes were fed from a plenum chamber with an inlet inclination angle of 90°, and secondly from an internal crossflow channel intended to mimic the serpentine passage upon a turbine blade. The necessary modifications to the facility, the desired range of operation and the uncertainties in measuring the flow condition are detailed.

3.1 Oxford Super Scale Cascade

The Oxford Super Scale Cascade was constructed previously by Palafox [73], and a plan view of the facility is shown in Fig. 3.1. Air is drawn into the cascade through a bellmouth intake and passes through a series of screens and flow straighteners. The horizontal and vertical beams present downstream of the intake within the investigation of Palafox were removed. The flow then enters the three passage linear cascade which features blades with a true chord equal to 1m and a span also equal to 1m. The blades are the low speed version of the RT27a blade which have been used previously by Gregory-Smith and Cleak [30]. The

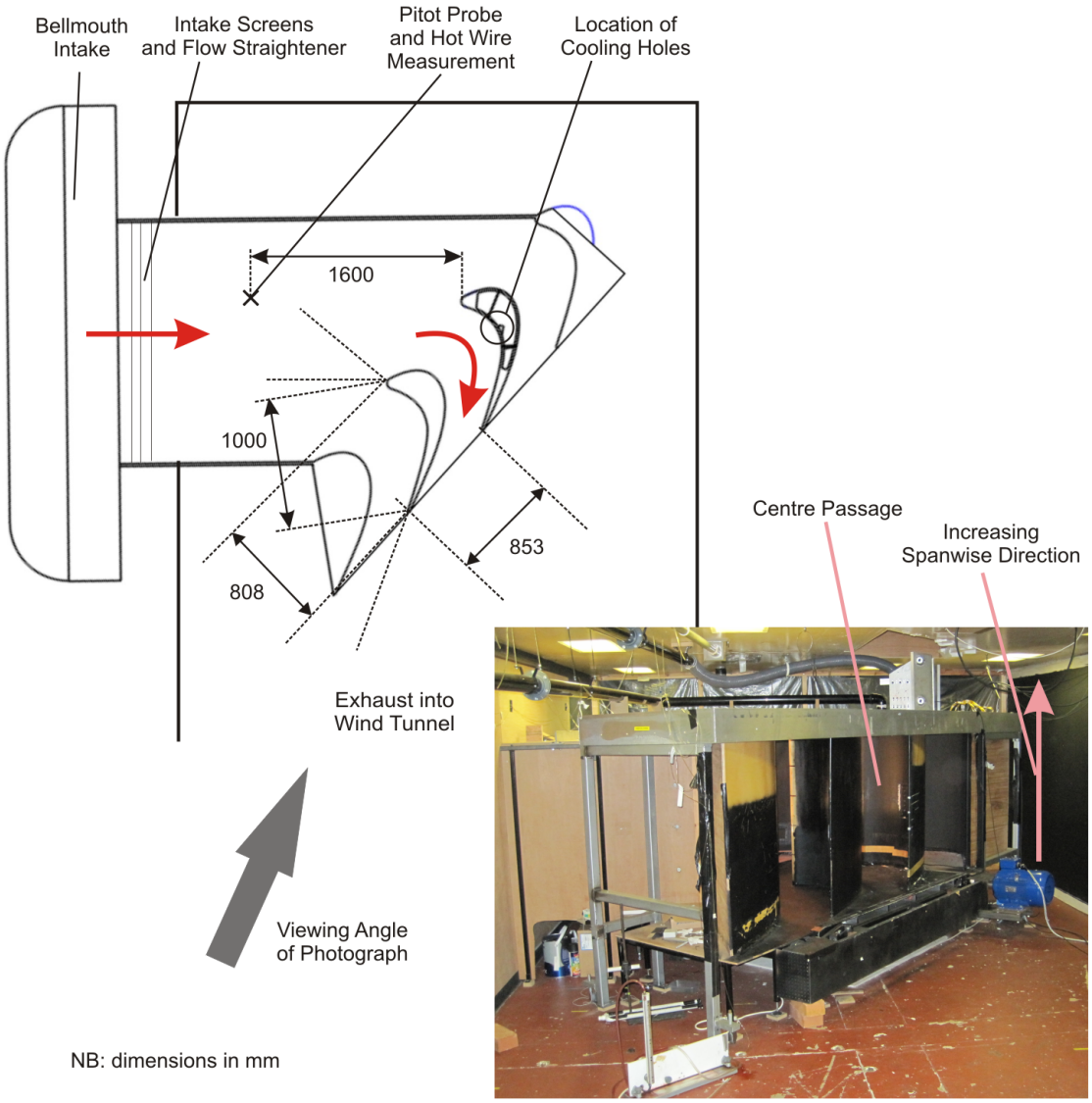

Figure 3.1: The Oxford Super Scale Cascade, (a) plan view of the cascade and (b) photograph looking towards the cascade exit plane.

profile of the low speed RT27a blade means that the C_p profile of the high pressure RT27a turbine blade can be matched in a low speed environment. The blades were flush to both endwalls so there was no tip gap present. On exiting the cascade the flow exhausts into a 4m by 2m wind tunnel, which has two fans located approximately 10m downstream of the cascade exit. A photograph looking towards the cascade trailing edge is also shown in Fig. 3.1 to show the scale of the cascade within the 4m by 2m wind tunnel.

The cascade exit Reynolds number used during the current investigation was an engine realistic 6×10^5, based on the cascade exit velocity and blade true chord, as shown in Eq. 3.1. Where V_e is the cascade exit velocity and C the blade true chord. During operation the exit

Reynolds number was adjusted using the wind tunnel speed control unit which was able to vary the pitch of the wind tunnel fan blades.

$$Re_e = \frac{\rho_\infty V_e C}{\mu} = \frac{\sqrt{2\rho_\infty (p_{01} - p_e)} C}{\mu} \tag{3.1}$$

The ideal gas equation was used to find the density (ρ) and an interpolation based on data-table values was used to calculate the dynamic viscosity (μ) from the static temperature. The static temperature was measured using a K-type thermocouple on the wall of the cascade upstream of the blades. The absolute pressure was measured using a mercury barometer within the control cabin next to the wind tunnel.

The low speed nature of the cascade (Mach No. < 0.03) meant that the flow could be considered incompressible with the cascade exit velocity (V_e) found according to the Bernoulli equation as shown in Eq. 3.2.

$$V_e = \sqrt{\frac{2(p_{01} - p_e)}{\rho}} \tag{3.2}$$

Here p_{01} is the total pressure measured 1.6m upstream of the blade leading edge, as shown in Fig. 3.1, at 75% span. The exit static pressure (p_e) was measured on the endwall of the cascade (100% span) at mid-pitch of the exit plane of the centre passage. The pressure differential was of the order of 50Pa, and was measured using a Sensortechnics HCLA02X5 0-250Pa pressure transducer.

The turbulence intensity (Tu), calculated according to Eq. 3.3, was measured to be 2% at midspan 1.6m upstream of the blade leading edge. The turbulence intensity was measured using the Hot Wire Anemometry setup described in the next chapter.

$$Tu = \frac{V_{rms}}{V} \tag{3.3}$$

The blade surface pressure coefficient (C_p) was calculated according to Eq. 3.4, where the inlet total pressure and exit static pressure were measured as stated previously.

$$C_p = \frac{p_{01} - p}{p_{01} - p_e} \tag{3.4}$$

Palafox [73] presented a C_p distribution obtained using static pressure tappings on both blade surfaces at 10% span. The C_p profile for the current study on the pressure surface is

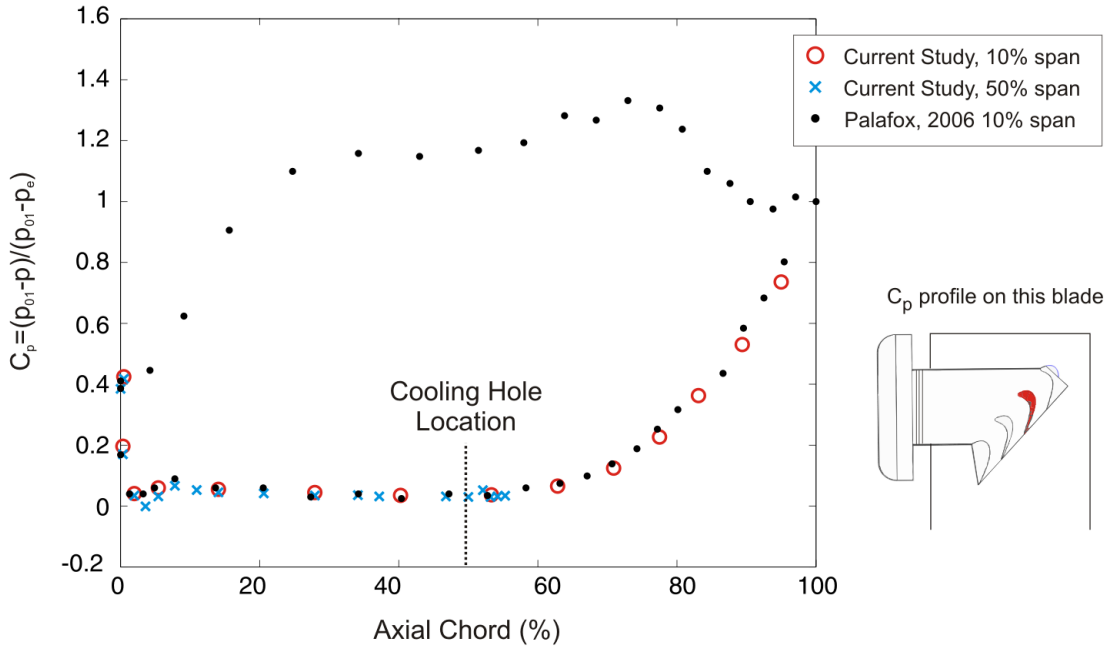

Figure 3.2: Blade pressure surface C_p profile at 50% and 10% span compared to Palafox [73].

Property	Current Value
Blade Chord - C (mm)	1000
Blade Axial Chord (mm)	808
Blade Span (mm)	1000
Blade Pitch (mm)	853
Exit Reynolds number - Re_e (-)	6×10^5
Inlet Turbulence Intensity (%)	2

Table 3.1: Oxford Super Cascade Geometry and Test Conditions.

shown in Fig. 3.2 for 10% and 50% span. It is seen that there was no significant variation in C_p between these two spanwise locations or with respect to the previous measurements of Palafox.

The low speed nature of the cascade meant that the pressure differential between the inlet total and the static pressure on the blade pressure surface was often less than 3Pa. To minimise the uncertainty in this measurement a Furness Controls FCO332 low pressure transducer with a range of 0-30Pa was used. This transducer had a measurement uncertainty of less than 1% for pressure differentials down to 1Pa.

The geometry of the Oxford Super Scale Cascade and the operating point of the current investigation, which have been explained in this section, are summarised in Table 3.1.

3.2 Plenum Fed Cooling Holes

3.2.1 The Cooling Hole Location

On high pressure turbine blades film cooling holes are predominantly located around the blade leading edge and on the pressure surface. The majority of previous film cooling research has been on a flat plate, and therefore most applicable to a blade surface away from the leading edge. The geometry of the cascade also limited the locations that could be investigated using the chosen measurement techniques to those locations downstream of the leading edge region.

On account of these two factors it was decided to place the cooling holes on the pressure surface at 50% axial chord. The cooling hole location has been highlighted in the cascade plan view in Fig. 3.1 and on the C_p distribution in Fig. 3.2. To simulate the effect of a row of cooling holes, rather than a single cooling hole, a row of five cooling holes was included. The centre hole of the five cooling holes was located at blade mid-span to minimise the impact of any secondary flow features generated in the endwall regions.

On account of the velocity gradient across the passage between the turbine blades, it was not possible to determine the boundary layer thickness at the cooling hole location based on the usual definition, whereby the velocity is 99% of that in the mainstream. The C_p profile in Fig. 3.2 shows that there was negligible pressure gradient upstream of the cooling holes. Consequently boundary layer growth was estimated based on the models for a flat plate.

The C_p at 50% axial chord was 0.032 and this was used to obtain the local mainstream velocity (V_∞). The upstream development length for the local boundary layer was made equal to the surface distance upstream of the cooling hole which was 0.5m. Using these parameters the surface Reynolds number was calculated to be 7×10^4, which was lower than the Reynolds number of 5×10^5 for transition on a flat plate [64]. Therefore the boundary layer was assumed to be laminar and its thickness estimated to be 0.8D.

The velocity profile in the boundary layer at 50% axial chord on the mid-span section of the pressure surface with no cooling holes included is shown in Fig. 3.3. The velocity profiles were obtained using the Particle Image Velocimetry (PIV) and Hot Wire Anemometry (HWA) techniques described in the following chapter. The distance normal to the surface

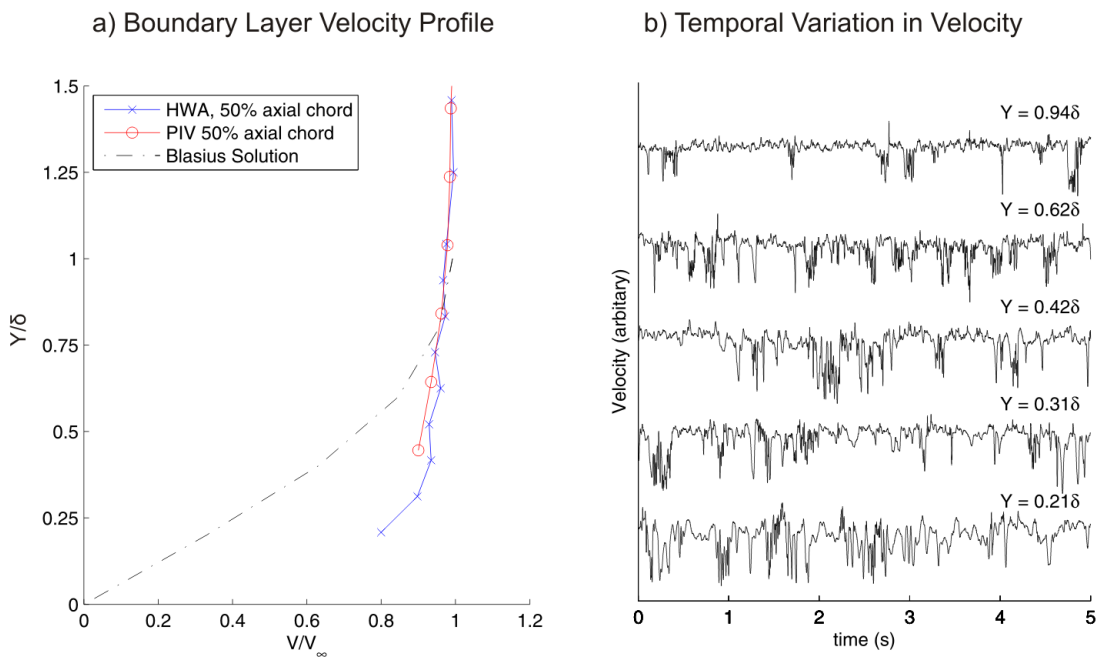

Figure 3.3: (a) The boundary layer velocity profile at 50% axial chord of the mid-span section of the pressure surface with no cooling holes. (b) Temporal variation in velocity with time within the boundary layer. Obtained using PIV and HWA.

(Y) has been normalised using the laminar boundary layer thickness (δ).

The Blasius solution for a laminar boundary layer is also included in Fig. 3.3. It can be seen that the current experiment had a fuller velocity profile close to the blade surface than the Blasius solution. The temporal variation in velocity, is also shown in Fig. 3.3 for five points in the boundary layer. The fluctuations in the velocity shown in these traces, suggest that the boundary layer profile was actually turbulent or transitional rather than laminar.

The velocity profile in the boundary layer was approximated with an exponential curve and the shape factor (δ^*/θ) was calculated to be 1.9. Here δ^* was the displacement thickness and θ was the momentum thickness. A shape factor of 1.9 denotes that the boundary layer is in a transitional state [90]. Mee et al [67] have presented boundary layer profiles about the high speed version of the RT27a blade used in this study, and their measurement of the shape factor at 62% axial chord on the pressure surface similarly indicated a transitional boundary layer.

3.2.2 Geometry of the Cooling Holes

The literature review has shown that the two cooling hole geometries typical of the location chosen for the cooling holes are cylindrical and shaped holes with an exit inclination angle of around 30°. Consequently within the current study both of these hole geometries were chosen for investigation.

To permit the cooling holes to be easily interchanged they were manufactured into removable modules made using stereolithography, as shown in the upper half of Fig. 3.4. Manufacturing using stereolithography was the best way to match the surface curvature of the blade. To receive the module a hole was cut into the blade surface. Along the spanwise edges of this hole supporting plates were added to support the rear of the removable module. Plasterscene was used to seal any gaps between the edge of the removable module and the blade surface.

The cooling hole geometries are shown in the lower half of Fig. 3.4. Here cross-section A is a spanwise plane and cross-section B is a plane with its axes in the spanwise direction and that of the hole axis.

The hole diameter (D) was used to non-dimensionalise the other dimensions in Fig. 3.4 and was set at 12mm to maintain the same ratio of true chord to hole diameter as in a typical high pressure turbine blade. The exit inclination angle of 30° was defined with respect to a plane tangent to the blade surface at its intersection with the hole axis. The hole length was 6D and the pitch spacing of the five cooling holes in the row was 3D. The shaped hole had a 14° lateral angle and 7° laidback angle, which began respectively 3D and 1D upstream of the hole exit centre. The inlet inclination of both cooling holes was 90°, which as shown in the literature review represents an 'ideal' inlet with minimal separation.

3.2.3 Coolant Supply

The blades within the cascade as detailed by Palafox [73] were hollow with a flexible plywood sheet fitted to the six ribs evenly spaced along the blade span. Within the current experiment the blade interior was turned into a plenum chamber to fed the cooling holes. As shown in Fig. 3.5 the plenum chamber extended from 20 to 100% span and from 0 to 70% axial chord. Plywood dividers were used to separate off the plenum from the sections of the blade that were not part of the plenum chamber, with plasterscene used to fill any

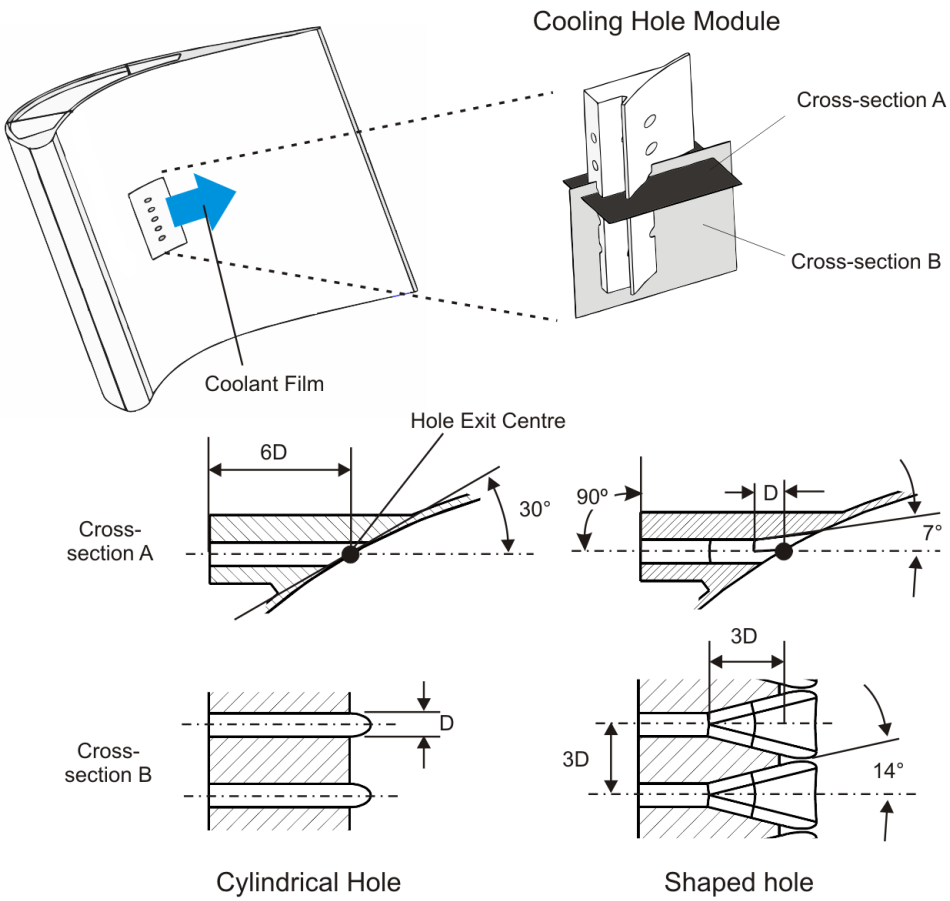

Figure 3.4: The cooling hole geometries, (upper) the removable module, (lower-left) cylindrical hole dimensions and (lower-right) shaped hole dimensions.

gaps. The location of the cooling hole inlet with respect to the interior of the plenum is shown in the photograph of Fig. 3.5. It should be clarified that the plenum was not split in two by the central divider, as this divider extended across only three quarters of the plenum height.

The plenum was supplied with high pressure air from the 690kPa (100psi) laboratory high pressure air supply, as shown schematically in Fig. 3.6. The mass flow rate was manually controlled by a valve, with an additional valve located upstream to act as a regulator. This regulator valve was needed for the safe variation of the mass flow rate using the control valve, as the pressure drop through the system was more than two orders of magnitude smaller than the laboratory air supply pressure. The air then passed through an orifice plate to measure the coolant mass flow rate ($\dot{m}_c$). Finally the coolant air entered the plenum chamber in the vertical direction at 100% span from a pipe of 72mm diameter.

The atomiser, shown in Fig. 3.6, was used predominantly to seed the coolant and will

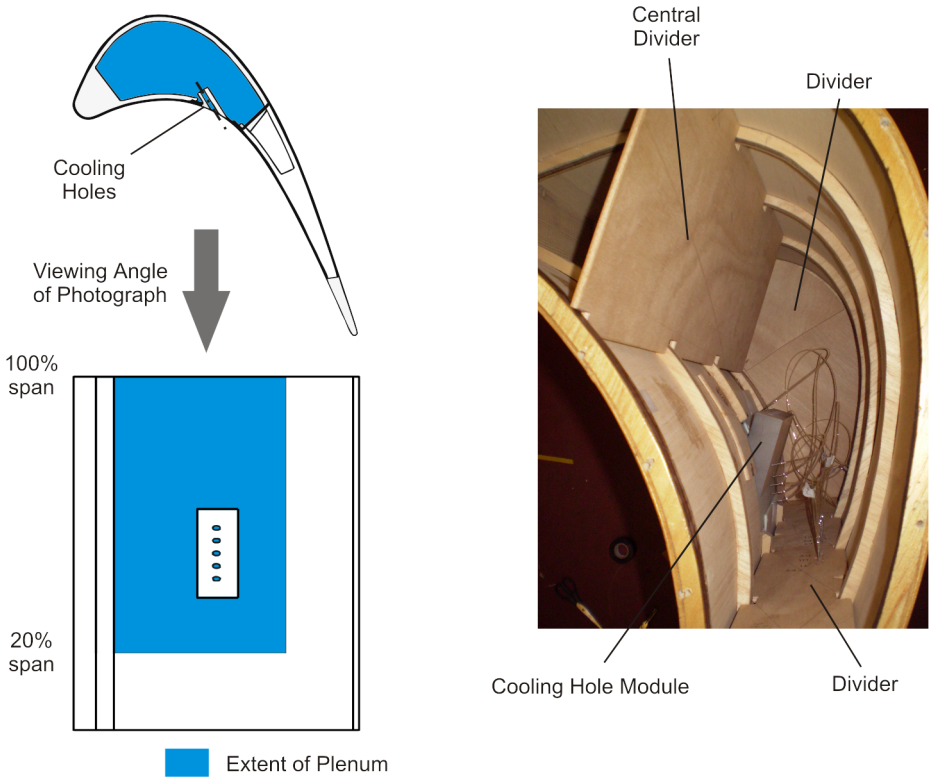

Figure 3.5: The blade interior, (left) the extent of the plenum and (right) photograph to show the cooling hole inlet.

be discussed in detail in the next chapter. However, it was also used to produce smoke for a visual inspection to confirm that there were no leaks in the pipework or plenum.

The orifice plate was designed according to the ISO standard [2] for a thin plate square edged orifice. In accordance with this standard the in-pipe diameter was chosen as 38.1mm (1.5") to ensure a sufficiently high pipe Reynolds number, and pipe lengths of greater than $60D_{pipe}$ upstream and $30D_{pipe}$ downstream were included.

The low speed of the flow through the in-pipe meant that it could be assumed incompressible, and so the mass flow through the orifice plate was found according to Eq. 3.5. Here C_D represents the coefficient of discharge found using the expression given in the ISO standard and A_{orf} was the area of the orifice. The pressure difference $\Delta p_{orf,in}$ was that between static pressure tappings $1D_{pipe}$ upstream and $0.5D_{pipe}$ downstream of the upstream face of the orifice plate. A Sensortechnics HCLA0025 0-2.5kPa pressure transducer was used to measure this pressure differential.

$$\dot{m}_c = C_D A_{orf} \sqrt{2\rho \Delta p_{orf,in}} \tag{3.5}$$

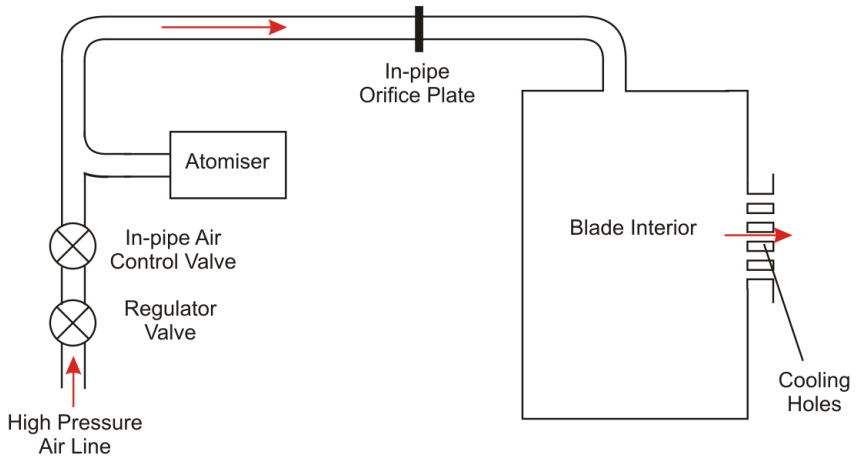

Figure 3.6: Schematic of the setup with plenum fed cooling holes.

3.2.4 Measurement of the Operating Point

Data Recording

The voltage outputs from all of the differential pressure transducers were sampled using a National Instruments USB-6211 Data Acquisition Unit (DAQ). This had an analogue to digital resolution of 2^{16} bits across a $\pm$10V range. The digital output from the DAQ unit was recorded by an IBM/Lenovo T43 laptop running LabView version 6.1. Within LabView 6.1 the voltages were averaged over a 20s period to obtain mean values. The voltage outputs were converted into pressure readings using calibration factors.

The calibration factors for the transducers with a pressure differential of less than 250Pa were obtained from either the manufacturer's calibration certificate or from an in-situ calibration with respect to a transducer which had a certificate. The transducer used to measure the larger pressure differential across the orifice plate was calibrated against a water manometer.

The measurements of the absolute pressure and temperature, used to calculate the density and dynamic viscosity, were not continuously updated and were modified manually as necessary.

How the obtained pressure and temperature values were used to quantify the cooling hole blowing ratio (BR) and the ideal blowing ratio (BR_{ideal}) will now be explained. To aid the reader the locations of the pressure measurement points are shown schematically in Fig. 3.7.

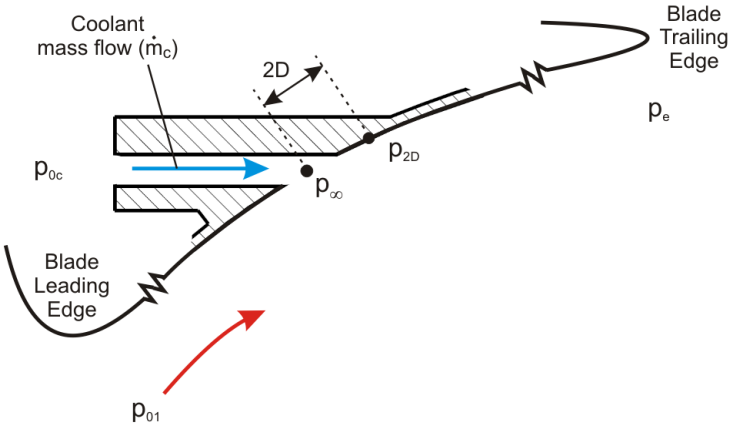

Figure 3.7: Location of the different pressure measurement points with plenum fed cooling holes.

Blowing Ratio

The blowing ratio (BR), shown in Eq. 3.6, has been introduced in the literature review and is the ratio of the coolant and mainstream mass fluxes.

$$BR = \frac{\rho_c V_c}{\rho_\infty V_\infty} = \frac{\dot{m}_c / A_c}{\sqrt{2\rho(p_{01} - p_\infty)}} \tag{3.6}$$

Here the coolant mass flux was obtained using the coolant mass flow rate ($\dot{m}_c$), and the throat area (A_c) of the five cooling holes. The mainstream mass flux was calculated using the Bernoulli equation and the assumption that there was no loss in total pressure in the mainstream.

Equation 3.6 required the static pressure at 50% axial chord (p_∞) to be measured, but this was not possible for this location now lay at the centre of the cooling hole exit. Therefore the C_p value of 0.032, shown in Fig. 3.4, measured at 50% axial chord with no cooling holes was used to infer this pressure based on the exit static pressure (p_e) as shown in Eq. 3.7.

$$BR = \frac{\dot{m}_c / A_c}{\sqrt{2\rho C_p(p_{01} - p_e)}} \tag{3.7}$$

The range of blowing ratios chosen for the current investigation was 0.5 to 2.0. The blowing ratio was varied by adjusting the coolant mass flow rate using the in-pipe control valve to within ± 0.05 of the desired value. The hole Reynolds number based on the coolant mass flux ($\dot{m}_c / A_c$) and the hole diameter (D) was 600 to 2600.

Previous research has obtained engine realistic density ratios by either cooling/heating or using a foreign gas for the coolant. On account of the large scale of the cascade and the long operating times that were envisaged it was impractical to use either of these methods. Therefore the density ratio was set at unity for all the experiments, and the corresponding range of the momentum ratio was 0.25 to 4.0.

In calculating the BR it was assumed that the coolant split uniformly across the five cooling holes. As such the BR values quoted represent mean values across the row of holes.

Ideal Blowing Ratio

The ideal blowing ratio (BR_{ideal}) is that assuming isentropic expansion through the cooling hole for a given pressure difference. It is calculated according to Eq. 3.8 as the ratio of the ideal and mainstream mass fluxes. Here p_{0c} is the coolant total pressure, which was measured using a static pressure tapping on the side wall of the plenum chamber.

$$BR_{ideal} = \frac{\rho_{ideal} V_{ideal}}{\rho_{\infty} V_{\infty}} = \sqrt{\frac{p_{0c} - p_{\infty}}{p_{01} - p_{\infty}}} \tag{3.8}$$

As was the case for the BR calculated according to Eq. 3.6, it was not possible to measure the static pressure at 50% axial chord. Therefore the cooling hole pressure differential ($p_{0c} - p_{\infty}$) was calculated by offsetting the pressure differential between the coolant total pressure and the static pressure 2D downstream of the hole exit centre ($p_{0c} - p_{2D}$) as shown in Eq. 3.9.

$$p_{0c} - p_{\infty} = (p_{0c} - p_{2D}) - ((p_{01} - p_{2D}) - (p_{01} - p_{\infty})) \tag{3.9}$$

The pressure differential across the cooling hole ($p_{0c} - p_{2D}$) reduced as the mass flow rate through the hole decreased, and for BR of 0.5 it was less than 1Pa. Similarly the pressure differential between the inlet total pressure and the static pressure 2D downstream of the hole exit centre ($p_{01} - p_{2D}$) was approximately 1.5Pa. To obtain high measurement accuracy across these small pressure differentials Furness Controls FCO332 0-30Pa pressure transducers were used.

The ideal blowing ratio was used in the current experiment to provide a measure of the operating point repeatability. Figure 3.8 shows the variation in the BR_{ideal} with the BR for the cylindrical and the shaped holes. The operating conditions in Fig. 3.8, were

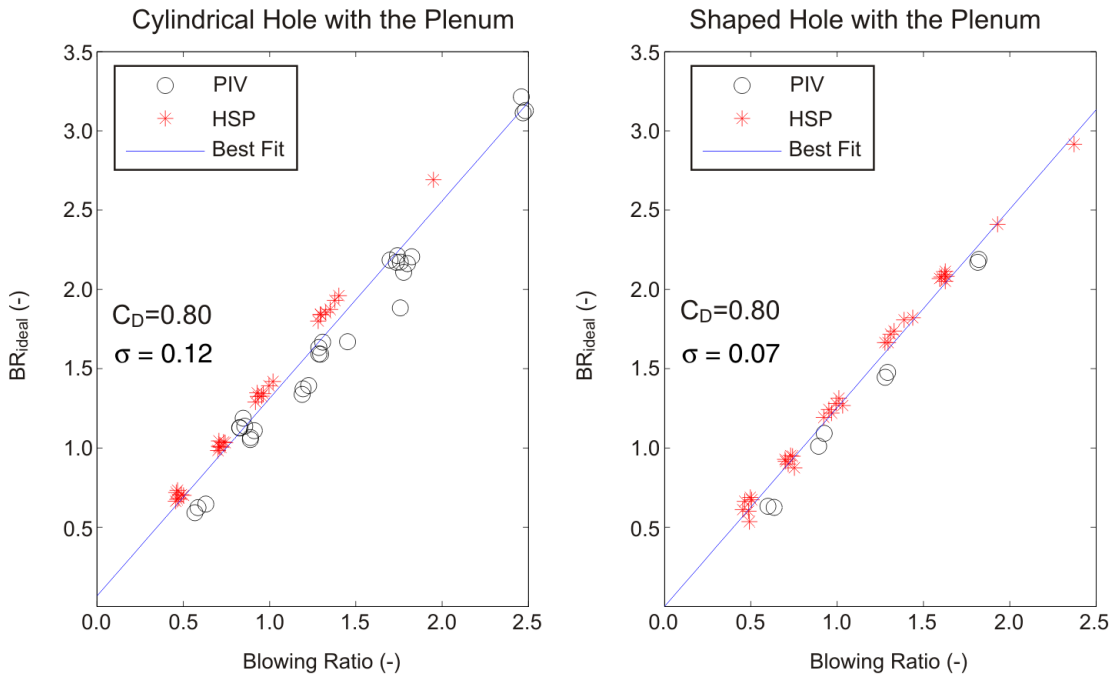

Figure 3.8: Variation of the ideal blowing ratio of the plenum fed cylindrical and shaped cooling holes with blowing ratio.

those at which measurements were made using the PIV and high speed photography (HSP) techniques that will be described in Chapter 4. A line of best fit has been applied, and the maximum standard deviation (σ) of the BR_{ideal} is that for the cylindrical hole, which is 0.12.

The gradient of the line of best fit in Fig. 3.8 corresponds to the discharge coefficient (C_D), and for both hole geometries it is equal to 0.80. Burd and Simon [13] for a cylindrical hole, with the same 90° inlet inclination angle as the current geometry, show a comparable C_D in the range of 0.75 to 0.80 for BR greater than 1.0. No studies are available in open literature for the C_D of a shaped hole with same inlet inclination angle as the current study.

3.3 Cooling Holes with Internal Crossflow

3.3.1 Crossflow Circuit

The Oxford Super Scale Cascade was modified to include a crossflow channel, orientated in the perpendicular (spanwise) direction, at the inlet of the cooling holes. The plenum fed cooling hole setup was changed to that shown schematically in Fig. 3.9. The photograph in

Fig. 3.9 shows the pipe network within the wind tunnel downstream of the cascade.

Within the plenum chamber a crossflow passage orientated in the spanwise direction was added. This had an out-pipe for the crossflow that did not exit through the cooling holes, which exhausted into the wind tunnel downstream of the cascade. The out-flow pipe required a second orifice plate to measure the mass flow rate and a blower to provide the necessary pressure differential. The increase in the mass flow rate with crossflow required the diameter of the pipe network to be increased, compared to the plenum fed case, to 59mm. The orifice plates were suitably redesigned according to the ISO standard [2]. With the increase in the mass flow rate the atomiser was found to provide a too low density of seeding particles, so was replaced with a smoke machine (which will be described in the following chapter). The carbon dioxide cylinder seen in Fig. 3.9, was required to pressurise the reservoir in the smoke machine from which the seeding particles were generated.

On account of the curved blade surface, the uncertainties in the spanwise location of the plenum floor and the limited room for access within the blade interior, the design of the crossflow passage was not straightforward. The chosen design is shown in Fig. 3.10.

The coolant enters the crossflow passage through the entry vanes. These turn the coolant through 90° with the aim of minimising the associated mixing losses and non-uniformities. The entry vane module was made of perspex with 1mm thick aluminium sheets used for the vanes. Adjustable feet were included so that the crossflow channel could be orientated correctly irrespective of the plenum floor uncertainties.

The channel section had a cross section of width 12D and height 4.2D, and, like the entry vanes, was made of perspex. The channel dimensions were made sufficiently large so that the sidewalls, which were located more than 4D from the hole inlet, would not be expected to influence the cooling hole entrance. The wall from which the cooling holes exited, called the collar in Fig. 3.10, was manufactured separately using stereolithography.

The method of assembly required the channel and entry vanes to be placed within the blade interior. The cooling hole module was then inserted through the blade surface, and the collar was lowered down to secure the inlet of the cooling hole module. The convergent nozzle, also made from stereolithography, was then lowered down on top of the channel. The convergent nozzle changed the channel cross-section from rectangular to circular as required for the out-pipe. The limited access within the blade interior required additional

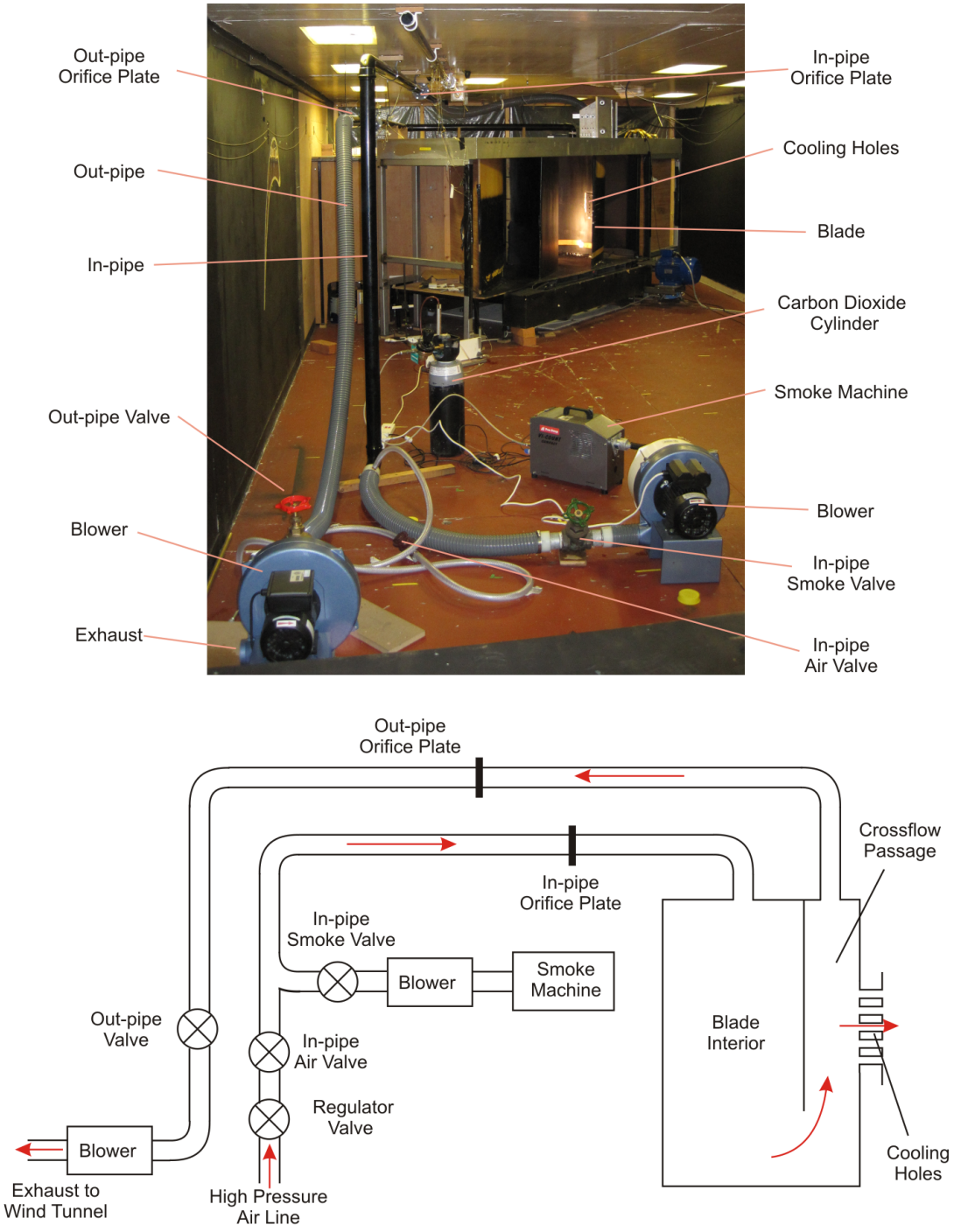

Figure 3.9: Internal crossflow within the Oxford Super Scale Cascade, (upper) photograph to show the external pipe network and (lower) a schematic view.

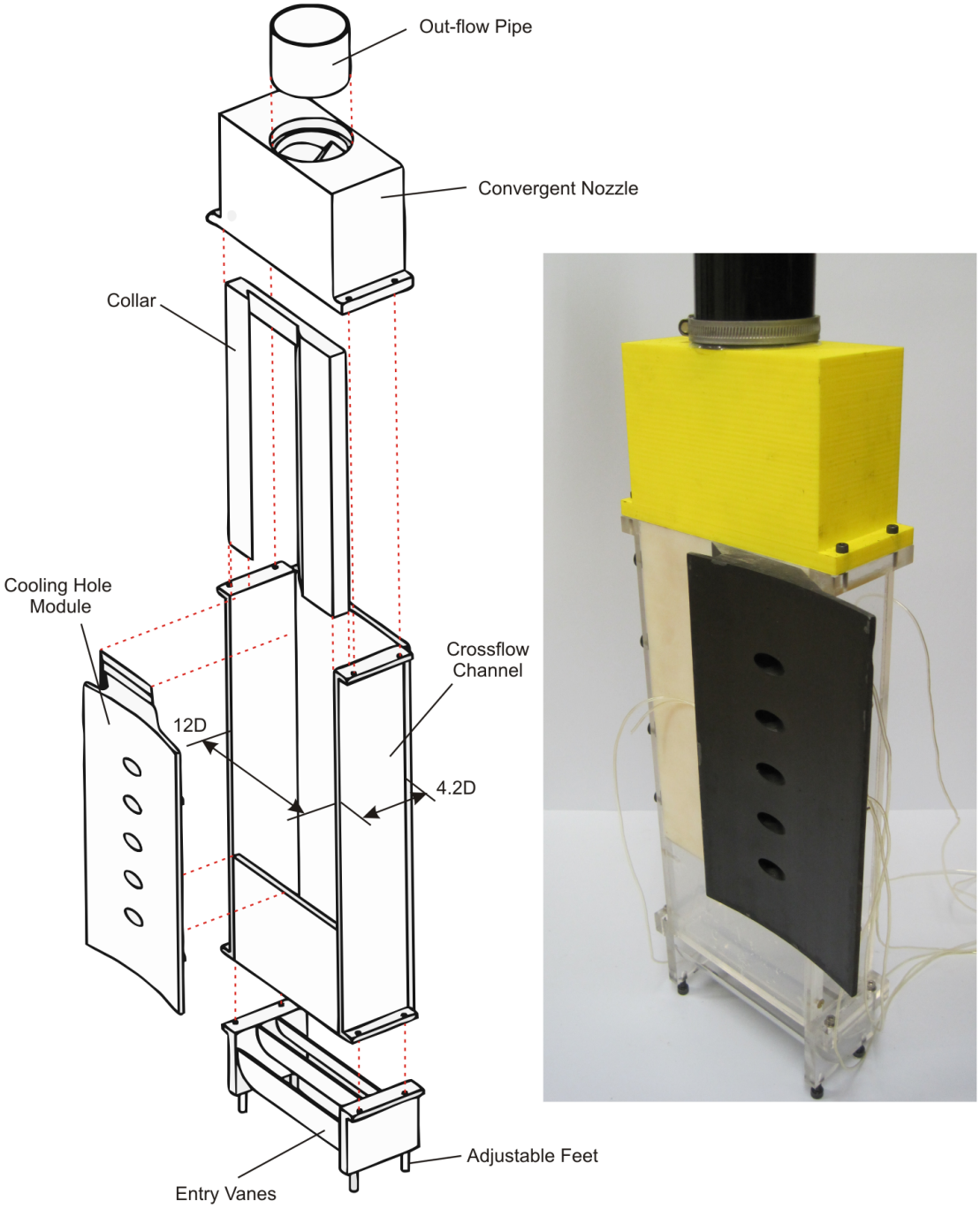

Figure 3.10: The internal crossflow channel (left) an exploded view and (right) a photograph of the final design.

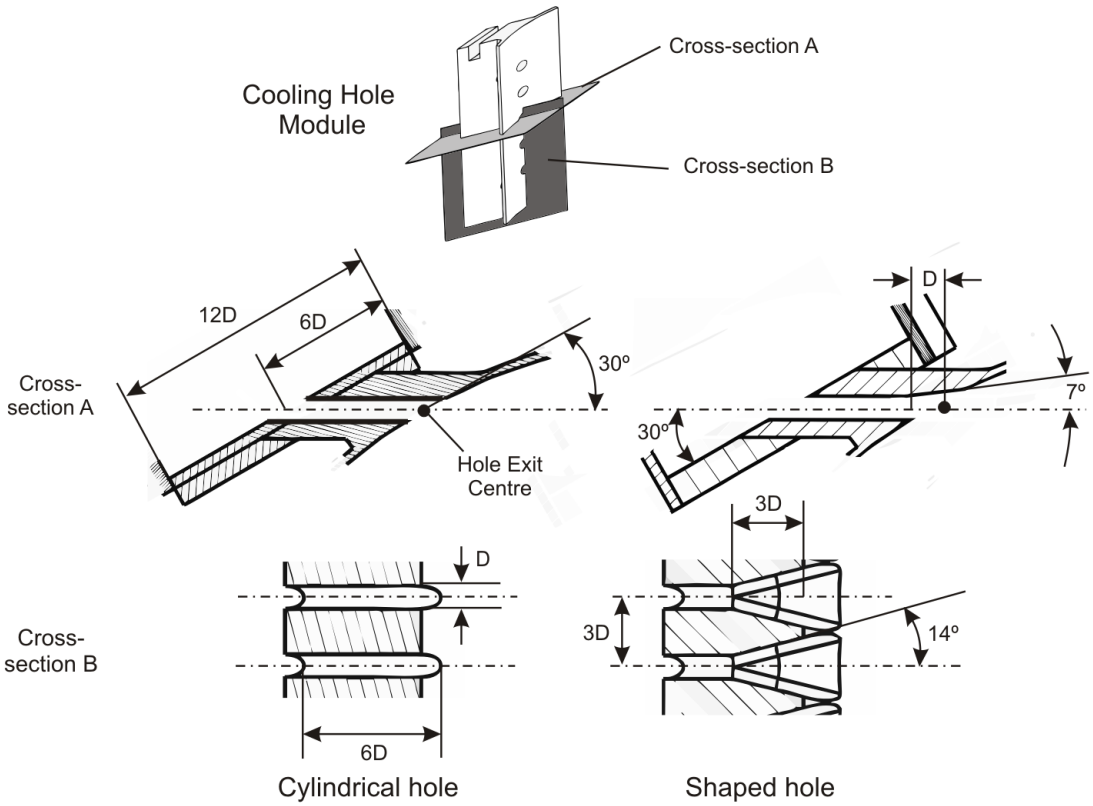

Figure 3.11: The cooling hole geometries with crossflow, (upper) the removable module, (lower-left) cylindrical hole dimensions and (lower-right) shaped hole dimensions.

consideration to ensure that all the components could be secured to each other.

3.3.2 Geometry of the Cooling Holes

To allow comparison with the plenum fed case the geometry of both cooling hole types was kept similar to those shown previously in Fig. 3.4. The only change concerned the hole inlet inclination angle, which as shown in Fig. 3.11, was reduced to 30° with respect to the side wall of the crossflow channel. The centre of the cooling hole inlet was located at the midpoint of the crossflow channel width. The spanwise height of this point was 18D downstream of the exit of the entry vanes.

3.3.3 Measurement of the Operating Point

Blowing Ratio

The blowing ratio was measured using the same method as for the plenum fed holes. A small modification was required, as shown in Eq. 3.10, as the coolant mass flow rate was now calculated as the difference between the mass flow rates through the in- and out-pipes (respectively $\dot{m}_{in}$ and $\dot{m}_{out}$).

$$BR = \frac{(\dot{m}_{in} - \dot{m}_{out})/A_c}{\sqrt{2\rho C_p(p_{01} - p_e)}} \tag{3.10}$$

Crossflow Ratio

The Crossflow Ratio (CFR) was introduced in the literature review as the ratio of the velocity in the crossflow channel to the bulk velocity through the cooling hole. These two velocities were found using the continuity equation as shown in Eq. 3.11. Here A_{cross} represents the cross-sectional area of the crossflow channel. Within the results section a CFR of 0.1 refers to the minimum crossflow case where all of the coolant in the crossflow channel exits through the cooling holes.

$$CFR = \frac{V_{cross}}{V_c} = \frac{\dot{m}_{in}/\rho A_{cross}}{(\dot{m}_{in} - \dot{m}_{out})/\rho A_c} = \frac{1}{1 - \frac{\dot{m}_{out}}{\dot{m}_{in}}} \frac{A_c}{A_{cross}} \tag{3.11}$$

The work of Kohli and Thole [47] and Saumweber and Schulz [89] (both introduced in the literature review), has shown a CFR of 0.4 to be sufficiently large to vary the in-hole and downstream flowfields. Therefore the maximum CFR used in the current investigation was 0.8.

The BR and CFR were both set by manually adjusting the in-pipe and out-pipe valves shown in Fig. 3.9. The operating point was considered to be set when the BR and CFR were both within ± 0.05 of their intended values.

Ideal Blowing Ratio

The ideal blowing ratio was measured using the same method as for the plenum case shown in Eq. 3.8. Due to the lack of a plenum chamber the coolant total pressure was instead measured using a Kiel probe within the crossflow channel. The Kiel probe was placed at midspan and no closer than 2D to the channel sidewalls.

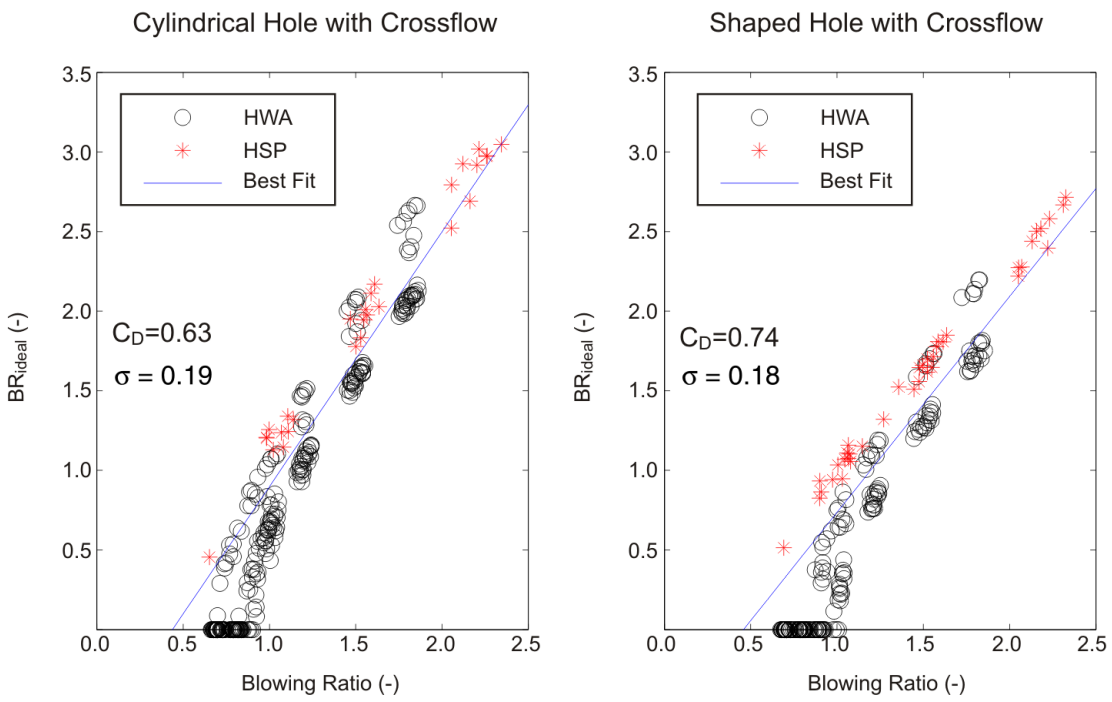

Figure 3.12: Variation of the ideal blowing ratio of the cylindrical and shaped cooling holes with crossflow at the hole inlet.

The trend in the ideal blowing ratio with changing BR is shown for both hole geometries in Fig. 3.12. The flow conditions shown, are those at which measurements were made using the high speed photography (HSP) and Hot Wire Anemometry (HWA) techniques that will be described in the Chapter 4. At low BR it was seen that the pressure difference across the cooling hole ($p_{0c} - p_{\infty}$), calculated according to Eq. 3.9, tended towards zero. This is apparent in Fig. 3.12 by the BR_{ideal} typically being zero for a BR less than 1.0.

It could be suggested that the low pressure difference across the cooling hole at midspan ($p_{0c} - p_{\infty}$), was due to the split in coolant across the five cooling holes not being uniform. However, whilst it was not confirmed explicitly that the split was uniform, the measurements made of the downstream jet, as will be shown in the results chapters, show that a jet was exiting the centre hole at low BR. The results also show qualitative trends that might be expected for a given change in BR.

Rowbury et al [86] showed that the presence of a crossflow at the hole exit could lead to a reduction in the hole exit static pressure compared to that assumed from the C_p profile with no cooling holes. This could explain why the pressure difference across the hole in the current investigation, calculated according to Eq. 3.9, could be zero, or indeed lower, as the static pressure at the hole exit (p_{∞}) was assumed equal to that when no cooling holes were

present.

To check if the explanation of Rowbury et al might be applicable to the current experiment, the pressure differences across both the cylindrical and the shaped holes were measured with no mainstream flow through the cascade. In this configuration the pressure difference across the holes, as with the plenum case in Fig. 3.8, did not go to zero at low mass flow rates. Thus, it appears that having a crossflow channel at the hole inlet, alters the velocity profile at the hole exit such that p_∞ decreases compared to the plenum case.

The reason for including Fig. 3.8 is to provide a measure of the repeatability of the operating point. Given the limitations at low BR, the linear line of best fit is based on BR greater than 1.2. The standard deviation (σ), based on the range of BR larger than 1.2, is larger than that with the plenum fed holes, being 0.2 for the cylindrical hole. This shows that although the measurement uncertainty, as will be shown in the next section, is relatively low there is less repeatability in the operating point.

The lines of best fit in Fig. 3.12 do not pass through the origin, and so the absolute value of the discharge coefficient provided by the gradient is not correct. However, it does show that the relative discharge coefficient is lower for the cylindrical hole than the shaped hole, which is consistent with the study of Gritsch et al [33] (introduced in the literature review) for cooling holes of a similar geometry on a flat plate.

The studies of Hay et al [38] and Gritsch et al [33], as discussed in the literature review, have shown the C_D to vary with changes in the crossflow velocity. However, in the current investigation this could not be confirmed repeatedly, and so no distinction is made between the different CFR in Fig. 3.12.

3.4 Estimates of the Uncertainty

The uncertainties in measuring the operating point of the experiment were calculated using the method described by Kline and McClintock [50], which is shown here as Eq. 3.12. In Eq. 3.12 R is the calculated variable, v_n refers to the variables from which it is calculated and $\varepsilon(v_n)$ is the maximum uncertainty in a variable.

$$\varepsilon(R) = \left(\left(\frac{\partial R}{\partial v_1} \right)^2 \varepsilon(v_1)^2 + \left(\frac{\partial R}{\partial v_2} \right)^2 \varepsilon(v_2)^2 + \ldots \left(\frac{\partial R}{\partial v_n} \right)^2 \varepsilon(v_n)^2 \right)^{1/2} \tag{3.12}$$

Equations 3.13 and 3.14 show this method applied to calculate the uncertainty in the exit Reynolds number.

$$\varepsilon(Re_e) = \left(\left(\frac{\partial Re_e}{\partial \rho_\infty} \right)^2 \varepsilon(\rho_\infty)^2 + \left(\frac{\partial Re_e}{\partial V_e} \right)^2 \varepsilon(V_e)^2 + \left(\frac{\partial Re_e}{\partial C} \right)^2 \varepsilon(C)^2 + \left(\frac{\partial Re_e}{\partial \mu_\infty} \right)^2 \varepsilon(\mu_\infty)^2 \right)^{1/2} \tag{3.13}$$

$$\frac{\varepsilon(Re_e)}{Re_e} = \left(\left(\frac{\varepsilon(\rho_\infty)}{\rho_\infty} \right)^2 + \left(\frac{\varepsilon(V_e)}{V_e} \right)^2 + \left(\frac{\varepsilon(C)}{C} \right)^2 + \left(\frac{\varepsilon(\mu_\infty)}{\mu_\infty} \right)^2 \right)^{1/2} \tag{3.14}$$

The uncertainty in the cascade exit Reynolds number calculated according to Eq. 3.14 was 2%. For the plenum fed cooling holes the uncertainty in the blowing ratio was 4%. The uncertainty in the ideal blowing ratio varied with BR due to the change in the pressure differential across the cooling hole. The uncertainty in the ideal blowing ratio for a BR greater than 1.0 was less than 2%, but at a BR lower than this the uncertainty in the ideal blowing ratio rose and was 4% at a BR equal to 0.5.

When the cooling holes were fed from the crossflow channel the coolant mass flow rate was calculated from the difference between the mass flow rates through the in-pipe and the out-pipe. At large CFR these mass flow rates were an order of magnitude higher than the coolant mass flow rate, and so the uncertainty in the BR rose with an increase in the CFR. For a BR of 1.0 and greater, the uncertainty increased from 3% at a CFR of 0.1 up to 32% at a CFR of 0.8. The relatively high uncertainty in the BR was tolerated, as the primary aim of this first of a kind study was to observe if coherent unsteadiness was present in film cooling flows. To do this the majority of measurements were taken at low CFR, and so it was considered satisfactory that the BR was only close to the desired range at high CFR.

The method for calculating the CFR was dependent on the ratio of the in-pipe and out-pipe mass flow rates rather than their difference. The uncertainty in the CFR was therefore less than 4% for a BR greater than 1.0. The uncertainty rose for BR less than 1.0, with a maximum of uncertainty of 9%.

It should be noted that the uncertainties presented here are comparatively low compared to the repeatability of the operating point shown in Fig. 3.8 and 3.12. There it is shown that the standard deviation of the ideal blowing ratio for a change in blowing ratio, is 0.1 with the plenum at the hole inlet and 0.2 with crossflow at the hole inlet.

3.5 Summary

Within this chapter the Oxford Super Scale Cascade has been described, which was a large scale 3 passage linear cascade with turbine realistic RT27a blades of true chord 1m. As part of the current study the facility was modified to include cooling holes upon the pressure surface of one of the blades at 50% axial chord. Cylindrical and shaped holes of length 6 hole diameters inclined at 30° to blade surface were chosen for the current investigation. Two cooling hole inlet conditions, namely plenum fed and perpendicular (spanwise) crossflow, were to be investigated and the required modifications to the blade interior and the manufacture of a coolant supply network are detailed within this chapter.

The cascade was operated at an exit Reynolds number of 6×10^5. The range of investigation for the cooling holes was across blowing ratios of 0.5 to 2.0 and crossflow to bulk jet velocity ratios of up to 0.8. The ideal blowing ratio was used during the investigation to provide a measure of the repeatability between runs. Within this chapter the methods used to calculate each of these parameters are detailed. Their measurement required some pressure differentials of less than 2Pa to be measured. These low pressure differentials required appropriate low pressure transducers to be chosen to minimise the uncertainty.

The uncertainties for the blowing ratio and crossflow to bulk jet velocity ratio were typically less than 4%, but could increase for extreme cases. A measure of the repeatability of the operating point was provided by the ideal blowing ratio, which had at a standard deviation of 0.1 for the plenum fed case and 0.2 for that with spanwise crossflow.

Chapter 4

Experimental Methods

To ascertain the presence of coherent unsteady features within the film cooling flow downstream of the cooling hole exit, and within the cooling hole, three experimental techniques were used. These were Particle Image Velocimetry (PIV), High Speed Photograghy and Hot Wire Anemometry (HWA).

PIV is a whole flowfield measurement technique and was used to obtain velocity vectors across 2-D planes downstream of the hole exit. The PIV system which was available for the current experiment had a maximum sampling frequency of 15Hz, and due to the geometry of the Oxford Super Scale Cascade provided a spatial resolution of $1/10^{th}$ of the hole diameter.

It was suggested from the literature review that some coherent unsteady features within the cooling jet were likely to have a Strouhal number of the order of 1.0. This corresponded to a frequency in the current experiment of 350Hz, so a sampling frequency which was at least double this was required. Therefore high speed photography, which was capable of a sampling frequency in excess of 1kHz and has a higher spatial resolution was used. High speed photography was used in the same 2-D planes downstream of the hole exit as PIV, but was only capable of providing a qualitative measure of the coherent unsteadiness.

HWA is a point measurement technique, that was able to provide high temporal resolution velocity measurements. In the flowfield downstream of the cooling hole, given the aims of the investigation, measurements were only taken with HWA at locations and at blowing ratios at which the high speed photography had shown coherent unsteadiness to be present. The geometry of the hot wire probe used in HWA also allowed it to be used to investigate the presence of coherent unsteadiness within the cooling hole tube.

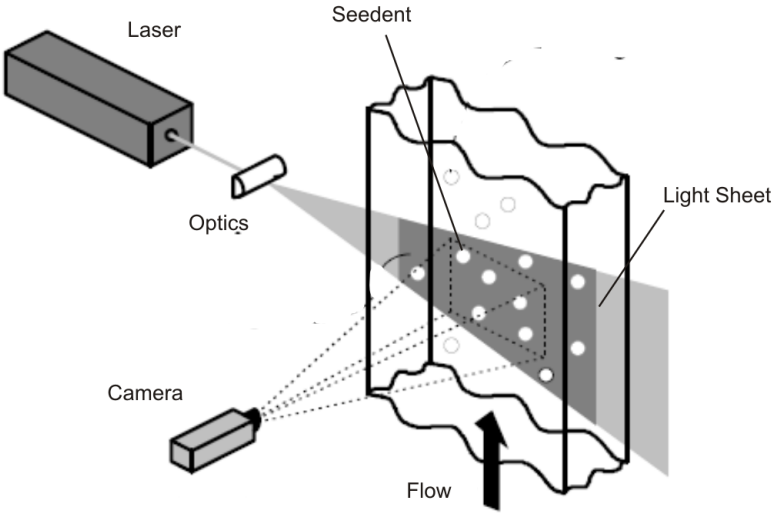

Figure 4.1: Basic principles of PIV, adapted from the Dantec Dynamics user guide [92].

This chapter explains all three of the measurement techniques in terms of their configuration within the current experiment and the measurement locations that were investigated. The post-processing of the measured values required to produce the results shown in the later chapters are explained, and the uncertainties in applying each method are outlined.

4.1 Particle Image Velocimetry

Particle Image Velocimetry (PIV) is a whole flowfield measurement technique in which the velocity field is inferred from the displacement of seeding particles suspended in the flow. These particles are of a sufficiently small diameter so as to be neutrally buoyant within the flow. The seeding particles are illuminated using a light sheet, as shown in Fig. 4.1. The small diameter of the seeding particles means that the light sheet often needs to be produced by a laser. On striking the seeding particles, light is scattered in all directions, and that scattered in the direction normal to the light sheet is detected by the camera. The laser light is pulsed and by timing the camera shutter with these pulses an image of the seeding particle positions is recorded. Two images are captured in short succession (less than 500μs) and by cross-correlating these images the displacement of the seeding particles can be determined.

This section explains the PIV system used in the current investigation, detailing how an image pair was obtained and then how this image pair was cross-correlated to find the

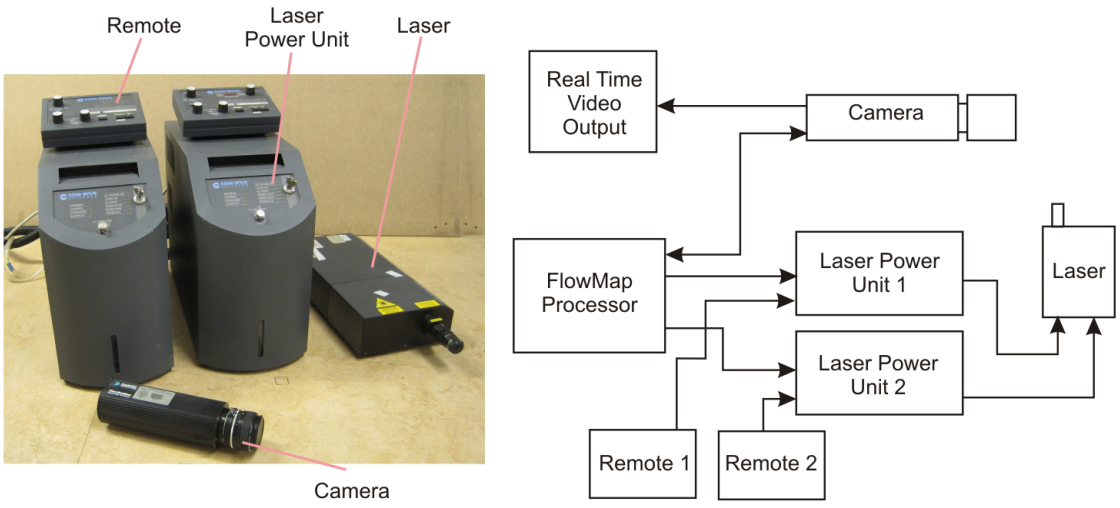

Figure 4.2: The PIV system, (left) New Wave Gemini laser and the Double Image 700 camera, and (right) a schematic of system.

velocity. PIV was used to observe two measurement planes downstream of the cooling hole exit when the cooling holes were fed from the plenum chamber. Here these two measurement planes, and the modifications that were made to the Oxford Super Scale Cascade to achieve them, are explained. The section finishes by showing the post-processing techniques and the uncertainties in the method.

Guidance in the general use of PIV, especially in setting the variables within the cross-correlation procedure, was obtained from the Dantec Dynamics user guide [92], Raffel et al [82] and Willert and Gharib [101].

4.1.1 Recording an Image Pair

The PIV system in the current experiment was supplied by Dantec Dynamics. Within this setup the laser illumination was provided by a pulsed New Wave Gemini Nd-YAG laser, shown in Fig. 4.2. To permit the time between the two frames in an image pair (the inter-frame rate) to be varied to as low as 2μs, the Gemini laser contained two laser cavities which could have their firing offset. In practice a minimum inter-frame rate of 120μs was used as the current system tended to be unreliable at lower inter-frame rates. The remote control units shown in Fig. 4.2 allowed manual control of the laser during alignment, but for measurement sequences the laser was controlled by a FlowMap1100 processor.

A Double Image 700 camera, shown in Fig. 4.2, was used to record the light scattered by the seeding particles. The Double Image 700 had a pixel count of 768×484, and a shift

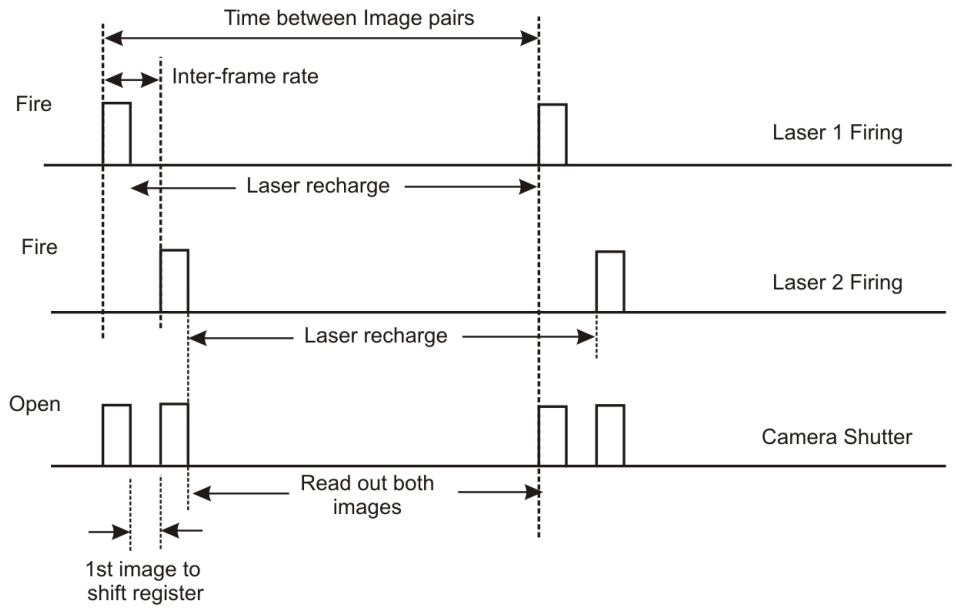

Figure 4.3: Timing diagram to showing the laser firing and camera shutter sequence.

register next to each pixel of the Charge Coupled Device (CCD) to store the first image whilst the second image was recorded. Both the first and second images were then read from the CCD in the time between image pairs.

The timing sequence for the two laser cavities and the camera shutter are shown in Fig. 4.3. The offset between the two laser firings specified the inter-frame rate. The time between image pairs was dictated by the time required for the laser to recharge after firing, and corresponded to the sampling frequency of the setup. In the current system the maximum sampling frequency was 15Hz.

Both the mainstream turbine passage flow and the cooling jet had to be seeded. The cooling jet was seeded with a glycerol/water mixture using the TSI systems 9306A atomiser, shown in Fig 4.4. The atomiser fed seeding particles into the in-pipe upstream of the orifice plate. The atomiser used high pressure air jets to atomise the liquid glycerol/water mixture. The quantity of seeding particles produced was controlled by either reducing the number of jets or their supply pressure.

Seeding the mainstream required a larger quantity of seeding particles to be produced than was possible with an atomiser. Therefore the Concept Smoke Systems ViCount smoke machine shown in Fig. 4.4 was used, this was capable of producing more than a 1000 times more smoke than the atomiser. The ViCount smoke machine used high pressure carbon dioxide to force a glycerine/water mixture though a heater element to atomise the particles.

Figure 4.4: The Concept Smoke Systems smoke machine and the TSI atomiser.

The atomised mixture was then diluted with air downstream of the heater.

The seeding particles produced by both the atomiser and the smoke machine, were quoted by their respective manufacturers as having a mean diameter of less than 0.5μm.

Experimentation showed that the best method of introducing smoke into the mainstream was through two horizontal rakes located approximately 2.5m upstream of the blade leading edge at midspan. The rakes were two pipes of 22mm diameter with holes of 4mm diameter through which the seeding particles entered the mainstream. The smoke machine was located in the tunnel downstream of the cascade and so a ACI 2MS8 blower was used to overcome the pressure differential with respect to the cascade inlet.

4.1.2 Measurement of the Velocity Vectors

The FlowManager software suite running on a Dell workstation was used to control the FlowMap processer and process the recorded images to obtain velocity vectors. Here this procedure is described.

Interrogation Windows

First the two recorded images within an image pair were divided into square interrogation windows of length 2^N pixels, where N could be any integer. Each interrogation window corresponded to a vector in the PIV output. The velocity vector obtained for the interrogation window depended on the displacement of the seeding particles between the two images and their inter-frame rate.

The smaller the dimensions of the interrogation window, the higher the resolution of the PIV velocity output. However, too small an interrogation window would result in 'loss

of pairs', whereby a seeding particle has moved such that it is not present in the same interrogation window in both images. Loss of pairs would increase the noise within the image. To counteract this it is typically recommended that 6 particles should be common to both interrogation windows, and the inter-frame rate should be such that the particles do not travel more than a quarter of a side of the interrogation window. Particles near the edge of an interrogation window are more subject to 'loss of pairs', so to make use of these interrogation windows are often overlapped.

Within the spanwise and secondary flow planes used in the current experiment, which are shown in Fig. 4.6 later in this chapter, the inter-frame rates were 120μs and 200μs respectively. The interrogation window size was 32×32 pixels, and they were overlapped by 50%.

Cross-Correlation

To determine the displacement of the seeding particles within an interrogation window the two images were cross-correlated with each other. For the size of interrogation windows used in PIV this is more computationally efficient if it is done in the frequency domain rather than the spatial domain.

An outline of cross-correlation using the frequency domain is shown in Fig. 4.5 and Eq. 4.1 to 4.3. For now the reader is asked to ignore the optional features.

The first step, as shown in Eq. 4.1, is to obtain the Fourier transform of the images within the interrogation windows ($f(m,n)$ and $g(m,n)$). Here m and n refer to the spatial domain and u and v refer to the frequency domain. The Fourier transforms are done using a Fast Fourier Transform (FFT) algorithm, which requires less computations than a standard Fourier transform.

$$F(u,v) = \mathrm{FFT}(f(m,n)) \tag{4.1}$$

Once in the frequency domain the two images ($F(u,v)$ and $G(u,v)$) are multiplied, as in Eq. 4.2, to obtain the cross conjugate multiple ($\Phi(u,v)$).

$$\Phi(u,v) = F(u,v) \cdot G(u,v) \tag{4.2}$$

An inverse Fourier transfrom is then used, as shown in Eq. 4.3, to change the cross conjugate multiple into the spatial domain. The spatial distance with the highest correlation

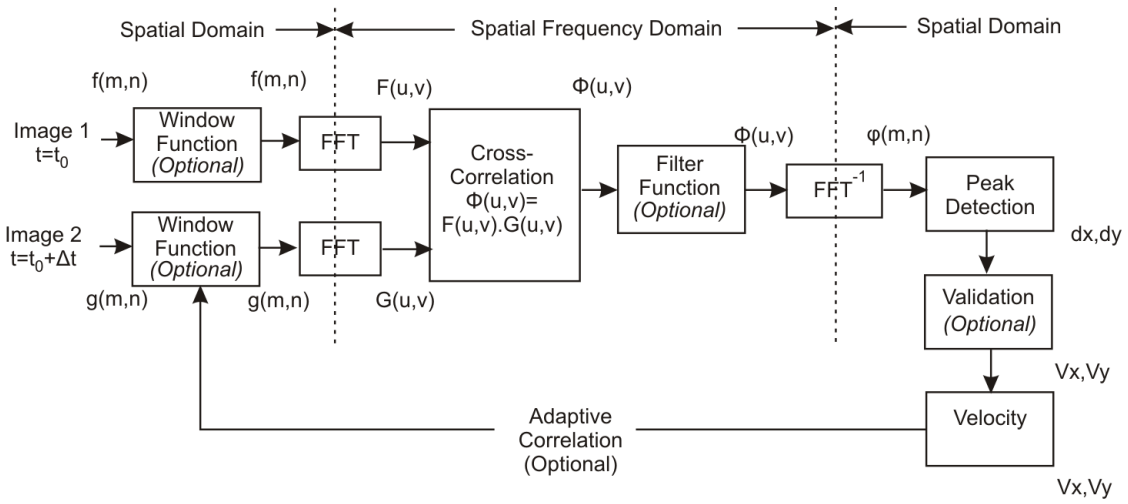

Figure 4.5: Schematic of cross-correlation method, based on that of Dantec Dynamics [92].

in $\phi(m,n)$ corresponds to the displacement of the seeding particles (dx and dy) between the images $f(m,n)$ and $g(m,n)$. The displacement is changed into the velocity (V_x and V_y) using the inter-frame rate.

$$\phi(m,n) = \mathrm{FFT}^{-1}(\Phi(u,v)) \tag{4.3}$$

If seeding particle displacements (dx and dy) were only permitted to be integer pixel values, then the uncertainty in a velocity vector would be large. To reduce this uncertainty Fig. 4.5 shows that sub-pixel interpolation is done in the spatial domain. Sub-pixel interpolation fits a parabolic curve to the correlation values neighbouring that of the peak correlation. The peak correlation is now found, with an uncertainty of $\pm 1/64$ of a pixel, as the maximum of the parabolic curve.

Adaptive Correlation

To reduce the size of the interrogation windows, and so increase the spatial resolution, without the limitation that the particle displacement cannot be larger than a quarter of their side, interrogation windows can be offset within the two recorded images. This spatial offset is determined by the velocity of the flow being measured.

In the current experiment the flowfield was not uniform, so the same offset could not be applied to all the interrogation windows. Therefore to find the local offset adaptive correlation was used. Adaptive correlation uses the same cross-correlation procedure as shown in Fig. 4.5, but uses the obtained displacement to find the local offset. First, cross-

correlation is done with a large interrogation window to find the local offset (dx and dy). The interrogation window size is then reduced, the local offset applied and the cross-correlation repeated. Within the current experiment this process was repeated 3 times beginning with interrogation windows of 128×128 which were reduced to 32×32.

Window Functions

The FFT algorithm assumes that the image inside the interrogation window is periodic. It is stated by the manufacturer of the PIV system (Dantec Dynamics) that this may introduce noise due to false correlations between particles near the edge of the interrogation window and 'ghost' particles immediately outside. Consequently a Gaussian window function, expressed as Eq. 4.4, was applied in the spatial domain as shown in Fig. 4.5. Here k had a value of 1.1 and M and N correspond to the dimensions of the interrogation window.

$$W(m,n) = \exp\left[-\left(\frac{1}{k}\right)^2\left(\left(\frac{2m}{M}\right)^2 + \left(\frac{2n}{N}\right)^2\right)\right] \tag{4.4}$$

Filters

To reduce the impact of noise on the correlation procedure, it is also recommended by the manufacture that a filter be used in the frequency domain after the cross-correlation. Within the current experiment the filter defined by Eq. 4.5 was used. This combines a direct correlation (DC) filter and an exponential low pass filter. The k value was 3 and U and V correspond to the maximum dimensions of the interrogation window in the frequency domain.

$$W(u,v) = \begin{cases} 0 & \text{for } (u,v) = (0,0) \\ exp\left(k^2 \frac{u^2+v^2}{UV}\right) & \text{otherwise} \end{cases} \tag{4.5}$$

Validation

The physical realism of the velocity vector map produced by the cross-correlation procedure can be checked using a range of validation functions. The peak validation function highlights the vectors that have a low signal to noise ratio, where the amplitude of the largest noise peak is similar to that of the correlation peak. Vectors that are un-realistically large or small

Validation Function	Vectors to Reject
Peak Validation	Signal/Noise<1.2
Range Validation	V<-10ms^{-1} or V>10ms^{-1}
Moving Average Validation	$\alpha > 0.05$

Table 4.1: Validations used in the current PIV system.

in terms of their velocity can be removed by the range validation function where upper and lower limits for the velocity are prescribed. The moving average validation assumes that the flowfield is continuous, and replaces vectors that are not within a prescribed fraction (referred to as acceptance factor (α)) of their neighbours. The moving average function is also used to replace the vectors removed by the other two validation functions.

The three validation functions described here were used in the current experiment, as summarised in Table 4.1. The range validation function was applied across a 5×5 grid of neighbouring vectors.

4.1.3 Measurement Planes

Setup

Velocity measurements were made in two planes downstream of the hole exit, as shown in Fig. 4.6. These were named the spanwise plane, which was normal to the spanwise direction, and the secondary flow plane which was normal to the axis of the cooling hole. In reality the secondary flow plane was not a true secondary flow plane as the mainstream flow was not orientated normal to the plane. The Cartesian co-ordinate system used for these two measurement planes was relative to the axis of the cooling hole, with the Hole Axial Direction (X_s) aligned with the cooling hole axis and the Hole Normal Direction (Y_s) aligned normal to the spanwise axis and the cooling hole axis. The origin of these axes was the hole exit centre shown in Fig. 3.4.

To measure the planes shown in Fig. 4.6 the camera and the laser were alternated between being positioned above the cascade endwall and positioned downstream of the cascade exit plane. Mounting above the endwall required a perspex window to be made in the endwall of the cascade to allow visual access. A traverse system was built above the endwall as shown in Fig. 4.7 (a), to allow the camera or laser to be traversed in the X_s

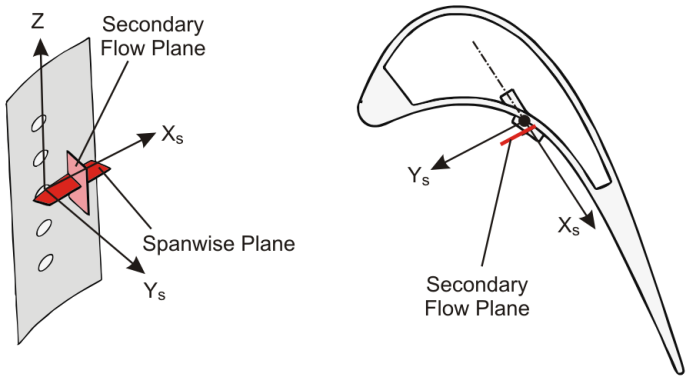

Figure 4.6: The spanwise and secondary flow planes.

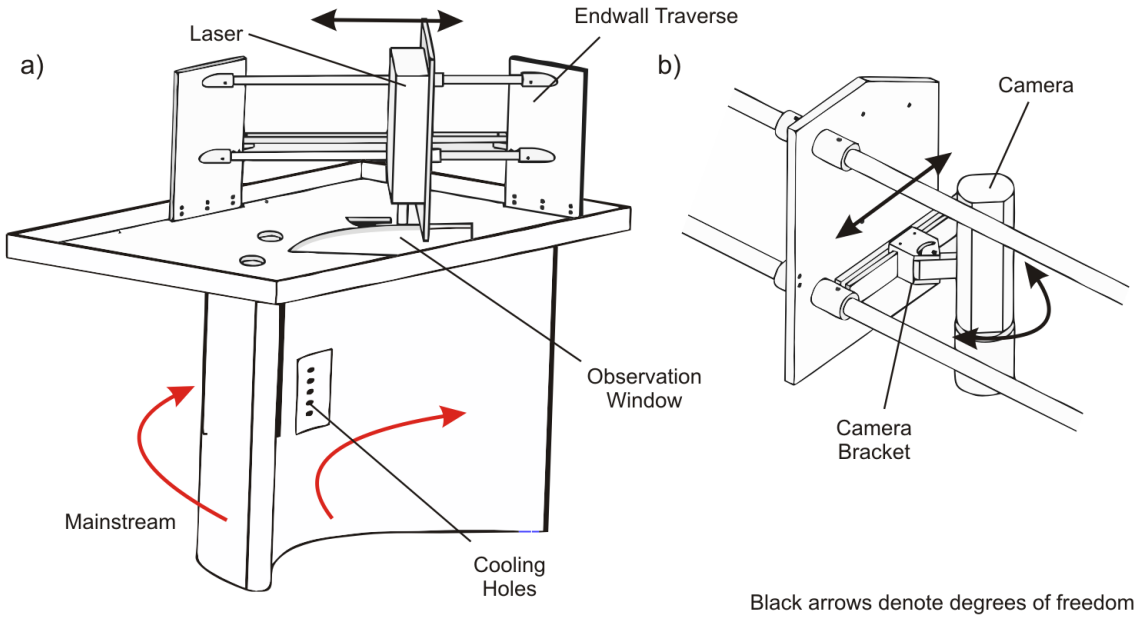

Figure 4.7: Endwall traverse with (a) the laser and (b) the camera for the PIV system.

axis. The camera or laser were mounted upon a steel plate that was cantilevered from two horizontal steel bars. The position of the plate in the X_s axis was varied manually, with adjustable bolts used to secure it in position during experiments.

The camera required additional degrees of freedom so that its field of view could be orientated with the curved surface of the blade. To achieve these an additional bracket was added to the traverse mechanism as shown in Fig. 4.7 (b). This bracket allowed movement in the Y_s axis and rotation about the Z axis.

Within the measurement planes it was desired to have a spatial resolution of approximately 10 vectors per hole diameter. The minimum distance between the camera and the measurement plane was dictated by the 0.5m distance between the endwall and the blade

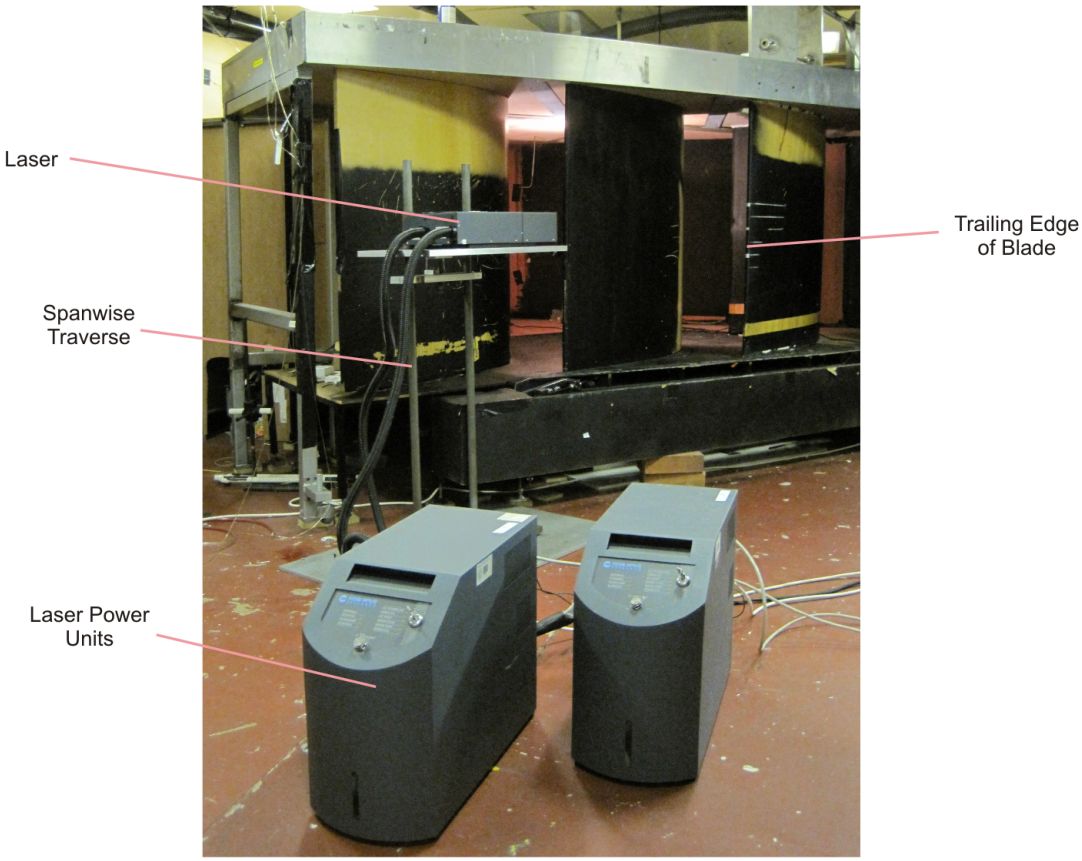

Figure 4.8: Laser on the spanwise traverse mechanism downstream of the cascade.

midspan. To achieve the specified resolution at this distance a Sigma 105mm EX DG Macro lens was used. The intensity of the light scattered by the seeding particles decreases with distance. To observe the seeding particles at 0.5m required the lens to be set with the lowest aperture 'f-stop' of 2.8.

When located downstream of the cascade exit the laser and camera were located on traverses free to move in the spanwise direction. Figure. 4.8 shows the laser supported on its traverse mechanism, which was formed of a steel plate cantilevered from two vertical steel bars. To minimise blockage of the cascade exit plane, due to the size of the laser, the leading edge of the laser was located more than 0.5m from the cascade exit plane.

To obtain the desired spatial resolution in the secondary flow plane, the camera had to be located 0.5m from the measurement plane. This required the camera spanwise traverse to be located at the cascade exit plane. To minimise the impact of the blockage, the camera was located away from the blade surface close to mid-pitch.

Alignment

To align the camera and laser to the measurement plane they were first orientated roughly in position. The laser light sheet was then aligned whilst running the laser on the minimum power setting at which it was visible to a user wearing the calibration laser safety goggles. The laser was aimed upon a calibration plate which had a 2mm thick black line on a white background. The traverse position and light sheet focus were adjusted as necessary.

The laser was then turned off and the camera calibration plate placed at the measurement location. This calibration plate featured a 10mm by 10mm grid of black lines upon which the camera was focused. The origin of this grid with respect to the hole exit centre was measured, and an image with the grid was recorded for use in post-processing.

The laser and camera were both then set to be controlled by the FlowMap processer and an image in which seeding particles were present was recorded. Due to the alignment procedure the camera was typically slightly out of focus when recording this first image. This was rectified by adjusting the camera focus and then repeating the measurement, this often required a number of attempts.

4.1.4 Post-processing

The co-ordinates applied by the camera were modified to be aligned with the axes scheme of the measurement plane with the origin at the hole exit centre. The instantaneous velocity vector maps could then be combined to form a time-mean velocity profile. The maximum number of image pairs that could be stored in the buffer of the FlowMap processor was 150. Comparison with the time-mean based on 80 image pairs showed that 150 image pairs was more than sufficient for the time-mean velocity profile.

As discussed previously the secondary flow plane was not a true secondary flow plane. To aid analysis of the secondary flow features, such as the CRVP, the time-mean V_{sy} component obtained from the spanwise plane with no cooling holes present was subtracted.

Large magnitudes of the root-mean squared velocity (V_{rms}) identify regions of high unsteadiness, either due to turbulence or coherent unsteadiness. The V_{rms} at each measurement point in the flowfield was calculated according to Eq. 4.6. Here V' is the instantaneous velocity, i is the sample number and n is the total number of recorded samples, of which the latter was 150 in the current case.

$$V_{rms} = \sqrt{\frac{\sum_{i=1}^{n}(V_i' - V)^2}{n}} \tag{4.6}$$

The vorticity was found on the 2-D secondary flow plane using the 'curl' function within Matlab R2008b, defined according to Eq. 4.7. Here ω is the vorticity and X_s, Y_s and Z are the Cartesian co-ordinates shown in Fig. 4.6.

$$\omega_{xs} = \left(\frac{dV_{sy}}{dZ} - \frac{dV_z}{dY_s}\right) \tag{4.7}$$

To establish if any of the unsteadiness observed within the rms velocity profiles was caused by coherent unsteady features, fourier analysis was performed upon the instantaneous velocity traces. The Fourier transform was performed using the FFT function within Matlab R2008b and was applied in the temporal domain.

4.1.5 Uncertainties

The uncertainty in the measurement of the seeding particle displacement was quoted by the manufacturer of the PIV system to be $1/10^{th}$ of a pixel. Based on the mean velocity obtained within a typical flowfield, the pixel uncertainty equated to an uncertainty in the measured velocity of 4% in the spanwise plane and 6% in the secondary flow plane.

In Cartesian co-ordinates the measurement planes were estimated to have a positional uncertainty of ±1mm in the axes of the measurement plane and ±2mm in the axis normal to the plane. The uncertainty due to rotational misalignment was estimated to be ±5° in the spanwise plane and ±10° in the secondary flow plane. These positional uncertainties were combined using the method of Kline and McClintock introduced in the previous chapter (Eq. 3.12) to calculate the uncertainty in the velocity measurement as 4% in the spanwise plane and 7% in the secondary flow plane.

A measure of the repeatability in the time-mean velocity profile is shown in Fig. 4.9. The left hand image shows the time-mean velocity profile in the spanwise plane at midspan, for a jet of BR equal to 1.5 from the cylindrical hole. The right hand image in Fig. 4.9 shows the difference between the time-mean velocity profile shown on the left and a repeated measurement. The features of the time-mean velocity profile in Fig. 4.9 will be explained in Chapter 6, but here it is seen that the repeatability is typically within 3%, with a reduction

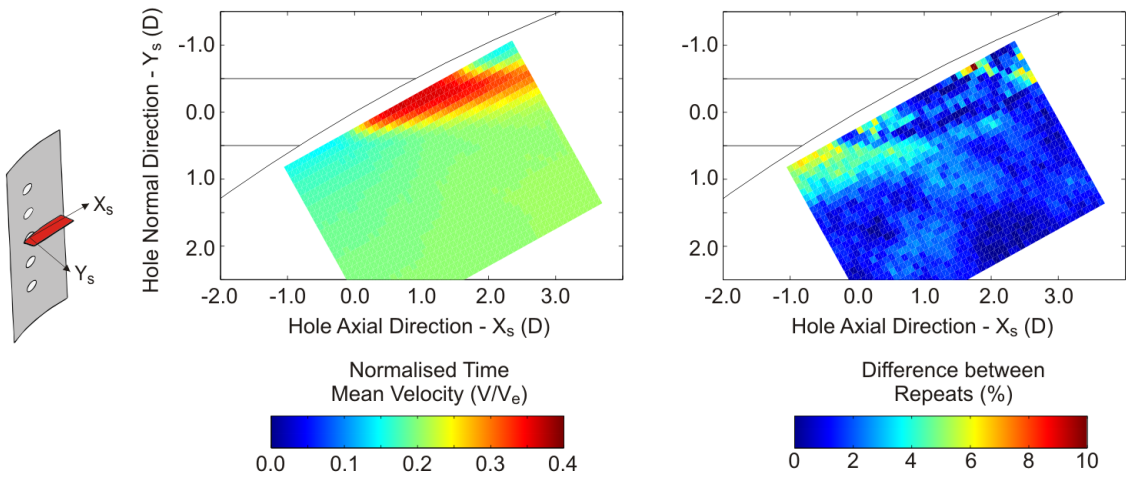

Figure 4.9: Repeatability in spanwise plane at midspan (left) time-mean velocity BR equal to 1.5 and (right) difference for a repeated measurement.

to within 6% in the low velocity regions. The repeatability in the secondary flow plane 2D downstream, is seen also to be of a similar level.

The seeding particles produced by either the atomiser or the smoke machine were quoted by the respective manufacturers as having a mean diameter of less 0.5μm. Applying Stokes' drag law on a particle of this diameter, the induced velocity due to gravity was insignificant for it was 4 orders of magnitude smaller than the measured mean velocity.

The seeding particle mass flow rate within the coolant or the mainstream was estimated to be a maximum of 0.5% of the air mass flow rate. This introduced an uncertainty of 0.5% in the density of the coolant flow, which did not significantly effect the measurement uncertainty in the blowing ratio or the ideal blowing ratio.

4.2 High Speed Photography

The high speed photography setup in the current investigation was similar to the PIV setup explained in the previous section. Like in Fig. 4.1, a pulsed laser was used to illuminate small diameter seeding particles within the flow and a high speed camera was used to record the scattered light. However, in contrast to the PIV setup the density of seeding particles was increased so that the entire flowfield was seen not just individual seeding particles. To enable features within the flow to be seen, therefore, only the jet was seeded.

Here the high speed photography system used in the current research to investigate the

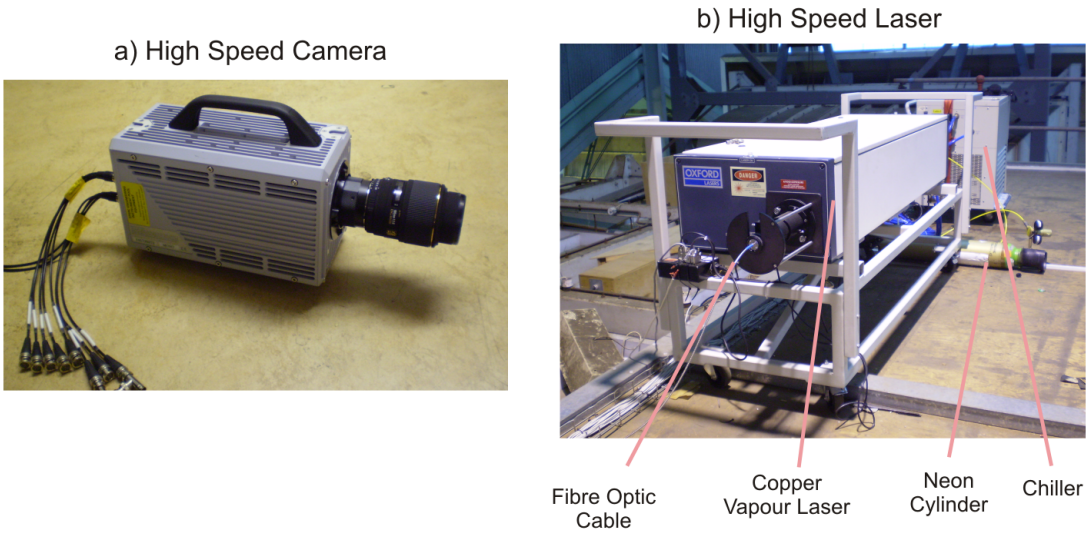

Figure 4.10: High Speed Photography equipment: (a) Photron High Speed Camera and (b) Oxford Lasers Copper Vapour Laser.

flowfield downstream of the cooling hole, when it was fed from either a plenum or internal crossflow, is explained. The equipment used and the measurement planes are first described. The section then describes the post-processing method and the uncertainties.

4.2.1 Current Setup

Two high speed cameras were used at different times during the current experiment, namely a Photron FastCam SA-3 camera and then a Photron FastCam AP-X camera. The AP-X camera is shown in Fig. 4.10(a). The significant difference between the two cameras was that the SA-3 recorded in 2^{16} bit greyscale whilst the AP-X recorded in 2^{8} bit grayscale. Otherwise both cameras had a pixel resolution of at least 768×608 across the range of frame-rates up to 3kHz at which recordings were taken, and could record sequences of up to 6000 frames.

To provide sheet illumination an Oxford Lasers LS20-50 copper vapour laser, shown in Fig. 4.10(b), was used which could be pulsed at up to 10kHz. The LS20-50, as shown in Fig. 4.10(b), required a chiller to cool the cooling water and a supply of Neon to maintain an inert environment within the laser tube. The fibre optic cable was used to carry the laser illumination to the measurement area.

Within the current experiment, sampling frequencies in the range of 1kHz to 3kHz were desired. The laser was only capable of operating continuously at either 4kHz or 10kHz. To

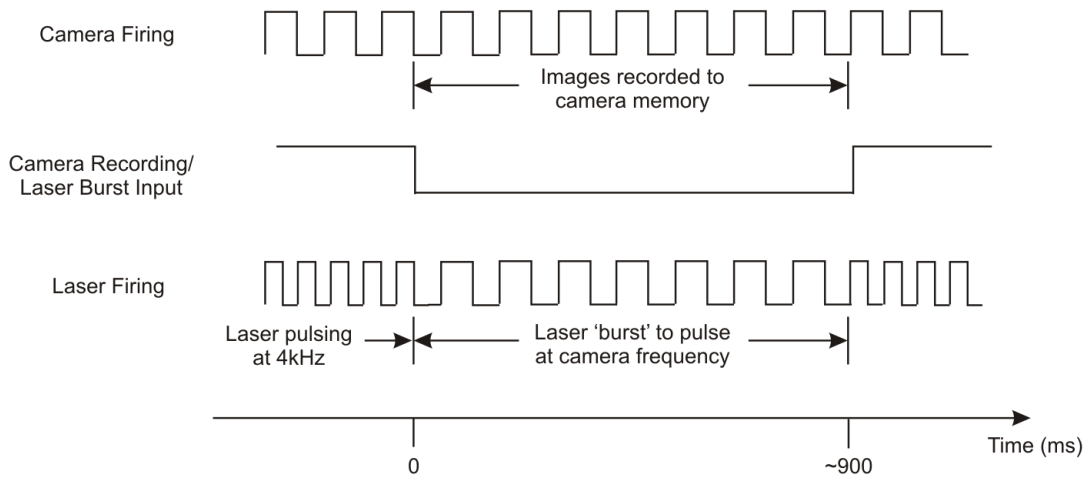

Figure 4.11: Timing diagram showing the effect of the burst input on the laser firing frequency.

achieve these lower frequencies therefore required the laser to be 'bursted' for short periods whilst measurements were taken. 'Bursting' placed an additional power load upon the capacitors within the laser, which caused them to fail if the 'bursting' time was excessive. On the advice of the manufacturer 'bursting' was limited to time periods of less than 900ms.

The high speed camera was operated using software called Photron Motion Tools running on a Dell workstation. The high speed camera was constantly capturing images at its recording frequency, as shown in the timing diagram of Fig. 4.11. When the camera was set to record images to its memory a low pulse was sent to the the 'burst' input of the laser. Figure 4.11 shows this modified the laser firing frequency to be the same as the camera recording frequency. When the recording sequence finished the laser pulsing frequency returned to its normal value.

The dimensions of the laser and the quantity of rejected heat from it, meant that it had to be located outside of the wind tunnel. The laser light was therefore delivered to the measurement location through the fibre optic cable. Bends in the fibre optic cable meant that the exiting beam was not of uniform intensity so could not be diverged into a sheet through a single lens. Instead Oxford Lasers supplied the splitter box shown in Fig. 4.12. Here the laser light entered from the fibre optic on the left. It was then reflected between the two parallel mirrors. There were slots in the right-hand mirror and at each reflection a portion of the light passed through a slot. A series of parallel beams were formed and these

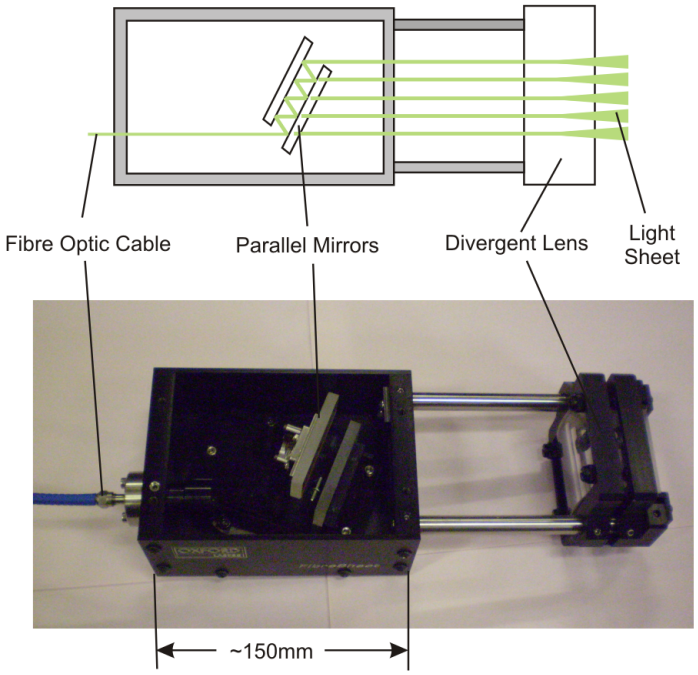

Figure 4.12: Splitter box with a schematic to show splitting of the laser beam.

passed through the divergent lens to form the downstream light sheet.

Forming the light sheet using the splitter box led to bands of alternating high and low light intensity, which are apparent in the example image of a jet in the spanwise plane shown in Fig. 4.13. Similar bands can be observed in the instantaneous images shown in the results chapters. The banding could have been reduced by moving the splitter box further from the measurement area, however this led to insufficient laser light to illuminate the jet. Consequently the position of the splitter box was a compromise between these two factors.

During high speed photography it was only required to seed the jet. For the plenum fed case the seeding particles were, as for the PIV measurements, a glycerol/water mixture supplied by a TSI systems 9306A atomiser. The higher flow rate when the cooling holes were fed from the crossflow channel required the seeding particles to be provided by the Concept Smoke Systems ViCount smoke machine, that had been used during the PIV measurements to seed the mainstream. To overcome the pressure difference between the smoke machine exit and the in-pipe to the cooling holes an ACI 4MS11 blower was used.

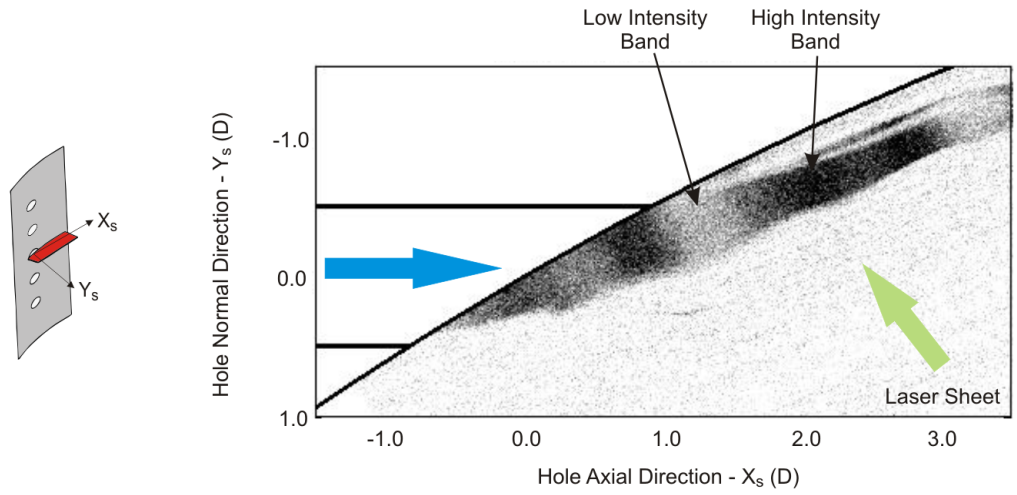

Figure 4.13: Banding in the pixel intensity seen in the spanwise plane.

4.2.2 Measurement Planes

Setup

The measurement planes investigated with high speed photography were the same spanwise and secondary flow planes, shown in Fig. 4.6, that were investigated using PIV. The high speed camera was located in the same positions as those described for the PIV camera. The Sigma 105mm EX DG Macro lens was fitted to the high speed camera. The spatial resolution was typically greater than 9 pixels per mm in the spanwise plane and 7 pixels per mm in the secondary flow plane.

The light sheet from the splitter box was of a lower power than the light sheet produced by the PIV laser. To provide enough illumination to observe the jet the splitter box had to be positioned close to the measurement location. Figure 4.14 shows the splitter box located within the turbine blade passage in the position used for illuminating the secondary flow plane. It was located away from the blade surface and angled upwards from its position below the blade midspan. To illuminate the spanwise plane the vertical traverse was kept in the same location. The splitter box was then raised vertically to the midspan and rotated to be in the correct plane. These positions did present a blockage to the mainstream passage flow, but they were considered acceptable as the hole discharge coefficient did not vary significantly from its value when the splitter box was not present.

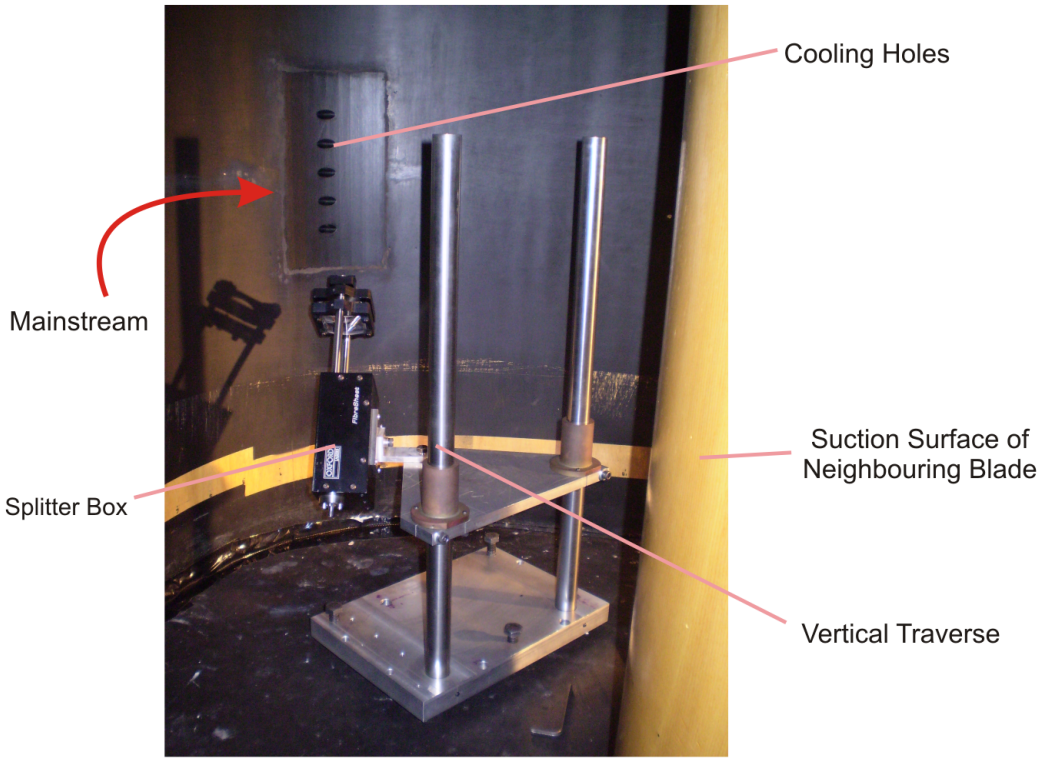

Figure 4.14: Splitter box orientated to illuminate the secondary flow plane.

Calibration

The calibration procedure was the same as that described for the PIV setup. With the laser first aligned with the measurement plane on low power, and the camera then focused on a 10mm×10mm grid located at the same measurement plane. The Photron Motion Tools software did not include a scaling function, so the images were recorded with pixel values as the co-ordinate scheme. The image taken with the 10mm×10mm grid was then used within Matlab 2008b to manipulate the images from the pixel co-ordinate scheme into that based on the blade co-ordinates.

4.2.3 Post-processing

Whilst the high speed camera was recording the images were saved to its internal memory. At the end of the recording time the images were downloaded to the Dell workstation using the Photron Motion Tools software. Each image was saved as a *.tif* file. These *.tif* files were then imported into Matlab 2008b where their colourmap and co-ordinate schemes were modified. The single images could then be saved or combined to create a video file.

Time-mean Images

To account for the banding in the light sheet the pixel intensities in the individual images were normalised to be either 0 or 1. Here 0 meant that the jet was not present and 1 meant that the jet was present. To achieve this normalisation a detector function was created.

The detector function first found the maximum intensity over the entire recording for a given location. For each image in the recording, if the intensity at that location was within 50% of the maximum intensity at that location the jet was classed as present, and a value of 1 assigned. If the intensity was less than 50% of the maximum at that location then a value of 0 was assigned. To avoid generating noise in the regions where the jet was never present a lower limit was set for the maximum intensity. This lower limit was set manually and was a compromise between highlighting the jet and reducing the background noise.

To reduce the computational time required for the detector function each image in a recording was first under-sampled to a pixel resolution of 2 pixels per mm. The intensity at the under-sampled position was the mean of the four neighbouring pixel values in the original image.

The normalised time-mean intensity (I) at each location in the under-sampled image was the mean of the normalised intensity, expressed according to Eq. 4.8. Here I' is the instantaneous pixel intensity, which, due to the normalisation, could only be 0 or 1, i is the image number and n is the number of recorded images.

$$I = \sum_{i=1}^{n} \frac{I'_i}{n} \tag{4.8}$$

To identify regions of high unsteadiness the variance (σ^2) was also calculated based on the normalised intensity values, as shown in Eq. 4.9. The normalised variance is the local variance divided by the maximum variance in the variance profile.

$$\sigma^2 = \frac{\sum_{i=1}^{n} (I'_i - I)^2}{n} \tag{4.9}$$

Figure 4.15 shows the effect of varying the cut-off in pixel intensity in the detector function from 50% of the maximum intensity at a given location. The time-mean pixel intensity and variance are shown for a jet from the cylindrical hole in the spanwise plane at midspan. It is seen that decreasing the cut-off in the intensity to 25% makes background

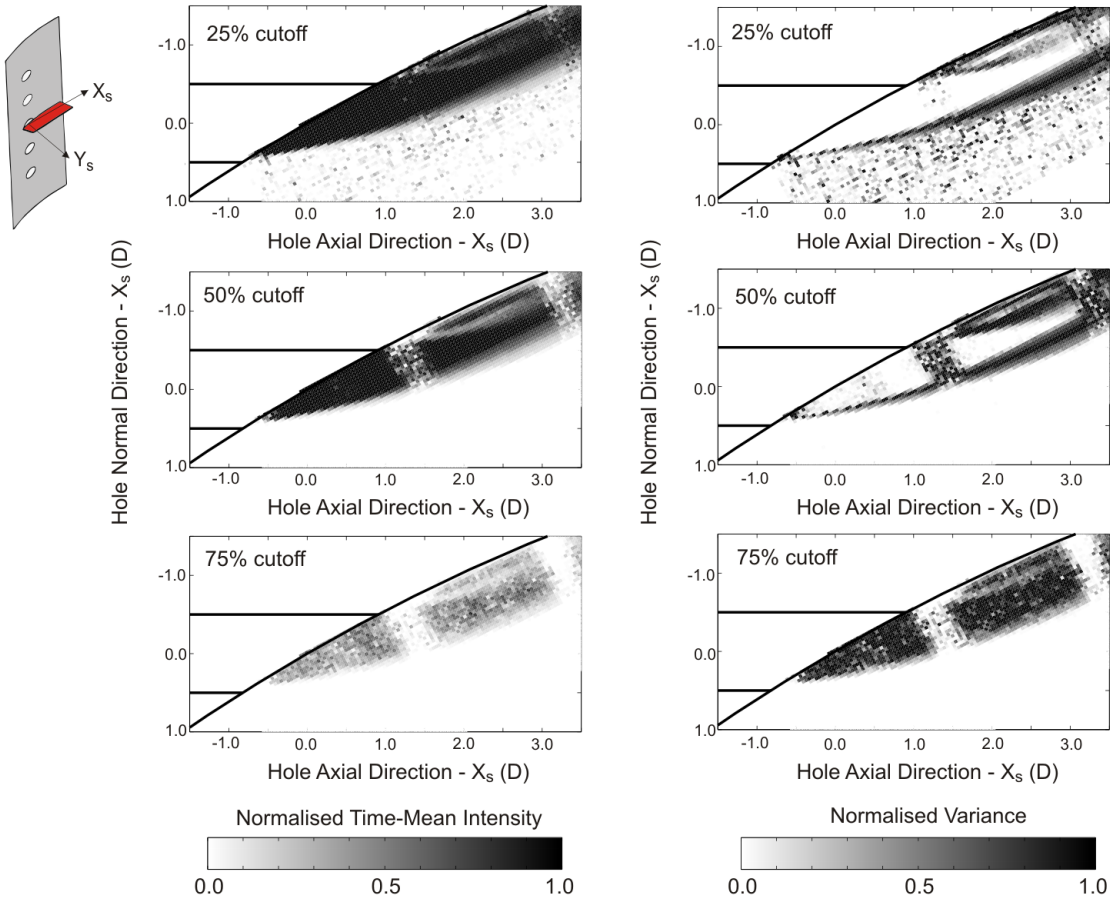

Figure 4.15: (Left) The time-mean pixel intensity and (right) variance of a jet from the cylindrical hole in the spanwise plane at midspan, with variation of the cut-off intensity in the detector function.

noise more visible in the mainstream. In contrast, increasing the cut-off to 75% means that the steady region of the jet is classed as only being present in approximately half of the images.

Coherent Unsteadiness

To identify a passing frequency for any coherent unsteady features seen within the jet, Fourier analysis was conducted based on the temporal variation in pixel intensity. To reduce the computational time the under-sampled image, described previously as the input for the detector function, was used. Coherent shear layer vortices are shown in Fig. 4.16(a) for a jet ejecting from the cylindrical hole. The image itself will be discussed in the results chapter, but is included here to demonstrate the method.

Figure 4.16(b) shows a trace of the pixel intensity variation with time for the point

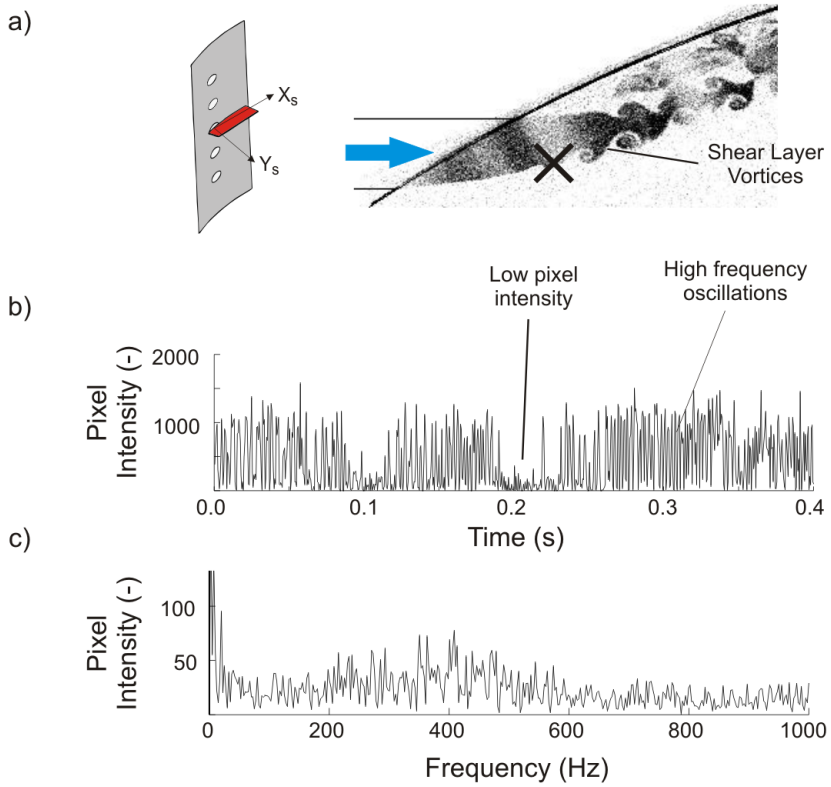

Figure 4.16: The method to identify coherent unsteadiness (a) shear layer vortices seen in the spanwise plane, (b) pixel intensity trace for the point marked with an 'X' and (c) the Fourier transform for this trace.

marked with an 'X' in Fig. 4.16(a). Within the pixel intensity trace two regimes are highlighted. One regime consists of high frequency oscillations which correspond to the passing of the shear layer vortices. The flat region of low pixel intensity occurred when the jet thickness decreased, and the shear layer vortices did not pass through the point.

Figure. 4.16(c) shows the obtained frequency spectra for point 'X'. In the spectra two peaks can be seen, a narrow peak close to the minimum frequency and a wide peak centred at approximately 400Hz. The low frequency peak was attributed to the time periods when the shear layer was not present at the point. The high frequency peak was associated with the passing of the shear layer vortices. The sample length was too short to reliably measure if the peak at the lower frequency was due to a coherent feature or an intermittent non-periodic change, so a mask was applied to discard frequencies of less than 30Hz. The passing frequency (f) of the coherent shear layer vortices was then taken as the higher frequency peak.

The high frequency peak shown in Fig. 4.16(c) does not have a large signal to noise

ratio. However, the strength of the technique was when it was applied to all the points in an under-sampled image, as all of the points for which coherent unsteady structures were seen showed the same peak frequency. This peak frequency was comparable with that estimated manually from a sequence of three images. The frequency was converted into a non-dimensionalised Strouhal number as shown in Eq. 4.10, where V_{str} was the velocity, estimated from a sequence of images, at which the coherent unsteady structures propagated downstream.

$$St = \frac{fD}{V_{str}} \tag{4.10}$$

4.2.4 Uncertainties

The positional uncertainties in the orientation of the two measurement planes investigated were estimated to be the same as those quoted for the PIV measurement planes. These corresponded to uncertainties of $\pm 0.8\%$ and $\pm 2.1\%$ in the distances within the spanwise and secondary flow planes respectively.

The mass flow rate of seeding particles was estimated to be a maximum of 1.5% of the coolant mass flow rate. This introduced an uncertainty of 1.5% in the measurement of the coolant density. This did not significantly increase the uncertainty in the blowing ratio or the ideal blowing ratio, with either the plenum or the crossflow channel at the hole inlet. The CFR uncertainty was not affected by the uncertainty in the measurement of the coolant density.

The uncertainty in the Strouhal number based on the change in pixel intensity with time was estimated to be ± 0.2. This was based on the uncertainty in identifying the maximum frequency in the frequency spectra and the estimation of the propagation velocity (V_{str}).

4.3 Hot Wire Anemometry

Hot Wire Anemometry (HWA) is a point measurement technique where the change in the resistance of a heated wire due to a moving airstream is measured. Figure 4.17 shows the heated wire to be of 15-20μm diameter and 3mm in length. The wire is typically made of platinum-plated tungsten. It is supported at either end by prongs that extend from a stem

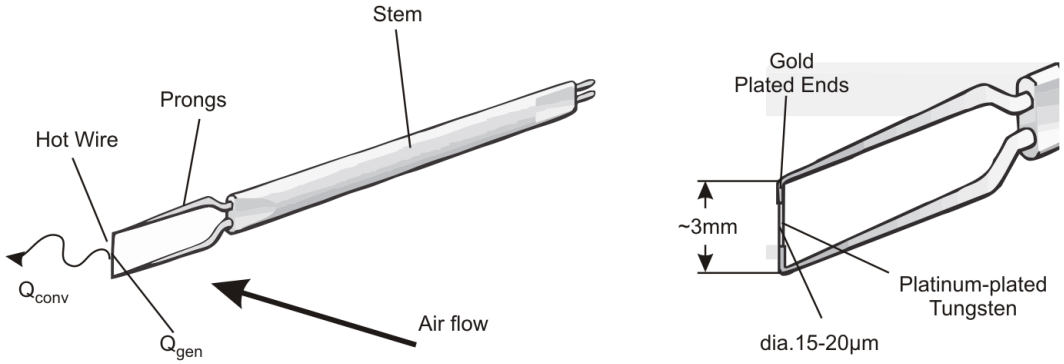

Figure 4.17: A Hot Wire Probe.

to form a hot wire probe. To increase the spatial resolution the measurement length of the wire can be reduced using gold plated ends of a higher diameter.

The wire is heated electrically such that the temperature of the wire is greater than that of the air and so heat is lost to the air by convection (Q_{conv}). The heat lost by convection is equal to the heat generated in the wire (Q_{gen}). When the velocity of the air under investigation is increased the heat lost by convection will increase. This decreases the temperature of the wire, and given its relationship to the wire temperature the wire resistance also decreases.

The hot wire forms one of the resistors in a Wheatstone bridge circuit and using this circuit the change in resistance with velocity can be measured. In most commercial applications a feedback loop is used to increase the heat generated (Q_{gen}) within the hot wire when the resistance decreases. This setup keeps the temperature of the wire constant and is called Constant Temperature Anemometry (CTA). The change in velocity is therefore measured as the change in voltage across the hot wire, and by operating at a constant temperature a frequency response in excess of 10kHz is possible.

Hot Wire Anemometry has been widely used in fluid mechanics. For more information than is possible here on the fundamentals of HWA the reader is referred to the book of Perry [75].

This section details the setup of HWA for the arrangement where the cooling holes were fed from an internal crossflow. The measurement locations are detailed, and the modifications that were made to the Oxford Super Scale Cascade to enable in-hole measurements are explained. The section finishes by explaining the post-processing procedure and the

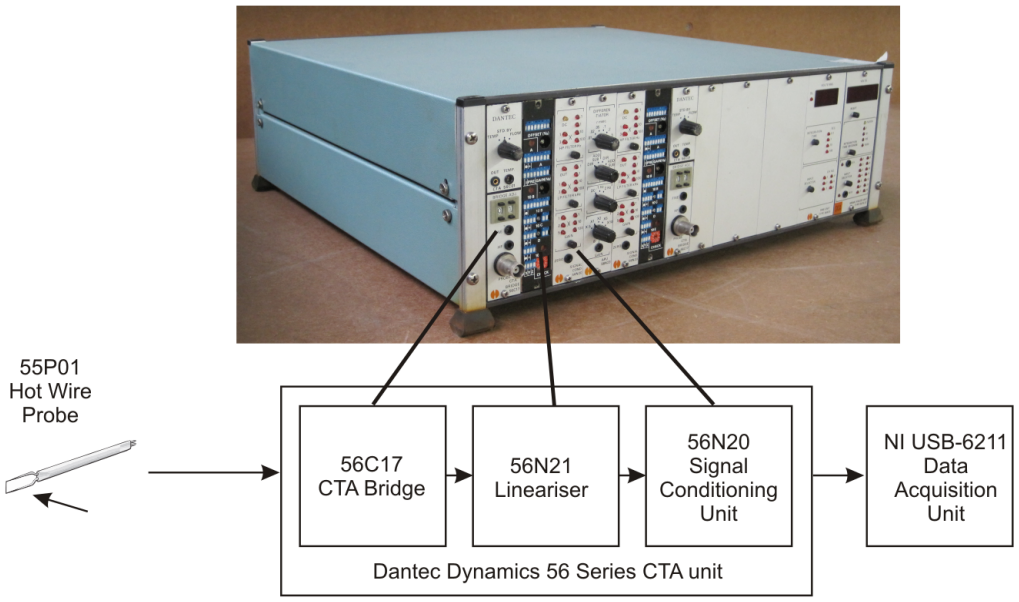

Figure 4.18: The Dantec Dynamics 56 Series CTA Unit.

uncertainties in the method.

4.3.1 Current Setup

Single sensor type 55P01 hot wire probes from the Dantec Dynamics range were used. The axis of the wire was perpendicular to the probe axis and supported by straight prongs. The hot wire itself was a platinum-plated tungsten wire of 15-20μm diameter and length 3mm with gold plating at each end so that the effective measurement length was 1.25mm. The hot wire probe was connected by a BNC cable to a Dantec Dynamics 56 series CTA unit, which is shown in Fig. 4.18.

The 56 series CTA unit consisted of a 56C17 CTA bridge module, 56N21 lineariser module and 56N20 signal conditioning module. The CTA bridge module contained the Wheatstone bridge and this was balanced for each individual hot wire probe. The overheat of the wire was set in this module, and for a velocity of approximately 2ms^{-1} the step response was seen using an oscilloscope to be less than 75μs. This implied that the maximum frequency response was 13kHz.

The output from the CTA bridge module was fed into the lineariser module where the non-linear variation in the voltage with velocity was modified into a linear relationship. The linearised output was then filtered within the signal conditioning module. Here a low pass Butterworth filter was applied with a cut-off frequency of 1.0kHz to remove any aliasing

due to high frequency noise. The filtered signal was then amplified if necessary.

The output from the signal conditioning module was sampled at 3.5kHz by a National Instruments USB-6211 data acquisition unit. This was significantly higher than the cut-off frequency of the low pass filter, which at this frequency had attenuated the signal by 90%. Labview V6.1 was used to read the digital output of the data acquisition unit and a datafile of the hot wire voltage with respect to time was stored. For each measurement point a sample length of 30 seconds was recorded.

The resolution of this configuration was less than $1 \times 10^{-5}\text{ms}^{-1}$. To confirm there was no aliasing in the setup, a measurement for which coherent unsteadiness had been observed was repeated with a 2.3kHz sampling frequency. There was no change in the resulting frequency of the coherent unsteadiness, and so it was considered unlikely that there was any aliasing in the setup.

4.3.2 Measurement Locations

Downstream of the Cooling Hole Exit

In the flowfield downstream of the cooling hole exit, measurements were taken upon planes aligned with the spanwise direction and that normal to the local blade surface, as shown in Fig. 4.19. Within these planes traverses could be made either normal to the blade surface (Y) or in the spanwise direction (Z). The origin of each traverse was taken to be the blade surface at midspan with no cooling hole present. Negative directions normal to the blade surface indicate that the measurement location was inside the cooling hole tube. For all the measurements taken the axis of the hot wire was aligned with the spanwise direction.

The traverse mechanism manufactured to allow the investigation of the flowfield downstream of the cooling hole exit is shown in Fig. 4.20. Figure 4.20 shows that the traverse mechanism was located in the blade passage and that the hot wire probe was positioned at the end of a cantilevered arm. The origin of each traverse was found by moving the hot wire to be offset by 4mm from the blade surface at the downstream distance of interest. The downstream distances were identified by markings upon the blade surface. The axis of the cantilever was then aligned by eye with the blade normal direction.

The distance normal to the blade surface (in the Y axis) was modified by extending or retracting the cantilever using an adjustable screw. The displacement of the cantilever

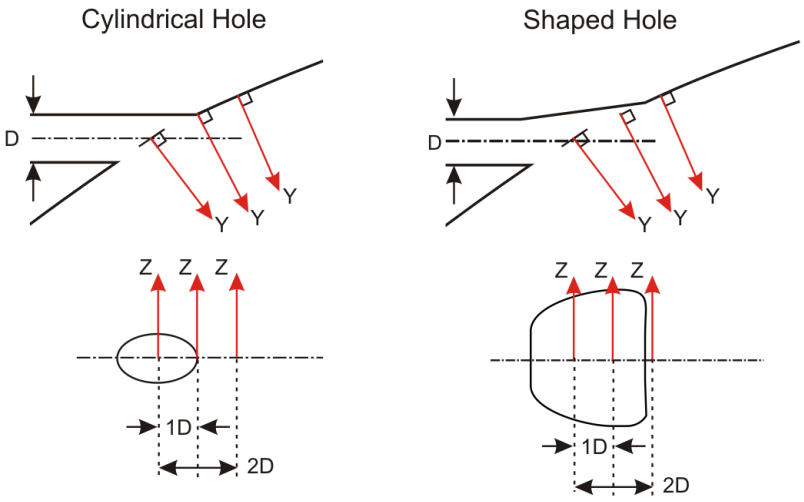

Figure 4.19: Hot wire measurement locations downstream of the cooling hole exit, showing the blade normal (Y) and spanwise (Z) axes.

was measured by the digital vernier calliper. In the spanwise direction (Z axis), adjustable screws were similarly used to move the hot wire probe. The displacement in this axis was measured using the needle gauge.

The hot wire was calibrated before use independent of the Super Scale Cascade using a convergent nozzle. The hot wire was located on the exit plane of the nozzle, with its axis normal to the flow. The mass flow rate through the nozzle was varied periodically through 6 cycles with a period of approximately 15s. The velocity at the nozzle exit plane was calculated based on the dynamic pressure, found using the static pressure at the nozzle exit and the total pressure from a pitot probe within the nozzle upstream of the convergence. The pressure difference was measured using a Sensortechnics BTEL5001 0-100Pa pressure transducer. The calibration curve for the hot wire was based on a velocity range of 2-6ms^{-1}.

Two typical calibration curves obtained approximately three hours apart are shown in Fig. 4.21. The velocity is that obtained from the dynamic pressure, and the voltage is that measured across the hot wire. Each of the calibration curves in Fig. 4.21 shows two linear fits to be possible. This is because the locations at which the total pressure and hot wire voltage are measured have different response rates to an increase or decrease in the nozzle mass flow rate.

The calibration curve used in the current experiment was based on the points recorded

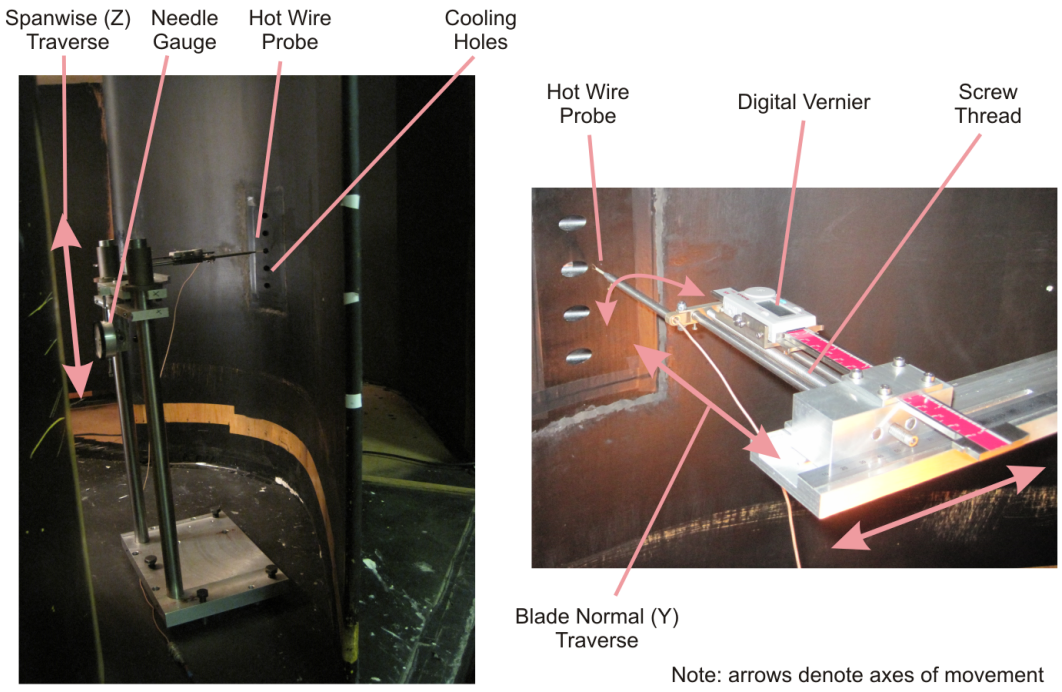

Figure 4.20: The traverse mechanism used to investigate the flowfield downstream of the cooling hole exit.

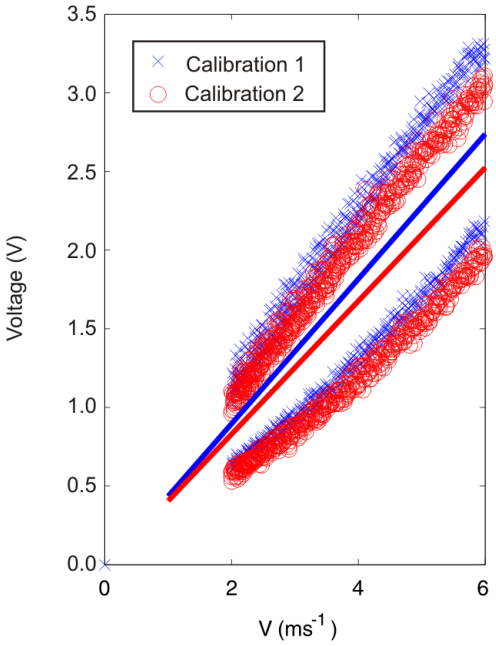

Figure 4.21: Comparison of two calibrations curves used for the out of hole measurements obtained approximately 3 hours apart.

with both increasing and decreasing mass flow rates. Comparing the calibration curves 1 and 2, shown in Fig. 4.21, led to a maximum difference of 7% in the measured velocity for typical points within the downstream jet.

Inside the Cooling Hole Tube

The measurement locations inside the cooling hole tube are shown in Fig. 4.22. For the cylindrical hole there were three planes normal to the hole axis in which the hot wire probe could be located. These planes were located at S equal to 0.5, 2.0 and 4.5D, where S is the distance upstream of the hole exit centre. The hot wire probe was orientated with the wire axis perpendicular to the axial direction. Geometric constraints meant that the probe axis had an angle of 20° to the blade spanwise direction. On each plane, measurement locations were restricted to that where the centre of the hot wire axis was located on the hole centreline and those 0.25D above and below the centreline.

The measurement locations inside the shaped hole are also shown in Fig. 4.22. Geometric constraints meant that only the planes at S equal to 2.0 and 4.5D could be investigated.

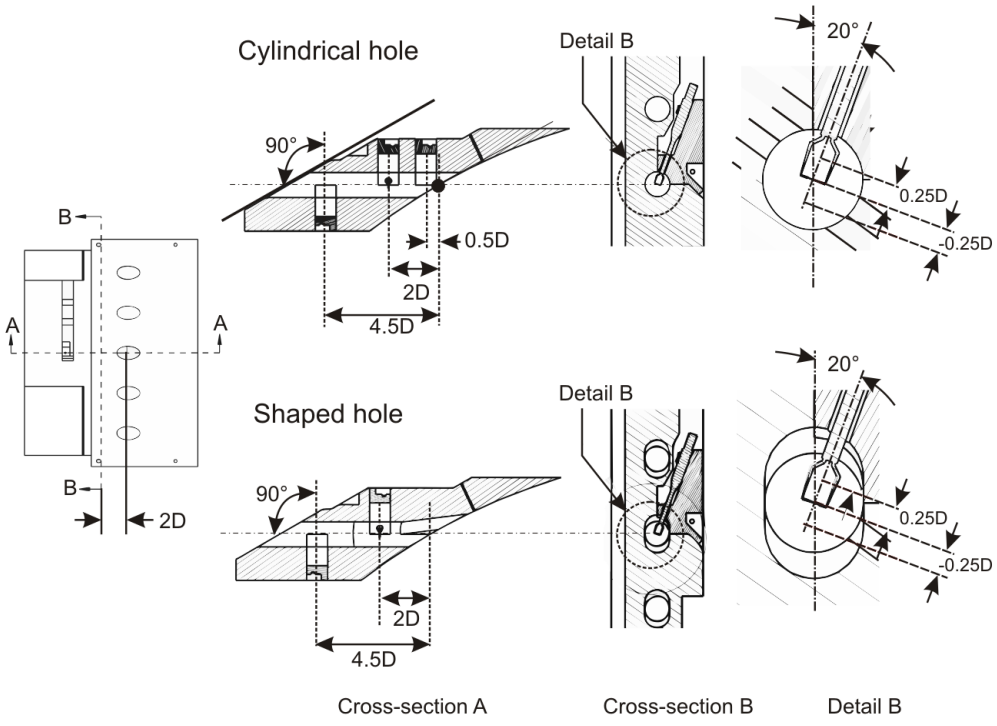

Figure 4.22: Measurement locations inside the cooling hole tube for investigation using HWA.

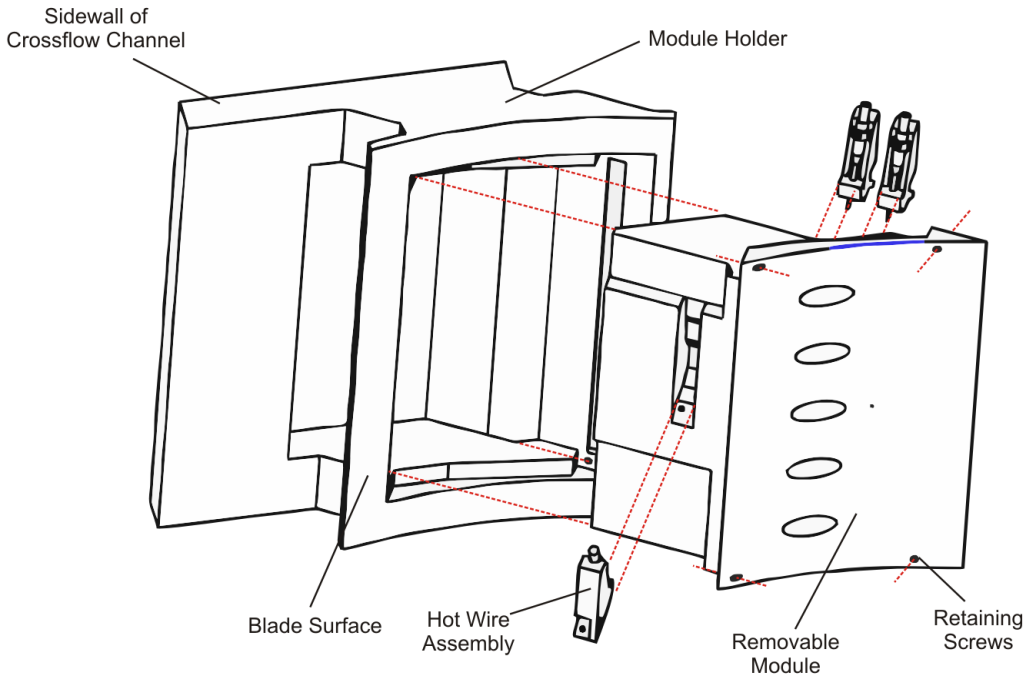

Figure 4.23: The modified removable cooling hole module to allow hot wire measurements inside the cooling hole tube.

On the plane at S equal to 4.5D the measurement locations were the same as those for the cylindrical hole. The 2.0D plane, as shown in Fig. 4.22, lay inside the expanding exit of the hole. At this plane the measurement locations were kept the same distance from the centre line, but compared to the plane at S equal to 4.5D they were further from the edges of the hole.

Previously to change the cooling hole module from one hole type to the other required the entire blade to be removed from the cascade. The position of the hot wire probe needed to be changed more regularly than the cooling hole geometry and so changing the hot wire position needed to be made easier. To achieve this the cooling hole module and collar shown in Fig. 3.10 were replaced by the configuration shown in Fig. 4.23. The module holder and the removable module were both made using stereolithography. The module holder was fixed into the crossflow passage and to the blade surface. The removable module which contained the hot wire probes could then be removed as required. Retaining screws were used to secure the removable module to the module holder and electrical tape was used to ensure there were no gaps.

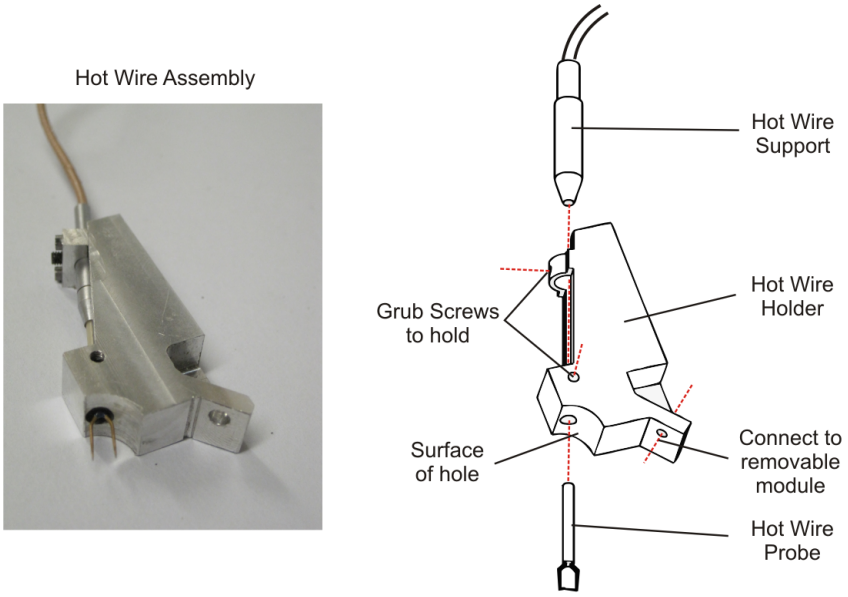

Figure 4.24: The Hot Wire Assembly to hold the hot wire probe within the cooling hole tube.

The hot wire probe was located on one of the hot wire assemblies shown in Fig. 4.23. An exploded view of one of these is shown in Fig. 4.24. The hot wire holder was made of aluminium and had a curved surface that formed part of the side of the cooling hole. There was a hole in the curved surface and the hot wire probe was inserted through this to be held by the hot wire support. Grub screws were used to hold the hot wire probe in position. The alignment with respect to the hole centreline was done with the aid of a ruler. Only one hot wire probe was present within the cooling hole tube at a time. Electrical tape was used to cover the holes in the hot wire holders that did not contain a hot wire probe.

The linear calibration curve for the hot wire in this configuration was found by plotting the variation of the average voltage at each blowing ratio with respect to the bulk velocity through the cooling hole. Figure 4.25 shows the calibration curve for the three measurement points on the plane at S equal to 4.5D. At all three locations it is seen that the relationship between the bulk velocity through the hole and the hot wire voltage is broadly linear.

The assumption in this method of calibration was that the flow through the cooling hole was uniform. Images presented in the results chapters suggest that the flow within the hole had some non-uniformity and Fig. 4.25 shows the calibration curves to have different gradi-

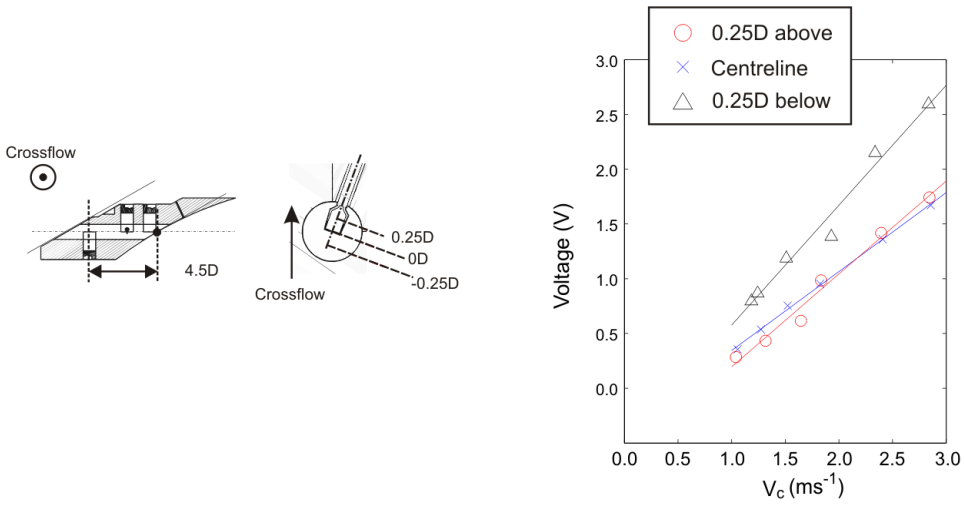

Figure 4.25: Typical calibration curves for the in-hole hot wire measurements, obtained for the three locations on the plane at S equal to 4.5D inside the cylindrical hole.

ents for different measurement points. However, the aim of the in-hole measurements was to identify any coherent unsteadiness not to obtain velocity profiles. The linear calibration in Fig. 4.25 does show that the uncertainty in the amplitude of the coherent unsteadiness could be reduced to that of the hot wire voltage measurement by scaling it with respect to the rms velocity. This also provides a measure of the coherent unsteadiness in regard to the total unsteadiness.

4.3.3 Post-processing

The coefficients for the linear calibration curves found for the respective measurement locations were used within Matlab 2008b to change the logged voltage output file into a velocity measurement. The time-mean and rms velocities were found using the complete 30 second sample, according to Eq. 4.11 and 4.12.

$$V = \sum_{i=1}^{n} \frac{V_i'}{n} \tag{4.11}$$

$$V_{rms} = \sqrt{\frac{\sum_{i=1}^{n} (V_i' - V)^2}{n}} \tag{4.12}$$

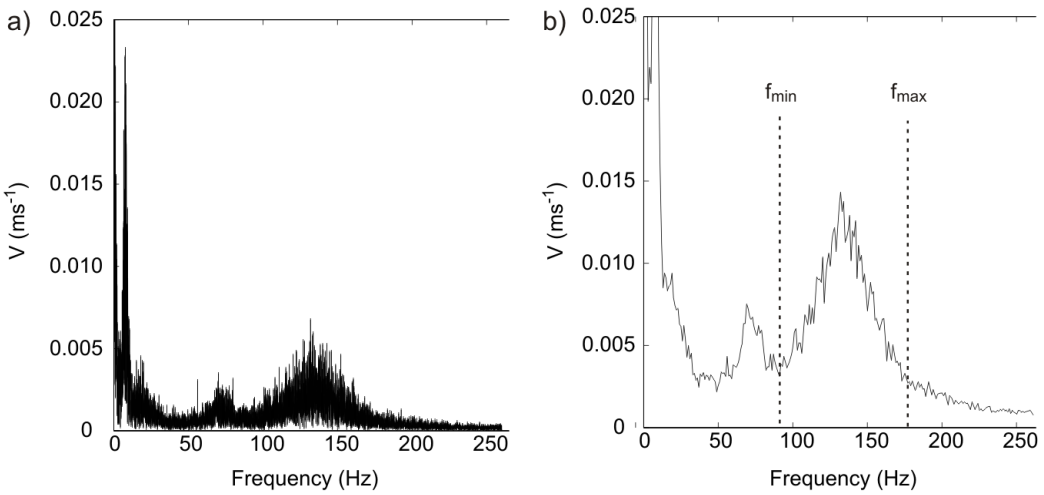

Figure 4.26: Frequency spectra for (a) the complete 30 second sample set and (b) the averaged 1 second samples.

To identify coherent unsteady structures frequency spectra were obtained using the FFT function in Matlab 2008b. If the entire 30 second sample was used as the input to the Fourier transform the resulting spectrum included a lot of noise as shown in Fig. 4.26(a). To reduce the noise the 30 second sample was divided into 1 second time periods and the frequency spectrum was found for each. These frequency spectra were then averaged and the mean spectrum is shown in Fig. 4.26(b). It is seen that averaging significantly reduces the noise and makes the frequency of coherent unsteadiness more identifiable.

The broadband peak shown in Figure 4.26 is typical of the peaks of coherent unsteadiness shown in the results chapters. To give a measure of the amplitude of coherent unsteadiness across a broadband peak, the term coherent turbulence intensity was introduced. Here frequency limits of the coherent unsteadiness (f_{min} and f_{max}) were defined manually for each frequency spectra, as shown in Fig. 4.26(b).

The instantaneous velocity profile was then filtered between these limits using the Butterworth filter function in Matlab 2008b. The rms velocity of coherent unsteadiness $V_{rms,coh}$ was then calculated from the filtered instantaneous velocity according to Eq. 4.13. The coherent unsteadiness intensity (I_{coh}), shown in Eq. 4.14, was subsequently found by normalising $V_{rms,coh}$ with respect to the local time-mean velocity.

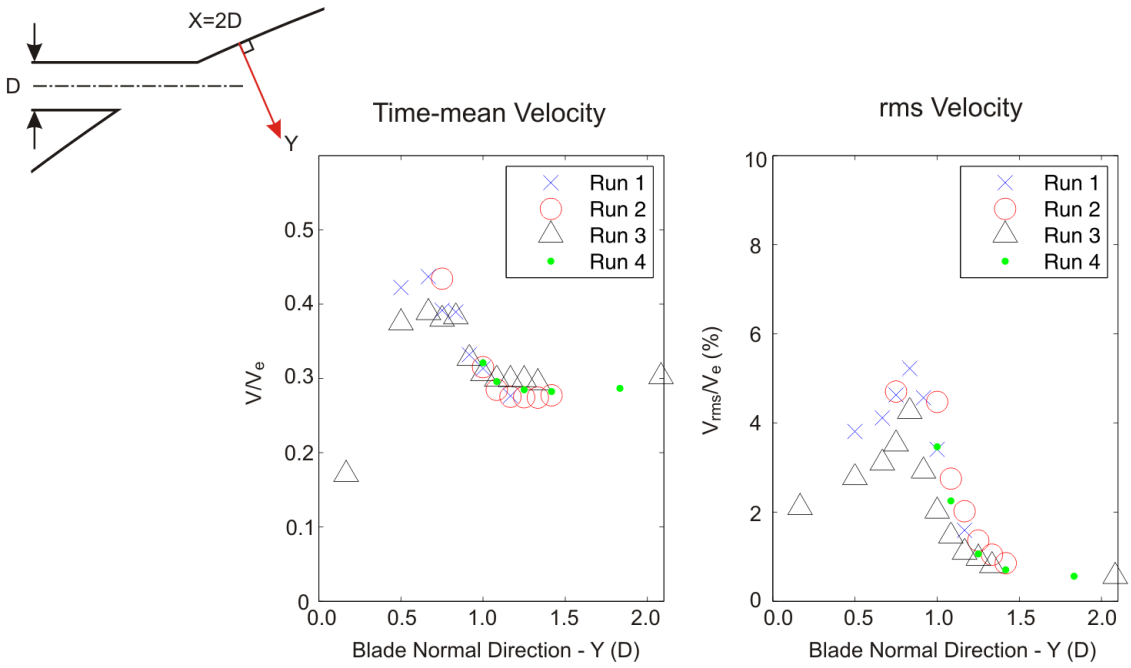

Figure 4.27: Repeatability of the (left) time-mean and (right) rms velocities on a blade normal traverse, 2D downstream at midspan. For the cylindrical hole with a BR equal to 1.8 and a CFR of 0.1.

$$V_{rms,coh} = \sqrt{\frac{\sum_{i=1}^{n}(V'_{i,filtered} - V)^2}{n}} \tag{4.13}$$

$$I_{coh} = \frac{V_{rms,coh}}{V} \tag{4.14}$$

4.3.4 Uncertainties

The positional uncertainty in the origin of the traverse was estimated to be ±1mm. The direction normal to the blade surface was found with an accuracy of ±10°. The uncertainty in the distance between the measurement locations within each traverse was two orders of magnitude smaller, as this was dependent on the measurement accuracy of the needle gauge and the digital vernier. The uncertainty in the position of the hot wire when located within the cooling hole was estimated to be ±0.5mm.

Previously it has been shown that the uncertainty in the velocity measurement downstream of the hole exit is greater than 7%. The purpose of this velocity measurement is to show the locations of coherent unsteadiness relative to the features of the jet. Figure 4.27 shows the repeatability in the measurement of the mean and rms velocities for a jet of BR equal to 1.8 on a blade normal traverse 2D downstream at midspan. In the mean velocity profile it is seen that there is a decrease in the mean velocity between Y equal to 0.8D and 1.2D which is common to all four runs. Whilst in the rms velocity profile, there is a common peak of 5% at Y approximately equal to 0.8D.

The linear relationship between the velocity and the hot wire voltage in the current setup, means that the uncertainty in the amplitude of the coherent unsteadiness has been reduced to the basic measurement accuracy of the hot wire voltage by normalising it with respect to the rms velocity.

The measurement of the frequency of coherent unsteadiness was estimated to introduce an uncertainty of $\pm 10\%$. Combining this with the uncertainty in the local time-mean velocity, the uncertainty in the Strouhal number measurement was 15% downstream of the cooling hole exit.

4.4 Summary

In this chapter the three measurement techniques used within the current experiment have been explained. Firstly, Particle Image Velocimetry (PIV) was used to investigate the spanwise and secondary flow planes downstream of the exit of plenum fed cylindrical and shaped holes. The chosen PIV setup used adaptive correlation, Gaussian window functions, a low pass filter and validation functions. The sampling frequency was 15Hz and sample lengths of 150 image pairs were recorded. The uncertainty in the velocity measurement was estimated to be less than 7%. The instantaneous velocity measurements could be used to obtain the time-mean vorticity and velocity, and the rms velocity.

High speed photography was used to observe the flowfield downstream of both cooling hole geometries with either a plenum or internal crossflow at their inlet. The same measurement planes as PIV were investigated at frame rates of up to 3kHz. It was possible to obtain instantaneous and time-mean pixel intensities, and the variance in pixel intensity, for sample lengths of up to 900 frames. It has been shown that it was possible to

obtain the frequency of coherent unsteadiness based on a Fourier transform of the change in pixel intensity with time. The uncertainty in the obtained Strouhal number of coherent unsteadiness was estimated to be ± 0.2.

The flowfields within the cooling hole tube and downstream of the cooling hole exit were investigated using Hot Wire Anemometry (HWA) for the case of crossflow at the hole inlet. A sampling frequency of 3.5kHz was used. To enable the in-hole measurements to be taken the cooling hole module described in the previous chapter was modified. This allowed the hot wire probe to be placed on one of 3 planes along the hole length. The uncertainty in the Strouhal number of any coherent unsteadiness in the mainstream was estimated to be 15%.

Chapter 5

Numerical Methods

Within the experimental measurements, discussed in the results chapters, coherent unsteadiness was observed inside the cooling hole with perpendicular crossflow at the hole inlet. A numerical model was used to help understand the cause of this coherent unsteadiness, and how it was effected by changes in the direction of crossflow at the hole inlet. The numerical model used the TBLOCK code developed by Denton [16] [17].

This chapter first provides a brief introduction to the TBLOCK solver, which has been adapted from that provided previously by Klostermeier [51]. The current numerical model and its boundary conditions are then described. The sensitivity of the numerical model to changes in grid resolution and the timestep is then explained.

5.1 The Solver

TBLOCK is a density based explicit solver, written in Fortran 77. In the current study version 38 was used. TBLOCK solves the continuity, momentum and energy equations, which are written in Eq. 5.1 as a generalised transport equation. Here C denotes the convective terms, D the diffusive terms and S the source terms. U denotes the variables being solved for which are listed in Eq. 5.2, where the velocities are in cylindrical co-ordinates and E is energy.

$$\frac{\partial}{\partial t}\int\int\int_V U dV = -\int\int_A C \cdot n dA + \int\int_A D \cdot n dA + \int\int\int_V S dV \qquad (5.1)$$

$$U = \begin{bmatrix} \rho \\ \rho V_x \\ \rho V_r \\ \rho r V_\Theta \\ \rho E \end{bmatrix} \tag{5.2}$$

The static pressure is calculated using the ideal gas equation and the static temperature is found using Eq. 5.3.

$$E = C_v T + \frac{V^2}{2} \tag{5.3}$$

TBLOCK is a structured solver and a hexahedral grid is used. The five flow variables in Eq. 5.2 are stored at the nodes of the grid. The value of a variable within a cell is the mean of the eight surrounding nodes, whilst that on a cell face is the mean of the four nodes at its corners.

The transient term calculated from the transport equations is used in the SCREE time-stepping procedure, shown in Eq. 5.4. Where n denotes the number of the timestep.

$$\Delta U = \left(2\frac{\partial U}{\partial t}|_n - \frac{\partial U}{\partial t}|_{n-1} \right) \Delta t* \tag{5.4}$$

The local timestep ($\Delta t*$) in Eq. 5.4 is not constant between cells. It is instead related to the length of the cell through the CFL number, which in the current investigation was set at 0.4. To increase the rate of convergence TBLOCK uses a multigrid procedure, where cells are grouped together and a step in U applied to all the cells at once. Three levels of multigrid are used, first one based on the entire block, then a grid of $9 \times 9 \times 9$ nodes and finally a grid of $3 \times 3 \times 3$ nodes.

For unsteady calculations Dual Time Stepping (DTS) is used, which has outer timesteps that step in real time (Δt). Between outer timesteps a series of inner timesteps, typically less than 100, must be solved. The inner time steps use the spatially varying timestep ($\Delta t*$) and the SCREE procedure in Eq. 5.4

When solving a DTS calculation the additional source term shown in Eq. 5.5 is added to the general transport equation in Eq. 5.1. Here m refers to the outer time steps, with U_m being the variable at the current outer time step.

$$\frac{1}{\Delta t}\left(\frac{3}{2}U_m - 2U_{m-1} + 0.5U_{m-2}\right) \tag{5.5}$$

5.1.1 Turbulence Modelling

TBLOCK uses a zero equation mixing length model to obtain closure of the Navier Stokes equation in Eq. 5.1. The mixing length (ℓ) is calculated for each cell as shown in Eq. 5.6 based on the distance of the cell from the nearest wall (c_w) and the Von-Karman constant (κ) which is equal to 0.41. An upper limit is applied to the mixing length when far from the wall and this is specified at a fraction of the hypotenuse of the block.

$$\ell_m = \kappa c_w \tag{5.6}$$

The mixing length is combined with the density and the gradient of the velocity within the cell to create an eddy viscosity term (μ_T), according to Eq. 5.7. This is combined with the laminar viscosity to give the overall viscosity.

$$\mu_T = \nabla V \rho \ell_m^2 \tag{5.7}$$

TBLOCK is capable of LES modeling as well as steady and unsteady RANS calculations. In LES modeling the same mixing length model is used as in Eq. 5.7, but as only the smaller scales of turbulence require modeling the definition of the mixing length is as shown in Eq. 5.8 based on the local cell size (c_L). C is the Smagorinsky factor which is typically set as 0.15 in TBLOCK.

$$\ell_m = C c_L \tag{5.8}$$

5.1.2 Wall Functions

Wall functions are used between the node nearest the wall and the wall. The wall Reynolds number (Re_w) is found for each near wall cell based on the distance between the node furthest from the wall and the velocity at that node. For a turbulent boundary layer Eq. 5.9 is applied if Re_w is less than 125, as the cell is judged to lie in the laminar subregion. Eq 5.10 is used if Re_w is greater than 125 and the cell is judged to lie in the log-law region.

$$C_{f,w} = \frac{1}{Re_w} \tag{5.9}$$

$$C_{f,w} = -0.0017677 + \frac{0.03177}{\ln Re_w} + \frac{0.25614}{\ln {Re_w}^2} \tag{5.10}$$

Transition is not predicted in TBLOCK, so the point of transition has to be specified. For a laminar solution only Eq. 5.9 is applied irrespective of the value of Re_w.

5.1.3 Pre and Post-Solver

TBLOCK has an inbuilt grid generation function, however within the current study the geometry was created in Matlab 2006b and saved as a binary file which was loaded into TBLOCK. The boundary conditions, flow properties and time-stepping procedure are written to an input parameter file which is called by the TBLOCK solver.

TBLOCK outputs the five variables at each node of the grid to a binary file. For a steady calculation this is done on completion of the specified number of iterations. When solving an unsteady calculation an output file is created after a specified number of outer time steps. The convergence of a model can be checked using the output log file which shows the maximum velocity in a block, and the average and maximum differences between iterations.

Within the current study the binary output files were modified using further scripts written in Fortran 77 to produce *.mat* files that could be read by Matlab 2006b. In Matlab 2006b functions were written that permitted the flow variables to be displayed. The binary output was also modified using Fortran 77 to create *.q* and *.x* files that could be imported into Paraview 3.8.

5.2 The Model

Within the current investigation TBLOCK was run on a Dell Precision 390 workstation with an Intel Core 2 processor running the SUSE flavour of Linux. The domain was that of a single cooling hole and the geometry was divided into the three blocks shown in Fig. 5.1, namely the mainstream, cooling hole and plenum. The grids were generated using Matlab

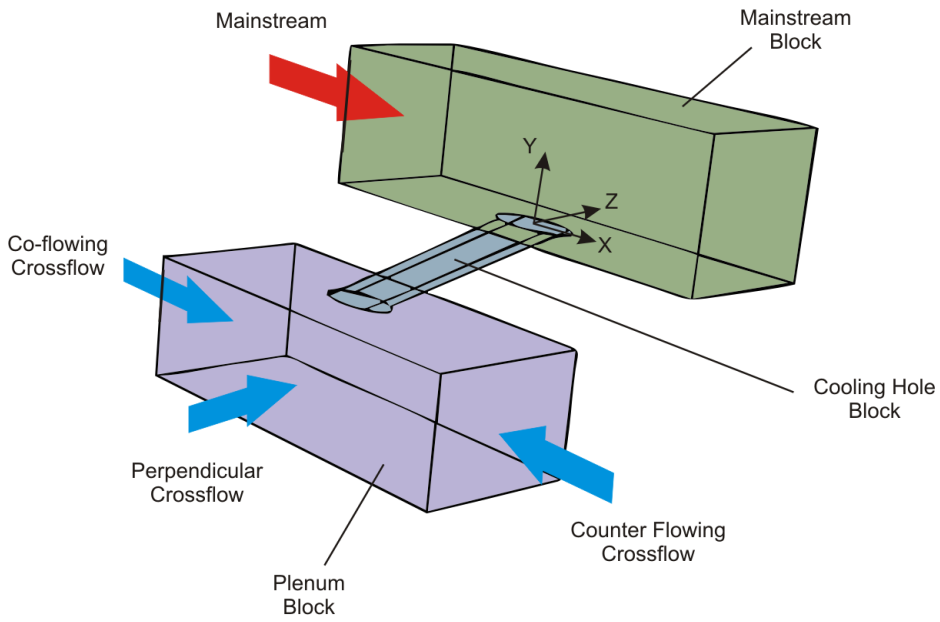

Figure 5.1: The three blocks in the model and the crossflow directions.

2006b using automated functions written by Wheeler [100], which required only a series of parameters to be defined.

The coherent unsteady features within the cooling hole were resolved by making the grid density sufficiently fine. As only a qualitative understanding of their characteristics was desired, it was decided to solve the model as a laminar flowfield. To do this the mixing length used in the turbulence model was set to zero and no transition of the boundary layer was specified within the domain. Wall functions were to be used so TBLOCK was run using the ILOS equal to 9 setting. With these settings the model could also be described as a coarse grid LES model with no explicit sub-grid scale modeling.

The velocities in the experimental investigation had a Mach number of less 0.03. As TBLOCK is a density based solver very low Mach numbers, such as those in the experiment, are not advised, for they are likely to lead to convergence problems. In the current investigation this problem was avoided by keeping the Mach number above 0.03.

The lower limit to the velocity in the numerical model meant that the velocities were scaled up by a factor of 52 compared to those in the experiment. The Reynolds number was kept the same as the experiment by increasing the dynamic viscosity by the same factor as the velocity.

If an unsteady DTS model was begun without a part converged initial solution field

unrealistic density profiles were seen within the solution. It was found that a part converged steady solution of 5000-10000 iterations, with the same boundary conditions as the unsteady solution, was sufficient for use as an initial solution field.

5.2.1 Crossflows to be Investigated

The three different crossflow directions shown in Fig. 5.1 were investigated. Both cylindrical and shaped holes of the same geometry as those in the experiment were investigated. To keep the test matrix a manageable size the blowing ratio was not varied, and was set at a constant value of 0.9. This BR was chosen as the experiments showed the presence of significant coherent unsteadiness within the cooling hole.

Experimental measurements were taken inside the cooling hole for CFR of 0.1, 0.2 and 0.6. The lower limit to the velocity meant that it was not possible to model the CFR equal to 0.1 case, where all of the coolant exits through the cooling hole. Therefore only the CFR equal to 0.2 and 0.6 cases were modeled numerically.

The BR and CFR were calculated according to Eq. 5.11 and 5.12. Here the mass flow rate through the cooling hole ($\dot{m}_c$) was found by integrating across the values for each cell face at the hole mid-height. The mass flow rate into the plenum ($\dot{m}_{in}$) was similarly found by integrating across the cells on its inlet plane. The mainstream density was found using the ideal gas equation, with the static pressure and temperature being those at the mainstream exit plane furthest from the blade surface. Within the CFR calculation it was assumed that the density in the plenum was equal to that in the cooling hole.

$$BR = \frac{\rho_c V_c}{\rho_\infty V_\infty} = \frac{\dot{m}_c / A_c}{\rho_\infty V_\infty} \tag{5.11}$$

$$CFR = \frac{V_{cross}}{V_c} = \frac{\dot{m}_c / A_c}{\dot{m}_{in} / A_{cross}} \tag{5.12}$$

5.2.2 Domain Size

The geometries of the cooling holes were the same as those when fed from a crossflow channel in the experimental setup which were shown in Fig. 3.11. Given the requirement for only a qualitative understanding of the flowfield inside the cooling hole the curved blade surface was made flat to reduce the meshing complexity. To reduce the required computational

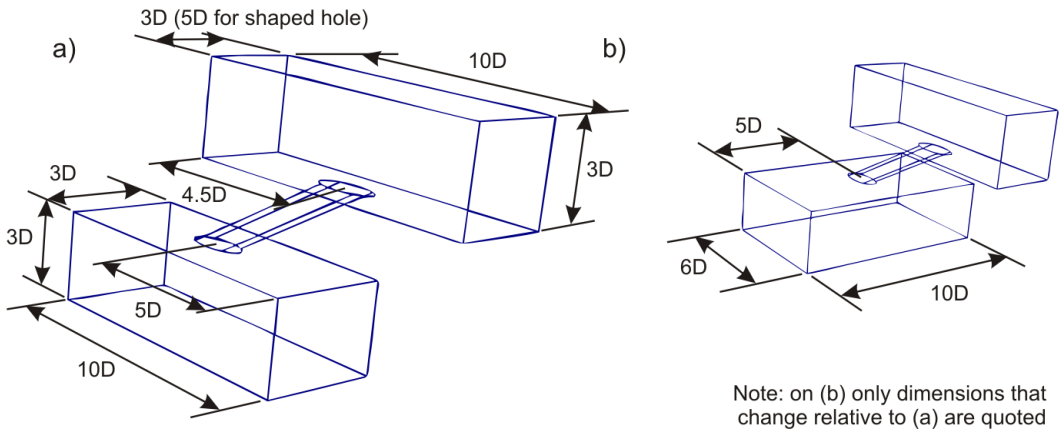

Figure 5.2: The dimensions of the domain for the cylindrical hole model for (a) counter and co-flowing crossflow and (b) perpendicular crossflow.

effort the domain size was made relatively small compared to other computational studies of film cooling, such as those of Leylek and Zerkle [58] and Tyagi and Acharya [97].

The dimensions of the domain are shown in Fig. 5.2 for the cylindrical hole. To ensure a suitable distance between the plenum inlet and the hole inlet the plenum chamber was rotated by 90° when modelling perpendicular crossflow. The size of the domain used for the shaped hole was the same as that shown in Fig. 5.2, except that the lateral extent of the mainstream block was increased to 5D on account of its laterally expanding exit.

5.2.3 Boundary Conditions

The boundary conditions for the domain are shown in Fig 5.3. The flow at the inlet to the mainstream block had a uniform total temperature of 300K specified and was orientated normal to the inlet plane. A fixed static pressure was specified on the exit plane opposite the blade surface, and at the exit plane opposite the inlet plane. Based on these exit static pressures the total pressure profile at the inlet plane was prescribed in accordance with the boundary layer profile shown in Fig. 3.3. A linear extrapolation was used to extend this profile to the maximum height of the block, and the scaled mainstream velocity was set to be the value at the maximum height of the block.

In Fig. 5.3 the plenum block is orientated for counter flowing crossflow. The boundary conditions were the same for the other crossflow directions, but with the plenum block rotated appropriately. The incoming flow was specified to be normal to the inlet plane. At the inlet plane a uniform total temperature of 310K was specified, which was larger than

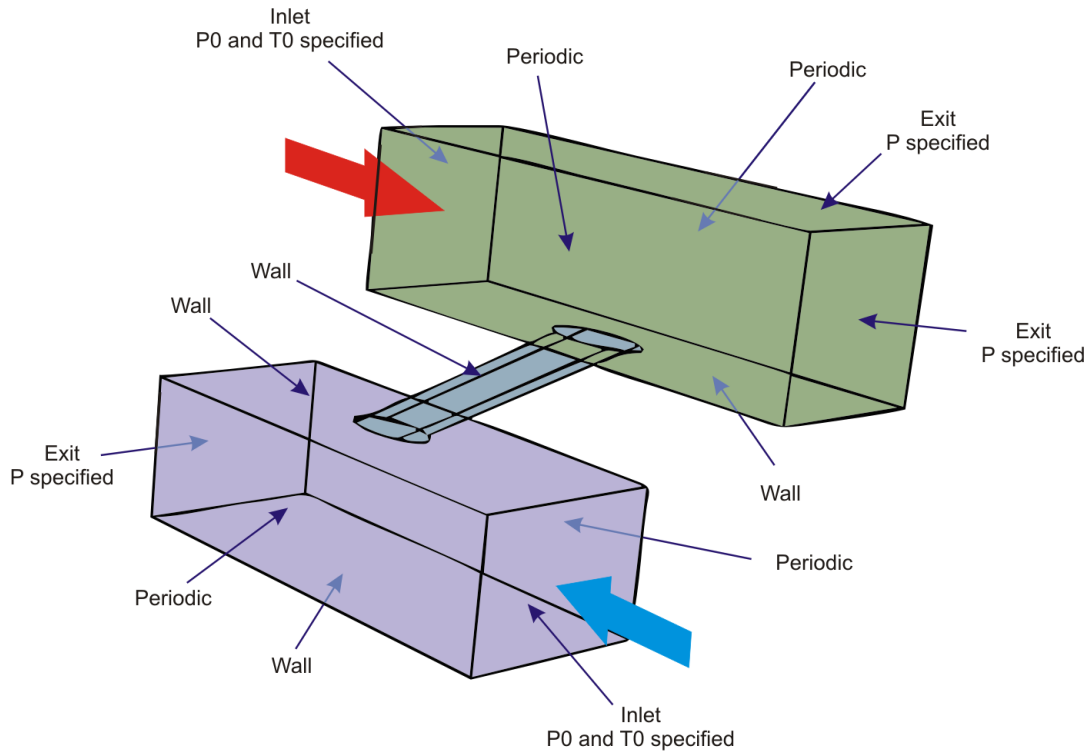

Figure 5.3: Boundary conditions for the model with counter flowing crossflow.

that at the inlet of the mainstream block. This meant that static temperature could be used as a tracer of the jet in the mainstream block. A uniform total pressure profile was specified at the inlet plane and an average static pressure at the exit plane. These were varied such that the BR and CFR were set to their desired values. The pressures were considered acceptable if the time-mean BR and CFR calculated from the unsteady solution were within ± 0.05 of their desired values.

The surfaces within all three blocks were set to be viscous walls with laminar wall functions applied. The pairs of sidewalls within the mainstream and plenum blocks were set to be periodic with each other.

5.2.4 Pseudo Hot Wire Probes

To reduce the storage requirement needed for the output of the unsteady solution, the complete flowfield could not be saved after every timestep of the calculation. However, to resolve the frequency of any coherent unsteadiness within the cooling hole it was desired to sample after every timestep. To do this a function was added to the TBLOCK source to replicate the hot wire probes used inside the cooling hole in the experimental investigation.

In the experiment the hot wire probe could be positioned at one of three locations upon each of the planes at S equal to 0.5D, 2.0D and 4.5D, as shown in Fig. 4.22. The reader is reminded that S is the distance upstream of the hole exit centre. In the computational grid the eight nodes surrounding each of these locations were identified. The variables at just these nodes were then saved after each timestep. The mean of the eight nodes surrounding nodes was then calculated to determine the variables at the pseudo probe. The velocity component in the XY plane (V_{xy}) was then found for each pseudo hot wire probe, this could then be plotted with respect to time and its frequency spectra found using Matlab 2006b. Only the XY velocity component was measured as this was the same as the velocity components measured experimentally.

5.3 Solution Sensitivity

The hypothesis developed in the results chapter to explain the formation of the coherent unsteadiness suggested that the coherent unsteadiness inside the cooling hole would be most apparent with a counter flowing crossflow. Therefore the counter flowing case with a CFR of 0.2 was used to check the sensitivity of the unsteady solution to variations in the grid density and the length of the timestep.

The experimental results showed that a Strouhal number of 1.0 was a likely upper limit for the frequency of coherent unsteadiness that may be observed in the computational model. With the bulk velocity within the hole being 75ms^{-1}, this Strouhal number corresponded to a frequency of 6kHz or a period of 170μs. As it was preferred to have at least ten timesteps across a period, a time step of less than 17μs was thought to be necessary.

The model was solved for a real time of at least 6ms in all of the cases in this section and in the later results chapters. This was a sufficient time for flow traveling at the bulk coolant velocity to travel the distance from the hole inlet to the exit of the mainstream block 3.5 times. The unsteady solution was taken as not more than the final third of the real time length. Time-mean flowfields, that are shown in the results chapters, are based on the instantaneous flowfields at 20 evenly spaced timesteps within the unsteady solution.

Nodes	Grid A	Grid B	Grid C	Grid D
Mainstream Block ($\times 10^{-3}$)	32	120	340	580
Cooling Hole Block ($\times 10^{-3}$)	4.4	25	51	80
Plenum Block ($\times 10^{-3}$)	12	66	230	380
All Blocks ($\times 10^{-3}$)	49	210	620	1000
Hole Circumference	60	100	128	160
Hole Height	20	40	50	58
	Grid A	Grid B	Grid C	Grid D
Time for one iteration (ms)	60	250	520	920

Table 5.1: Grid details.

5.3.1 Grid Resolution

To assess the sensitivity of the model to grid density it was solved for the four different grid resolutions shown in Table 5.1. Compared to previous LES studies of film cooling even the finest of these grids would be classified as a coarse grid, with Peet and Lele [74] and Renze et al [83] respectively using 1300×10^3 and 350×10^3 nodes in a hole of comparable length. However, the intension of these previous studies was to quantitatively match experimental results, which as stated previously is not the aim of the current work.

Across the grids in Table 5.1 the ratio of nodes between the different block edges was approximately constant. The expansion factors to increase the node spacing in the plenum and mainstream blocks away from cooling hole also remained constant between the different grids. The hole height in Table 5.1 refers to the direction normal to the blade surface not the distance along the hole axis. The nodes were evenly spaced across the hole height for all grid densities. An outer timestep (Δt) of 10μs was used for the grid sensitivity.

Figure 5.4 shows the velocity profile on the hole centreline for a timestep within the unsteady solution with variation in grid density. These timesteps were considered typical of what was seen across all the saved timesteps at their respective grid densities. The coarsest grid (Grid A) gave a steady solution. At the hole inlet Fig. 5.4 shows this steady solution to have a high velocity jetting region at the leading edge and a separation bubble at the trailing edge.

On increasing the grid density through Grids B to D, the velocity profile inside the

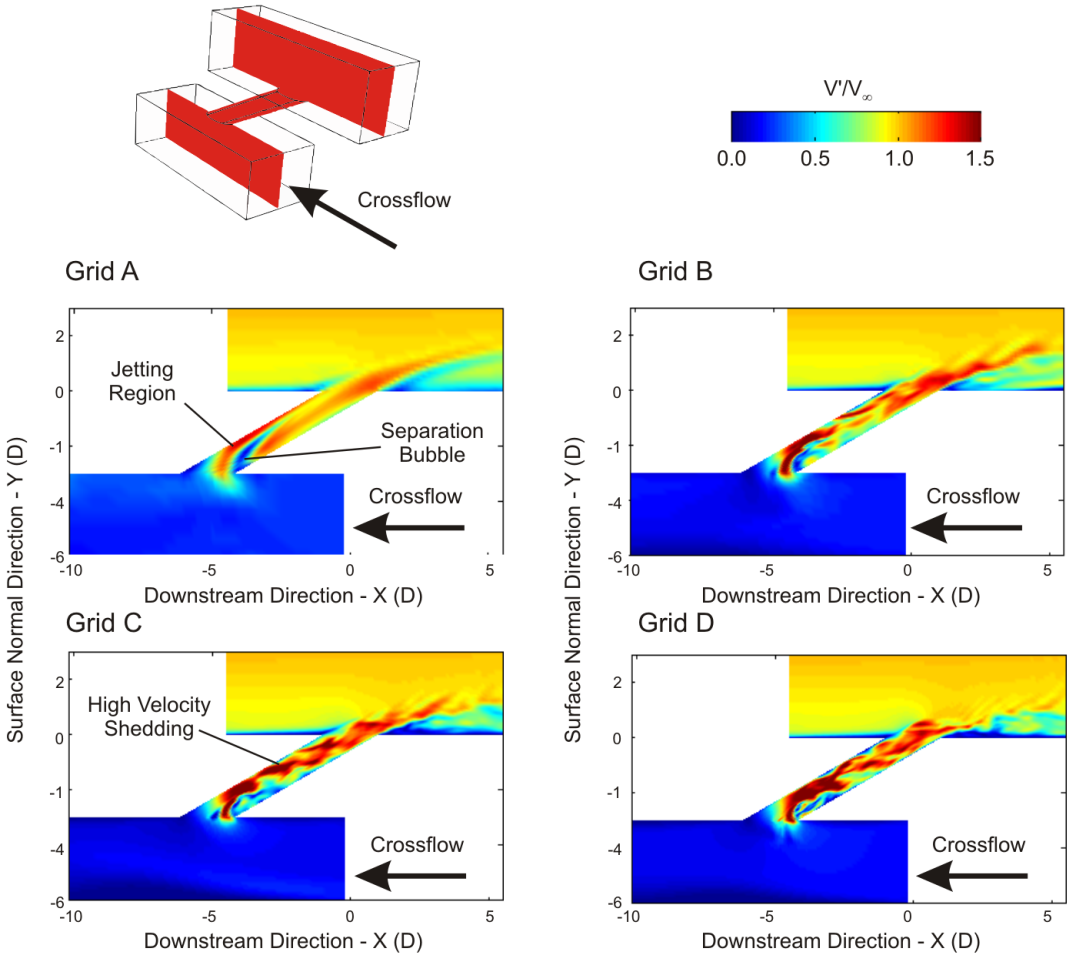

Figure 5.4: Typical instantaneous velocity profiles on the hole centreline for varying grid density for a BR of 0.9 and a counter flowing CFR of 0.2.

cooling hole as shown in Fig. 5.4 became unsteady. Here the jetting region broke up near the hole inlet and periodic patches of high velocity were seen to be shed and pass along the hole tube. This shedding of high velocity was seen most clearly in Grid C. The reader is reminded that the aim here is only to establish a sufficient grid density for observing in-hole coherent unsteadiness. A discussion of the formation of this coherent unsteadiness can be found in Chapter 8.

The frequency spectra shown in Fig. 5.5 are for the velocity variation at each of the probes on the hole centreline for Grids B through D. The Strouhal number was calculated based on the hole diameter and the bulk velocity through the cooling hole. For each of the grid densities the peak frequency at each of the three locations had a Strouhal number in the range of 0.6 to 0.8. This Strouhal number was consistent with that of the shedding of high velocity shown in Fig. 5.4.

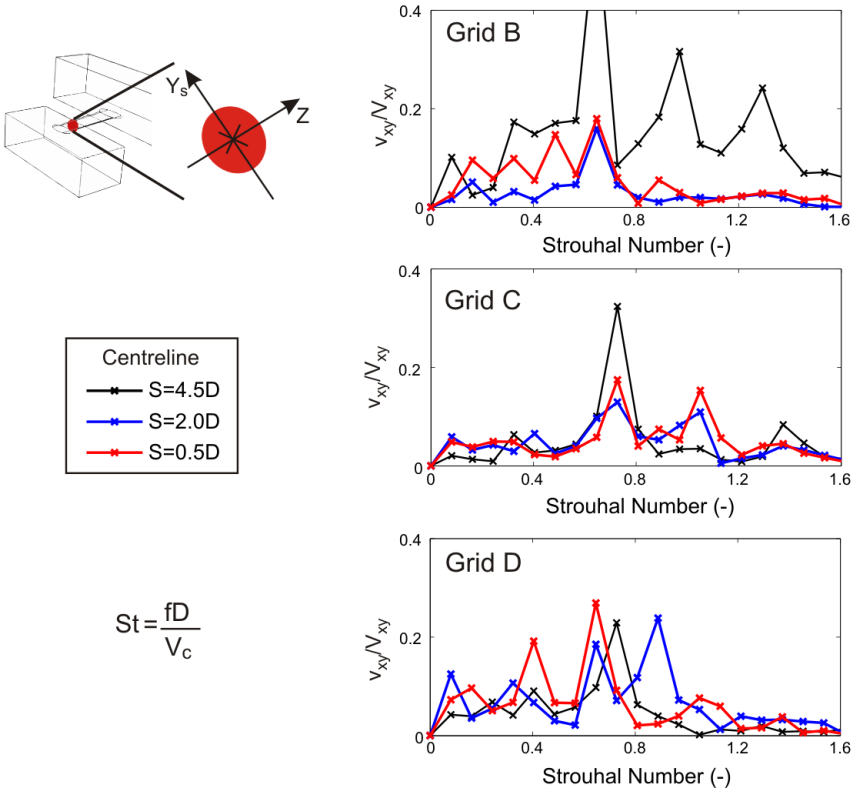

Figure 5.5: Frequency spectra of the velocity fluctuations inside the cooling hole with variation in grid density for the cylindrical hole.

In Grid B a large number of additional peaks are seen in the frequency spectrum for the probe nearest the hole entrance. These are not seen with the increase in the grid density to that of Grid C or D, so are therefore likely to have arisen due to insufficient spatial resolution in Grid B. Figure 5.5 shows that with Grid D multiple peaks appeared in the centreline velocity of the 2D and 0.5D planes. These are likely to have arisen due to the resolving of the smaller scales of turbulence. These smaller scales of turbulence were also apparent from the increase in random unsteadiness seen within the centreline velocity profile.

A similar grid sensitivity study was also performed using the shaped hole for grids with a comparable number of nodes to Grids B through D. Although, as seen by comparing Grid C in Fig. 5.6, the expanding exit of the hole meant that the nodes were distributed differently for the shaped hole to the cylindrical hole. However, the grids for the shaped hole showed a similar pattern to that shown in Fig. 5.5, with a consistent frequency peak at a Strouhal number of 0.6 to 0.8 for the centreline of the 4.5D plane.

Given the aims of this computational study the frequency spectra in Fig. 5.5 and the centreline velocity profiles in Fig. 5.4 were comparable between Grids C and D. Therefore

Grid C, which was 40% faster per iteration than Grid D, was selected for the other models with co-flowing and counter flowing crossflow. The node distribution of Grid C close to the hole inlet and exit is shown in Fig. 5.6 for both the cylindrical and the shaped holes.

The y^+ value inside the hole was less than 3.0 for both the grids shown in Fig. 5.6. This was based on the bulk velocity through the cooling hole, with the y direction taken to be the direction normal to the hole circumference and the wall shear stress calculated using the wall function shown in Eq. 5.9.

5.3.2 Temporal Resolution

To determine the sensitivity of Grid C to changes in the length of the timestep further simulations were run where this was varied from 20μs to 4μs. At all four of the time steps considered, high velocity shedding, like that shown in Fig. 5.4, was seen inside the cooling hole tube.

Figure 5.7 shows the frequency spectra obtained for the velocity variation at each probe on the hole centreline for the four different lengths of timestep. At 20μs there was not a peak frequency common across the different probes, but the peak of maximum amplitude was on the 4.5D plane at a Strouhal number of 0.4. The velocity frequency spectra obtained with a timestep of 10μs are the same as those shown in Fig. 5.5 and showed a peak Strouhal number of 0.7. On decreasing the timestep length to 6.25μs the frequency of coherent unsteadiness increased to be of a Strouhal number close to 0.9 and with 4μs timesteps it's Strouhal number was 1.0. A similar rise in the frequency of coherent unsteadiness with decreasing timestep size was also seen for the shaped hole for the same grid density.

In Fig. 5.7 there are no other frequency peaks when the time step was 4μs. The additional peaks arising at larger timesteps are possibly because the timestep was too large for some of the cells within the grid. However, the case with Δt equal to 4μs developed unrealistic small oscillations in the mass flow rate in and out of the plenum block. These oscillations, which were not seen at other timesteps, were possibly attributed to a numerical instability in the DTS calculation, as the outer time step (Δt) was close to that of the inner timestep ($\Delta t*$) at some locations in the domain.

Consequently a timestep of 6.25μs was judged to be the most appropriate to use with Grid C in the current investigation. At this timestep there was no oscillation in the plenum

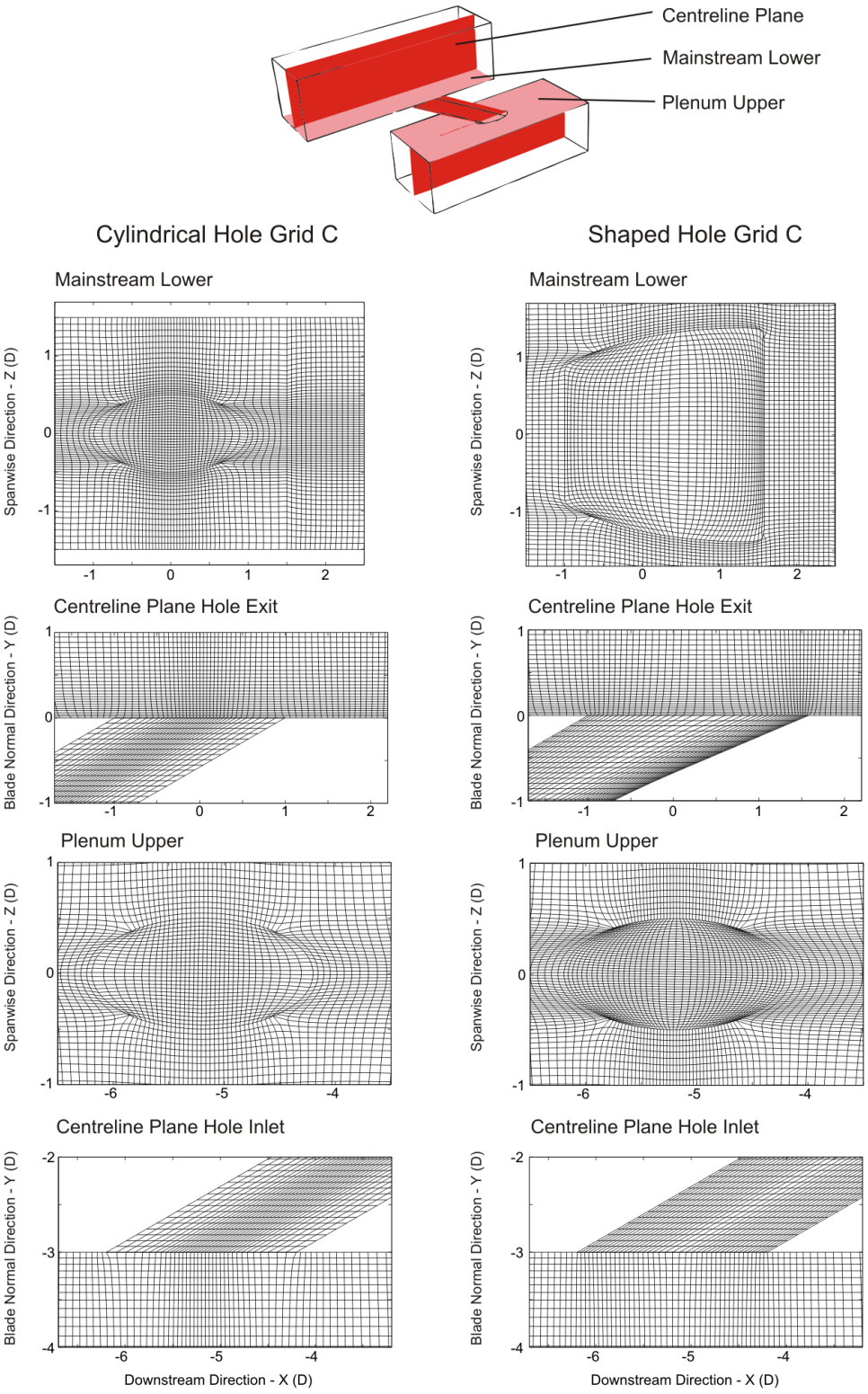

Figure 5.6: The node distribution in Grid C for the cylindrical and the shaped hole.

mass flow rate and there almost appeared to be convergence in the frequency of coherent unsteadiness.

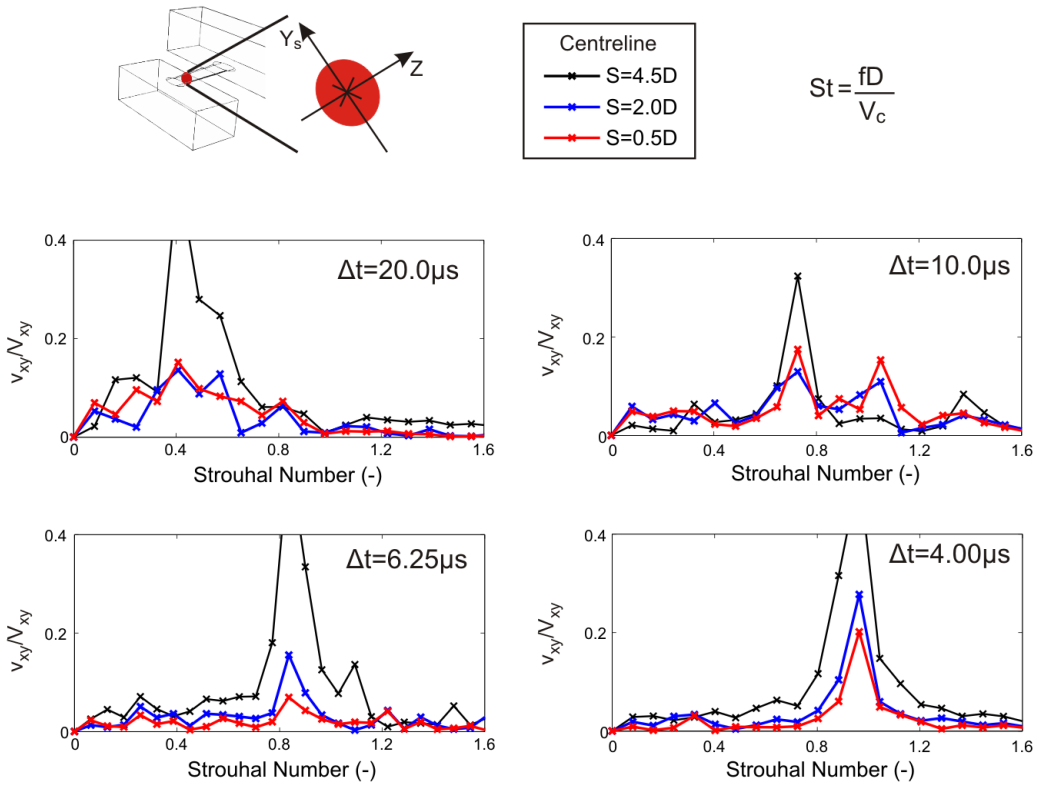

Figure 5.7: Frequency spectra of the velocity fluctuations inside the cooling hole with variation in outer time step for the cylindrical hole and Grid C.

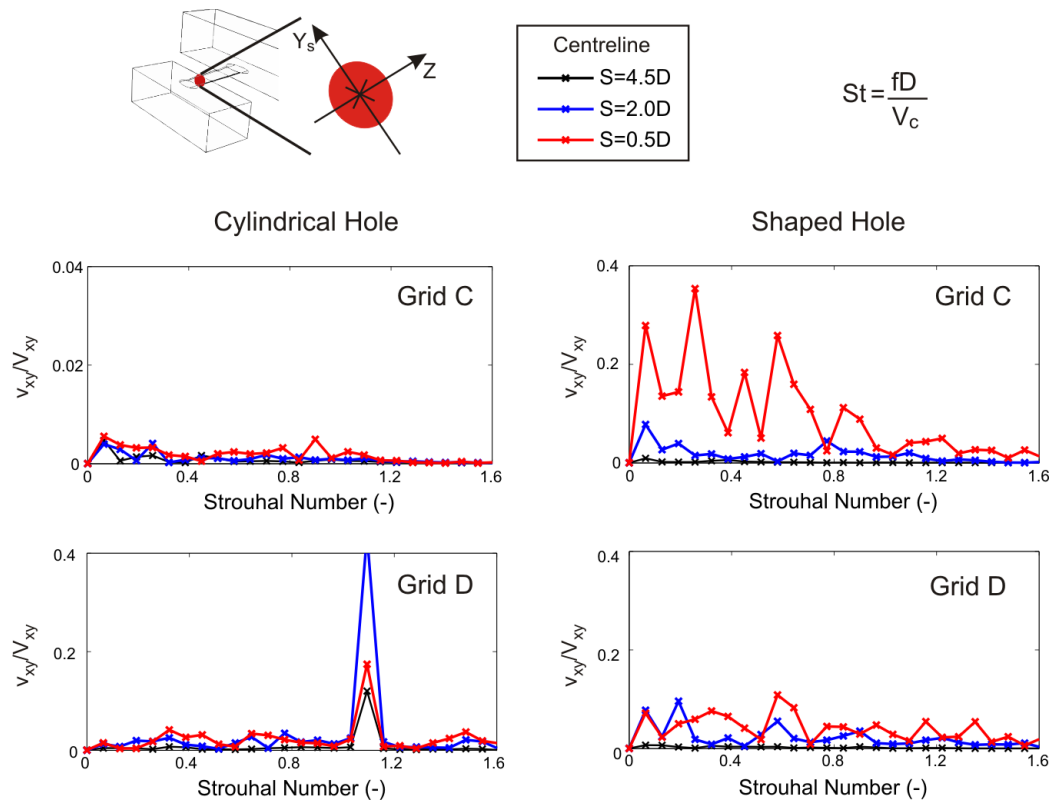

Figure 5.8: Frequency spectra of the velocity fluctuations inside the cooling hole with variation in grid density for perpendicular crossflow. Outer time step equal to 6.25μs.

5.3.3 Perpendicular Crossflow

With perpendicular crossflow the grid was largely identical to that for the co-flowing and counter flowing cases discussed previously, the exception being some minor changes in the plenum block. However, the direction of the crossflow meant that the grid at the lateral edges of the cooling hole inlet was more important than the grid at the leading and trailing edges. The sensitivity of the solution for perpendicular crossflow of CFR equal to 0.2 was checked for the finer Grids C and D with a timestep of 6.25μs.

The frequency spectra for the probes on the hole centreline are shown in Fig. 5.8 for both the cylindrical and shaped holes with both grid densities. The frequency spectra show that no coherent unsteadiness was resolved inside the cylindrical hole when using the coarser Grid C, but it was resolved within the finer Grid D. The peak of the coherent unsteadiness seen with Grid D had a Strouhal number of 1.1, and this was consistent with high velocity shedding seen in the instantaneous velocity profiles. The shaped hole did not show any coherent unsteadiness for the finer grid.

Figure 5.8 shows that coherent unsteadiness was present with Grid D for the cylindrical

hole but not for the shaped hole. It will be explained in Chapter 8 that coherent unsteadiness was not necessarily expected inside the cooling hole with perpendicular crossflow of CFR equal to 0.2. Thus, the lack of coherent unsteadiness inside the shaped hole when using Grid D, did not mean that the grid was not sufficiently fine. Grid D was therefore used when modeling both the cylindrical hole and the shaped hole with perpendicular crossflow.

5.4 Summary

In this chapter a computational model has been developed to allow the impact of the internal crossflow direction and magnitude on the in-hole coherent unsteadiness to be investigated further. The crossflow at the hole inlet can be varied to be co-flowing or counter flowing with respect to the mainstream flow in addition to the perpendicular direction studied experimentally in the Oxford Super Scale Cascade.

Version 38 of the TBLOCK solver, written by Denton, was used to solve a three block model including the plenum, cooling hole and mainstream. The requirement was for a qualitative understanding of the flowfield, and so a coarse grid LES model with no sub-grid scale modeling was solved. The occurrence of coherent unsteadiness inside the cooling hole tube at a blowing ratio equal to 0.9 with a crossflow to bulk jet velocity ratio of 0.2 was used to evaluate the sensitivity of the model to changes in the grid density and the time step.

A model of 600×10^3 nodes, of which 51×10^3 were inside the cooling hole tube, was found to be sufficient for co-flowing and counter flowing crossflow. With perpendicular crossflow a grid of 1000×10^3 nodes, of which 80×10^3 nodes were inside the cooling hole tube, was preferred. A timestep of 6.25μs appeared to be optimal for all models.

Chapter 6

Coherent Unsteadiness with Plenum Fed Cooling Holes

In this chapter the flowfields immediately downstream of the exit of cylindrical and shaped holes, when fed from the plenum chamber explained in Chapter 3, are shown. These cooling hole geometries have an 'ideal' hole inlet with an inlet inclination angle of 90°. The flowfield is observed in both the spanwise and secondary flow planes from measurements obtained using Particle Image Velocimetry (PIV) and high speed photography.

Time-mean velocity and vorticity profiles, obtained using PIV, and time-mean intensity profiles, obtained using high speed photography, are shown for both cooling hole geometries. To identify the regions likely to contain coherent unsteady structures, profiles of the rms velocity and the variance in pixel intensity are also presented. Movement of the whole jet, and structures seen within the jet core, are then investigated to establish if they are random or coherent. Thus an understanding of the coherent unsteadiness in the jet emerging from cooling holes with an 'ideal' hole inlet is developed.

6.1 Jet from the Cylindrical Hole

6.1.1 Time-mean Flowfield

The effect of blowing ratio (BR) on the time-mean velocity, obtained with PIV, is shown in Fig. 6.1 for the cylindrical hole. The time-mean velocity in Fig. 6.1 is normalised with respect to the cascade exit velocity. The upper image in Fig. 6.1 is for the case with no

cooling holes present. To achieve this the cooling holes were covered with tape to provide a continuously smooth surface. It can be seen that there is a velocity gradient normal to the wall, which is consistent with the existence of a boundary layer and a cross passage pressure gradient. The acceleration along the blade surface downstream of the cooling hole is to be expected given the surface C_p profile shown in Fig. 3.2. At the edge of the boundary layer the normalised velocity is approximately 0.19. This compares favourably with the value of 0.17 predicted from the C_p value at 50% axial chord.

Figure 6.1 shows that at BR equal to 0.8 the low velocity region near the blade surface is thicker than for the case with no jet. This shows that the jet is attached to the blade surface. At a BR equal to 1.5 the high velocity region in Fig. 6.1 shows that the jet has separated from the blade surface. The separation of the jet at BR equal to 1.5 causes the mainstream flow to decelerate upstream of the jet due to the increased jet blockage. The mainstream flow is then forced to accelerate around this blockage. This separation of the jet from the blade surface at higher BR is consistent with the previous studies discussed in the literature review.

Large magnitudes for the rms velocity (V_{rms}) identify regions of high unsteadiness, either due to random turbulence or coherent unsteadiness. Figure 6.1 shows the change in the V_{rms} contours with blowing ratio. For the case with no jet, the V_{rms} contours indicate turbulence levels of around 3% of the exit velocity in the mainstream passage flow. The presence of the cooling jet of BR equal to 0.8 leads to a rise in the V_{rms} to 4% in the region near the blade surface immediately downstream of the hole trailing edge. The V_{rms} contours for a jet of BR equal to 1.5 show that there are regions of high unsteadiness in the wake underneath the separated jet and the shear layer between the jet and the mainstream.

The mean jet profile in the spanwise plane at midspan can also be inferred from the time-mean intensity plots in Fig. 6.2 obtained using the high speed photography. Here it should be remembered that the bands in the time-mean intensity normal to the blade surface were caused by variations in the light sheet intensity. Although the recordings were taken over a shorter time period than the time-mean velocity profiles shown in Fig. 6.1, they are consistent with the trends discussed previously. Plotting the time-mean pixel intensity also shows, that although the jet is separated from the blade surface, some of the fluid in the jet enters the wake underneath it at BR equal to 1.4 and 2.0.

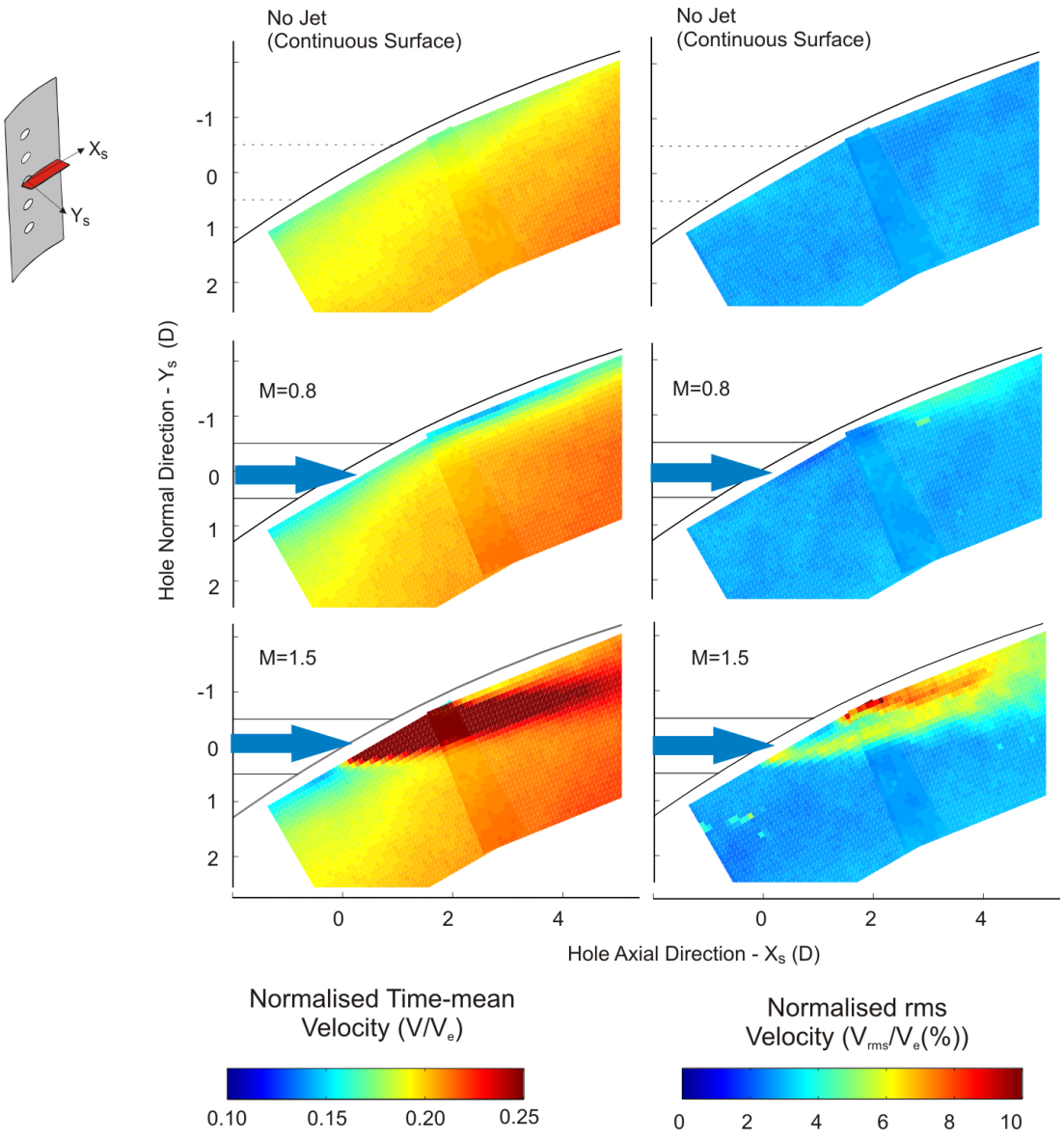

Figure 6.1: (Left) Time-mean velocity and (right) rms velocity with the cylindrical hole in the spanwise plane at midspan. Obtained using PIV.

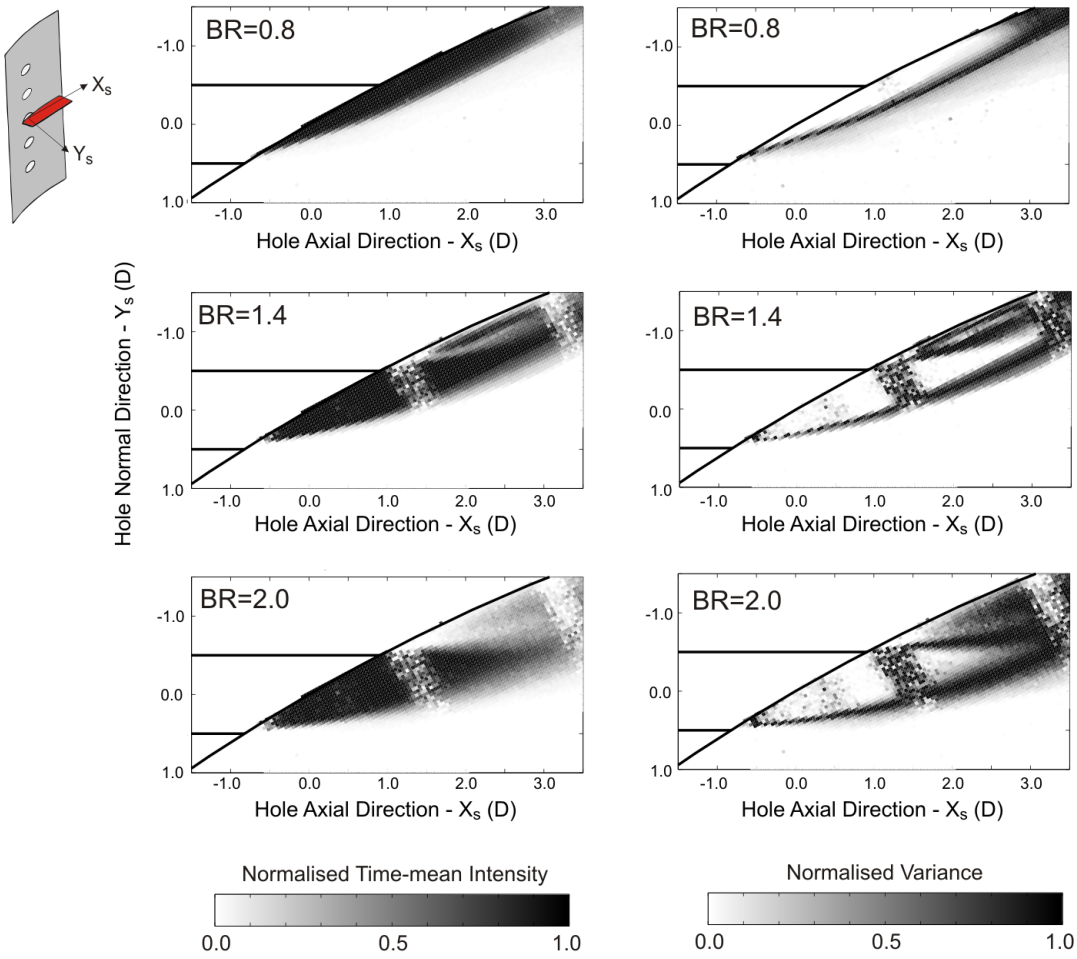

Figure 6.2: (Left) Time-mean pixel intensity and (right) variance of the jet from the cylindrical hole in the spanwise plane at blade midspan. Obtained using high speed photography.

The variance in the pixel intensity is shown in Fig. 6.2. Like V_{rms}, regions of high variance denote high levels of unsteadiness in the jet. In the near hole region a steady jet core can be seen across all the blowing ratios. Regions of high variance are found around this steady core in the shear layer and the wake underneath the separated jet. The banding in the light sheet, discussed previously, is the reason for the bands of high variance perpendicular to the jet direction.

The time-mean pixel intensity in the secondary flow plane 2D downstream is shown in Fig. 6.3. In addition to the jet from the centre hole its lower spanwise neighbour is also shown. At BR equal to 0.5 the jets are attached to the blade surface. Increasing the BR to 1.0 shows the jets to be still attached, with negligible growth in their spanwise width. For BR equal to 1.4 the jet, as is shown in the spanwise plane in Fig. 6.2, separates from the blade surface. Figure 6.3 shows that the jet core at BR equal to 1.4, as denoted by

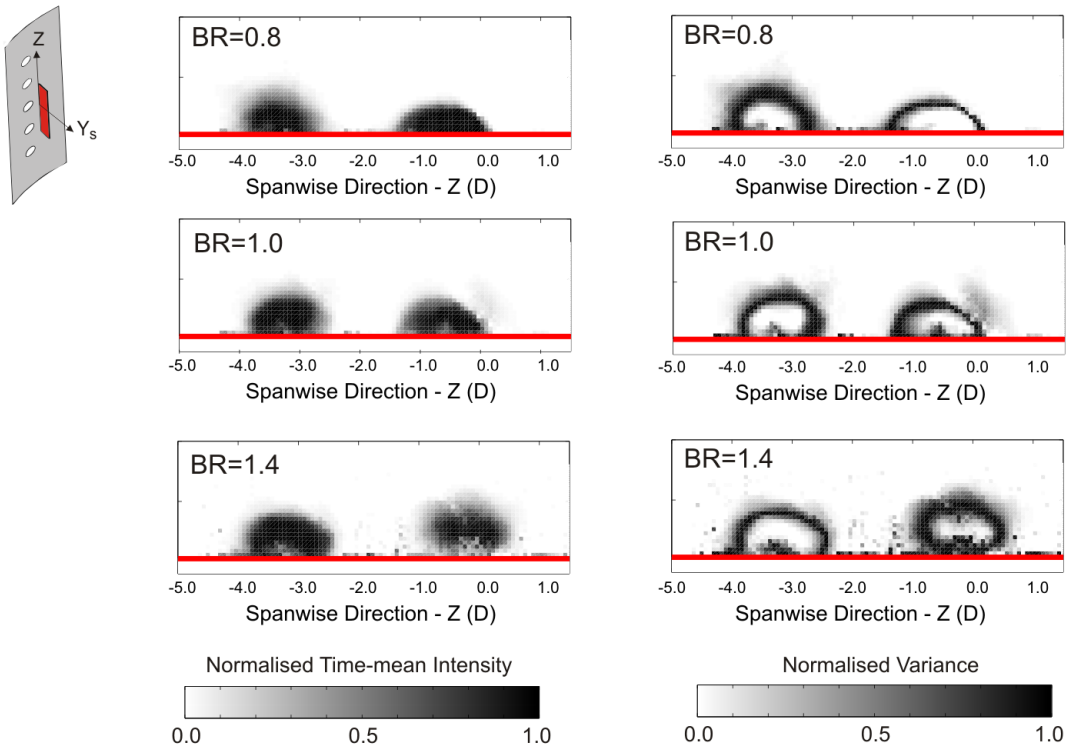

Figure 6.3: (Left) time-mean pixel intensity and (right) variance of the jet from the cylindrical hole in the secondary flow plane 2D downstream. Obtained using high speed photography.

the region of high intensity, begins to form the shape of a CRVP (Counter Rotating Vortex Pair).

The variance profiles in Fig. 6.3 show there are high levels of unsteadiness in the shear layer between the jet and the mainstream. This is consistent with the regions identified in the spanwise plane.

The time-mean normalised vorticity contours in Fig. 6.4 were obtained using PIV, and show the presence of the CRVP in the jet cross section for BR equal to 1.0 and 1.4. At BR less than 1.0 no significant vorticity was seen within the jet. The peak time-mean vorticity in the plane 2D downstream, normalised with respect to the hole diameter and the mainstream velocity at 50% axial chord, is approximately 1.0 for a BR of 1.0 and 2.5 for a BR of 1.4. These values are similar to the value of 2.0 found computationally by Walters and Leylek [98] in a plane 0.6D downstream for a BR of 1.0.

It can be seen in the secondary flow plane 4D downstream in Fig. 6.4, that due to the jet mixing with the mainstream, the vortices of the CRVP increase in size with distance from

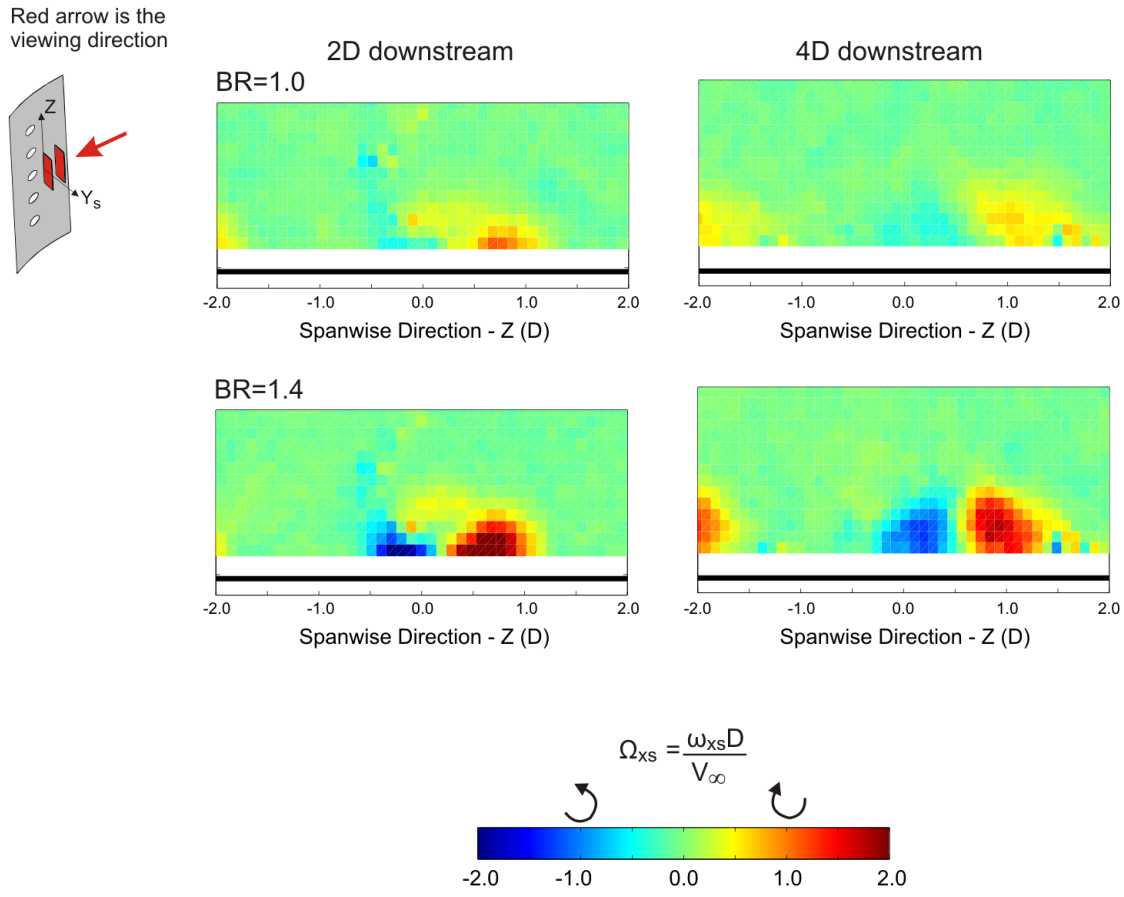

Figure 6.4: Normalised time-mean vorticity with the cylindrical hole in the secondary flow planes 2D and 4D downstream. Obtained using PIV.

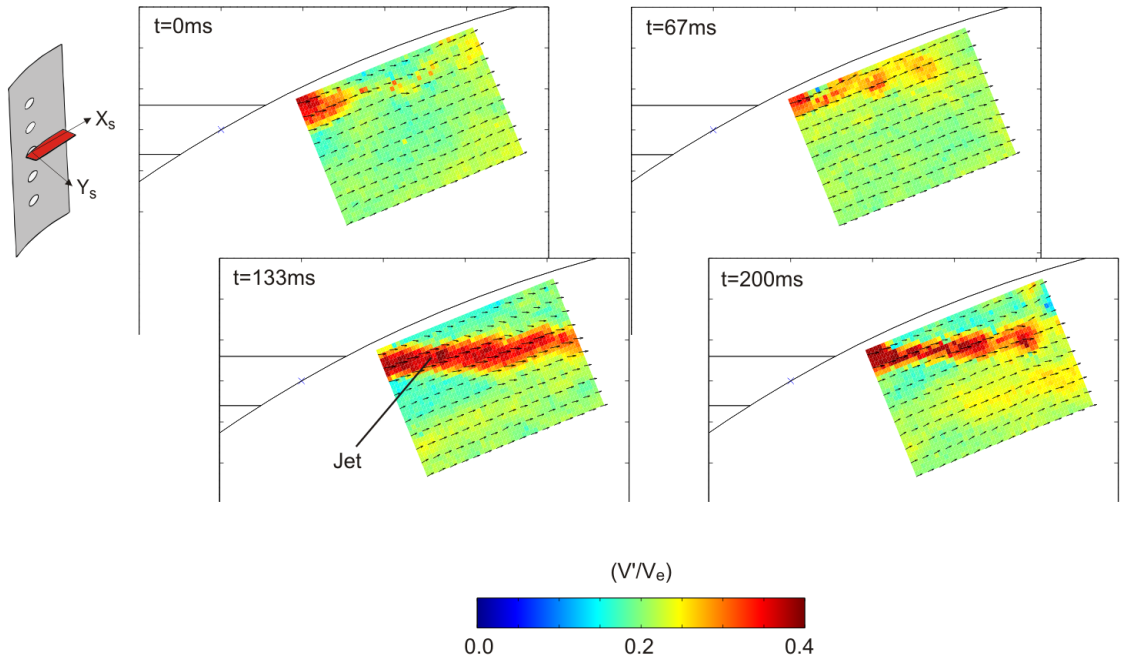

Figure 6.5: Typical variation in the instantaneous velocity in the spanwise plane at midspan, for a jet of BR equal to 1.5 from the cylindrical hole. Obtained using PIV.

the hole exit. Thus the magnitude of the maximum vorticity reduces to be approximately 0.5 at a BR of 1.0 and 1.5 at a BR of 1.4.

6.1.2 Unsteady Flow Structures

Low Frequency Sampling

The instantaneous velocity profiles, averaged to create the time-mean velocity profiles shown in Fig. 6.1, show the jet to move in the direction normal to the blade surface. In Fig. 6.5 a typical sequence of four instantaneous velocity profiles, with a timestep of 67ms between them, are shown for a blowing ratio of 1.5. The jet of BR equal to 1.5 can be identified in all of the images in Fig. 6.5 by the region of velocity larger than the mainstream velocity.

The field of view in Fig. 6.5 is smaller than that shown in Fig. 6.1 in which two fields of view are combined. It should also be noted that the 67ms long timestep between the velocity profiles shown in Fig. 6.5 is larger than the 30ms required for the mainstream flow to cross the field of view.

In the first velocity profile in Fig. 6.5 the jet ends abruptly within 1D of the trailing edge of the hole exit. It is not expected that the jet would fully mix into the mainstream

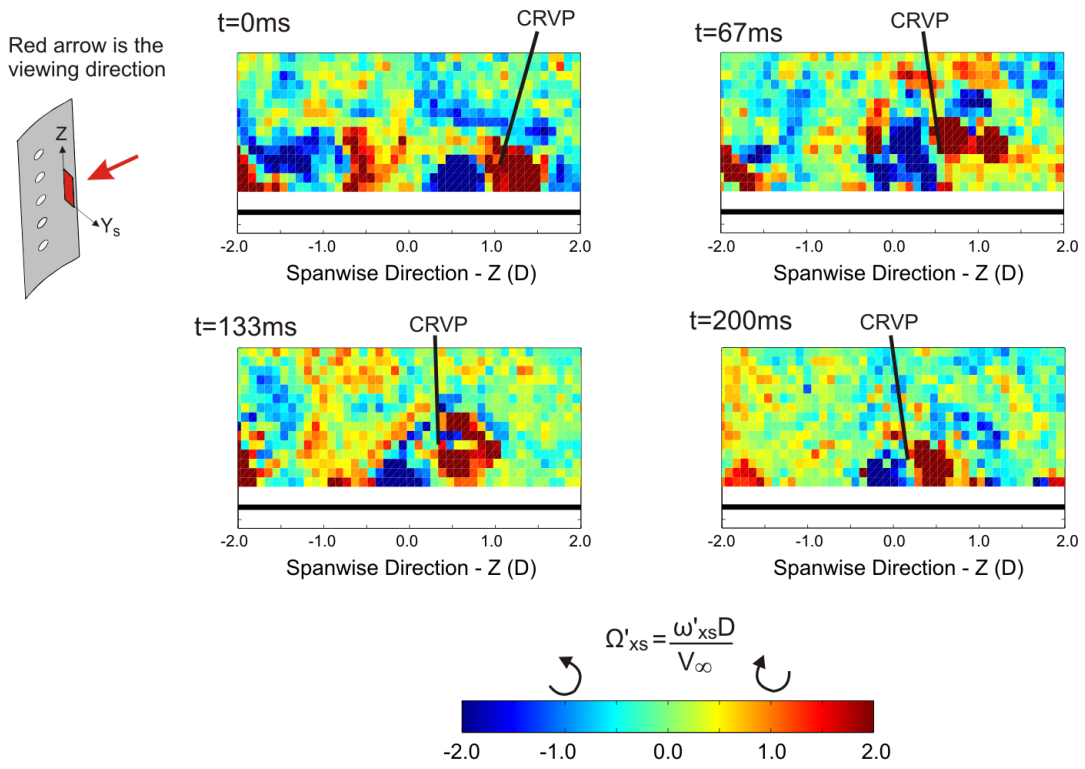

Figure 6.6: Normalised instantaneous vorticity profiles showing the movement of the CRVP with time in the secondary flow plane 4D downstream, for a jet of BR equal to 1.4 from the cylindrical hole. Obtained using PIV.

within such a short distance, which suggests that instead the jet may have moved out of the observed spanwise plane. The second velocity profile shows the jet to move back into the midspan measurement plane and to be attached to the blade surface. In the third and fourth velocity profiles the jet is seen to be separated from the blade surface which, as shown in the time-mean velocity profile, is the more common jet position at this blowing ratio.

Figure 6.6 shows four instantaneous vorticity profiles obtained with PIV of a jet of BR equal to 1.4 in the secondary flow plane 4D downstream. In each image, neighbouring regions of large positive and negative vorticity can be seen near the blade surface at a spanwise distance of approximately 0.5D. These two regions show the location of the two vortices of the CRVP present in the jet core.

The four vorticity profiles in Fig. 6.6 show that the jet moves in the spanwise direction, as was suggested when discussing the instantaneous velocity profile in the spanwise plane. To establish the range of spanwise movement the jet position was traced through a sequence of 150 vorticity profiles. To do this the centre of the jet was assumed to be the point between

the two opposing vortices.

The variation in the jet spanwise position 4D downstream for a BR of 1.4 is approximately ±0.3D. However, a fourier transform of the jet spanwise position with time shows there to be no periodicity associated with this spanwise movement in the frequency range up to 7.5Hz. It is not possible to do the same analysis at BR equal to 1.0, as the vorticity magnitude of the CRVP is in some instances too small to identify the jet position.

High Frequency Sampling

Typical instantaneous images, obtained with high speed photography, of the jet from the cylindrical hole in the spanwise plane at midspan are shown in Fig. 6.7 at different blowing ratios. At a BR of 0.5 Fig. 6.7 shows the jet to be attached to the blade surface downstream of the hole exit. In Image A the jet ends rather abruptly around 2D downstream, and as with the instantaneous velocity profile shown in Fig. 6.5, this is suspected to be due to spanwise movement of the jet. Image B at a BR of 0.5 shows the jet to remain in the measurement plane for a larger downstream distance. In both images the jet appears to be of a low turbulence intensity with some oscillations in the profile of the apparently laminar shear layer.

As shown previously in the time-mean intensity profile, Images C and D show that when the BR is equal to 0.8 the jet is attached to the blade surface. At this BR the jet has a larger thickness normal to the blade surface than for a BR of 0.5. There are also oscillations in the profile of the shear layer and Image D shows those with the largest amplitude. Increasing the BR to 1.0, sees the jet, although generally being attached as shown in Image E, occasionally separating from the blade surface as is the case in Image F. The largest BR shown in Fig. 6.7 is 1.4, and Images G and H show, as was apparent in the time-mean intensity profile, the jet to be separated from the blade surface. The band of coolant in the wake below the main jet in both images is believed to be the underside of the CRVP, as shown in the insert in Fig. 6.7.

Typical images of the jet in the secondary flow plane are shown in Fig. 6.8. As in the time-mean intensity profile in Fig. 6.3 both the centre jet and its lower spanwise neighbour are shown. At a BR of 0.5 the jet is always attached to the blade surface, but as shown in Image B offshoots into the mainstream are often seen from the upper surface of the jet.

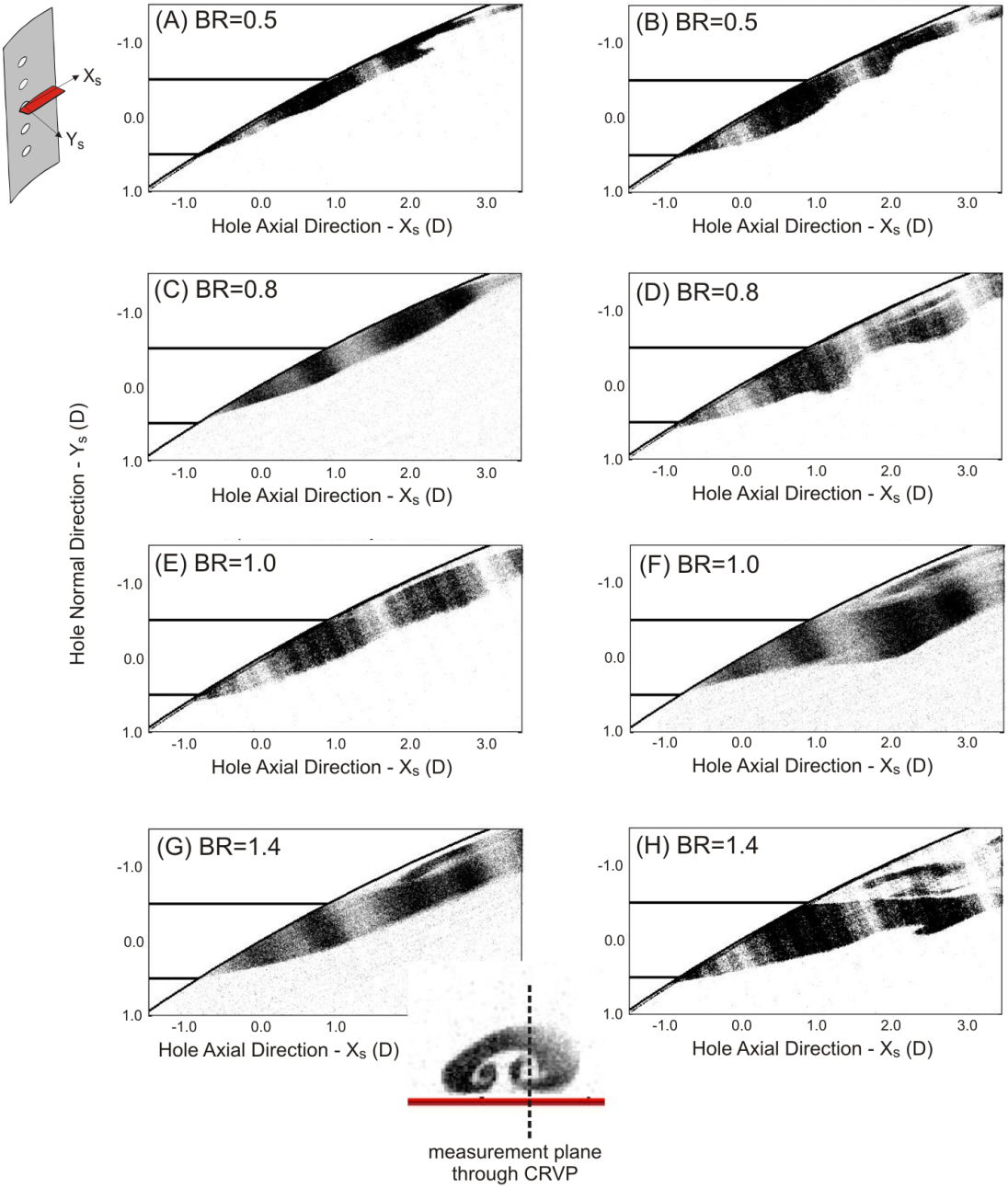

Figure 6.7: Instantaneous images of the jet from the cylindrical hole in the spanwise plane at midspan. Obtained with high speed photography.

With increasing downstream distance the offshoots develop into stretching and movement of the entire jet cross section. It is suspected that this arises due to the low momentum jet being influenced by turbulence in the mainstream.

At a blowing ratio of 0.8 the CRVP is seen intermittently in the attached jet, this is the case in Image D of Fig. 6.8 but not in Image C. On increasing the BR to 1.0 the CRVP is a consistent presence in the jet core as shown in Images E and F. Images D and F show that at both BR equal to 0.8 and 1.0 there are offshoots from the upper surface of the jet.

Images G and H of Fig. 6.8 show at a BR of 1.4 the jet to separate from the blade surface with its cross-section taking the shape of a CRVP. In the shear layer the offshoots observed at lower blowing ratios are seen, and as shown in Images G and H appear to form a pair of vortices with the same sense of rotation as the CRVP. These vortices are consistent with the secondary unsteady vortices seen previously by Haven and Kurosaka [36] and New et al [72] that were introduced in the literature review. The secondary vortices were seen intermittently within the jet of BR equal to 1.4, but on observing a 900ms long sequence of images they did not appear to be coherent.

Across the blowing ratio range of 0.5 to 1.4, shown in Fig. 6.7 and 6.8, there was no evidence to suggest that there were coherent unsteady structures within the jet. However, on increasing the BR to 2.0 regular vortices are seen to be present in the shear layer between the jet and the mainstream, as shown in the two image sequences in Fig. 6.9. These vortices are suspected to be the shear layer vortices, introduced in the literature review, which form due to a Kelvin-Helmholtz instability in the shear layer.

A Kelvin-Helmholtz instability is initiated by velocity perturbations normal to the shear layer, which initially cause oscillations to be seen in shear layer profile. These oscillations are seen to occur at lower blowing ratios as shown in Fig. 6.7 and in the shear layer upstream of the shear layer vortices in Fig. 6.9. These oscillations grow in amplitude and cause the shear layer vorticity to accumulate at distinct locations and so form discrete vortices. The shear layer vortices in Fig. 6.9 are seen to have a clockwise rotation, which is is due to the velocity of the jet being larger than that of the mainstream. At a lower BR, although oscillations in the shear layer profile are seen, it is believed that the velocity difference across the shear layer is not large enough to initiate a Kelvin-Helmholtz instability.

To determine if the shear layer vortices shown in Fig. 6.9 have a characteristic passing

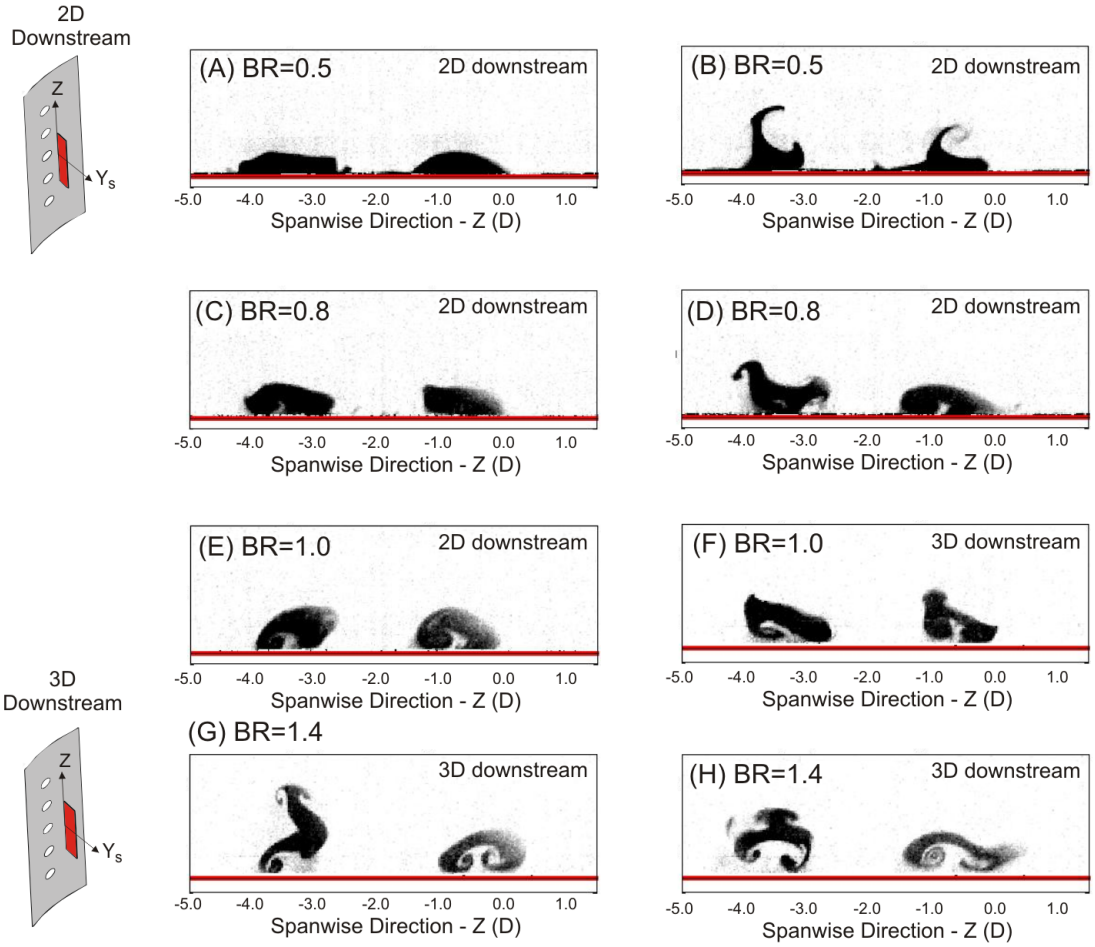

Figure 6.8: Instantaneous images of the jet from the cylindrical hole in the secondary flow plane, either 2D or 3D downstream. Obtained with high speed photography.

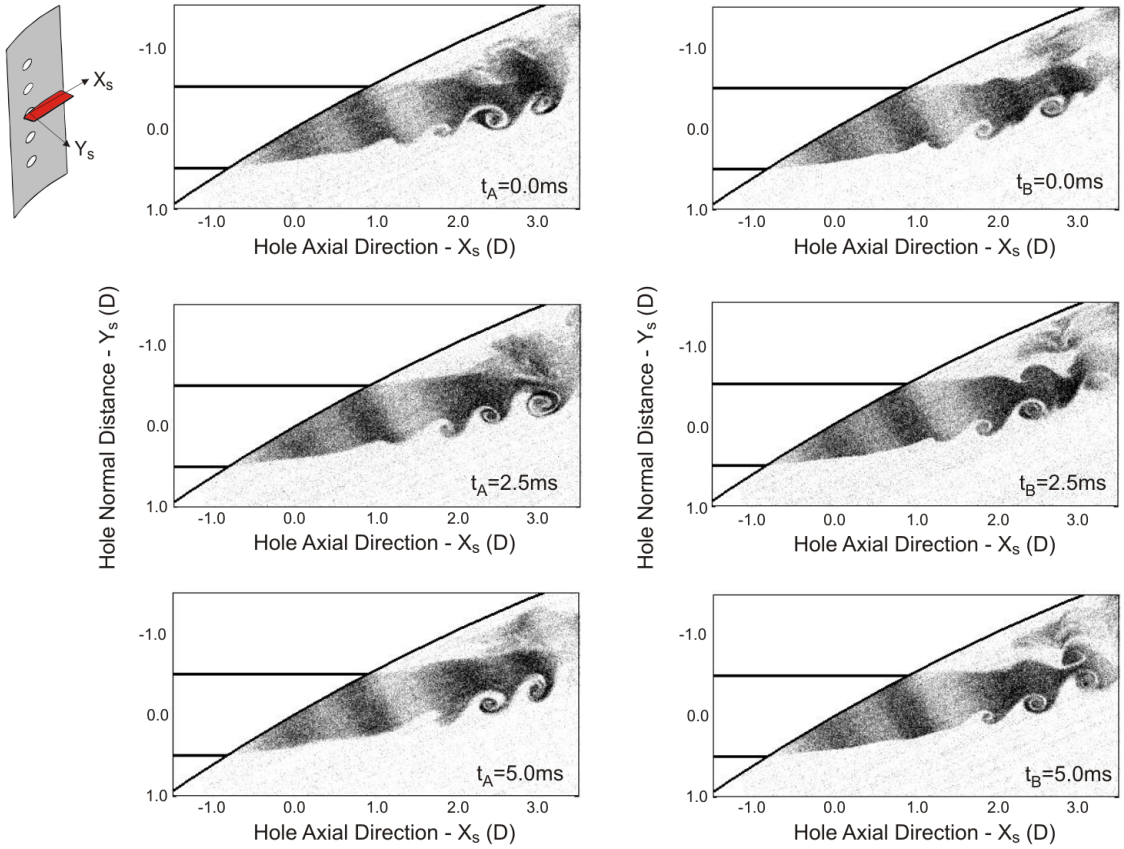

Figure 6.9: Two image sequences in the spanwise plane at midspan for a jet of BR equal to 2.0 from the cylindrical hole. Obtained with high speed photography.

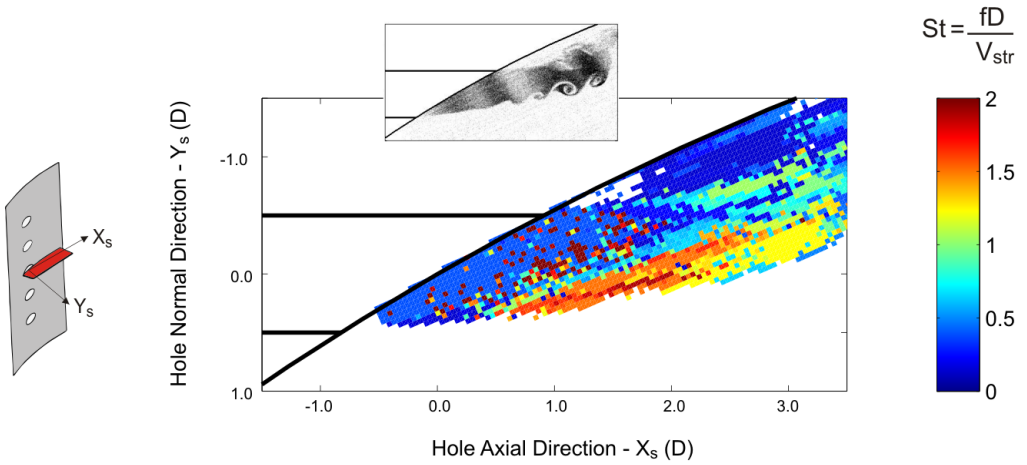

Figure 6.10: The local peak frequency of unsteadiness in the spanwise plane at midspan for a jet of BR equal to 2.0 from the cylindrical hole. Obtained with high speed photography.

frequency, a Fourier transform was done on the temporal variation in pixel intensity through a 350ms long image sequence according to the method detailed in Chapter 4. The peak frequencies from the local frequency spectra are shown in Fig. 6.10. The frequencies are non-dimensionalised into a Strouhal number according to Eq. 4.10, where the velocity of the shear layer vortices (V_{str}) is estimated based on a sequence of images to be 3.0ms^{-1}. The regions outside of the jet with low time-mean pixel intensity have been blanked off.

Figure 6.10 shows a region of constant Strouhal number in the shear layer of the jet where the shear layer vortices are observed. This Strouhal number is consistent with that estimated from the images in Fig. 6.9. In the shear layer of the jet near the hole exit the vortices have a Strouhal number of 1.5. The Strouhal number in the shear layer decreases to 1.3 further downstream. This decrease can be attributed to the reduction in the local velocity due to mixing with the mainstream, whilst the Strouhal number is calculated based on a constant velocity. The Strouhal number shown in Fig. 6.10 is consistent with the values of 1 to 2 shown in the literature review for shear layer vortices seen in jets of a similar hole Reynolds number.

To confirm that a Kelvin-Helmholtz instability is the correct mechanism to describe the formation of a shear layer vortex, the theory presented by Faber [23] was used to determine a typical Strouhal number. Here the mean velocity profile in the shear layer is assumed to be similar to that expressed in Eq. 6.1, where z is the distance normal to the shear layer and σ is the mixing layer thickness. For such a case Faber [23] states that the perturbation

wavelength (λ) most likely to cause a Kelvin-Helmholtz instability is given by Eq. 6.2. The mixing layer 2D downstream of the hole exit at BR equal to 1.5, (shown in Fig. 6.1) has a thickness of approximately 0.5D. Applying Eq. 6.2 suggests that a Kelvin-Helmholtz instability in this mixing layer would have a wavelength of 1D. Equation 2.9 shows that this corresponds to Strouhal number of 1.0, which is consistent with the value of 1.5 shown in Fig. 6.10 for the current experiment.

$$v = Vtanh\left(\frac{z}{\sigma/2\pi}\right) \tag{6.1}$$

$$\lambda \approx 4\pi\frac{\sigma}{2\pi} = 2\sigma \tag{6.2}$$

6.2 Jet from the Shaped Hole

6.2.1 Time-mean Flowfield

The time-mean pixel intensity on the spanwise plane located 0.5D below the hole axis is shown for the jet from the shaped hole in Fig. 6.11. The plane 0.5D below midspan is shown due to the non-symmetric profile of the jet within the exit of the shaped hole, which is apparent when observing the secondary flow plane.

For the three blowing ratios shown in Fig. 6.11 the jet remains attached to the blade surface downstream of the hole trailing edge. With increasing BR there is an increase in the film thickness normal to the blade surface. However, unlike the cylindrical hole, there is no separation of the jet at higher blowing ratios. This difference is explained in the literature review as being due to the lower momentum of the jet at the exit of the diffusing shaped hole for a given BR.

The variance profiles in Fig. 6.11 show high levels of unsteadiness across the majority of the jet cross section. Apart from the near hole region of the jet of BR equal to 1.0, there is not the distinction between the steady jet core and the unsteady shear layer seen in the jet from a cylindrical hole shown in Fig. 6.2.

The secondary flow plane 1D downstream cuts across the expanding exit of the shaped hole. The time-mean pixel intensity in this plane is shown in Fig. 6.12 for the centre hole and its lower spanwise neighbour. The boundaries of the shaped holes are denoted by the

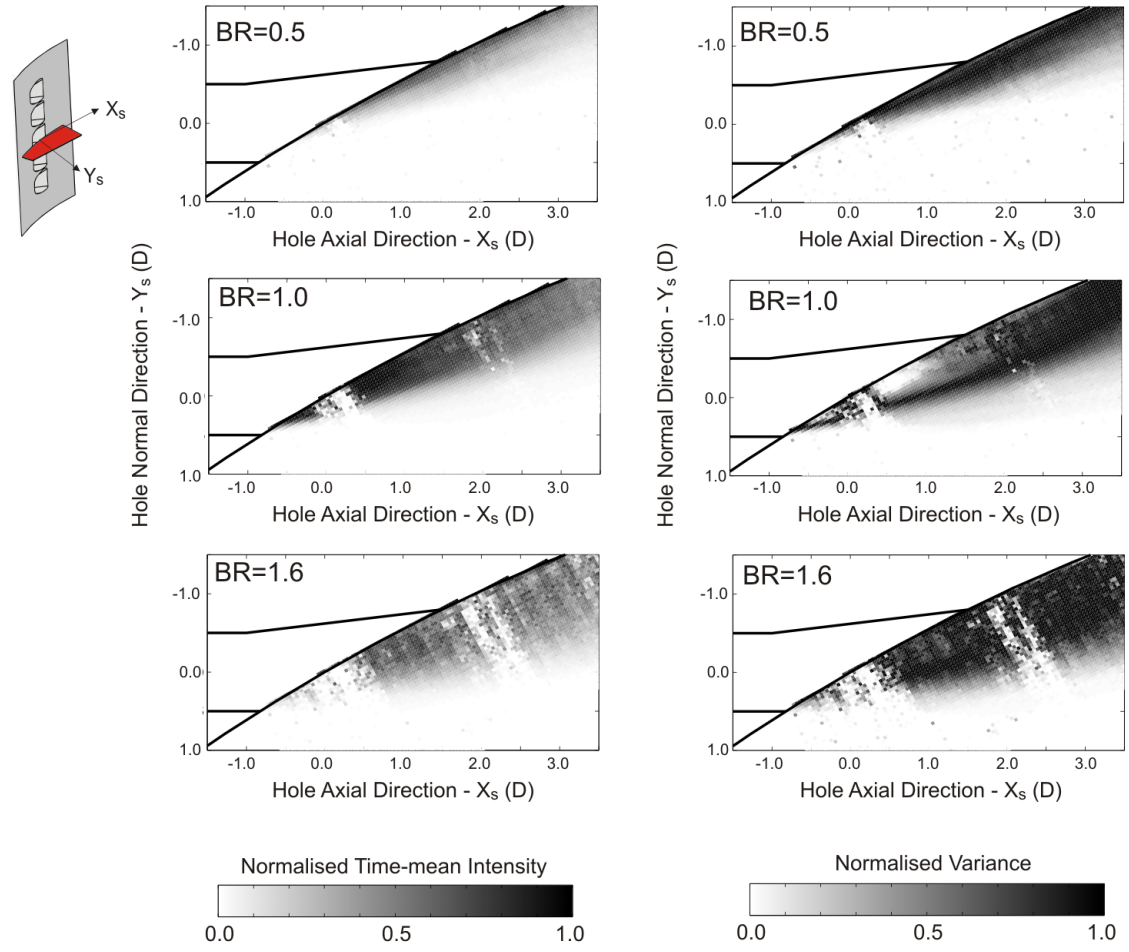

Figure 6.11: (Left) Time-mean pixel intensity and (right) variance of the jet from the shaped hole in the spanwise plane 0.5D below midspan. Recorded at 1kHz. Obtained with high speed photography.

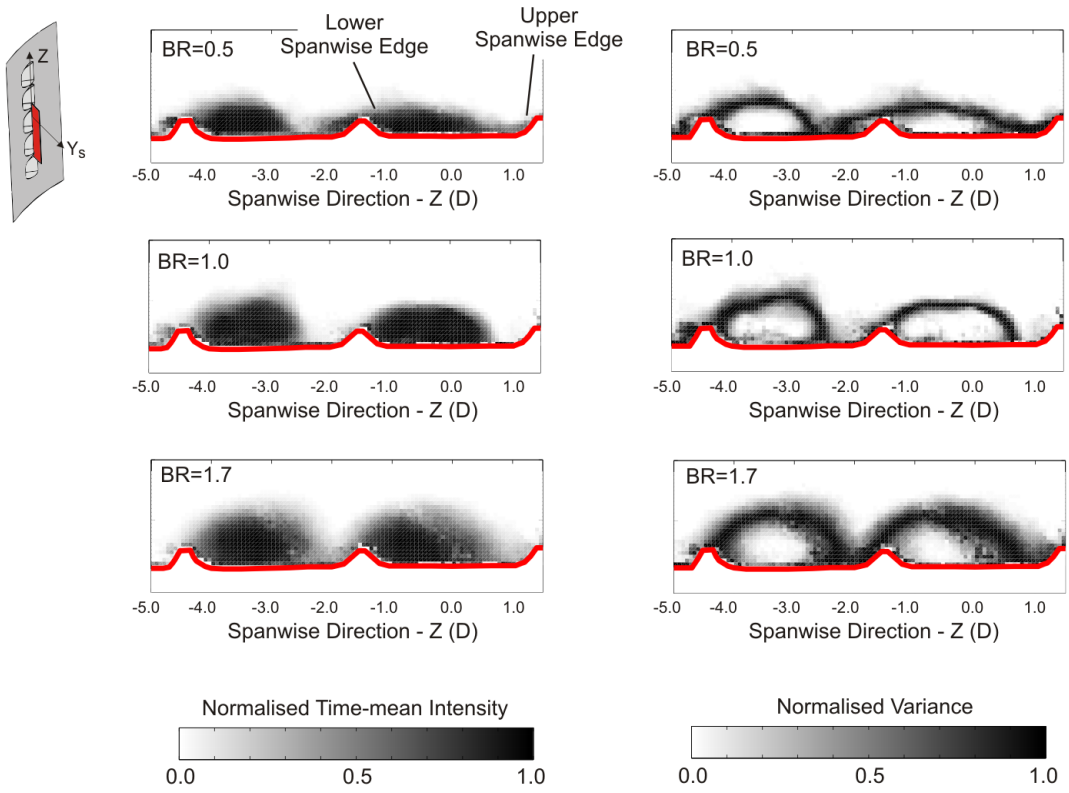

Figure 6.12: (Left) Time mean pixel intensity and (right) variance of the jet from the shaped hole in the secondary flow plane 1D downstream. Obtained with high speed photography.

solid red line. It is seen that the jet is biased towards the lower spanwise (left in Fig. 6.12 edge of the expanding exit at all BR. This bias is the reason for showing the spanwise plane 0.5D below midspan in Fig. 6.11. The bias being to the lower spanwise edge rather than the upper spanwise edge is believed to be a factor of the flow conditions at the cooling hole inlet and exit.

The low time-mean pixel intensity at the upper spanwise edge in Fig. 6.12, shows that the jet is not oscillating between the two edges of the expanding exit. This suggests that the increase in the lateral spread of coolant downstream of a shaped hole when compared to a cylindrical hole is not due to periodic oscillations of the jet across the expanding exit. Interestingly, in Fig. 6.12, there also appears to be an occasional spill over of coolant from the centre hole into the exit of its lower spanwise neighbour.

The variance profile in Fig. 6.12 shows that unsteadiness in the jet is concentrated in the shear layer between the jet and the mainstream. This appears inconsistent with the spanwise plane shown in Fig. 6.11. However the steady region of the jet in Fig. 6.12 is predominantly below the blade surface, and so cannot be seen in the spanwise plane.

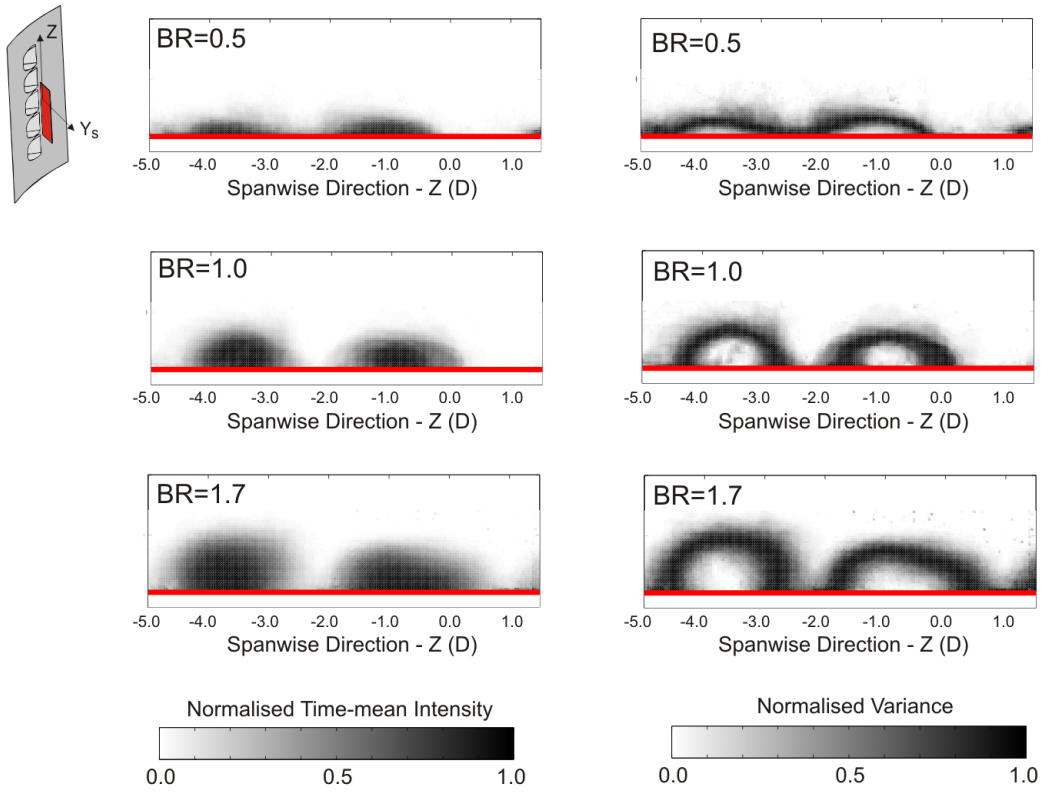

Figure 6.13: (Left) Time mean pixel intensity and (right) variance of the jet from the shaped hole in the secondary flow plane 2D downstream. Obtained with high speed photography.

The time-mean pixel intensity in the secondary flow plane 2D downstream is shown in Fig. 6.13. Here it can be seen that the jet from the shaped hole has a larger lateral spread than the jet from the cylindrical hole shown in Fig. 6.3. Taking the jet width to be the distance between the outer limits of the shear layer, the lateral spread of the jet is approximately 2D for all BR, in contrast to a width of 1D with the cylindrical hole.

The variance profile in Fig. 6.13 shows that, as is the case 1D downstream, the unsteadiness is concentrated in the jet shear layer. It can also be seen that the jet deflects, as in the diffusing exit, in the negative spanwise direction with its centre lying at approximately -0.7D. This deflection explains why the steady region at the jet centre is not apparent in the spanwise plane 0.5D below midspan shown in Fig. 6.11.

The time-mean normalised vorticity is shown in the secondary flow plane 2D downstream in Fig. 6.14. The blanked out areas hide regions that were biased by reflections from the edges of the diffusing hole exit.

Figure. 6.14 shows two neighbouring regions of opposing vorticity in the jet of BR equal to 1.0. These are indicative of the presence of a CRVP and have a similar magnitude to

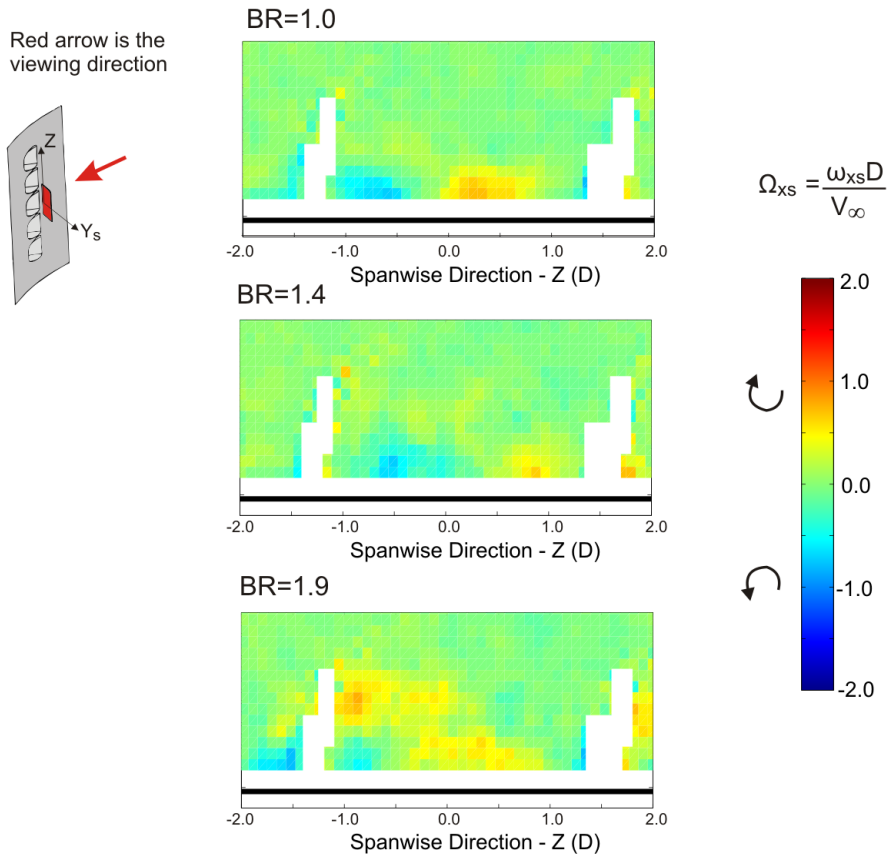

Figure 6.14: Normalised time-mean vorticity in the secondary flow plane 2D downstream with a jet from the shaped hole. Obtained with PIV.

the CRVP in the cylindrical hole for the same BR. On increasing the BR to 1.4 the two opposing regions of vorticity are seen to remain, but do not increase in magnitude. At a BR of 1.9, although there are significant regions of positive vorticity, the vorticity profile does not show the presence of a CRVP. This suggests that the CRVP is only present for a shaped hole at a BR close to 1.0, and unlike the cylindrical hole, is not present at higher BR.

6.2.2 Unsteady Flow Structures

The images in the spanwise plane shown in Fig. 6.15 show a jet from the shaped hole of BR equal to 0.5. The two columns are of image sequences recorded 2ms apart and these show the passage of wave-like structures along the blade surface. These wave-like structures indicate the passage of hairpin vortices. Hairpin vortices were introduced in the literature review as having been seen previously by Matsuda et al [65] and Tyagi and Acharya [97].

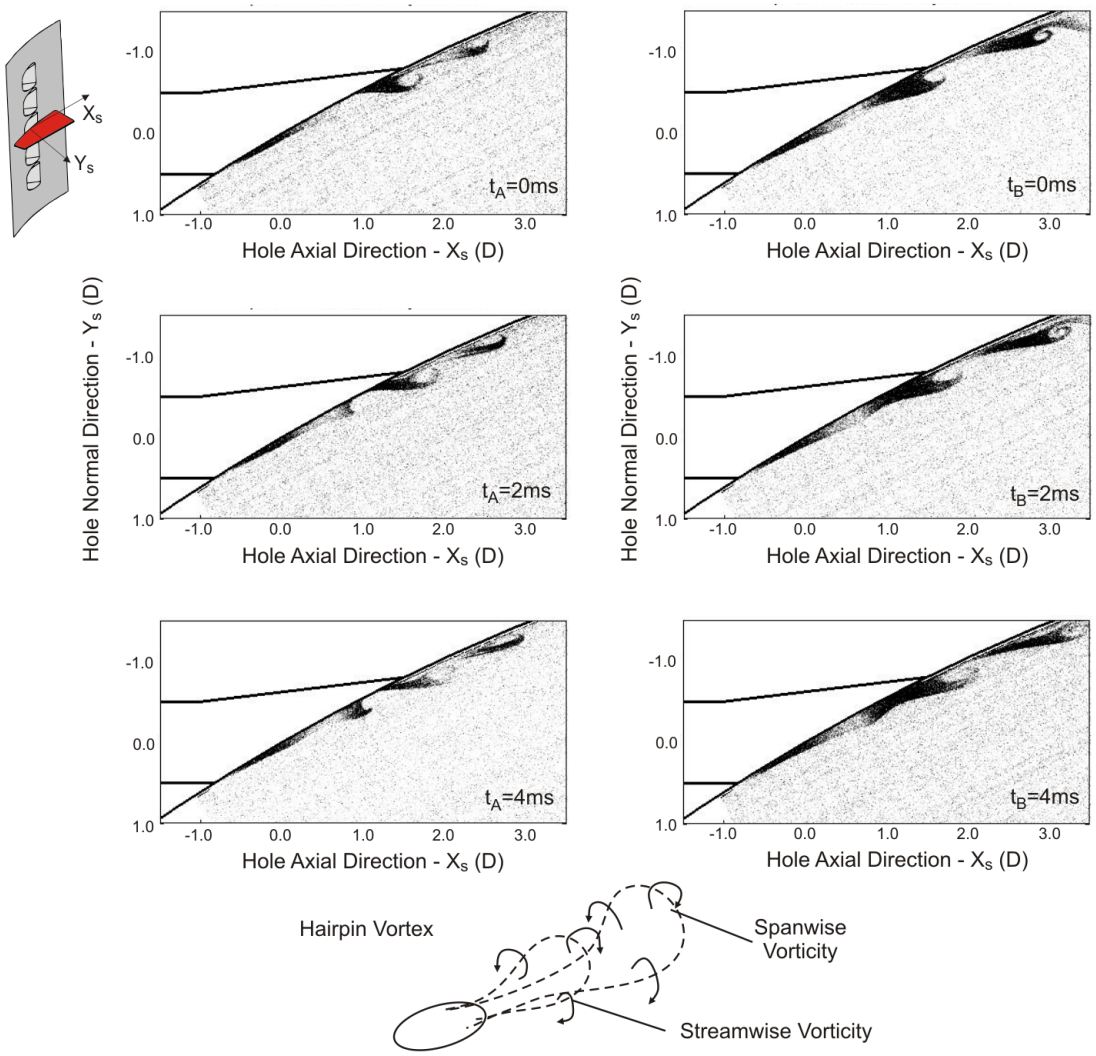

Figure 6.15: Hairpin vortices in the spanwise plane at midspan within a jet of BR equal to 0.5 from the shaped hole. Obtained with high speed photography.

A schematic of a hairpin vortex is shown at the bottom of Fig. 6.15, and the reader should imagine that the spanwise plane is passing through the vortex line when it is perpendicular to the jet direction.

The hairpin vortices shown in Fig. 6.15 have an anti-clockwise rotation when looking into the page. This direction of rotation is the opposite of that for the shear layer vortices seen in the jet from the cylindrical hole of BR equal to 2.0 (shown in Fig. 6.9). This difference is due to the reversal in the shear layer velocity gradient, as the jet velocity is lower than the mainstream velocity when the BR is equal to 0.5.

The two sequences of images in Fig. 6.16 show the passage of a hairpin vortex through the secondary flow plane 2D downstream of the hole exit centre. The hairpin vortex enters

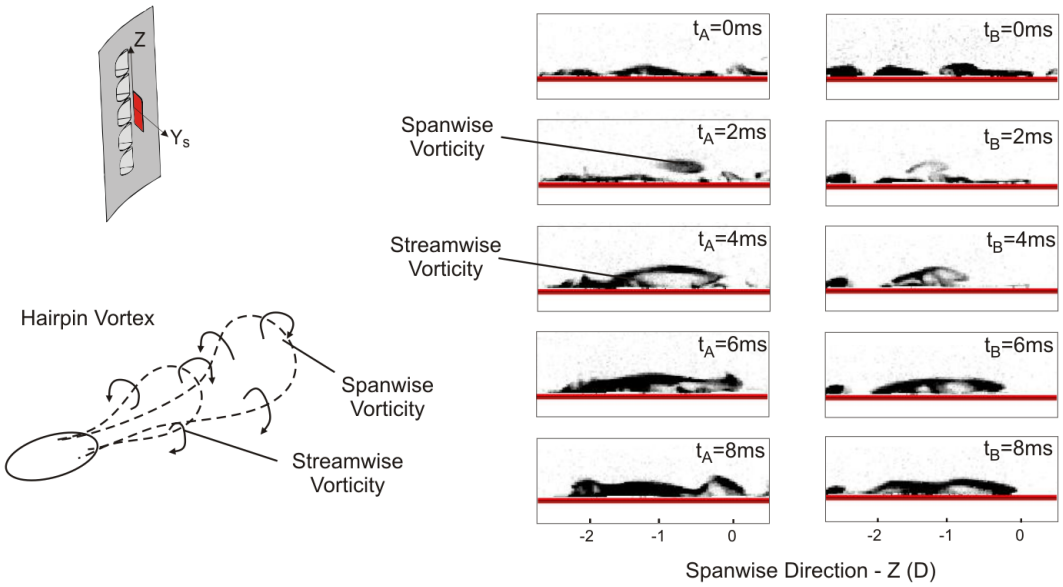

Figure 6.16: Hairpin vortices in the secondary flow plane 2D downstream for a jet of BR equal to 0.5 from the shaped hole. Obtained with high speed photography.

the measurement plane in the 2ms image, and is identified by the detached region of seeding particles above the attached jet. This is the leading face of the part of the hairpin vortex aligned in the spanwise direction. The images at 4ms and 6ms show that the vortex line of the hairpin vortex has turned to form the two streamwise vortices at opposite ends of the previously detached region. At 8ms the image shows that the streamwise vortices have passed through the measurement plane as the jet is attached to the blade surface.

The hairpin vortices shown in Fig. 6.15 and 6.16 are only seen intermittently within the jet of BR equal to 0.5. Consequently it is not possible to identify a Strouhal number for the passage of the hairpin vortices based on the change in the pixel intensity with time. Instead their Strouhal number is estimated to be in the range of 0.5 to 0.8 based on the distance between successive hairpin structures (λ) within the images.

The jet from the cylindrical hole does not show any evidence of hairpin vortices at a BR of 0.5. This difference is likely to be due to the expanding exit of the shaped hole reducing the jet velocity relative to that from the cylindrical hole of the same BR. Thereby there is a larger velocity gradient across the shear layer with the shaped hole.

When hairpin vortices are not present in the jet of BR equal to 0.5, the jet from the shaped hole appears similar to the jet from the cylindrical hole of the same BR shown in Fig. 6.7. Further from the hole exit in the secondary flow plane 4D downstream, like for

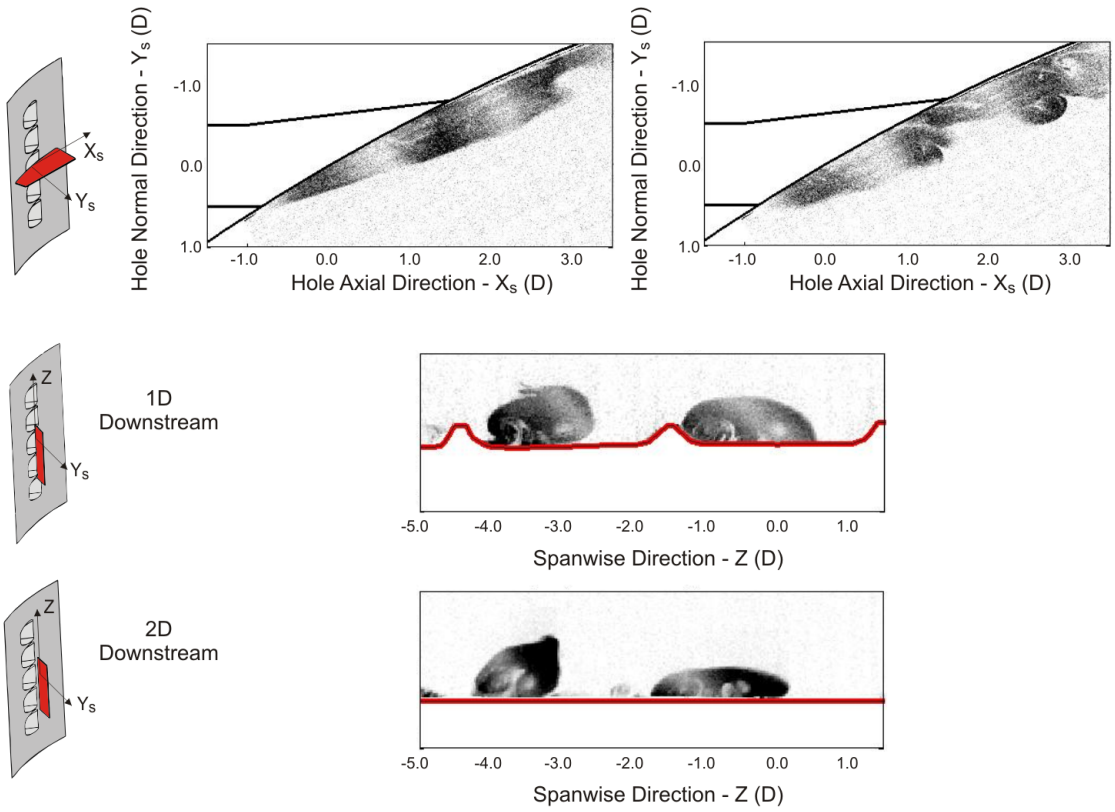

Figure 6.17: Instantaneous images of a jet with BR equal to 1.0 from the shaped hole in the spanwise and secondary flow planes. Obtained with high speed photography.

the cylindrical hole, the jet is stretched and moved in a random manner by the turbulence within the mainstream.

On increasing the BR to 0.8 and 1.0 hairpin vortices are no longer seen in the jet from the shaped hole. Figure 6.17 shows typical images of the jet in the spanwise and secondary flow planes when the BR is equal to 1.0. The left hand of the images in the spanwise plan shows the typical profile of the jet, with it being attached to the blade surface and having an apparently laminar shear layer. A partial movement of the jet out of the measurement plane can be seen 3D downstream.

There are instances when large scale fluctuations can be seen in the jet core at a BR of 1.0, as shown in the right hand spanwise image of Fig. 6.17. These fluctuations signify increased turbulence in the jet. In contrast, turbulence of such a large scale is not seen in the jet from the cylindrical hole for a BR of up to 2.0. This difference between the two hole geometries is attributed to the over-expansion of the flow within the expanding exit of the shaped hole.

The images in the secondary flow plane 1D and 2D downstream included in Fig. 6.17

show the existence of a CRVP in the jet core. Its direction of rotation is the same as that of the CRVP in the jet from the cylindrical hole. However, the CRVP differs in cross-section to that in the jet from the cylindrical hole as a column of non-rotating fluid exists between the pair of vortices. The CRVP is a steady feature of the jet at a BR of 1.0, and hence is apparent in the time-mean vorticity profile shown in Fig. 6.14.

On increasing the blowing ratio to 1.4 the fluctuations within the jet are always present, and show that the jet is more turbulent than at lower BR. A sequence of images taken in the spanwise plane 0.5D below midspan is shown on the left of Fig. 6.18. These images show the clockwise vortices that are present in the shear layer of the jet at this BR. These vortices have a clockwise rotation, as at this BR the jet velocity is larger than that of the mainstream.

In the secondary flow plane at a blowing ratio of 1.4 the CRVP shown in Fig. 6.17 is present in the jet close to the blade surface and above it lies a region of non-rotating fluid. The sequence of images on right of Fig. 6.18 in the secondary flow plane 1D downstream shows that the thickness of this non-rotating fluid changes with time. At 0ms only the CRVP is present in the jet, but 4ms later the jet thickness is seen to have doubled. The jet thickness then reduces such that the image at 8ms is similar to that at 0ms. This variation in the thickness of the non-rotating fluid is believed to indicate the passing of the shear layer vortices shown in the spanwise plane.

The shear layer vortices at a BR of 1.4 were seen more regularly than the hairpin vortices seen at a BR of 0.5. Using the method described in Chapter 4, the peak frequency profiles shown in Fig. 6.19 were obtained based on an image sequence of 700ms in length. These two spanwise planes show a region with a constant Strouhal number of approximately 0.7 in the shear layer 1D-2D downstream. This location is the same as that for the shear layer vortices shown in Fig. 6.18.

On increasing the BR from 0.5, when hairpin vortices are present, to a BR of 1.4, when shear layer vortices are present, no coherent unsteady features were observed in the jet from the shaped hole for the two BR investigated. At these BR, of 0.8 and 1.0, the velocity difference across the shear later would be expected to be lower than for those BR at which coherent unsteady structures were observed. Consequently it appears that the velocity difference across the shear layer is an important factor in the formation of coherent

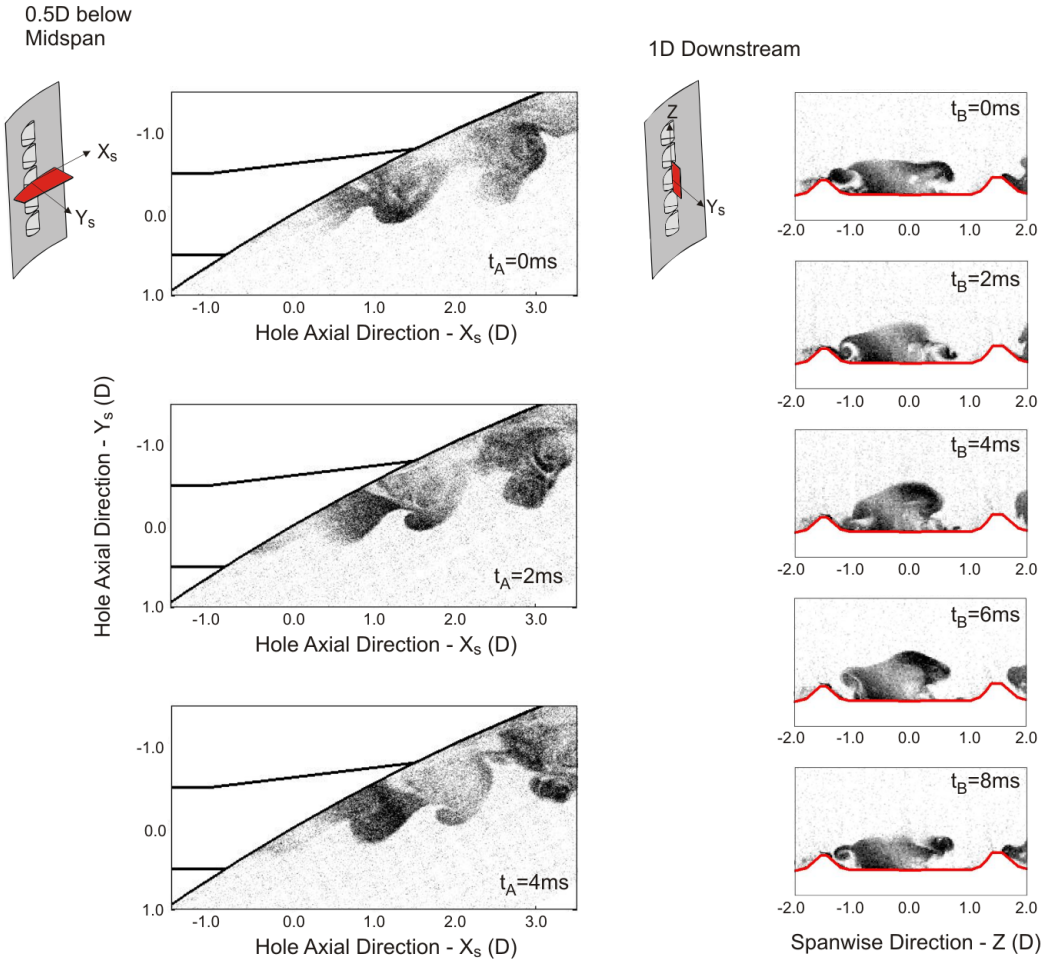

Figure 6.18: Shear layer vortices in a jet from the shaped hole of BR equal to 1.4 in the spanwise and secondary flow planes. Obtained with high speed photography.

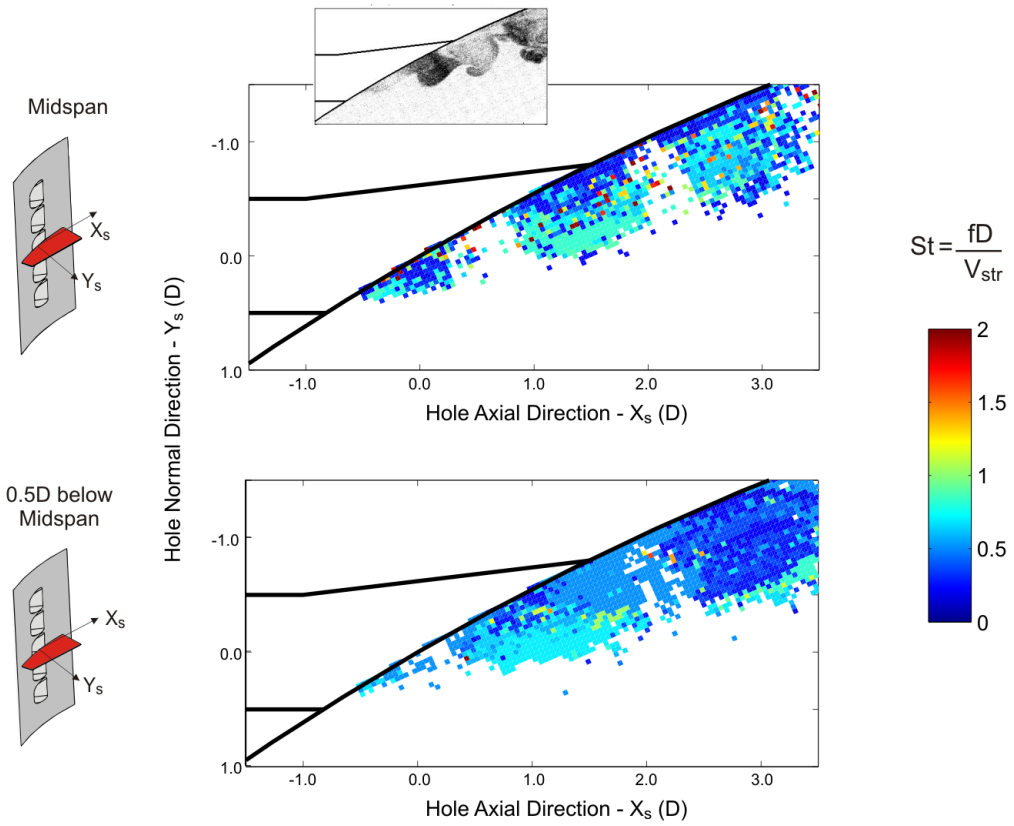

Figure 6.19: Local peak frequency of unsteadiness for a jet of BR equal to 1.4 from the shaped hole, in the spanwise plane (upper) at midspan and (lower) 0.5D below midspan. Obtained with high speed photography.

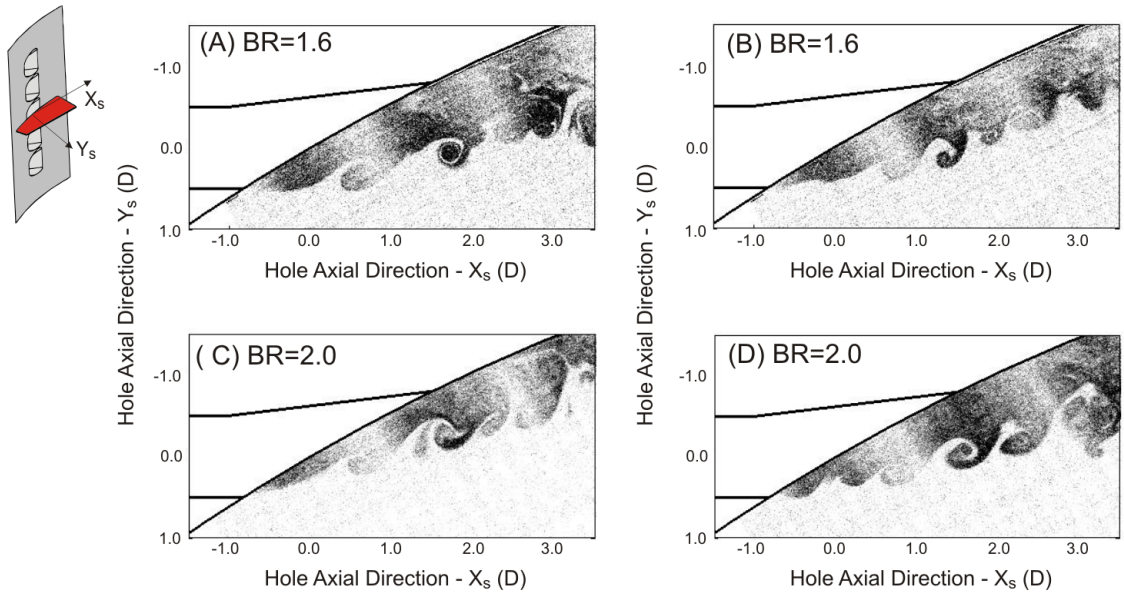

Figure 6.20: Shear layer vortices in jets of BR equal to 1.6 and 2.0 with the shaped hole in the spanwise plane at midspan. Obtained with high speed photography.

unsteadiness within the jet from a cooling hole.

Typical instantaneous images in the spanwise plane of jets with BR equal to 1.6 and 2.0 are shown in Fig. 6.20. At these blowing ratios as at a BR of 1.4 clockwise vortices are present in the shear layer between the jet and the mainstream. However, unlike at a BR of 1.4 there are wide variations in the spatial distance between successive shear layer vortices. This is apparent in Fig. 6.20 with Image A having a spacing between shear layer vortices which is approximately double that in Image B. On account of this change in wavelength no region with a constant peak frequency could be found from the change in pixel intensity.

Images of the jet when the BR is equal to 1.7 are shown in the secondary flow planes 1D and 2D downstream in Fig. 6.21. These images are typical of the jet at this BR, and show that as the jet is turbulent there are multiple eddies in the shear layer. It was not possible to relate the changes in these eddies in the shear layer to the passage of the vortices in the spanwise plane shown in Fig. 6.20.

6.3 Conclusions

In this chapter the naturally occurring unsteadiness in the cooling jet downstream of the cylindrical and shaped holes when fed from a plenum chamber has been shown. These two

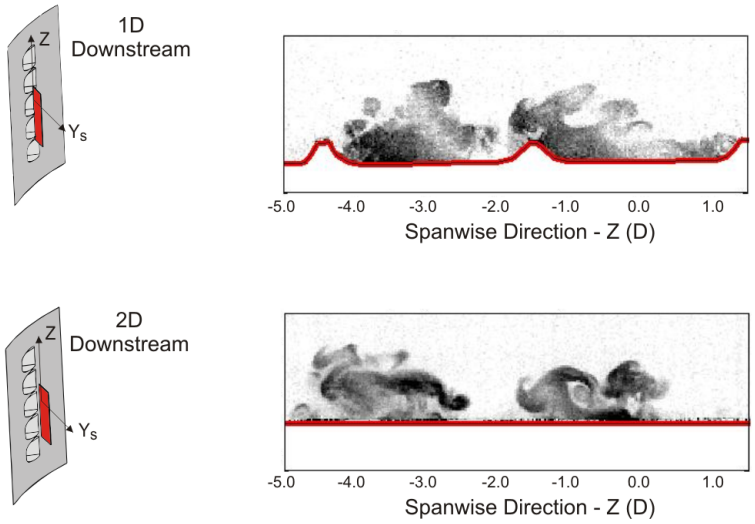

Figure 6.21: Instantaneous images of the jet from the shaped hole of BR equal to 1.7 in the secondary flow planes 1D and 2D downstream. Obtained with high speed photography.

hole geometries had an 'ideal' hole inlet with an inclination angle of 90°.

Within the downstream range investigated the jet from the cylindrical hole appears to be of a low turbulence intensity for blowing ratios (BR) of up to 2.0. At all BR investigated fluctuations are seen in the profile of the shear layer. The velocity gradient across the shear layer at a BR equal to 2.0 is such that a Kelvin-Helmholtz instability occurs due to these fluctuations, and discrete vortices are seen in the shear layer. These vortices have a Strouhal number of approximately 1.5, and their direction of rotation is dictated by the velocity gradient through the shear layer.

At a BR of 0.5 the jet from the shaped hole shows the existence of hairpin vortices with a Strouhal number in the range of 0.5 to 0.8. The reversal of the velocity gradient through the shear layer means that the hairpin vortices rotate in the opposite direction to the shear layer vortices. At a BR of 1.4 coherent vortices with a Strouhal number of 0.7 can be seen in the shear layer. Shear layer vortices are still seen with increasing BR up to 2.0, but their wavelength is not constant. For BR greater than 1.0. the jet from the shaped hole also appears to have a higher level of turbulence than the equivalent jet from the cylindrical hole.

For both the cylindrical and shaped holes up to 2D downstream of the hole exit there is no large scale spanwise unsteadiness in the jet. Instead the spanwise position of the jet is largely steady downstream of both hole geometries.

The results show that the velocity difference in the shear layer is key to the development of shear layer and hairpin vortices. Of the two hole geometries it appears that coherent unsteadiness is more important for the shaped hole, as it occurs when the jet is attached to the blade surface and is thus more likely to influence film effectiveness.

Chapter 7

The Effect of Crossflow upon Coherent Unsteadiness

In the previous chapter with plenum fed cooling holes, it has been shown that two coherent unsteady structures occur within the jet downstream of cylindrical and shaped cooling holes, namely the shear layer vortices and the hairpin vortices. In this chapter the impact of perpendicular internal crossflow is examined, first upon the time-mean flowfield and then the two coherent unsteady structures. Perpendicular crossflow is orientated perpendicular to the mainstream flow at the hole exit, as shown in Fig. 2.4 of the literature review. Within this chapter, as only one crossflow direction is investigated, the use of the term 'crossflow' will refer to perpendicular crossflow.

To investigate the impact of crossflow, the Oxford Super Scale Cascade was setup in the second configuration shown in Chapter 3, in which the internal crossflow channel was present inside the blade interior. The perpendicular direction of the crossflow channel meant that it was orientated in the spanwise direction. A combination of the high speed photography and the Hot Wire Anemometry techniques described in Chapter 4, has been used to observe the jet time-mean profile and the coherent unsteady features present.

7.1 Time-mean Flowfield

7.1.1 Cylindrical Hole

Figure 7.1 shows the time-mean pixel intensity of the jet leaving the cylindrical hole for changing crossflow velocity. The spanwise plane at midspan is shown for jets of BR equal to 1.1 and 1.6. The Crossflow Ratio (CFR), as defined in Eq. 2.2 of the Literature Review, is the ratio of the crossflow velocity to the bulk velocity through the cooling hole. The reader is reminded here, that the bands of low pixel intensity normal to the jet direction are due to the banding in the light sheet explained in Chapter 4.

In Chapter 6 it was seen that for the plenum fed cylindrical holes the jet separates from the blade surface at a BR equal to 1.4 and greater. The time-mean pixel intensity for a BR of 1.6 in Fig. 7.1, shows that the presence of a crossflow does not appear to effect this, as the jet is separated at all the CFR shown. Figure 7.1 shows that for a BR equal to 1.1 the jet is attached to the downstream blade surface for a CFR of 0.1 and 0.2. However, at a CFR of 0.6 it appears that the jet may separate from the blade surface.

Regions of high variance in pixel intensity, identify locations at which coherent unsteady structures may be present. For all the cases for which the time mean pixel intensity is shown in Fig. 7.1, as with the plenum fed holes shown in Fig. 6.2 of Chapter 6, the regions of high unsteadiness are to be found in the shear layer and the wake underneath the jet core.

For both of the BR shown in Fig. 7.1, it appears that the jet has a noticeably larger thickness normal to the blade surface when the CFR is 0.6. Taking the edge of the jet as the point where the time-mean pixel intensity has reduced to zero, it is approximately 15% further from the blade surface 1D downstream for a CFR of 0.6 compared to the lower CFR.

The time-mean pixel intensity in the secondary flow plane 2D downstream in Fig. 7.2 shows that varying the CFR, for the same BR as shown in Fig. 7.1, causes the jet to be rotationally displaced. This is illustrated in Fig. 7.2 by the rotation of the Counter Rotating Vortex Pair (CRVP), which is apparent in the outline of the jet cross section. At a CFR of 0.1 the jet core is rotated in the clockwise direction (looking upstream towards the hole exit) by approximately 20°, at a CFR of 0.2 the jet has no rotation, whilst a CFR of 0.6 causes the jet core to rotate anti-clockwise by 20°.

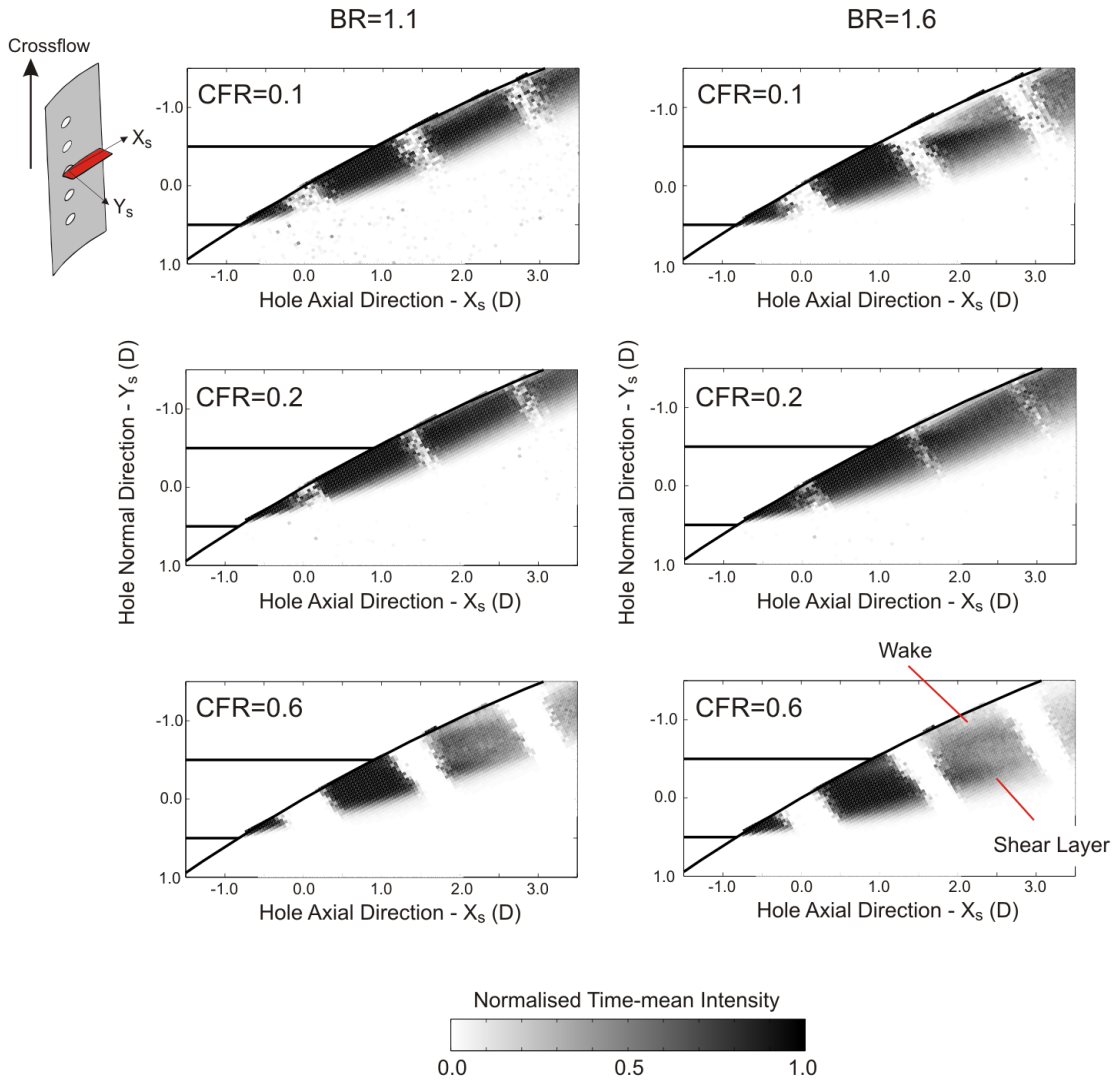

Figure 7.1: Time-mean pixel intensity of the jet from the cylindrical hole in the spanwise plane at midspan. Obtained using high speed photography.

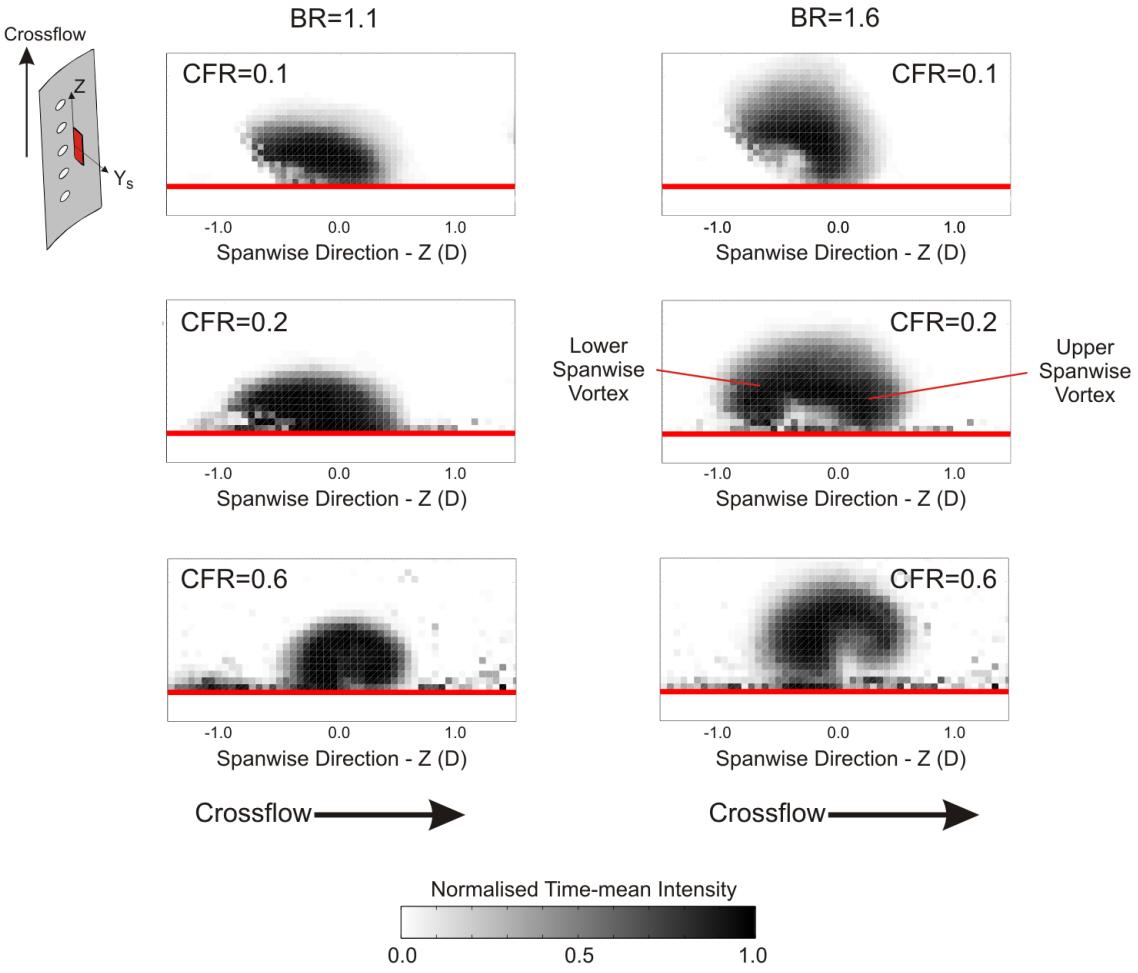

Figure 7.2: Time-mean pixel intensity of the jet from the cylindrical hole in the secondary flow plane 2D downstream. Obtained using high speed photography.

At a CFR of 0.6 the anti-clockwise rotation appears to lift the upper spanwise (right hand in Fig. 7.2) vortex of the CRVP away from the blade surface, whilst the lower spanwise (left hand in Fig. 7.2) vortex remains close to the blade surface. The diameter of the upper spanwise vortex also appears to be the smaller of the two. This rotation of the jet could possibly contribute to the increase in jet thickness in the spanwise plane which is apparent in Fig. 7.1. A similar increase in jet thickness is not seen in the spanwise plane at a CFR of 0.1, despite the CRVP also being rotated, as the largest thickness is shown in Fig. 7.2 to be at a spanwise position lower than midspan.

The time-mean and rms velocities, obtained using Hot Wire Anemometry, are shown in Fig. 7.3 along a traverse in the spanwise (Z) direction located 1D downstream. The traverse is located 0.5D from the blade surface (Y) direction and cuts across a jet of BR equal to 1.8. Two different crossflow velocities, of CFR equal to 0.2 and 0.6, are compared. The orientation of the hot wire probe, means that the velocities in Fig. 7.3 are the combination of the two velocity components normal to the spanwise direction.

There is a rise in the rms velocity in the jet core, for a BR of 1.8, compared to the mainstream. The locations in Fig. 7.3 with an rms velocity close to 6% of the cascade exit velocity, therefore correspond to the jet core. The rms velocity profiles show that at neither CFR is the jet symmetrical about the midspan, with a slight deflection in the lower spanwise (left in Fig. 7.3) direction for a CFR of 0.2, and in the upper spanwise (right in Fig. 7.3) direction for a CFR of 0.6.

Figure 7.3 shows for a CFR of 0.2, that the time-mean velocity in the core of the jet is approximately constant, being in the range of 0.35 to 0.40 times the cascade exit velocity. At a CFR of 0.6 though, Fig. 7.3 shows that the time-mean velocity is not uniform across the jet core, with a large increase at a spanwise distance of 0.3D. Here the time-mean velocity is approximately 0.50 times the cascade exit velocity, compared to the value of close to 0.35 across the remainder of the jet core.

It has been shown in Fig. 7.2, that a jet fed from a crossflow of CFR equal to 0.6 appears to rotate anti-clockwise about the jet axis. The high velocity region in Fig. 7.3 is at the upper spanwise side of the jet core, and here the apparent rotation of the jet means that the vortex is separated from the blade surface. The higher velocity on the upper spanwise side of the jet, means that the local BR is larger than on the lower spanwise side. In the

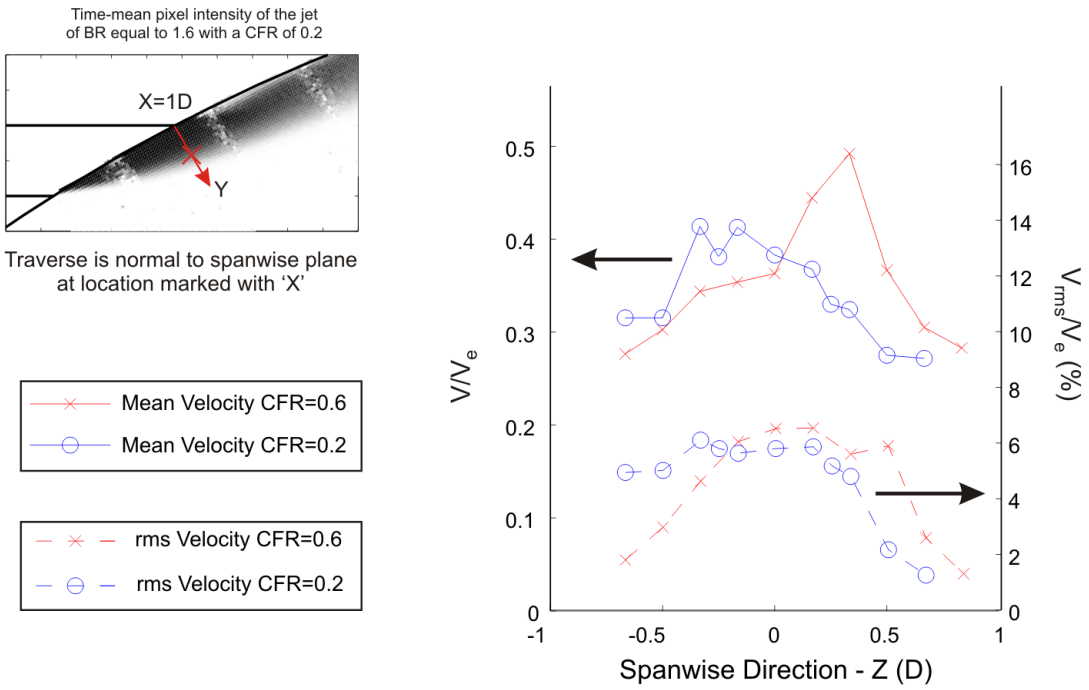

Figure 7.3: The time-mean and rms velocities, within a jet from the cylindrical hole of BR equal to 1.8, across a traverse in the spanwise (Z) direction, 1D downstream and at Y equal to 0.5D. Obtained using Hot Wire Anemometry.

literature review, it has been shown that a larger BR means that a jet will separate further from the blade surface. The spanwise variation in the local BR, could therefore be the reason for the apparent rotation of the jet, seen in Fig. 7.2, within the secondary flow plane 2D downstream.

Increasing the crossflow velocity, it has been shown in the literature review, leads to an increase in the discharge coefficient within the cooling hole. This change implies that the mean velocity profile within the hole is altered with increasing crossflow. This variation in the in-hole velocity profile, could therefore be the reason for the larger time-mean velocity in Fig. 7.3 for a CFR of 0.6 in the upper spanwise part of the jet.

The anti-clockwise rotation of the CRVP seen for a CFR of 0.6 is consistent with the rotation seen computationally by Saumweber and Schulz [89] for a jet of BR equal to 1.0 and a CFR of 1.0, which was introduced in the literature review. Saumweber and Schulz also show experimentally obtained film effectiveness distributions downstream of the exit of a cylindrical hole. From these it was seen that for a BR at which the jet would be expected to be separated, an increase in the CFR led to an increase in the film effectiveness. This

increase was suggested by Saumweber and Schultz to be because the rotation of the jet causes the lower spanwise vortex to be attached to the blade surface. The results of the current study, suggest that this rotation may arise because of a variation in the jet velocity across the spanwise width of the jet.

7.1.2 Shaped Hole

To identify if the variation in crossflow velocity has a similar impact upon the jet from the shaped hole as that from the cylindrical hole, the time-mean pixel intensity is shown in Fig. 7.4 of the jet from the shaped hole in the secondary flow plane 1D downstream. This plane cuts across the exit of the shaped hole, and the edge of the hole is shown by the red line in Fig. 7.4. At both the blowing ratios shown, it is apparent that with a CFR of 0.1 the jet lies in the centre of the hole. On increasing the CFR to 0.2 the jet appears to become biased towards the lower spanwise (left in Fig. 7.4) edge of the hole for both BR. At the largest CFR of 0.6, the jet appears to split into two parts, which lie at the lower and upper spanwise edges of the hole. Of the two parts, that closest to the upper spanwise edge appears to be larger than that at lower spanwise edge.

It is also seen in Fig. 7.4 that at a CFR of 0.2 and 0.6 there is some coolant spilling across the edge between the centre hole and its lower spanwise neighbour. However, Fig. 7.4 shows the spilling over of coolant to be less common across the edge between the centre hole and its upper spanwise neighbour.

Figure 7.5 shows the time-mean pixel intensity of the jet from the shaped hole in the same secondary flow plane 2D downstream as for the cylindrical hole in Fig. 7.2. Here the jets from the holes neighbouring the centre hole are also shown. The upper images of Fig. 7.5 show that at a CFR of 0.2 the film emerges as a series of single jets attached to the blade surface for both blowing ratios. The bias of the jet towards the lower spanwise direction, seen 1D downstream, is also apparent in this plane, for the jet from the centre hole is that located at a spanwise position of -1.0D.

The lower half of Fig. 7.5 shows the resultant film for a CFR of 0.6. Here the split jet, seen inside the expanding hole exit in Fig. 7.4, is seen to form two 'mini' jets. The 'mini' jet at a spanwise position of 0.5D is that from the upper spanwise edge of the centre hole and that at a spanwise position of -1.5D is that from the lower spanwise edge.

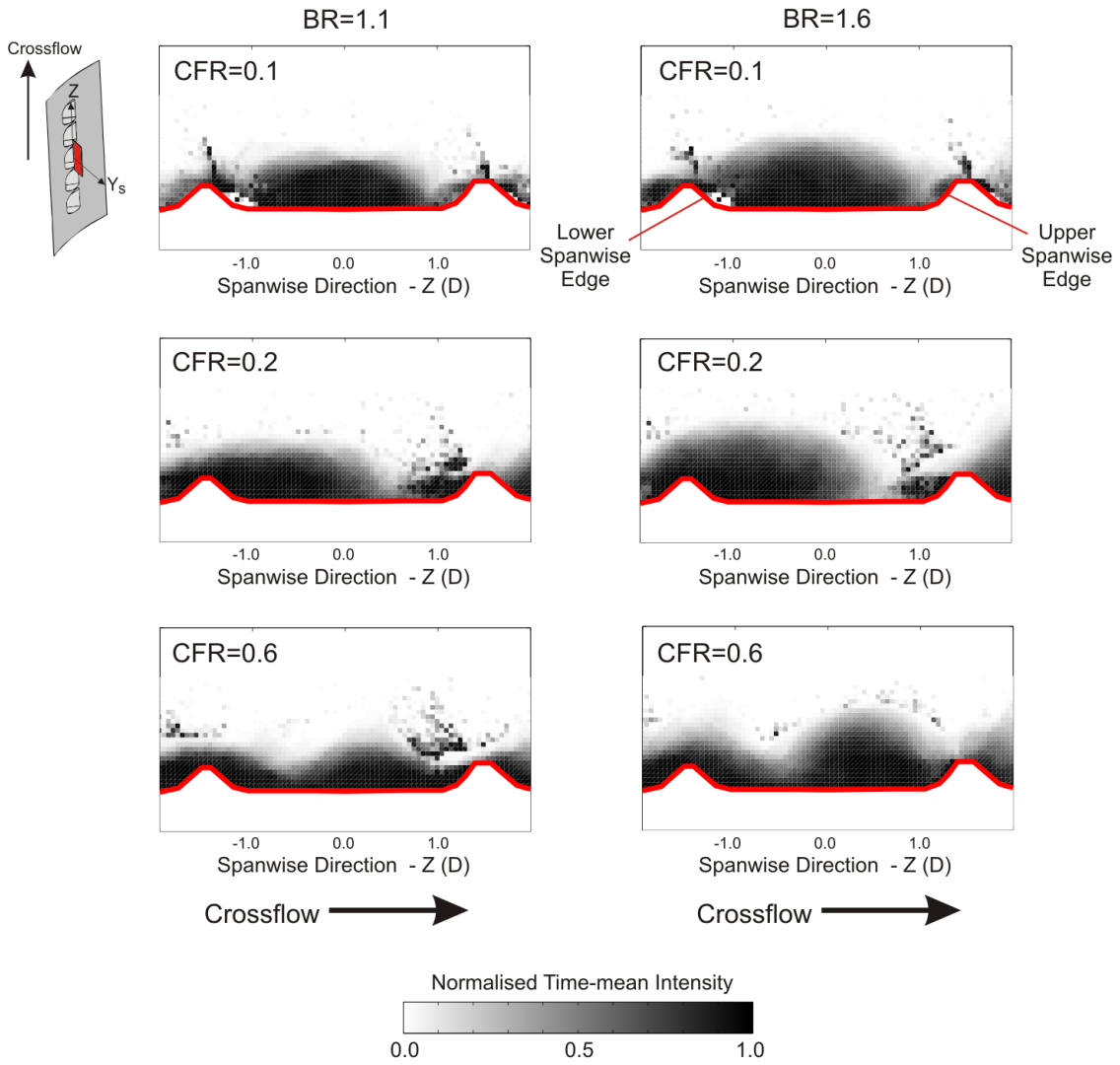

Figure 7.4: Time-mean pixel intensity of the jet from the shaped hole in the secondary flow plane 1D downstream. Obtained with high speed photography.

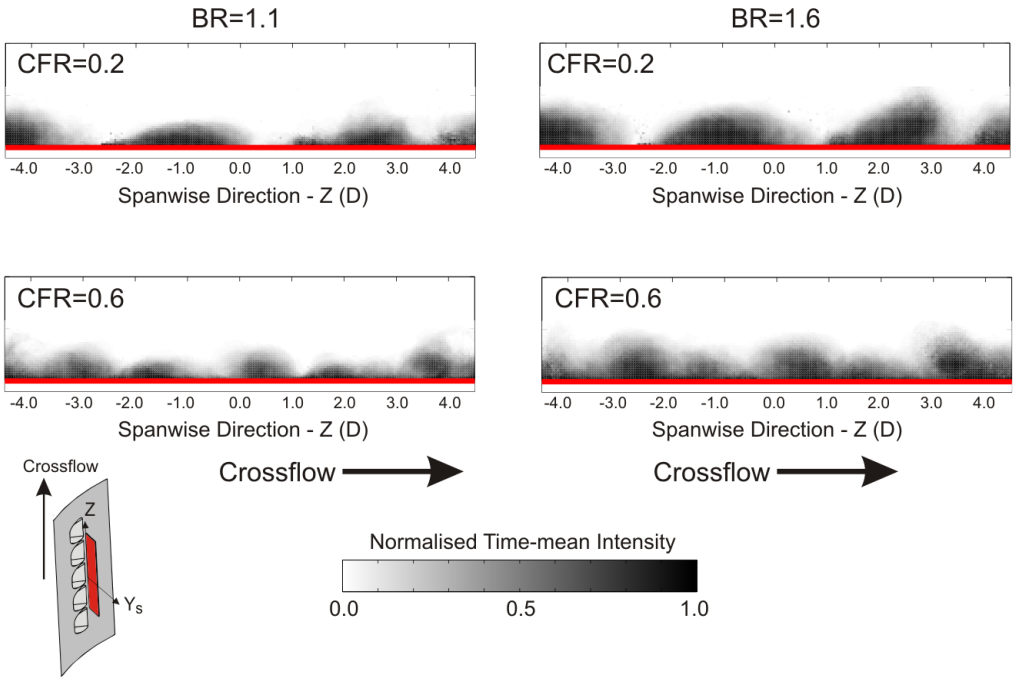

Figure 7.5: Time-mean pixel intensity of the jet from the shaped hole in the secondary flow plane 2D downstream. Obtained with high speed photography.

Film effectiveness is also presented by Saumweber and Schulz [89] upon the surface downstream of a shaped hole, with a similar geometry, fed by crossflow. Their profiles also show the splitting of the jet seen in the current experiment, with peaks of high film effectiveness at both the upper and lower spanwise edges of the hole for CFR of 0.7 and above. For a CFR between 0.2 and 0.6, Saumweber and Schulz also show the tendency for the jet to bias to an edge of the hole, as shown in the current investigation for a CFR of 0.2. Overall though, the biasing and splitting of the jet was shown by Saumweber and Schulz to lead to a reduction in the laterally averaged film effectiveness compared to the case with no crossflow.

It should be noted here that the biases shown by Saumweber and Schulz are to the opposite edges of the shaped hole from those shown in the current experiment. For they show with a CFR equal to 0.2 the jet biases to the upper spanwise edge, and the larger part of the split jet at higher CFR biases to the lower spanwise edge. Drawing on the computational work of Kholi and Thole [47] (also introduced in the literature review), Saumweber and Schulz attribute their bias to a spiral motion of the in-hole flowfield.

7.2 Shear Layer Vortices

7.2.1 Cylindrical Hole

Previously, in Chapter 6 shear layer vortices have been shown to arise, in the jet from the cylindrical hole of BR equal to 2.0, and from the shaped hole of BR equal to 1.4, when fed from the plenum chamber. It was concluded that these vortices are due to a Kelvin-Helmholtz instability in the shear layer between the jet and the mainstream.

In this section the impact of crossflow on the formation of shear layer vortices in the jet from the cylindrical hole is shown in Fig. 7.6 to 7.8. Figures 7.6 to 7.8 show frequency spectra obtained within a jet of BR equal to 1.8 for points upon a traverse in the blade normal (Y) direction. The origin of the traverse is 2D downstream at the blade midspan. The temporal variation in velocity has been measured using Hot Wire Anemometry. The orientation of the hot wire probe is described in Chapter 4 and means that the velocity measured is that normal to the spanwise direction. The reader is reminded that there is also a change in the inlet inclination angle, between the case with a plenum and the current one with crossflow, from 90° to 30°.

Figure 7.6 shows the case for a jet of BR equal to 1.8 with a CFR of 0.1. The time-mean velocity profile shows a clear high velocity region, of approximately 0.4 times the cascade exit velocity, which indicates the core of the jet. The lower velocity at Y equal to 0.2 indicates that the jet separates from the blade surface, with a wake region forming between the jet and the blade surface. At larger Y locations the time-mean velocity decreases to the mainstream value of 0.3 times the cascade exit velocity. The rms velocity is 0.5% in the mainstream and rises through the shear layer between the jet and the mainstream to have a peak value of greater than 4.0%. The rms velocity decreases through the jet core and the wake, but at all Y locations the rms velocity remains larger than the mainstream value.

It should be noted that the time-mean velocity of the mainstream shown in Fig. 7.6, is 40% larger than the value obtained with PIV for the plenum fed cylindrical hole, shown in Fig. 6.1 of Chapter 6. This difference is either due to an increased blockage of the mainstream by the jet when fed with crossflow, or the uncertainties in the two experimental techniques. The reader is advised here, that this difference does not effect the usefulness of the velocity profile in locating the position of the coherent unsteadiness within the jet cross

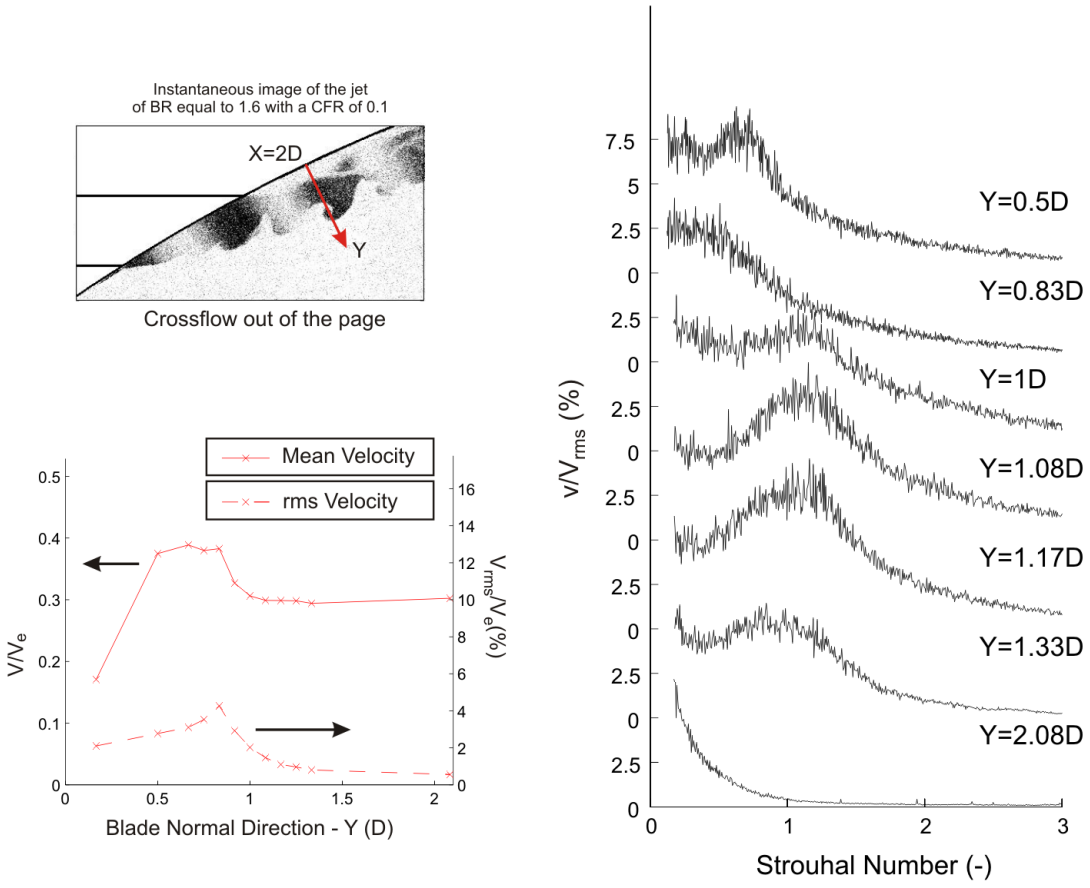

Figure 7.6: Frequency spectra at locations upon a blade normal (Y) traverse with its origin at midspan 2D downstream. For a jet from the cylindrical hole of BR equal to 1.8 with a CFR of 0.1. Obtained using Hot Wire Anemometry, with the instantaneous image recorded using high speed photography.

section.

Frequency spectra are shown in Fig. 7.6 for seven points upon the traverse in the Y direction. In these spectra the frequency has been non-dimensionalised using the local time-mean velocity, and the amplitude non-dimensionalised using the local rms velocity. The origin of the amplitude has been offset for each spectrum.

The frequency spectra shown for points at Y equal to 1D, 1.08D and 1.17D show a frequency peak which is indicative of coherent unsteadiness with a Strouhal number of 1.1. At Y equal to 1.33D there is coherent unsteadiness with a slightly lower Strouhal number of 1.0. Referring to the mean and rms velocity profiles in Fig. 7.6, these Y locations are at the edge of the shear layer closest to the mainstream. Frequency spectra, not included here, show coherent unsteadiness of Strouhal number equal to 1.1 to also be present in the

shear layer 1D downstream at midspan.

Figure 7.6 also includes a typical image of the jet in the spanwise plane at midspan obtained using high speed photography for a BR of 1.6. Here clockwise (on looking into the page) vortices are present in the shear layer of the jet. The passage of the shear layer vortices, based on the temporal variation in pixel intensity, was found to be of a Strouhal number in the range of 1.0 to 1.2. Thus the coherent unsteadiness seen in the frequency spectra of Fig. 7.6 is suspected to be due to the passage of shear layer vortices.

The broadband nature of the frequency peaks in Fig. 7.6, signifies that there is some variation in the passing frequency of the shear layer vortices. This is also apparent when viewing the jet at BR equal to 1.6 with high speed photography. To account for this variation, the coherent unsteadiness intensity has been defined in Eq. 4.14 of Chapter 4. Thus the frequency peak of the maximum amplitude in the Fig. 7.6, at Y equal to 1.08D, has a coherent unsteadiness intensity of 6%. It should be reminded here that the coherent unsteadiness intensity is similar to turbulence intensity, except that only the contribution to the rms velocity due to coherent unsteadiness is included.

Frequency spectra are also shown in Fig. 7.6 for points in the mainstream and the jet core. In the mainstream no coherent unsteadiness is seen and there is less unsteadiness at higher frequencies. The spectra at Y equal to 0.5D shows there to be coherent unsteadiness of a Strouhal number equal to 0.8. This point is close to the shear layer between the jet and the wake, and so possibly indicates there are also vortices in this shear layer.

Figure 7.7 is of the same layout as Fig. 7.6, and shows the coherent unsteadiness in the jet of BR equal to 1.8 on increasing the crossflow velocity to be of a CFR equal to 0.2. The time-mean velocity profile in Fig. 7.7 is similar to that shown in Fig. 7.6, with a high velocity jet core and a wake region near the wall. The rms velocity profile also shows the same features as in Fig. 7.6 for a CFR of 0.1, but with a larger rms velocity across the jet core and a rise in the rms velocity in the wake relative to that in the jet core.

The points between Y equal to 1.17D and 1.42D, on referring to the time-mean velocity profile in Fig. 7.7, are seen to be towards the outer edge of the shear layer between the jet and the mainstream. The frequency spectra obtained at these points, as for a CFR of 0.1, show the presence of coherent unsteadiness. The maximum amplitude of the coherent unsteadiness is found at Y equal to 1.33D and the coherent unsteadiness intensity is found

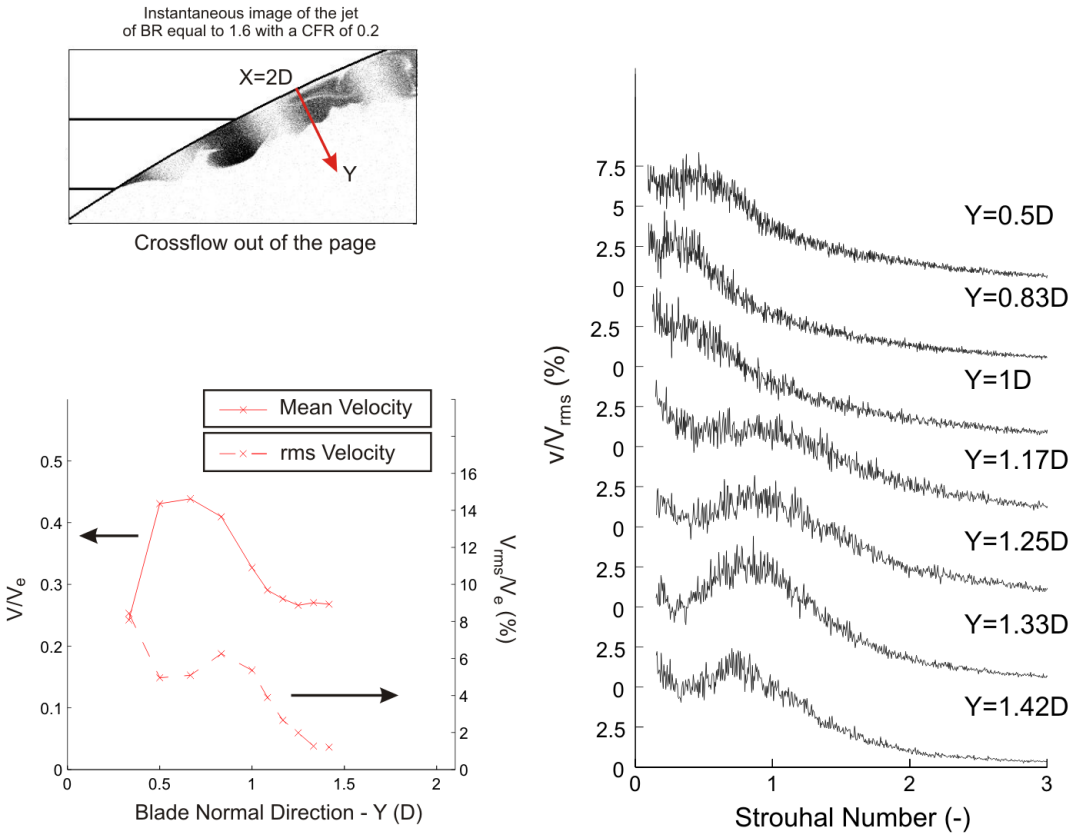

Figure 7.7: Frequency spectra at locations upon a blade normal (Y) traverse with its origin at midspan 2D downstream. For a jet from the cylindrical hole of BR equal to 1.8 with a CFR of 0.2. Obtained using Hot Wire Anemometry, with the instantaneous image recorded using high speed photography.

here to be 3%.

Figure 7.7 shows the Strouhal number of the coherent unsteadiness to decrease from 1.0 to 0.8 with increasing distance from the blade surface. Coherent unsteadiness in the same frequency range, is also present in the shear layer 0.25D below midspan at the same downstream location. No coherent unsteadiness is present in the jet core or in the shear layer close to the jet core, as shown in the frequency spectra recorded at the three Y locations closer to the blade surface in Fig. 7.7.

The Strouhal number of the coherent unsteadiness shown in Fig. 7.7 is of a lower frequency than the shear layer vortices seen at a CFR of 0.1. However, it has been shown in Chapter 6, when comparing the shear layer vortices from the two hole types, and in the literature review, that shear layer vortices do not always have a constant Strouhal number across different flow conditions. Consequently it is thought likely that the coherent un-

steadiness at a CFR of 0.2, for a jet of BR equal to 1.8 shown in Fig. 7.7, also indicates the passing of shear layer vortices.

When the crossflow is increased to be of a CFR equal to 0.6, it is apparent in Fig. 7.8 that, unlike at the lower CFR cases shown previously, there is no high velocity jet core at midspan. The location of the shear layer between the jet and the mainstream is apparent from the reduction in the rms velocity with increasing distance from the blade surface. It also appears that the jet is attached to the blade surface as no wake region is present. This change, compared to the lower CFR cases, is likely to be due to the non-symmetrical variation in mean velocity of the jet in the spanwise direction shown earlier in this chapter.

The frequency spectra shown in Fig. 7.8 show that with a CFR of 0.6 coherent unsteadiness is only present, as at the lower CFR, at the outer edge of the shear layer between the jet and the mainstream. Here the reader is asked to ignore the sharp peaks seen in some of the spectra in Fig. 7.8 with a Strouhal number close to 1.0. These are attributed to a harmonic of the noise at 50Hz caused by the blower on the out-pipe from the crossflow channel.

The coherent unsteadiness in the frequency spectra recorded at Y equal to 1.25D and 1.33D has a Strouhal number of 1.2. It is shown in Fig. 7.8 that it has an amplitude of 7% of the rms velocity. The coherent unsteadiness intensity is calculated to be 5% for the frequency peak at Y equal to 1.33D, which is similar to the values seen at the lower CFR. Coherent unsteadiness with a Strouhal number of 1.2 is also present within the shear layer 0.25D above the centreline at a CFR of 0.6.

Images in the secondary flow plane 2D downstream, recorded with high speed photography, are shown in Fig. 7.9 of a jet of BR equal to 1.6 also with a CFR of 0.6. The two image sequences show the passage, which is seen regularly, of an unsteady structure through the secondary flow plane. The images at 1ms show a band of fluid (labeled 'Fluid A' in Fig. 7.9), to arise on the upper surface of the jet. This band of fluid is detached from the jet on the upper spanwise (right hand in Fig. 7.9) side of the jet. With increasing time, it is seen that the band of fluid rotates around the jet towards its lower spanwise side. At 4ms it is seen that the band of fluid merges into the lower spanwise vortex of the CRVP.

The sequence of images shown in Fig. 7.9 are 4ms in length. Non-dimensionalising the frequency, using the time-mean velocity in the jet core at a BR of 1.8 shown in Fig. 7.8,

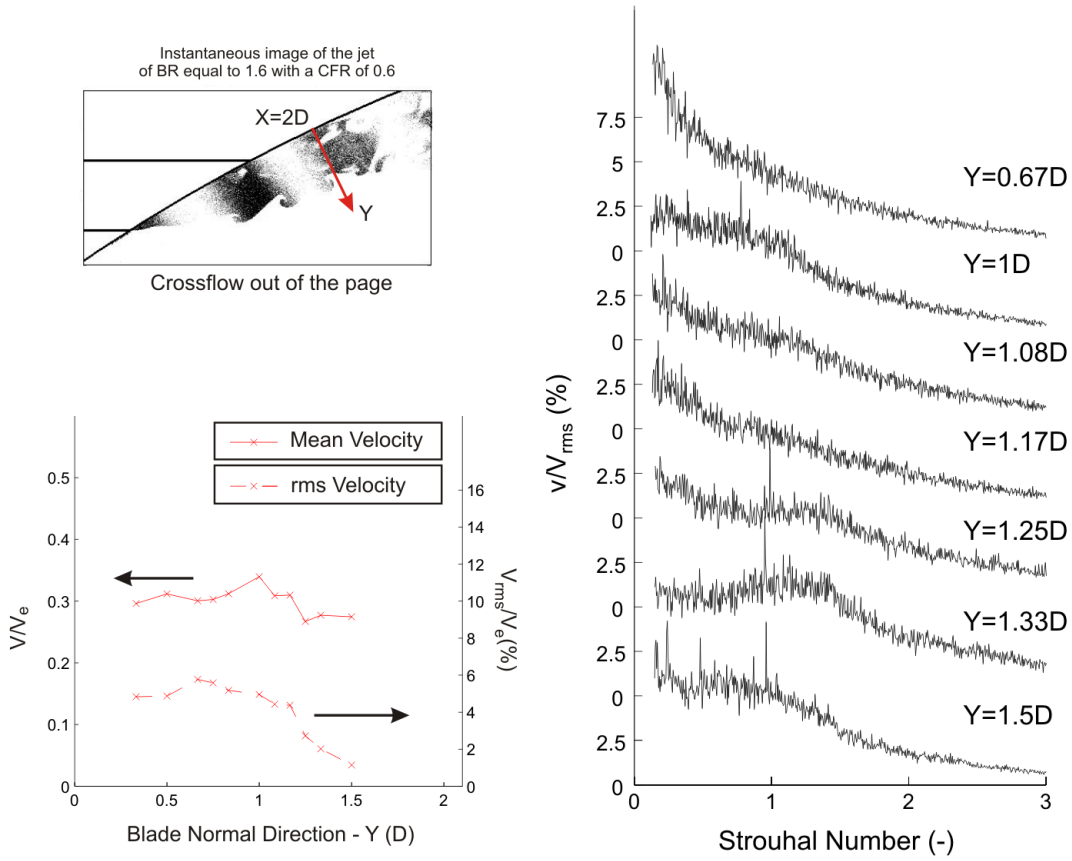

Figure 7.8: Frequency spectra at locations upon a blade normal (Y) traverse with its origin at midspan 2D downstream. For a jet from the cylindrical hole of BR equal to 1.8 with a CFR of 0.6. Obtained using Hot Wire Anemometry, with the instantaneous image recorded using high speed photography.

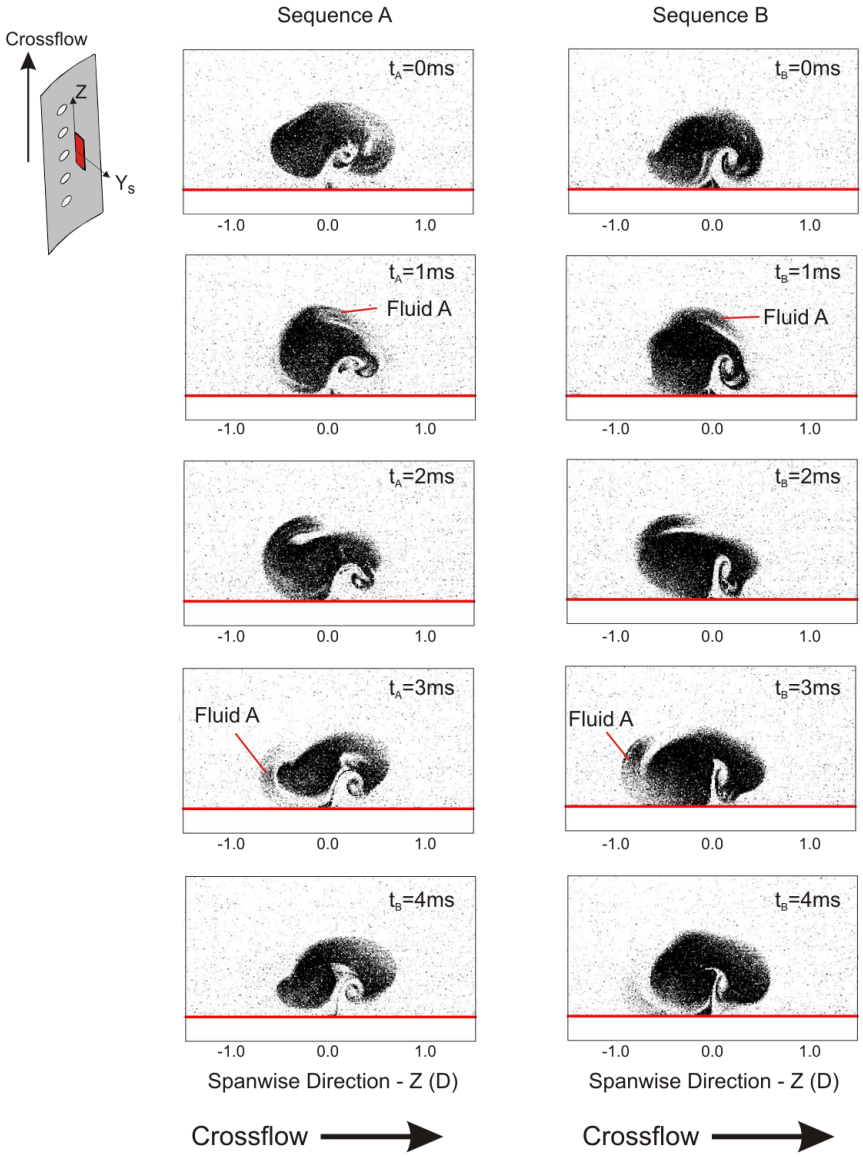

Figure 7.9: Two sequences of instantaneous images showing the jet from the cylindrical hole in the secondary flow plane 2D downstream, with a BR of 1.6 and a CFR of 0.6. Obtained with high speed photography.

this equates to a Strouhal number of approximately 1.1. This is the same as the Strouhal number of the passing of the shear layer vortices, which suggests that the rotation of the detached band of fluid shown in Fig. 7.9 may be related. Previously in Fig. 7.3 it has been seen that there is a spanwise variation in the mean velocity at a CFR of 0.6. This implies their may be a spanwise variation in the convection speeds of the shear layer vortices, which could lead to the apparent rotation shown in Fig. 7.9.

Shear layer vortices were seen in Chapter 6 to occur in the jet from the plenum fed cylindrical hole of a BR equal to 2.0. The evidence in this section shows that coherent shear layer vortices still occur in the shear layer between the jet and the mainstream when crossflow is present at the hole inlet, being seen here for blowing ratios of 1.6 and 1.8. Shear layer vortices are seen to be present at all three crossflow velocities investigated. However, there is variation in the value of the Strouhal number of the shear layer vortices for changes in the crossflow velocity and relative to the value of 1.5 seen for the plenum fed case.

7.2.2 Shaped Hole

Coherent shear layer vortices were seen in Chapter 6, to be present in the jet of BR equal to 1.4 emerging from the shaped hole when it is fed from the plenum chamber. Vortices were also present in the shear layer at BR equal to 1.6 and 2.0, but in these cases a regular spacing was not seen between the vortices.

Vortices did not appear to be present in the shear layer of the jet from the shaped hole, for BR equal to 1.6 and 2.0 with varying crossflow velocity. Figure 7.10 shows typical instantaneous images, recorded with high speed photography, at BR equal to 1.6 and 2.0 with crossflow velocities of CFR equal to 0.1 and 0.6. In all four images, the jet appears to contain more turbulent eddies than in the jet of equivalent BR from the cylindrical hole. The turbulent eddies mean that there are vortices in the shear layer, but frequency spectra, obtained based on the temporal variation in pixel intensity, did not show their passage to be coherent. The case of CFR equal to 0.2 is not shown in Fig. 7.10, but there is no significant difference to those jets shown with CFR equal to 0.1 and 0.6.

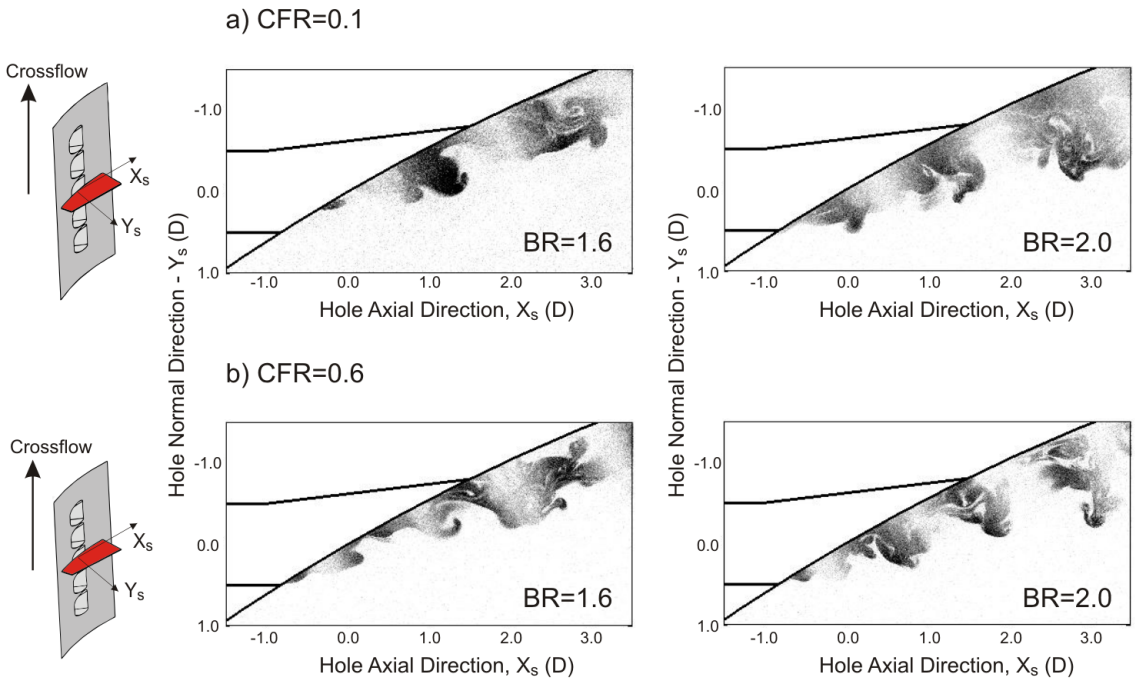

Figure 7.10: Instantaneous images in the spanwise plane (a) at midspan and (b) 0.5D above midspan of the jet from the shaped hole. Obtained with high speed photography.

7.3 Hairpin Vortices

7.3.1 Cylindrical Hole

The second coherent unsteady structure, seen in Chapter 6 for the case of plenum fed cooling holes, is the hairpin vortex. In chapter 6 hairpin vortices were only seen to be present in the jet from the shaped hole of BR equal to 0.5. In this section it is seen that with crossflow the hairpin vortices are also present in the jet from the cylindrical hole.

The two image sequences in Fig. 7.11 of the spanwise plane at midspan were recorded using high speed photography. The jet in both sequences is from the cylindrical hole and has a BR equal to 0.7. The sequence on the left has a crossflow at the hole inlet with a CFR equal to 0.5 and that on the right has a CFR equal to 0.8. Both sequences show the passage of anti-clockwise vortices in the jet, and it has been noted in Chapter 6 that these are the spanwise projection of the hairpin vortices.

The similarity between the two image sequences in Fig. 7.11 suggests that a change in the crossflow velocity does not significantly impact the formation of hairpin vortices. In Chapter 6 it was concluded that the presence of hairpin vortices is determined by the velocity difference across the shear layer between the jet and the mainstream. Thus the

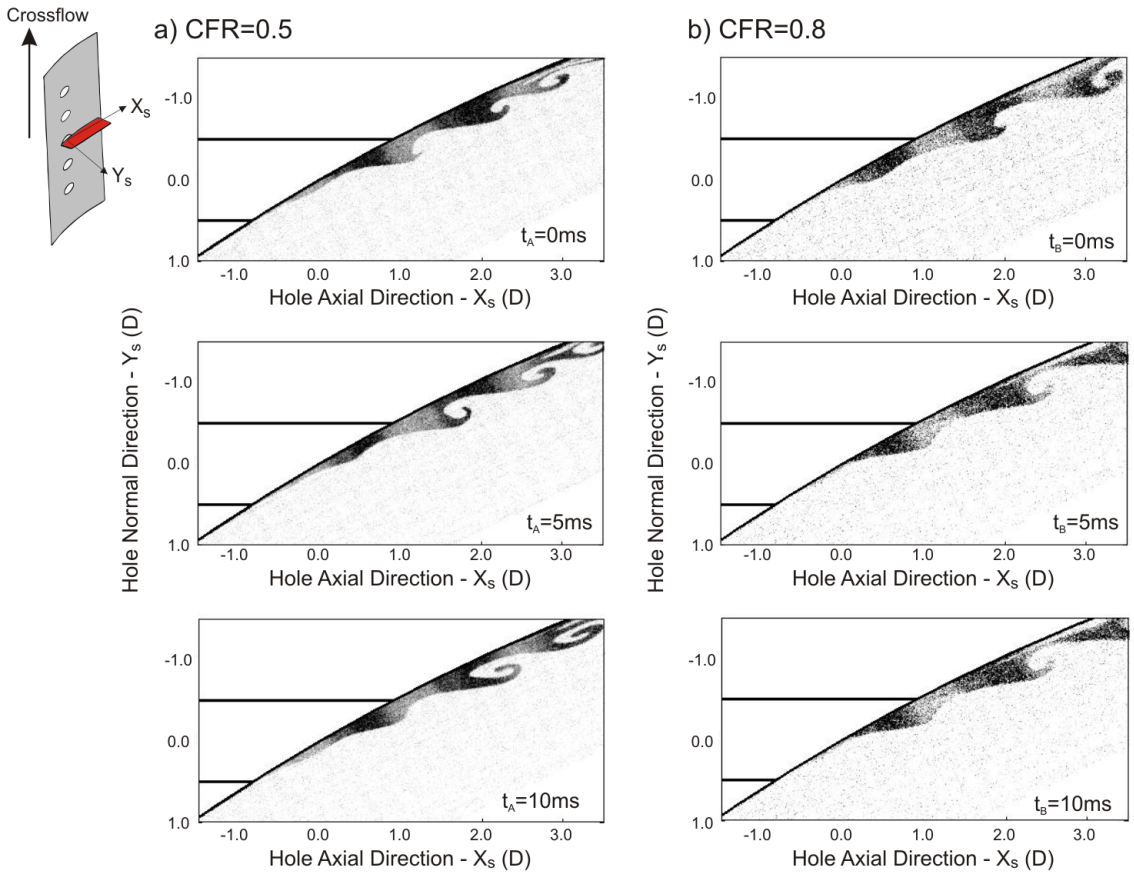

Figure 7.11: Image sequences recorded in the spanwise plane at midspan, showing the passage of hairpin vortices in a jet of BR equal to 0.7 from the cylindrical hole. Crossflow velocities of CFR equal to (a) 0.5 and (b) 0.8 are shown. Obtained with high speed photography.

change in CFR, does not appear to alter the velocity profile in the shear layer such that hairpin vortices are not formed. At a BR equal to 1.1, at which the velocity difference across the shear layer is likely to be smaller, hairpin vortices are not seen in the spanwise plane for crossflow velocities with a CFR of 0.6 or lower.

The passage of a hairpin vortex in the secondary flow plane 2D downstream of the cylindrical hole is shown in Fig. 7.12. The BR is equal to 0.7 and the CFR is 0.5, and in both sequences similar features to those shown in the images within Fig. 6.16 of Chapter 6 can be identified. The images at 2ms in Fig. 7.12 show the leading face of the hairpin vortex where the vortex line is orientated in the spanwise direction. With increasing time the vorticity becomes orientated in the streamwise direction, and the images at 4ms and 6ms show the streamwise vortices at the spanwise extremes of the jet. 10ms after the hairpin

vortex began to pass through the plane, the gap between hairpin vortices is reached and the final images in Fig. 7.12 show the jet to contract back down onto the blade surface.

Figures 7.13 and 7.14 show frequency spectra for points upon blade normal (Y) traverses. The Y traverses have their origin at midspan 0D and 1D downstream. Jets of BR equal to 0.7, 0.8 and 0.9 are shown, and in each case the crossflow has a CFR equal to 0.1. As for the frequency spectra shown in the previous section, the frequency is non-dimensionalised using the local time-mean velocity. To show the location of the frequency spectra within the jet, the mean and rms velocity profiles are included in both Fig. 7.13 and 7.14. The reader is reminded that the origin in the Y direction is the blade surface with no cooling hole, and so negative values on traverses 0D downstream refer to points inside the cooling hole tube.

The time-mean velocity profiles 0D downstream, shown in Fig. 7.13, show there to be a region of constant velocity across the jet core at each BR. As is to be expected, there is an increase in the velocity in the jet core with increasing BR. The shear layer begins 0.3D from the blade surface and leads to an increase in the mean and rms velocities.

Four frequency spectra are included in Fig. 7.13 for each BR. Comparing their locations with the time-mean velocity profile it is seen that the three Y locations closest to the blade surface are in the jet core, whilst that furthest away is in the shear layer. Across all three BR the frequency spectra inside the jet core show the presence of broadband coherent unsteadiness with a Strouhal number of 0.5. In contrast, the frequency spectra in the shear layer show no coherent unsteadiness to be present.

The amplitude of the coherent unsteadiness relative to the local rms velocity rises with the increase in blowing ratio, with that at Y equal to -0.17D seen in Fig. 7.13 to increase from 5 to 12%. The coherent unsteadiness intensity, calculated according to Eq. 4.14, is approximately 3% for all three BR.

The time-mean velocity profiles in Fig. 7.14 show at all three BR the jet to be attached to the blade surface 1D downstream. The shear layer between the jet and the mainstream, as has been shown to also be the case 0D downstream, begins close to Y equal to 0.3D. The largest rms velocity seen in the shear layer for these BR is 2.5%, and this occurs for a BR of 0.7 which has the largest velocity difference across the shear layer.

Four frequency spectra are shown in Fig. 7.14 for each BR. Referring to the time-mean

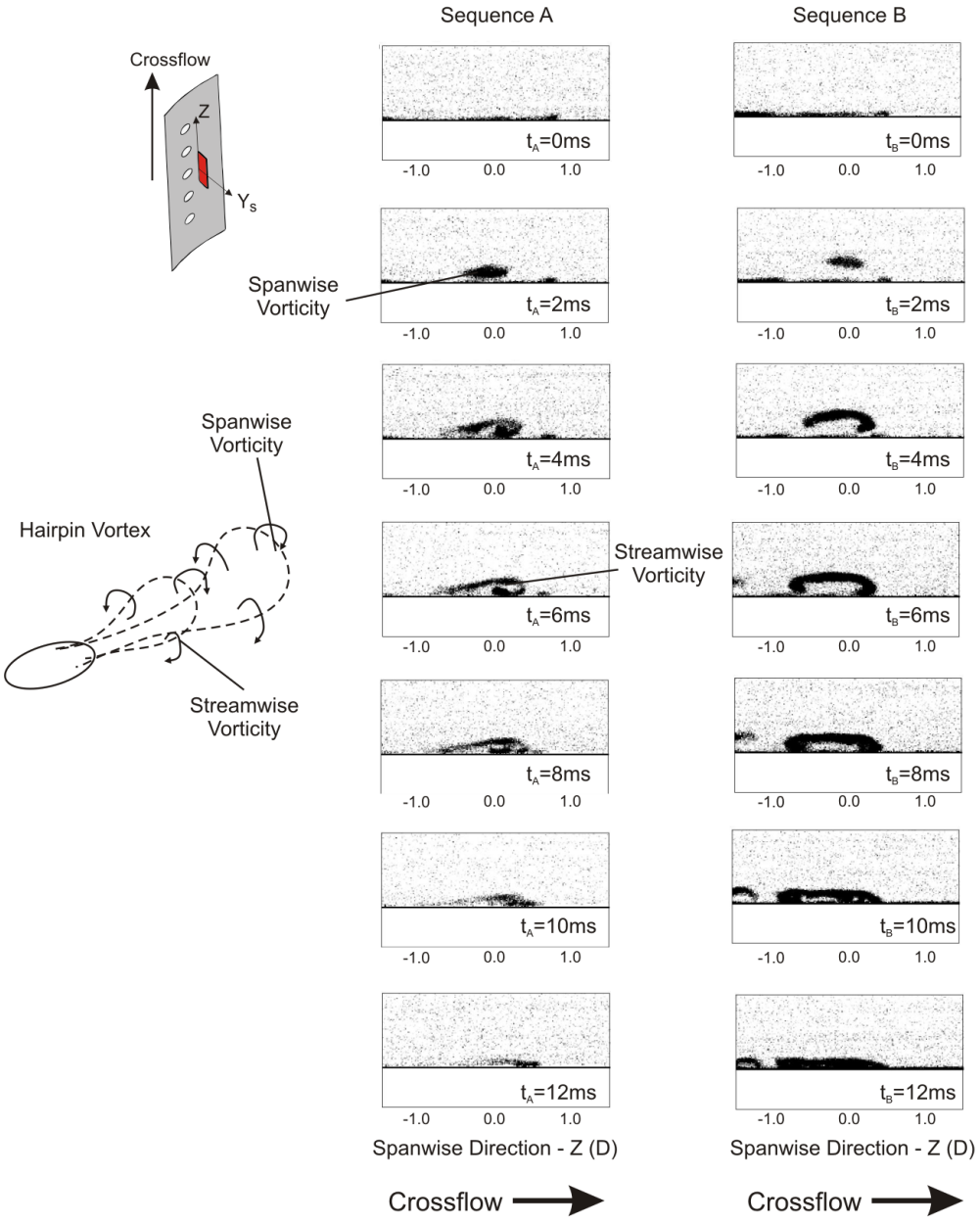

Figure 7.12: Image sequences recorded in the secondary flow plane 2D downstream, showing the passage of hairpin vortices in a jet of BR equal to 0.7 from the cylindrical hole. The crossflow has a CFR equal to 0.5 in both sequences. Obtained with high speed photography.

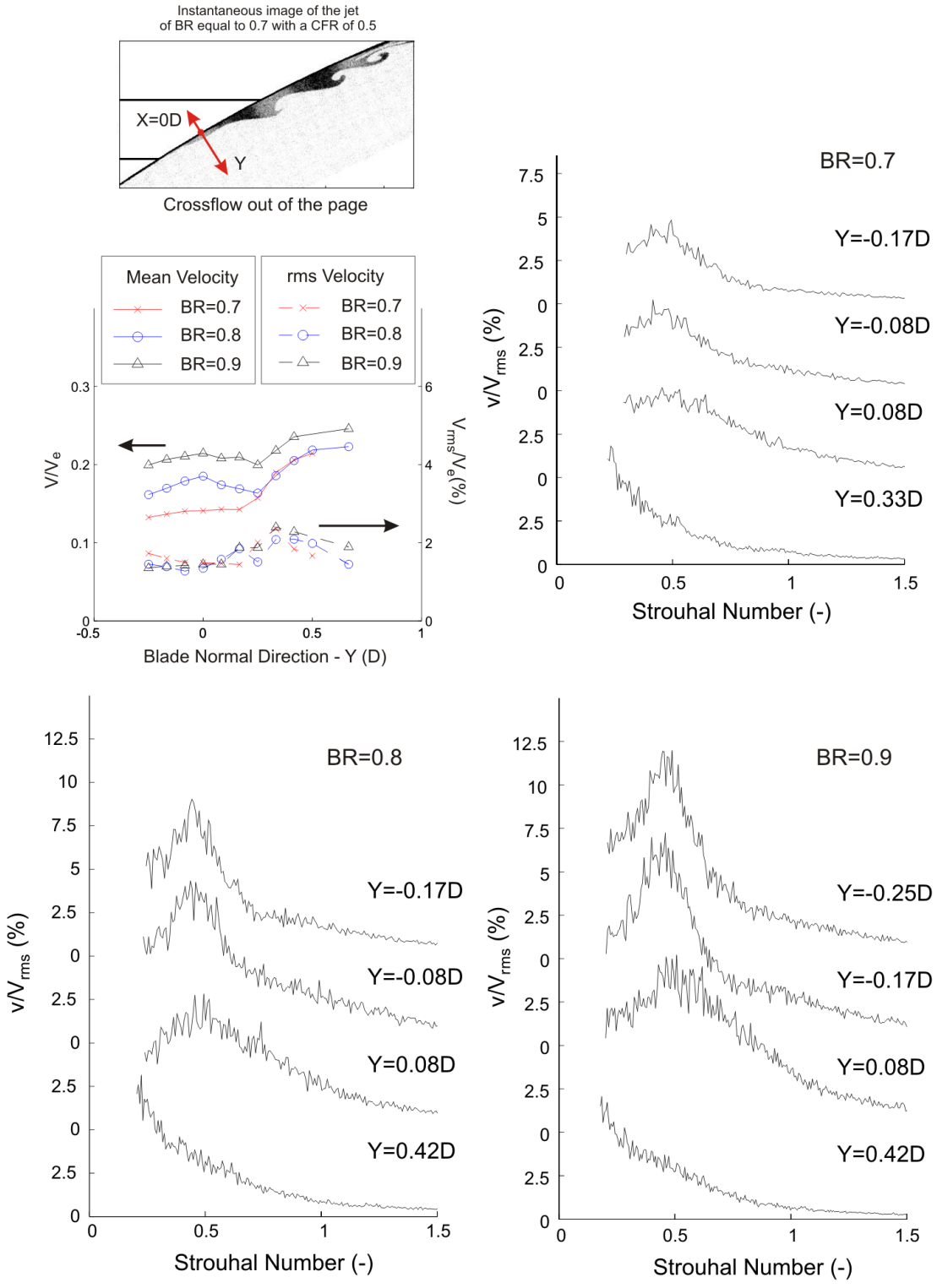

Figure 7.13: Frequency spectra 0D downstream of the hole exit for a jet from the cylindrical hole of BR in the range of 0.7 to 0.9 with a CFR of 0.1. Obtained using Hot Wire Anemometry, the instantaneous image was recorded using high speed photography.

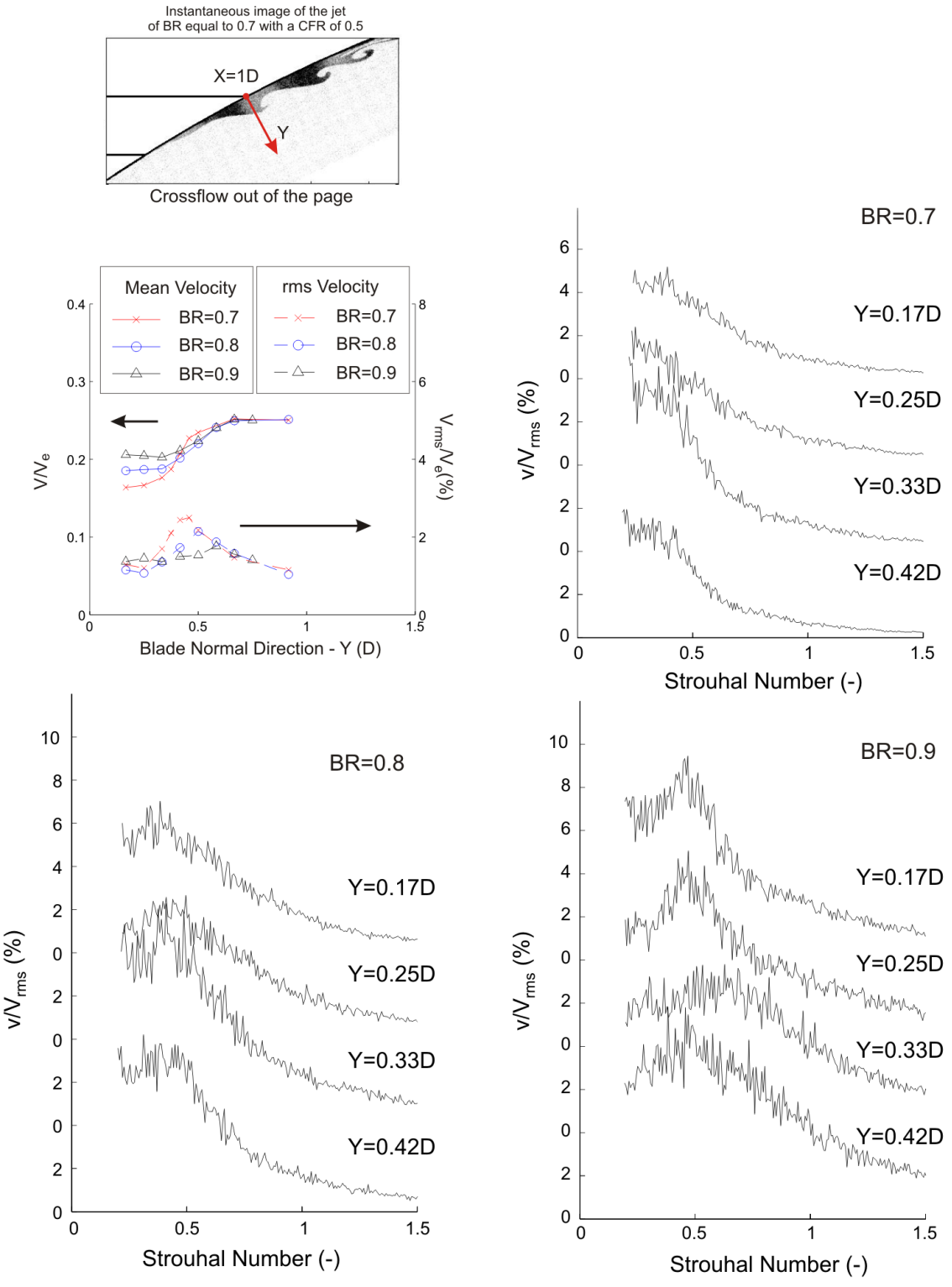

Figure 7.14: Frequency spectra 1D downstream of the hole exit for a jet from the cylindrical hole of BR in the range of 0.7 to 0.9 with a CFR of 0.1. Obtained using Hot Wire Anemometry, the instantaneous image was recorded using high speed photography.

velocity profile, it is seen that these locations are either in the jet core or the part of the shear layer close to the jet core. The coherent unsteadiness of the largest amplitude at Y equal to 0.25D has a coherent turbulence intensity of close to 2% at both BR equal to 0.8 and 0.9. No coherent unsteadiness is seen to occur outside these locations. The Strouhal number of the coherent unsteadiness is close to 0.5, which is the same as that of the coherent unsteadiness shown previously in Fig. 7.13 to be present upstream.

The maximum amplitude of coherent unsteadiness, compared to the local rms velocity, is shown in Fig. 7.14 to have decreased compared to the amplitude of coherent unsteadiness 0D downstream. Additionally the frequency spectra in Fig. 7.14 show no coherent unsteadiness to be present in the jet of BR equal to 0.7. This decrease in coherent unsteadiness across all three BR, might occur due to mixing with the mainstream or the trajectory of the jet being such that the coherent unsteadiness moves out of the midspan plane.

The image sequences shown in Fig. 7.11 show that hairpin vortices are present in the jet from the cylindrical hole for a BR of 0.7 at CFR greater than 0.1. The local peak frequency of unsteadiness with a CFR of 0.5 and 0.8, based on the temporal variation in pixel intensity, is shown in Fig. 7.15. Here the region with a constant Strouhal number of 0.7 in Fig. 7.15, corresponds to the location of the observed hairpin vortices. The image sequences, from which the frequency profiles shown in Fig. 7.15 have been calculated were 550ms in length. From these images the propagation velocity of the hairpin vortices, used in Eq. 4.10 to calculate the Strouhal number, was estimated to be 0.15 times the cascade exit velocity.

Figures 7.13 and 7.14 have shown that the coherent unsteadiness in the jet downstream of the cylindrical hole with a CFR of 0.1, has a Strouhal number of 0.5. This is lower than the frequency calculated for the passing of the hairpin vortices shown in Fig. 7.11. In the previous section it was shown that the measured Strouhal number of the shear layer vortices changes with the crossflow velocity. It is likely that this may also be the case for the hairpin vortices as well, and so the coherent unsteadiness with a CFR equal to 0.1 is likely to also indicate the passing of hairpin vortices.

In Chapter 6 it was proposed that hairpin vortices are formed, like the shear layer vortices seen at larger BR, due to shear between the jet and the mainstream. However, the frequency spectra shown in Fig. 7.13 and the image sequences in Fig. 7.11, suggest that the

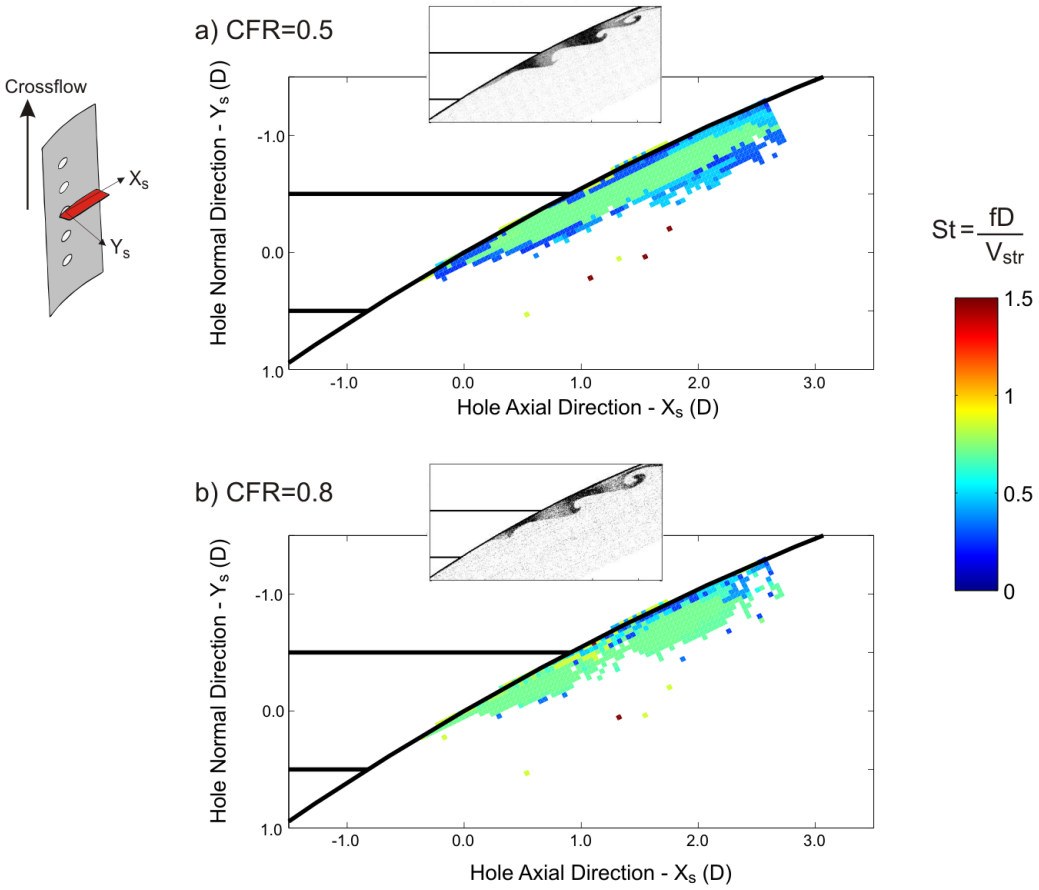

Figure 7.15: Local peak frequency of unsteadiness in the spanwise plane at midspan for a jet of BR equal to 0.7 with (a) a CFR of 0.5 and (b) a CFR of 0.8 from the cylindrical hole. Based on images recorded with high speed photography.

hairpin vortices begin to form before the jet has exited the cooling hole. Assuming that the shear hypothesis is correct, this suggests that either mainstream fluid is being entrained at the leading edge of the cooling hole or a velocity profile is developing inside the cooling hole.

The results shown in Chapter 6 did not show any evidence for the existence of hairpin vortices in the jet from the plenum fed cylindrical hole in the range of BR investigated. However, the results shown in this section show that the hairpin vortices are present for the cylindrical hole with crossflow at a BR close to 0.7. In addition to the introduction of crossflow, this change may also depend on the reduction in the inlet inclination angle to 30°. The observed formation of hairpin vortices at a BR at which they were not seen previously, could be due to a change in the velocity gradient within the jet caused by a different in-hole velocity profile.

7.3.2 Shaped Hole

In Chapter 6 it has been shown that hairpin vortices arise in a jet of BR equal to 0.5 from the shaped hole fed from a plenum chamber. Hairpin vortices are also present in the jet from the shaped hole with crossflow, as shown from the images obtained with high speed photography in Fig. 7.16 for a BR equal to 0.9 with a CFR of 0.1. In the sequence of images on the left the anti-clockwise vortex loops, which indicate the presence of hairpin vortices, are shown in the spanwise plane. As in the jet from the cylindrical hole, shown in Fig. 7.11, the hairpin vortices in the jet from the shaped hole also appear to form upstream of the hole exit plane.

The right hand sequence in Fig. 7.16 shows the passing of a hairpin vortex through the secondary flow plane 2D downstream. As with previous image sequences in Fig. 6.16 and 7.12, the leading face of the vortex is seen first at 2ms. The hairpin vortex then aligns into the streamwise direction at 4ms, and contracts down onto the blade surface at 12ms.

Figure 7.17 is of the same arrangement as Fig. 7.13 and 7.14, and shows the variation in coherent unsteadiness along a blade normal (Y) traverse at midspan 0D downstream. Jets of BR equal to 0.9, 1.0 and 1.2 from the shaped hole are shown. The time-mean velocity profile, included in Fig. 7.17, shows these BR to have a similar velocity difference across the shear layer between the jet and the mainstream as for jets with a BR of 0.7 to 0.9 from the cylindrical hole. Figure 7.17 also shows that raising the BR from 0.9 to 1.2 leads to a doubling of the rms velocity in the jet core.

The frequency spectra shown in Fig. 7.17 are for Y locations at which coherent unsteadiness is seen to be present. The largest amplitude of coherent unsteadiness relative to the local rms velocity is at Y equal to 0.25D. At this location the coherent unsteadiness intensity, defined in Eq. 4.14, shows the amplitude of the broadband coherent unsteadiness to 3% of the time-mean velocity for a BR equal to 0.9 and 5% for a BR equal to 1.0.

The locations shown in Fig. 7.17 where coherent unsteadiness is present are all in the shear layer between the jet and the mainstream. This contrasts with the case of the cylindrical hole, where the coherent unsteadiness is predominantly found in the jet core. The coherent unsteadiness has a Strouhal number of 0.5, which is the same as within the jet from the cylindrical hole shown in Fig. 7.13. Frequency spectra obtained for points upon blade normal traverses with origins 0.25D above and below the midspan, showed no coherent

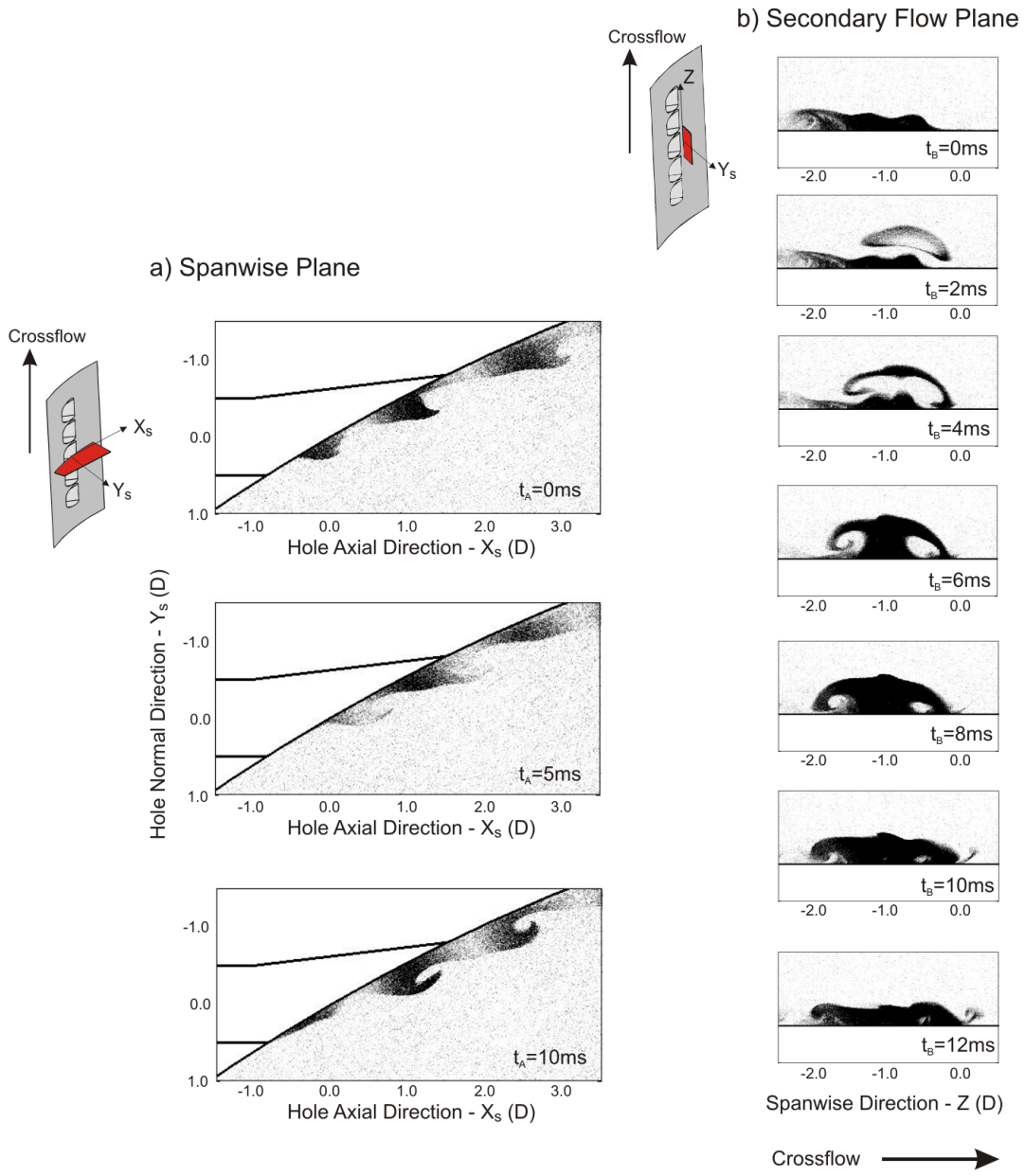

Figure 7.16: Image sequences recorded in (a) the spanwise plane 0.5D below midspan and (b) the secondary flow plane 2D downstream, showing the passage of hairpin vortices in a jet of BR equal to 0.9 from the shaped hole with a CFR of 0.1.

unsteadiness to be present.

The Strouhal number of the passing of the hairpin vortices, shown in Fig. 7.16, in the jet of BR equal to 0.9 with a CFR of 0.1 is calculated to be 0.6. This is based on the temporal variation in pixel intensity through a 550ms long sequence of images. The coherent unsteadiness shown in the frequency spectra of Fig. 7.17 has a Strouhal number of 0.5, and so it is suspected that it is caused by the passing of hairpin vortices.

Figure 7.18 shows a sequence of images, recorded with high speed photography, in the spanwise plane 0.5D above midspan for a jet of BR equal to 1.1 with a CFR of 0.6. This spanwise plane, as can be seen on referring to Fig. 7.5, intersects the part of the split jet at this CFR which leaves from the upper spanwise edge of the shaped hole. The images in Fig. 7.18 show the passage of the anti-clockwise vortices which are indicative of hairpin vortices. Although the hairpin vortices were seen regularly in this spanwise plane, the spacing between them varies such that no frequency of coherent unsteadiness could be obtained based on the temporal variation in pixel intensity. Instead a Strouhal number of 1.0 has been estimated based on the spacing of the hairpin vortices in Fig. 7.18.

Two image sequences of the jet of BR equal to 1.1 with a CFR of 0.6 in the secondary flow plane 2D downstream are shown in Fig. 7.19. The upper spanwise part of the split jet is located at a spanwise location of approximately 0.5D and the lower spanwise part at approximately -1.5D. In the left hand sequence of images the passage of a hairpin vortex within the upper spanwise part of the jet is shown. The features of the hairpin vortex are the same as those shown in Fig 7.12 and 7.16, with its leading face seen at 0ms, by 2ms it is aligned in the streamwise axis and by 6ms it is shown to collapse onto the blade surface. The right hand sequence in Fig. 7.19 shows that it is occasionally seen that hairpin vortices pass through both the upper and lower spanwise parts of the jet simultaneously.

Based on the Strouhal number of 1.0, estimated for the passage of hairpin vortices in the spanwise plane, the time between consecutive hairpin vortices is 7ms. This time is consistent with the time period for the passage of hairpin vortices in the secondary flow plane shown in Fig. 7.19.

In Chapter 6 it was shown that hairpin vortices are present in the jet of BR equal to 0.5 from the shaped hole fed from a plenum. In this section, as for the cylindrical hole, it is seen that hairpin vortices form, with varying crossflow velocity at the hole inlet, for

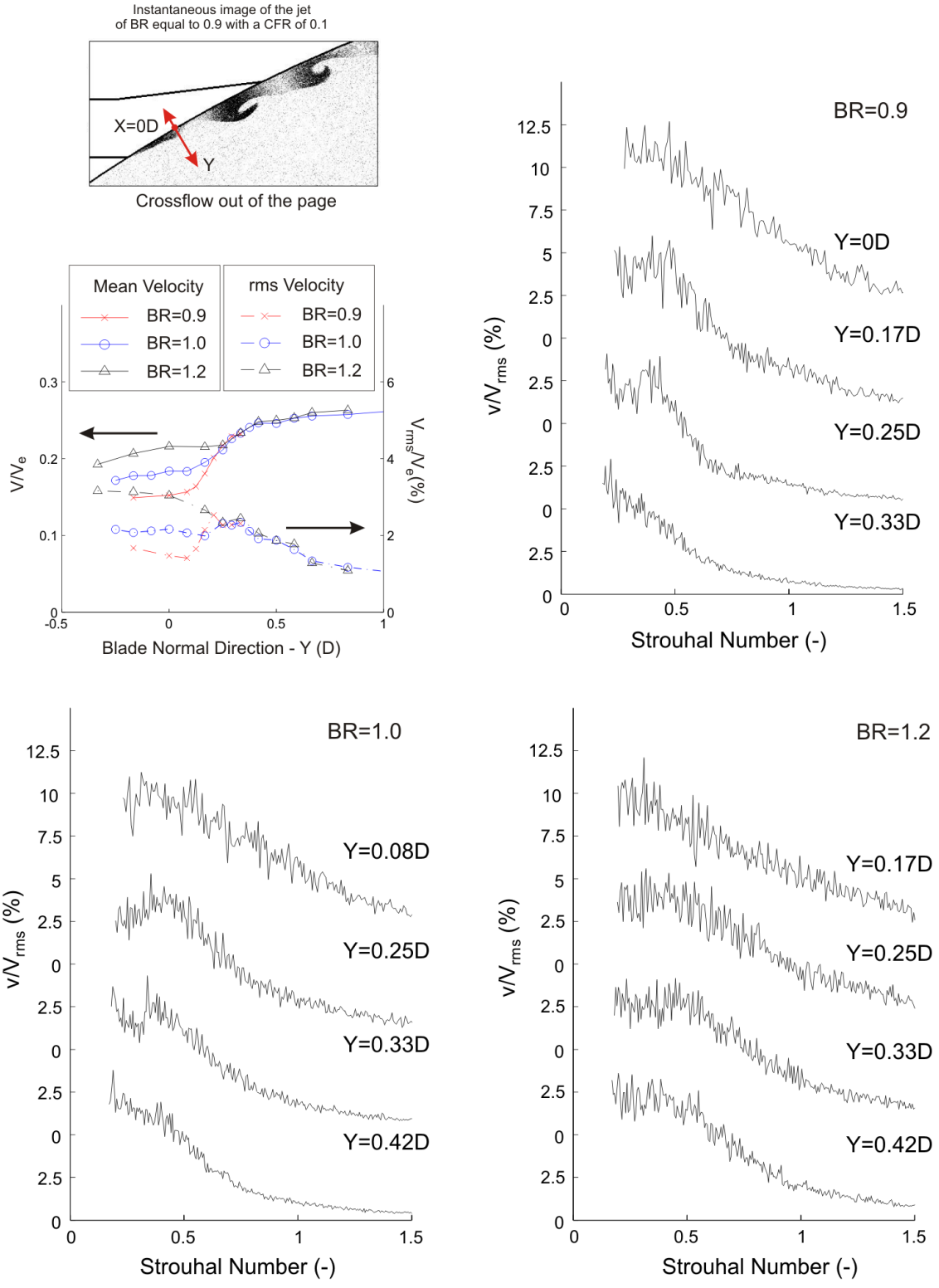

Figure 7.17: Frequency spectra 0D downstream of the hole exit for a jet from the shaped hole of BR in the range of 0.9 to 1.2 with a CFR of 0.1. Obtained using Hot Wire Anemometry, the instantaneous image was recorded using high speed photography.

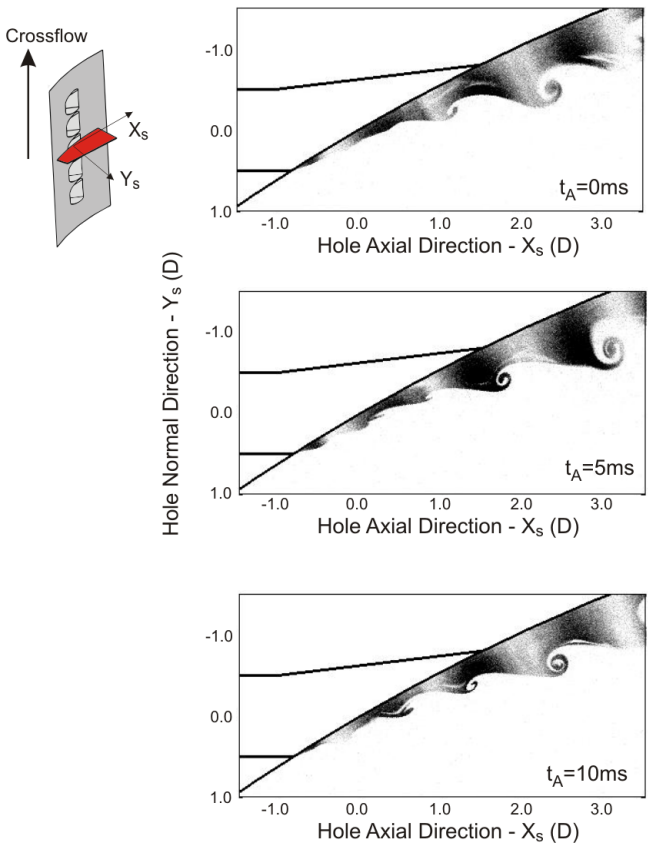

Figure 7.18: Hairpin vortices in the spanwise plane 0.5D above midspan for a jet from the shaped hole of BR equal to 1.1 with a CFR of 0.6. Images obtained with high speed photography.

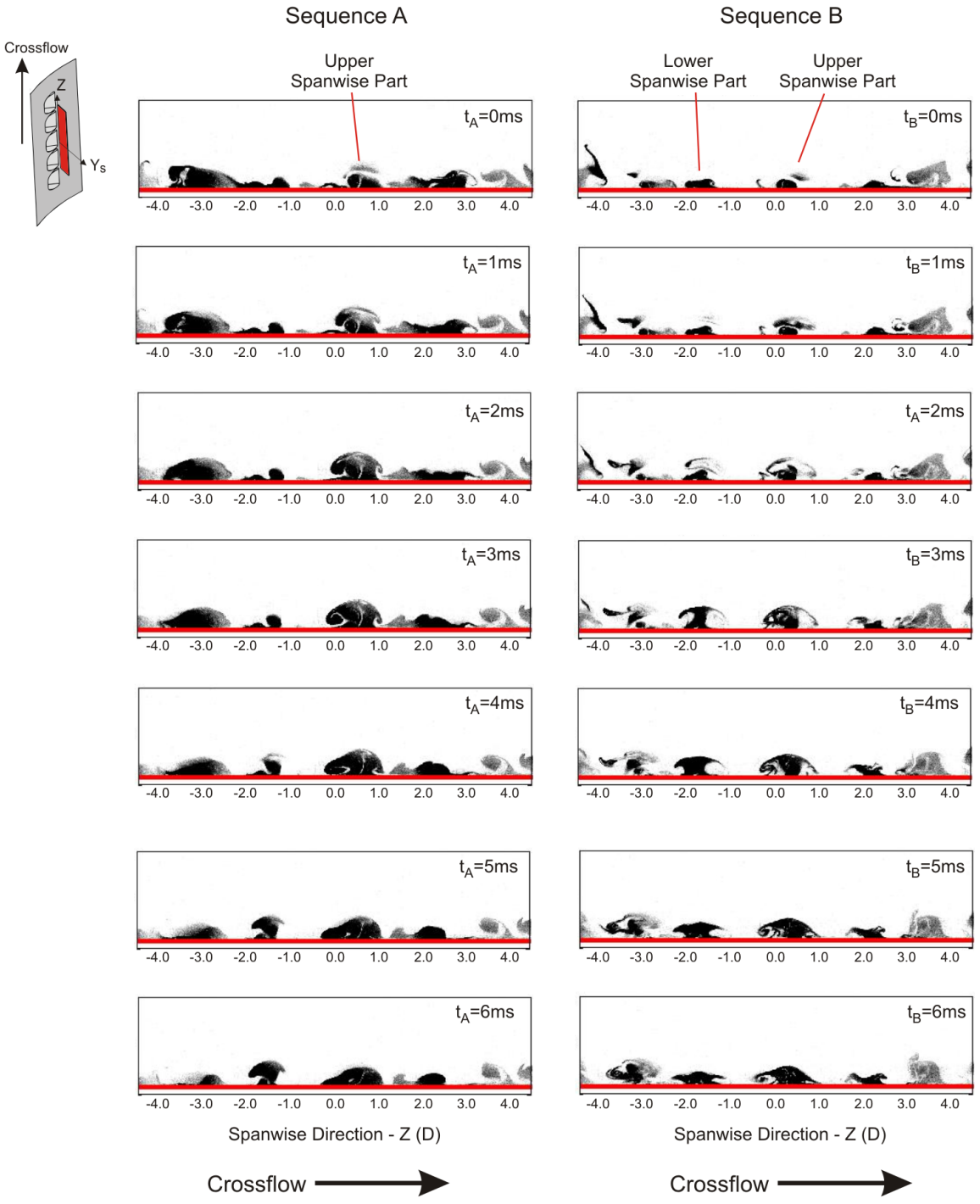

Figure 7.19: Passage of the hairpin vortices through the secondary flow plane 2D downstream for a jet from the shaped hole of BR equal to 1.1 with a CFR of 0.6. Images obtained with high speed photography.

blowing ratios at which hairpin vortices are not present for the 'idealised' configuration of Chapter 6.

Hairpin vortices are seen in this section, to form in a jet of higher BR with the shaped hole than for the cylindrical hole. As described in Chapter 3, the BR is based on the throat area of the cooling hole. Thus, for the same BR, the expanding exit of the shaped hole means that the velocity at the hole exit will be lower than that at the exit of the cylindrical hole.

7.4 Conclusions

In this chapter the impact of an internal perpendicular crossflow, referred to within this chapter solely as 'crossflow', on the jet downstream of the cylindrical and shaped holes is described. For both hole geometries it is shown that changes arise in the time-mean flowfield and that coherent unsteady structures are present within the jet.

The ratio of the crossflow velocity to that of the coolant bulk velocity is seen to influence the time-mean profile of the jet. The jet from the cylindrical hole is seen to rotate around the jet axis. With the shaped hole it is seen that the jet becomes biased to different edges of the hole exit. Comparing these observations with the experimental results of Saumweber and Schulz [89], shows that these changes could have a detrimental impact on film effectiveness for the shaped hole, but a beneficial impact for the cylindrical hole.

Coherent shear layer vortices and hairpin vortices are seen in the jet downstream of the cooling holes fed with crossflow. These are the same two coherent unsteady structures seen in the jet downstream of the plenum fed cooling holes, which have been introduced in Chapter 6.

Hairpin vortices occur in the jet from the cylindrical hole for a BR close to 0.7. For the shaped hole the expansion of the hole exit means that hairpin vortices occur at a slightly larger BR. At neither of these BR are hairpin vortices seen in the jet from the equivalent plenum fed hole. The hairpin vortices are coherent with a Strouhal number in the range of 0.5 to 0.7 for minimal crossflow velocity at the hole inlet. Increasing the crossflow velocity does not appear to inhibit the formation of hairpin vortices, despite the changes in the time-mean jet profile. However, there is some variation in the Strouhal number with changing the crossflow velocity.

Shear layer vortices are seen in the jet downstream of the cylindrical hole for BR of 1.6 and 1.8, and have a Strouhal number close to 1.0. They are seen at crossflow velocities of up to 0.6 times the bulk velocity through the hole. Shear layer vortices are not present in the jet from the shaped hole, unlike for the plenum fed case in Chapter 6.

The greater prevalence of hairpin vortices and the change in the time-mean profile compared to the 'idealised' case in Chapter 6, are suspected to arise due to a change in the in-hole flowfield. Additionally it is apparent that the hairpin vortices may begin to form upstream of the hole exit.

Chapter 8

Coherent Unsteadiness Inside the Cooling Hole

In Chapter 7 it was shown that changing the cooling hole inlet inclination angle and the magnitude of the internal crossflow, affected both the presence of hairpin vortices and the time-mean flowfield. In this chapter the flowfield inside the cooling hole is investigated for changes in the perpendicular crossflow at the hole inlet. The aim being to ascertain if any coherent unsteadiness occurs inside the cooling hole and how it is affected by changes in the perpendicular crossflow velocity.

The results presented here were obtained experimentally using Hot Wire Anemometry. They were obtained with the Oxford Super Scale Cascade configured, as in Chapter 7, with the perpendicular (spanwise) crossflow channel at the cooling hole inlet. First the baseline case with a minimal perpendicular crossflow is shown. This is then followed by the cases with a higher perpendicular crossflow velocity. As in Chapter 7 the term 'crossflow' in this chapter refers solely to 'perpendicular crossflow.'

8.1 Minimal Crossflow Velocity

8.1.1 Cylindrical Hole

The minimal crossflow case corresponds to a CFR of 0.1, in which all of the coolant in the crossflow channel exits through the five cooling holes. Frequency spectra, obtained using HWA, of the velocity fluctuations on the plane at S equal to 4.5D are shown in Fig. 8.1 for

the cylindrical hole. Here it is reminded that S refers to the distance upstream of the hole exit. Figure 8.3 shows frequency spectra across a blowing ratio (BR) range of 0.7 to 1.8, on the hole centreline and 0.25D above and below the centreline. It should be reminded here that geometric constraints mean that the axis of the hot wire probe, as shown in Fig. 4.22, is aligned at 20° to the spanwise direction.

The frequency spectrum on the hole centreline in Fig. 8.1 for a BR of 1.8, shows the presence of coherent unsteadiness with a Strouhal number of approximately 1.1. This coherent unsteadiness has an amplitude of 7% of the rms velocity. On decreasing the BR to 1.5, Fig. 8.1 shows no coherent unsteadiness to be present. However, on decreasing the blowing ratio further to a BR of 1.2, Fig. 8.1 shows that, as at a BR of 1.8, there is coherent unsteadiness with a Strouhal number of 1.1. At a BR of 1.0 the Strouhal number of the coherent unsteadiness has increased to 1.2, with its amplitude being 10% of the rms velocity. At this BR, the frequency spectrum also shows there to be coherent unsteadiness of a smaller amplitude. This lower amplitude peak has a Strouhal number of approximately 0.6. On lowering the BR to 0.8, it is seen that there are also two frequency peaks associated with coherent unsteadiness, but that the one at the lower Strouhal number now has the larger amplitude. At a BR equal to 0.7 coherent unsteadiness is only present with a Strouhal number of 0.7.

The coherent unsteadiness on the centreline in Fig. 8.1, and in the subsequent locations in this chapter, causes a broadband peak in the frequency spectra. Previously the coherent unsteadiness intensity has been defined in Eq. 4.14 to relate the velocity fluctuations due to broadband coherent unsteadiness to the local mean velocity. Here the coherent unsteadiness intensity is found to be in the range of 2% to 5% for the coherent unsteadiness shown in Fig. 8.1 on the hole centreline.

Frequency spectra are also shown in Fig. 8.1 for the points 0.25D above and below the centreline. It is seen that these spectra show a similar trend, in regard to the change in the frequency of coherent unsteadiness with BR, to that seen on the centreline. The amplitude of the coherent unsteadiness present 0.25D above and below the centreline is noticeably lower relative to the rms velocity than that on the centreline.

The frequency spectra shown in Fig. 8.2 are for the variation with BR on the hole centreline at S equal to 2.0D. In comparison with those for points at S equal to 4.5D

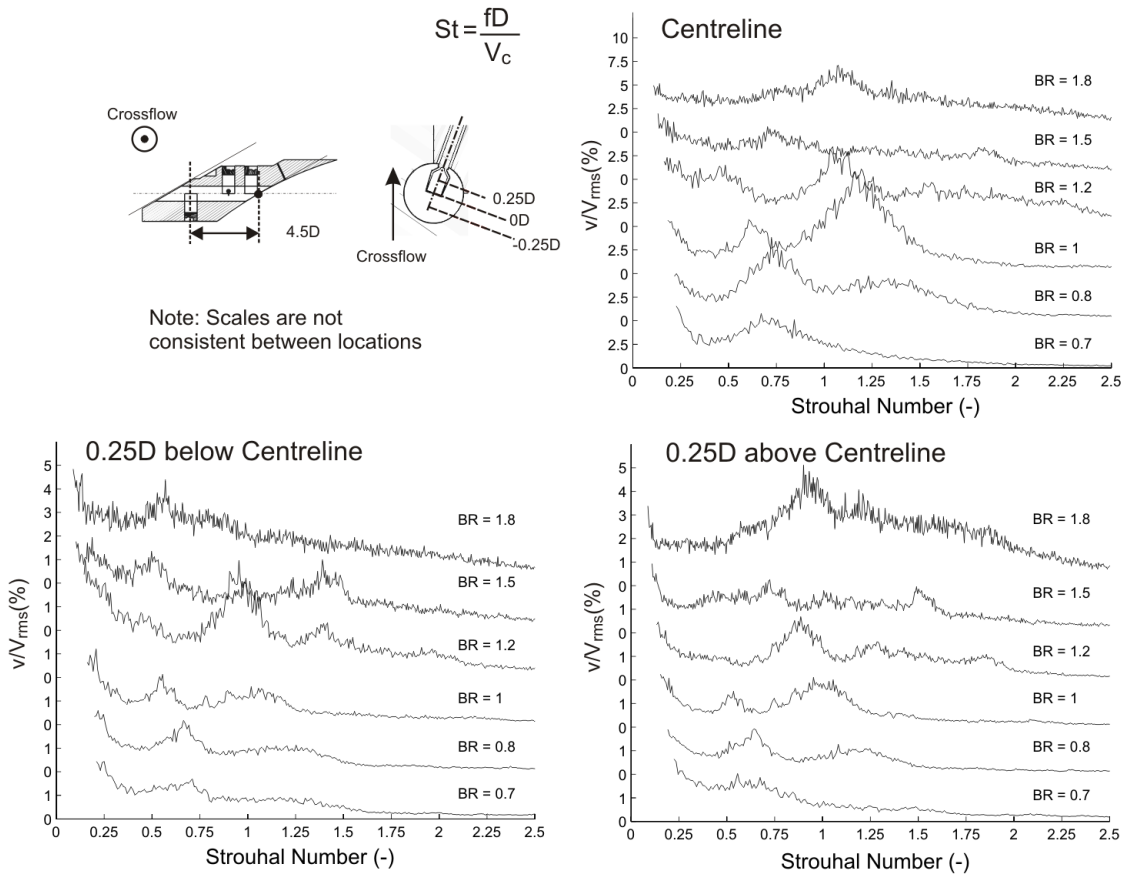

Figure 8.1: Frequency spectra on the hole centreline and 0.25D above and below it, at S equal to 4.5D for the cylindrical hole with a CFR of 0.1. Obtained using HWA.

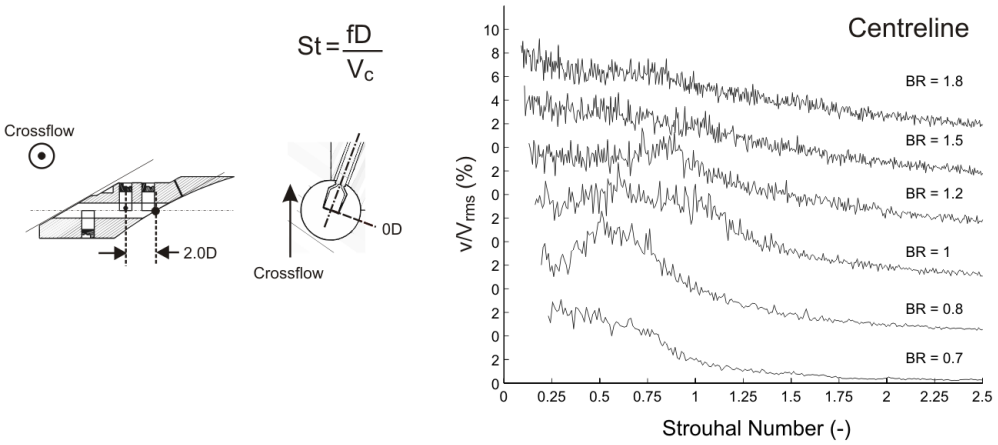

Figure 8.2: Frequency spectra on the centreline, at S equal to 2.0D for the cylindrical hole with a CFR of 0.1. Obtained using HWA.

(shown in Fig. 8.1), it is apparent that there are fewer occurrences of coherent unsteadiness in the frequency spectra in Fig. 8.2. Coherent unsteadiness with a Strouhal number of 0.8 is seen to be present for a BR of 1.2. Whilst coherent unsteadiness with a Strouhal number in the range of 0.5 to 0.7 occurs for a BR of 0.8. At a BR of 1.0 there appears to be a wide peak of coherent unsteadiness which covers a Strouhal number range of 0.5 to 1.2.

Figure 8.3 shows frequency spectra for points at S equal to 0.5D on the centreline and 0.25D above and below the centreline. Across the three points coherent unsteadiness is only seen for a BR equal to 1.0 and lower. On the centreline the coherent unsteadiness is seen to have a Strouhal number of 0.6 for BR of 0.7 and 0.8. Below the centreline the coherent unsteadiness has a Strouhal number of 0.7 across a BR range from 0.7 to 0.9. Above the centreline coherent unsteadiness is seen for a BR of 0.9 and 1.0 with a Strouhal number of 0.5. Across the three measurement locations shown in Fig. 8.3 the Strouhal number of the coherent unsteadiness is seen to be reasonably constant. However, the variation in the BR at which coherent unsteadiness occurs shows that its position is sensitive to the blowing ratio.

Chapter 7 shows coherent hairpin vortices to be present in the jet downstream of the cylindrical hole for a BR range of 0.7 to 0.9 with a crossflow of CFR equal to 0.1. These have, 1D downstream of the hole exit, a Strouhal number of 0.5. The Strouhal number and the range of BR for which hairpin vortices are present, is therefore similar to that of the coherent unsteadiness that is seen to be present at each of the in-hole measurement planes.

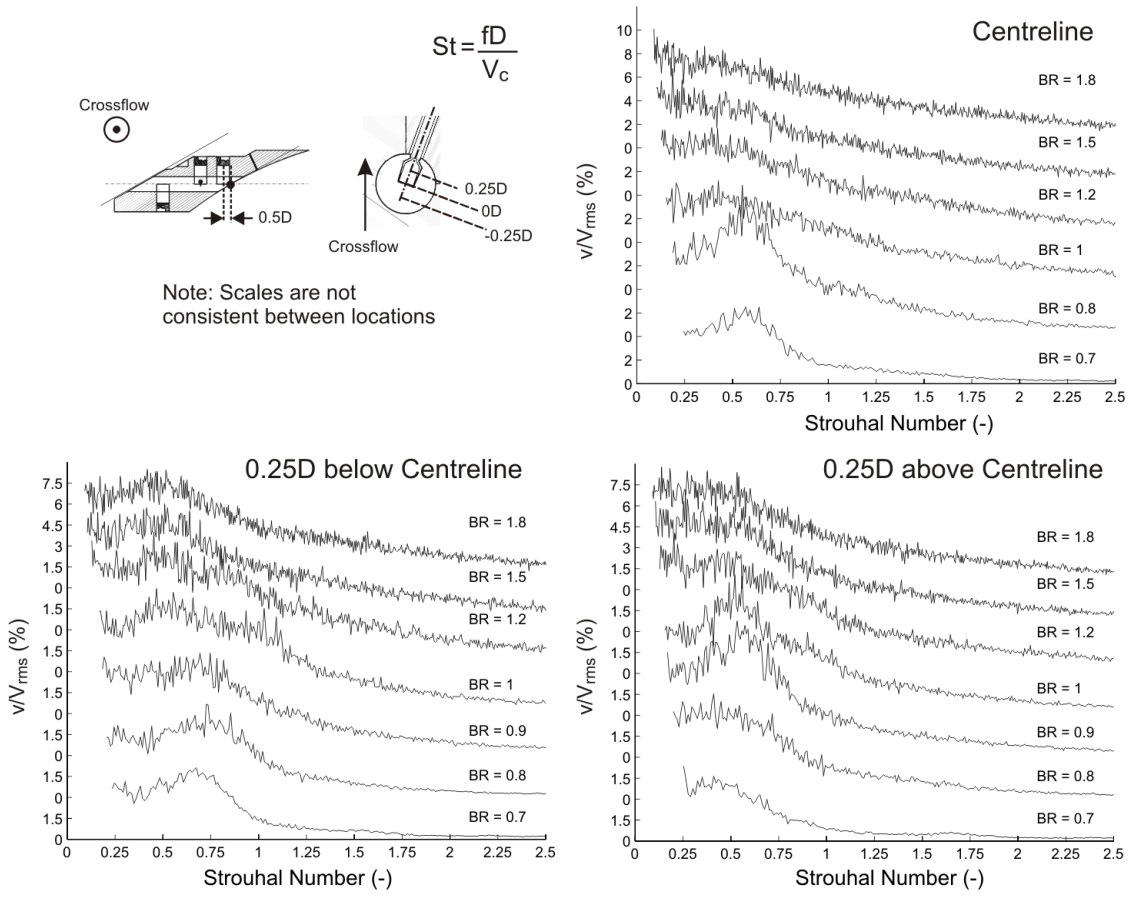

Figure 8.3: Frequency spectra on the hole centreline and 0.25D above and below it, at S equal to 0.5D for the cylindrical hole with a CFR of 0.1. Obtained using HWA.

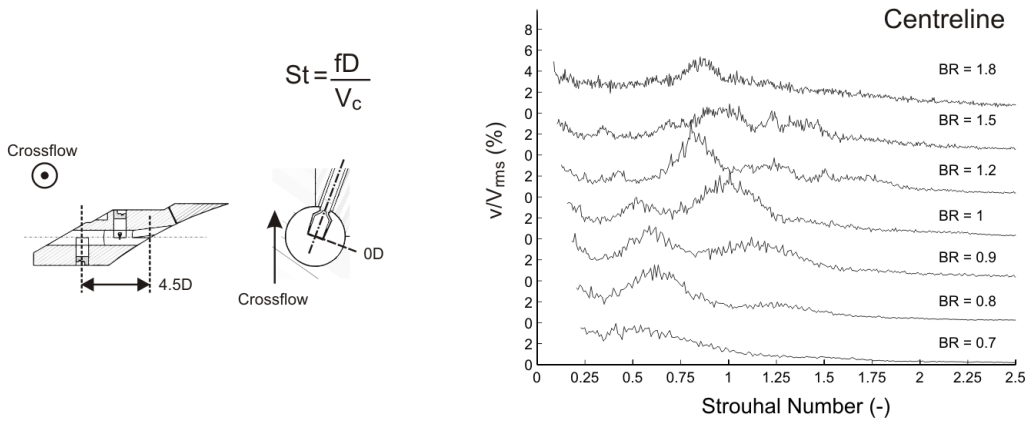

Figure 8.4: Frequency spectra on the centreline, at S equal to 4.5D for the shaped hole with a CFR of 0.1. Obtained using HWA.

This suggests that there may be a link between the two coherent unsteady features.

8.1.2 Shaped Hole

Frequency spectra obtained on the centreline at S equal to 4.5D in the shaped hole are shown in Fig. 8.4. Coherent unsteadiness with a Strouhal number of 0.9 is present at the highest BR of 1.8, whilst at a BR of 1.2 coherent unsteadiness is seen with a Strouhal number of 0.8. At a BR of 1.0, coherent unsteadiness, as is the case inside the cylindrical hole, is present at two different Strouhal numbers. On decreasing the BR to 0.8, coherent unsteadiness is seen only for a Strouhal number of approximately 0.6. The coherent unsteadiness intensity is found to be approximately 2% for the coherent unsteadiness at BR of 0.8 and 1.2 in Fig. 8.4.

The change in coherent unsteadiness with BR shown in Fig. 8.4, is broadly the same as that seen previously within the cylindrical hole at the same location. The expansion of the shaped hole does not begin until downstream of this location, and so the cross-section of the two cooling holes is the same. The similarity in the presence of coherent unsteadiness possibly indicates that the inlet velocity profile is common across both hole geometries.

With distance along the shaped hole, as is the case for the cylindrical hole, the coherent unsteadiness at higher blowing ratios appears to decay. This is apparent in Fig. 8.5, with coherent unsteadiness present only for BR less than 1.2 in the frequency spectra at S equal to 2D. Of the three locations shown, coherent unsteadiness is present only at those locations

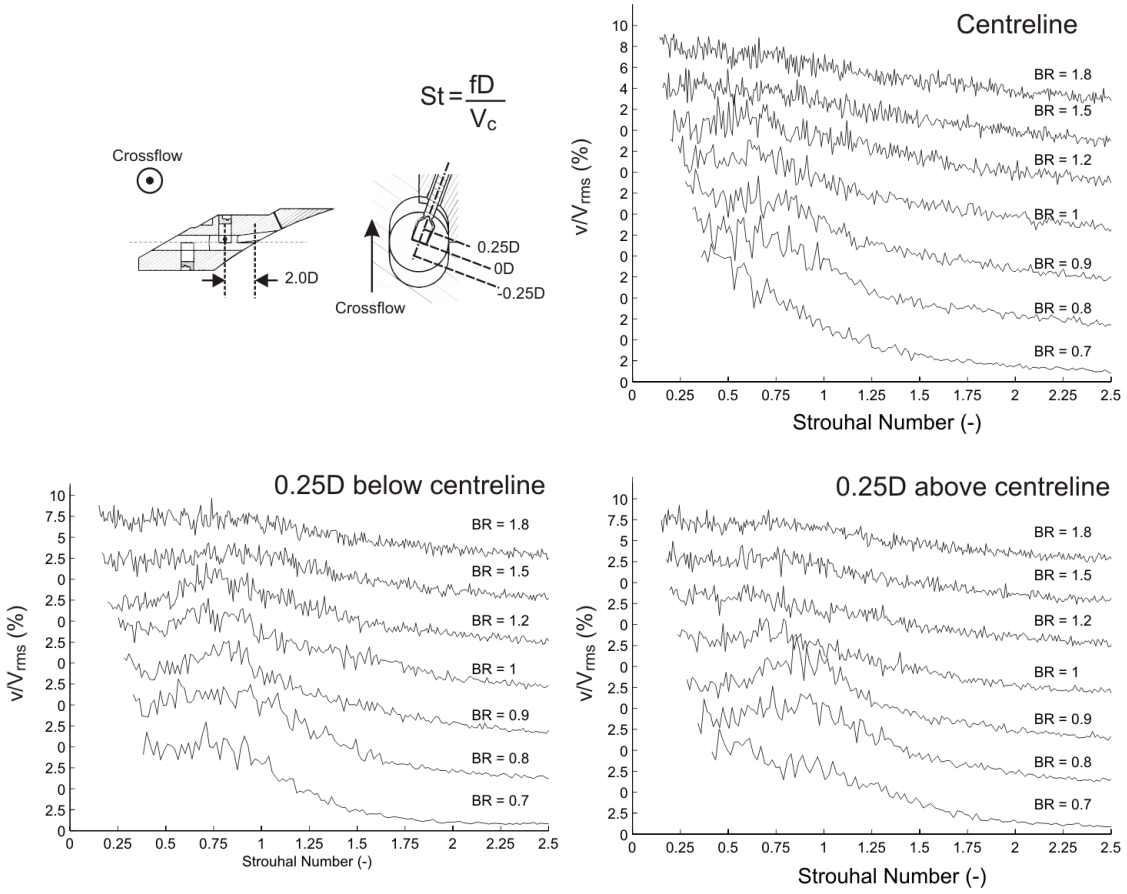

Figure 8.5: Frequency spectra on the centreline, at S equal to 2.0D for the shaped hole with a CFR of 0.1. Obtained using HWA.

0.25D above and below the centreline.

Above the centreline, coherent unsteadiness is present for BR of 0.8 and 0.9 with a Strouhal number of 0.9. Below the centreline coherent unsteadiness is present, with a Strouhal number of 0.8, for BR of 0.8 through to 1.2. This variation in the BR at which coherent unsteadiness is seen, suggests that close to the hole exit the position of the coherent unsteadiness within the hole, like for the cylindrical hole, is sensitive to the BR.

The hairpin vortices, seen in Chapter 7 to be present in the downstream jet, occur for a BR range of 0.9 to 1.2, and have a Strouhal number of 0.5 in the plane 0D downstream of the hole exit. The coherent unsteadiness in the plane at S equal to 2.0D shows coherent unsteadiness across a similar range of blowing ratios. The Strouhal number of the in-hole coherent unsteadiness is also similar to that in the downstream jet. This suggests that, as with the cylindrical hole shown earlier in this chapter, there may be a link between the in-hole coherent unsteadiness and that in the downstream jet.

Within this chapter the frequency of the in-hole coherent unsteadiness has been non-dimensionalised to form a Strouhal number. On the plane at S equal to 4.5D, Figs. 8.1 and 8.4 have shown the Strouhal number of the coherent unsteadiness to vary with blowing ratio. If however the frequency is considered, instead of the Strouhal number, then the coherent unsteadiness is seen to have a frequency of either 70Hz, 140Hz or 210Hz.

The variation in the frequency of the coherent unsteadiness with blowing ratio and distance along the hole length is shown in Fig. 8.6 for both hole geometries and a CFR of 0.1. No distinction is made in Fig. 8.6 between the three possible locations on a measurement plane. In addition to the coherent unsteadiness seen in the frequency spectra shown in this section, Fig. 8.6 includes the coherent unsteadiness seen in additional repeats, and so highlights the repeatability of the observations. A 'run' in Fig. 8.6, refers to a set of measurements made for blowing ratios spread over the range from 0.7 to 1.8.

In Figure 8.6 it is apparent that on the plane at 4.5D coherent unsteadiness can have a frequency of either 70Hz, 140Hz or 210Hz. Which of these frequencies the coherent unsteadiness has depends on the BR. Coherent unsteadiness with a frequency of 210Hz is present at the higher blowing ratios. Coherent unsteadiness with a frequency of 140Hz is seen across the mid-range blowing ratios, whilst coherent unsteadiness at 70Hz occurs at BR lower than 1.2. It is likely that the three frequencies in Fig. 8.6 are harmonics of each other, with that close to 70Hz being the fundamental harmonic. Consequently they have been classified within Fig 8.6 as either the first, second or third harmonic.

Previously in this chapter it has been shown that the coherent unsteadiness at higher BR decays on passing along the cooling hole. Figure 8.6 shows that it is the higher order harmonics that decay with distance along the hole, which means that only coherent unsteadiness at the fundamental harmonic is present on the measurement plane closest to the hole exit.

The trend in Fig. 8.6 suggests that perhaps a flow of constant velocity, such as the mainstream velocity at the hole exit, should be used in the Strouhal number definition. However, for consistency with other chapters the bulk jet velocity will continue to be used to non-dimensionalise the frequency of the coherent unsteadiness.

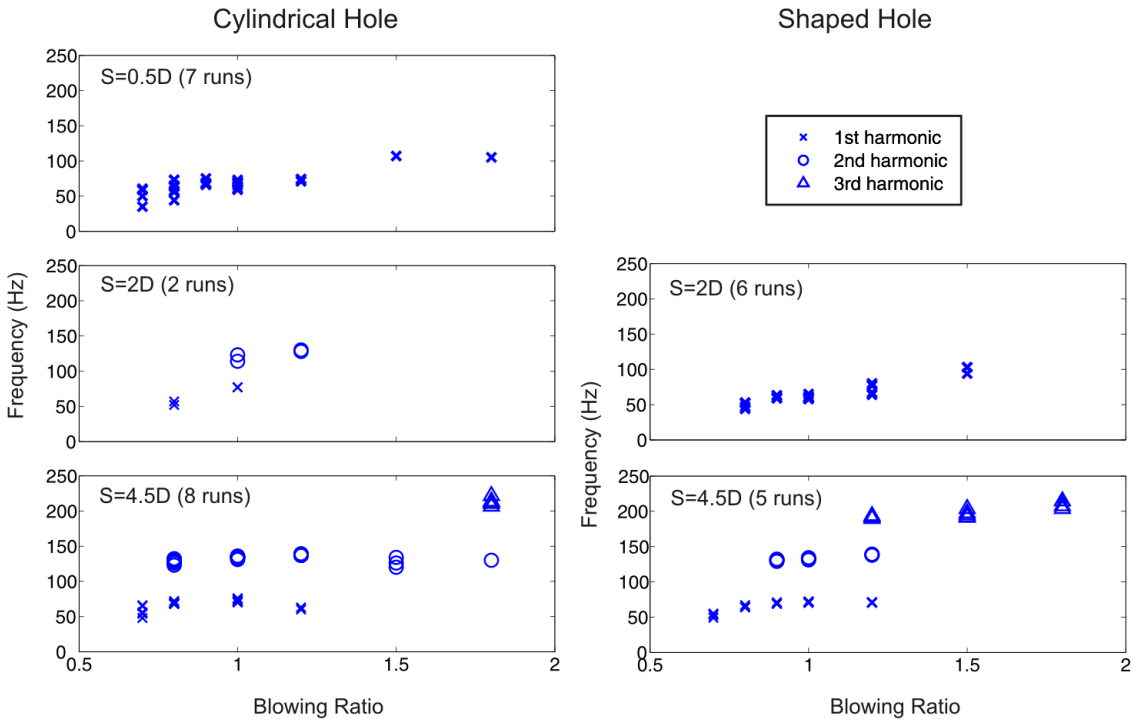

Figure 8.6: Variation of the frequency of coherent unsteadiness inside both the cylindrical and shaped hole with a CFR of 0.1, where S is the distance from the hole exit. Summary of all measurements obtained with HWA.

8.2 Increased Crossflow Velocity

8.2.1 Close to the Hole Inlet

In this section frequency spectra for the same locations as for the case of minimal crossflow are shown, but with an increased crossflow velocity at the cooling hole inlet. Crossflow ratios (CFR) of 0.2 and 0.6 are presented in this section for both cooling holes.

Figure 8.7 shows the frequency spectra at the point on the hole centreline at S equal to 4.5D for a CFR of 0.2. Spectra of the velocity variation within both the cylindrical hole and the shaped hole are shown. In these frequency spectra the reader should ignore the narrow frequency peaks of relatively large amplitude, as these are attributed to noise with a frequency of 50Hz caused by the blower on the out-pipe from the crossflow passage.

In contrast to the case of minimal crossflow, shown in Figs. 8.1 and 8.4 no coherent unsteadiness is seen at a BR of 1.8 in Fig. 8.7. In both the cylindrical and shaped holes coherent unsteadiness at the second harmonic is present for a BR of 0.8 through to 1.0. This has a Strouhal number of approximately 1.0 and a maximum amplitude relative to the rms velocity at a BR of 0.9. The coherent unsteadiness at the second harmonic is also apparent below the centreline for the same range of BR, but of a lower amplitude relative to the rms velocity. The fundamental harmonic is shown in Fig. 8.7 only to be present inside both holes for a BR of 0.8, where it has a Strouhal number of 0.6. The intensity of the coherent unsteadiness at the fundamental harmonic is calculated to be less than 1%, which is lower than that calculated previously for this harmonic when the CFR is equal to 0.1.

Figure 8.8 shows the frequency spectra at the same point on the centreline at S equal to 4.5D upstream of the hole exit as in Fig. 8.7, but for an increased CFR of 0.6 at the hole inlet. In contrast to the lower CFR case, Fig. 8.8 shows that for both the cylindrical and the shaped hole, no coherent unsteadiness is present when the CFR is equal to 0.6 across the BR range of 0.7 to 1.8.

Comparison of Figs. 8.1, 8.4 and 8.7 shows that on increasing the CFR of the crossflow from 0.1 to 0.2, the coherent unsteadiness occurs across a smaller range of BR, and that there is a reduction in the value of the coherent unsteadiness intensity. This trend appears to continue through for a crossflow of CFR equal to 0.6, where no coherent unsteadiness is present on the plane at S equal to 4.5D.

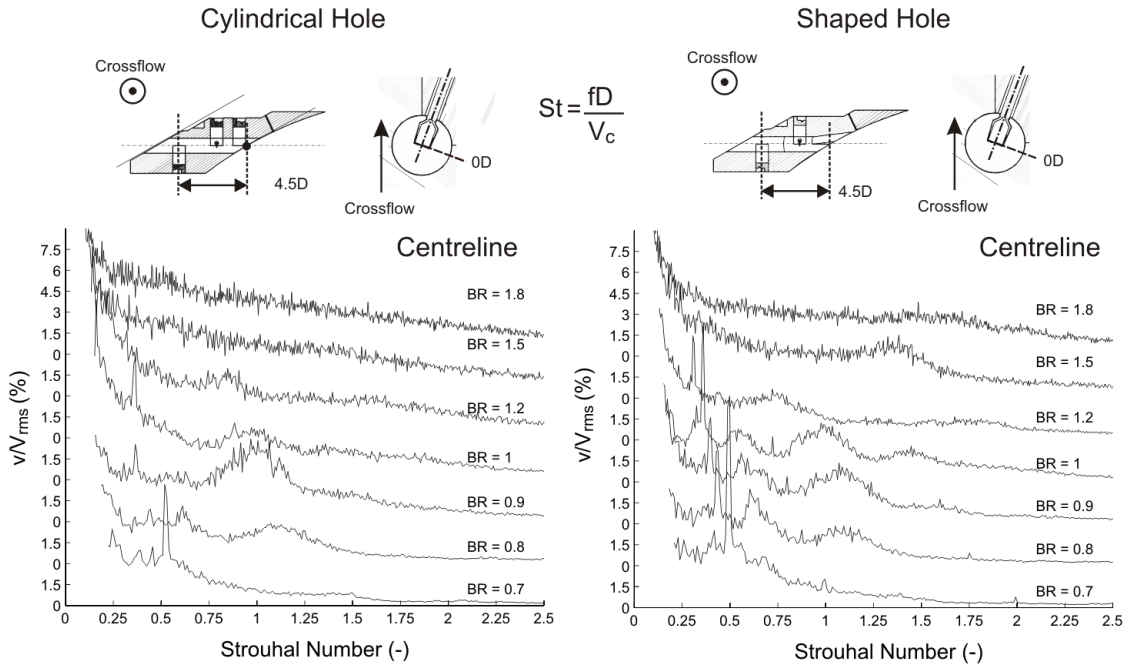

Figure 8.7: Frequency spectra on the centreline, at S equal to 4.5D for both the cylindrical and the shaped hole with a CFR of 0.2. Obtained using HWA.

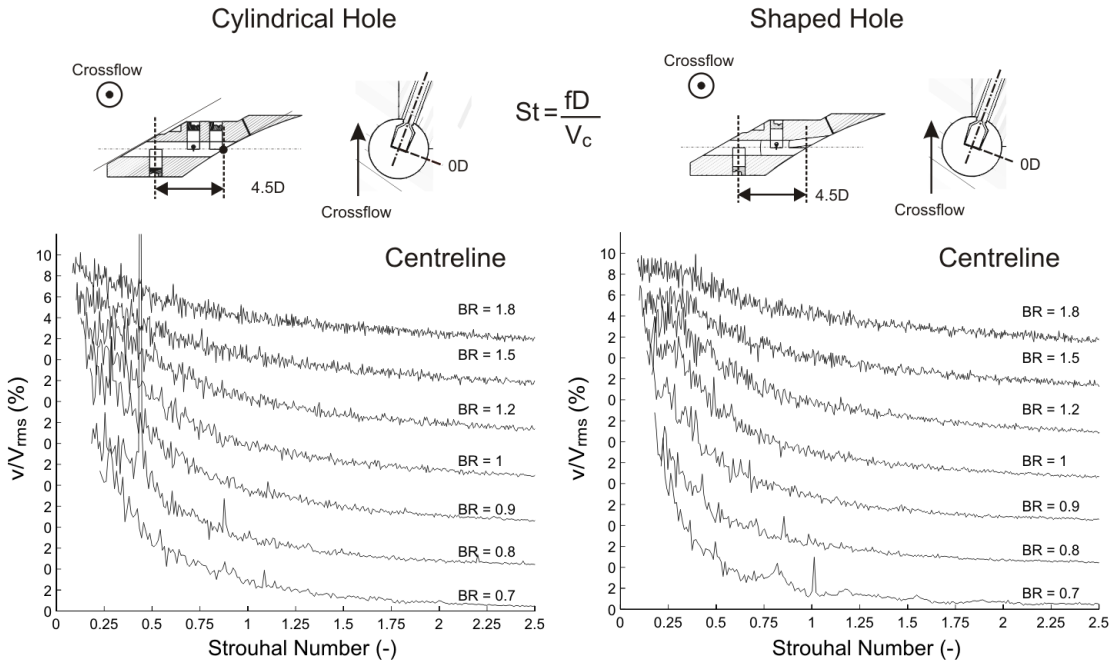

Figure 8.8: Frequency spectra on the centreline, at S equal to 4.5D for both the cylindrical and the shaped hole with a CFR of 0.6. Obtained using HWA.

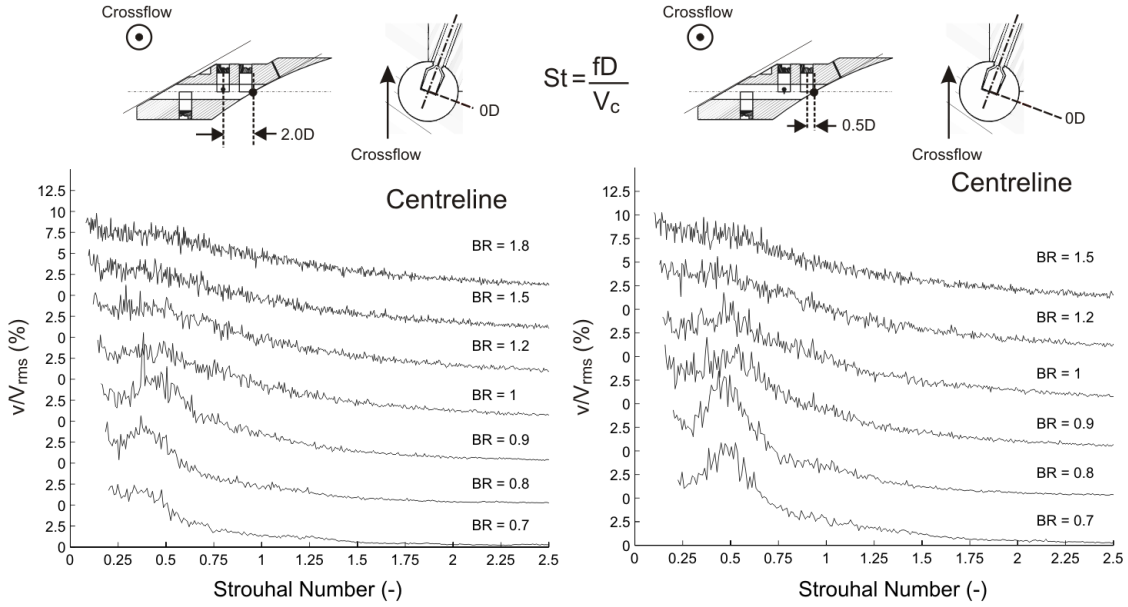

Figure 8.9: Frequency spectra on the centreline, at S equal to 2.0D and 0.5D for the cylindrical hole with a CFR of 0.2. Obtained using HWA.

8.2.2 Close to the Hole Exit

Frequency spectra are shown in Fig. 8.9 for the centreline of the cylindrical hole at S equal to 2.0D and 0.5D. The crossflow at the hole inlet has a CFR of 0.2. The frequency spectra obtained at S equal to 2.0D shows only the presence of coherent unsteadiness at the fundamental harmonic for a BR of 0.8 to 0.9. This has a Strouhal number which increases with BR from 0.4 to 0.5. In comparison, in the plane at S equal to 4.5D, shown in Fig. 8.7, coherent unsteadiness of the second harmonic is seen for a similar BR range.

Figure 8.9 shows, that upon the measurement plane at S equal to 0.5D coherent unsteadiness is present at the fundamental harmonic across a BR range from 0.7 to 1.0. The coherent unsteadiness has a Strouhal number of 0.5 and has a maximum amplitude relative to the rms velocity of greater than 10% for a BR of 0.8 and 0.9.

Spectra obtained 0.25D above the centreline, not included here, do not show the presence of any coherent unsteadiness within the BR range of 0.7 to 1.8. Frequency spectra taken at the point 0.25D below the centreline, also omitted here, show coherent unsteadiness with a Strouhal number of 0.5 at BR of 0.8 and 0.9.

The coherent unsteadiness on the plane at S equal to 2.0D for the shaped hole is shown in Fig. 8.10 for a crossflow of CFR equal to 0.2. Frequency spectra are shown for the point

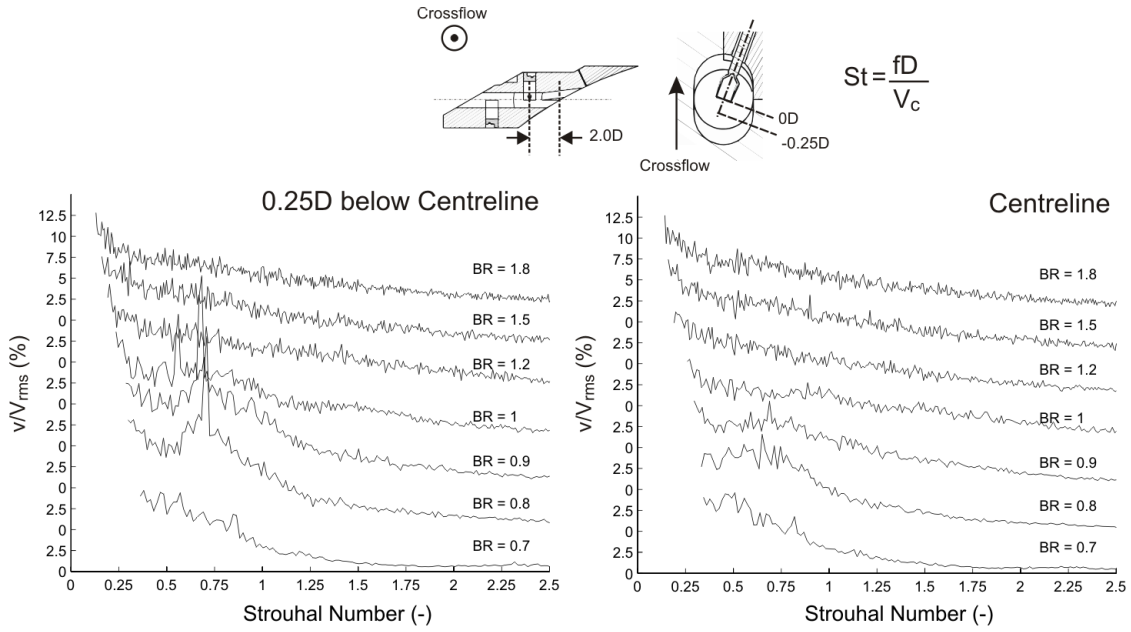

Figure 8.10: Frequency spectra on the centreline and 0.25D below it, at S equal to 2.0D for the shaped hole with a CFR of 0.2. Obtained using HWA.

on the hole centreline. Additionally those for the point 0.25D below the centreline are also shown in Fig. 8.10, as the time-mean pixel intensity in Chapter 7 shows the jet at this CFR to be biased to the lower spanwise edge of the diffuser.

Below the centreline the frequency spectra in Fig. 8.10 show the fundamental harmonic to be present with a Strouhal number of 0.7 for a BR range of 0.8 to 0.9. On the centreline coherent unsteadiness also with a Strouhal number of 0.7 is present for a BR of 0.8. The BR at which coherent unsteadiness is present in the 2.0D plane, is consistent with that of coherent unsteadiness of the second harmonic in the plane at S equal to 4.5D that has been shown in Fig. 8.7. This change in harmonic between the two planes is the same as the trend seen in the cylindrical hole.

It is a concern, that the Strouhal number of the coherent unsteadiness in Fig. 8.10 is often the same as that of the 50Hz noise peak. However, the similarity in the change of coherent unsteadiness with that in the cylindrical hole, in which the coherent unsteadiness had a frequency greater than 50Hz, and the broadband nature of the peaks suggest that they are likely to be independent of the noise source.

With a crossflow of CFR equal to 0.6 at the hole inlet, coherent unsteadiness similar to that seen at lower CFR is not present within the cylindrical hole on the planes at S equal to 2.0D and 0.5D. This is consistent with the lack of coherent unsteadiness on the plane at

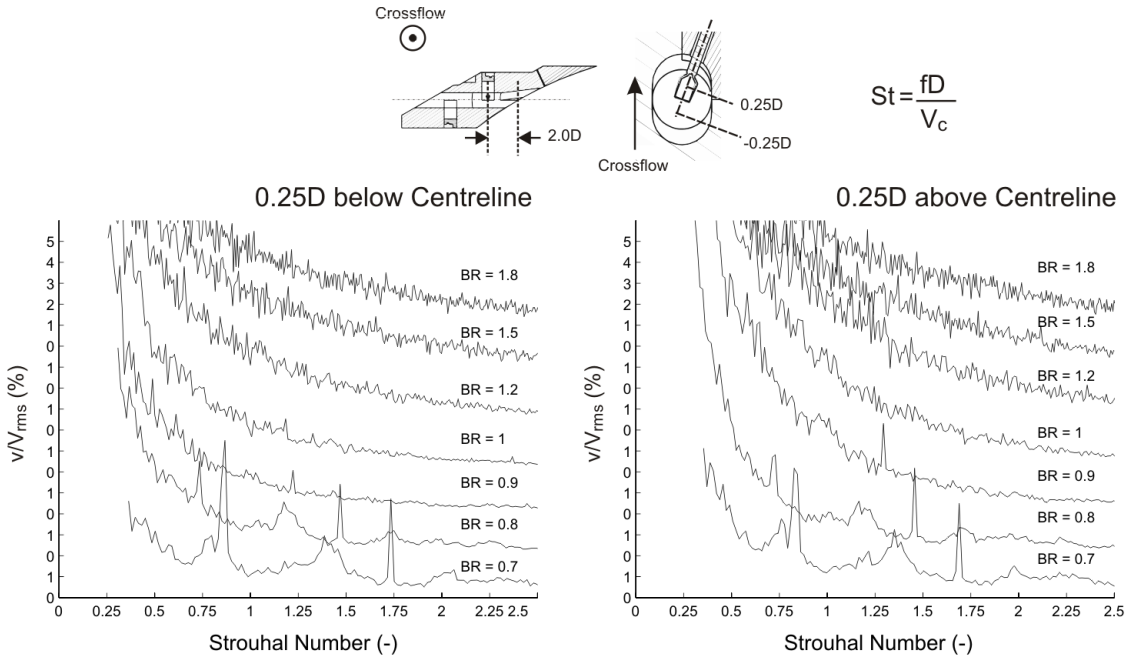

Figure 8.11: Frequency spectra 0.25D above and below the centreline at S equal to 2.0D for the shaped hole with a CFR of 0.6. Obtained using HWA.

S equal to 4.5D, shown previously in Fig. 8.8. Coherent unsteadiness is also not seen inside the shaped hole on the plane at S equal to 2.0D for a crossflow of CFR equal to 0.s6.

There is however, for both cooling hole geometries, coherent unsteadiness present at the lowest BR investigated which does not have a frequency that coincides with that of the harmonics shown in Fig. 8.6. The frequency spectra shown in Fig. 8.11, show this coherent unsteadiness to be present inside the shaped hole for a BR of 0.7 and 0.8. This has a Strouhal number of 1.4 at a BR of 0.7 and 1.2 at a BR of 0.8.

Earlier in this chapter the observation has been made that the Strouhal number of the coherent unsteadiness immediately upstream of the hole exit and the BR at which it is present, are both similar to those for the hairpin vortices in the downstream jet. Hairpin vortices are shown in Chapter 7 to be present with a crossflow with a CFR of up to 0.8. However, in this chapter it has been shown that there is a reduction in the in-hole coherent unsteadiness for an increase in the crossflow to a CFR of 0.6. This difference implies that the in-hole coherent unsteadiness is not the only reason for the formation of hairpin vortices in the downstream jet.

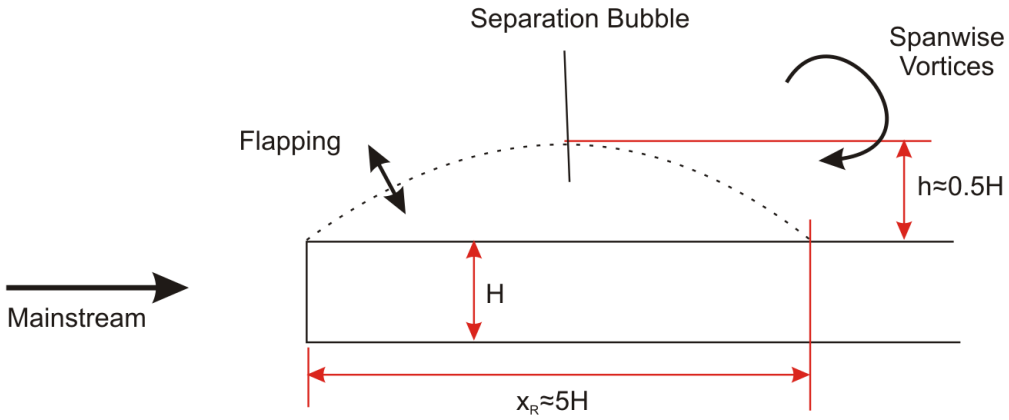

Figure 8.12: Schematic of the dimensions of a separation bubble at the leading edge of a blunt flat plate, based on Kiya and Sasaki [48] and Cherry et al [14].

8.3 Discussion of In-hole Coherent Unsteadiness

The inlet inclination angle in the current experiment is 30°, and for such a case it was shown in the literature review that a relatively large separation bubble is likely at the trailing edge of the hole inlet. The trailing edge of the hole inlet is shown in Fig. 2.1, and is defined relative to the direction of the mainstream flow at the hole exit. It has been shown by Kiya and Sasaki [48] [49], and Cherry et al [14], that coherent unsteadiness can be caused by a separation bubble.

Figure 8.12 shows schematically the separation bubble at the leading edge of a flat plate investigated by Kiya and Sasaki and Cherry et al. The approximate time-mean dimensions are shown in Fig. 8.12. The boundary of the separation bubble was taken by both groups of authors as being the dividing streamline. The maximum height of the separation bubble (h) was approximately half way along the reattachment length (x_R). The Reynolds number of the studies, based on the height of the blunt edge (H), was approximately 20×10^3 and the turbulence intensity was less than 0.2%.

The review of Bradshaw and Wong [9] classifies the characteristics of a separation bubble in terms of the h/δ ratio, with a value in excess of 1.0 meaning that the separation bubble has an 'overwhelming influence on the flow'. Here δ is taken to be the boundary layer height for an equivalent development length with no separation. The h/δ ratio for the current experiment is estimated, based on the results of Leylek and Zerkle [58], to be 8. Whilst that for the separation bubble in Fig. 8.12 is comparable, having a ratio of 10.

Both Kiya and Sasaki, and Cherry et al, showed coherent velocity fluctuations with a Strouhal number of 0.7 in the region downstream of the maximum height of the bubble. Where the separation bubble height (H) and the mainstream velocity where used to non-dimensionalise the frequency. Smoke visualisations and ensemble averaged velocity profiles showed that this was due to the passage of spanwise vortices, as denoted in Fig. 8.12. These vortices, like the shear layer vortices in the downstream jet shown in Chapters 6 and 7, were attributed to a Kelvin-Helmholtz instability in the shear layer. Within the boundary layer downstream of the reattachment they were also shown to form into hairpin vortices. Upstream of the maximum height of the separation bubble, the vortices in the shear layer were seen to coalesce.

Coherent unsteadiness was also seen by Kiya and Sasaki, and Cherry et al, towards the front of the separation bubble. This had a Strouhal number of 0.1, and was described as being due to a 'flapping' motion of the shear layer. This is also indicated in Fig. 8.12.

There are notable geometric differences between the blunt flat plate and the current experiment, which will influence the characteristics of the separation bubble. Therefore it is not appropriate to directly compare the Strouhal numbers of coherent unsteadiness. However, it is likely that the coherent unsteadiness shown inside the hole in this chapter is of one of the two modes introduced in this section. The more likely case being that of the shed spanwise vortices, on account of coherent unsteadiness of the fundamental harmonic being present all along the hole length.

In the literature review it has been described, based on the results of Hay et al [38], that the hole discharge coefficient is increased with perpendicular crossflow. This indicates a change in the in-hole flowfield. This is likely to mean that the separation bubble will become biased towards the edge of the hole inlet with approaching crossflow, and the size of the separation associated with the inlet inclination angle may decrease. Such changes in the size and shape of the separation bubble, could therefore be associated with the observed lack of coherent unsteadiness seen with increasing crossflow.

8.4 Conclusions

Within this chapter the coherent unsteadiness arising within the cylindrical and the shaped holes is presented. Hot Wire Anemometry has been used to show how the occurrence of

coherent unsteadiness varies, with changes in the magnitude of crossflow at the hole inlet. The crossflow, as in Chapter 7, is orientated in the perpendicular (spanwise) direction.

Frequency spectra, obtained using Hot Wire Anemometry, show that increasing the crossflow from a CFR of 0.1 through to 0.6 qualitatively alters the in-hole coherent unsteadiness. For the minimal crossflow case, coherent unsteadiness is seen shortly downstream of the hole inlet for both the cylindrical and the shaped hole which has a Strouhal in the range of 0.6 to 1.2. The frequency of the coherent unsteadiness is either 70Hz, 140Hz or 210Hz. These three frequencies appear to be harmonics of each other, and which frequencies are present inside the hole depends on the BR. Typically coherent unsteadiness at 210Hz is seen for a BR close to 1.8, at 140Hz for a BR of approximately 1.2 and at 70Hz for a BR close to 0.9.

Before the hole exit is reached the coherent unsteadiness at higher blowing ratios is seen to decay, with only that at lower BR being present at the hole exit. On increasing the magnitude of the crossflow to a CFR of 0.2, coherent unsteadiness is seen to be present for a smaller range of BR. At the maximum crossflow velocity investigated of CFR equal to 0.6, no coherent unsteadiness is present inside either the cylindrical or the shaped hole.

Interestingly the Strouhal number of the coherent unsteadiness close to the hole exit and the range of BR for which it occurs, is consistent with that of the hairpin vortices shown previously to occur in the downstream jet. However, hairpin vortices are still seen in the downstream jet with a crossflow of CFR equal to 0.6, at which no coherent unsteadiness is seen inside the hole. Therefore it appears that in-hole coherent unsteadiness is not the primary reason for the formation of hairpin vortices.

The results in this section show for the first time the presence of coherent unsteadiness inside a cooling hole. Comparison with other studies, upon a more fundamental geometry, suggests that the coherent unsteadiness may be largely due to vortex shedding from a separation bubble at the cooling hole inlet.

Chapter 9

Effect of Crossflow on the In-hole Coherent Unsteadiness

Coherent unsteadiness has been shown in Chapter 8 to be present inside the cooling hole of both the cylindrical and the shaped hole when fed from a perpendicular crossflow. Coherent unsteadiness is most apparent with low velocities of perpendicular crossflow, and is not present on increasing the velocity of perpendicular crossflow. It has been proposed in Chapter 8 that the in-hole coherent unsteadiness is caused by vortex shedding from a separation bubble at the cooling hole inlet.

Within this chapter, the numerical model described in Chapter 5 is used to investigate further if vortex shedding is the cause of the in-hole coherent unsteadiness. The numerical model is also used to examine why coherent unsteadiness is not present with increasing perpendicular crossflow. Additionally the effects of co-flowing and counter flowing crossflow, which were not studied experimentally in Chapter 8, are investigated. These three crossflow directions, are shown in Fig. 2.4 of the literature review, and are clearly identified on all the figures in this chapter. In all cases in this chapter the BR is equal to 0.9, and this lies in the range in which coherent unsteadiness has been shown to occur experimentally.

9.1 Counter Flowing Crossflow

9.1.1 Low Crossflow Velocity

Cylindrical Hole

The discussion section of Chapter 8 led to the suggestion that the in-hole coherent unsteadiness is caused by vortex shedding from a separation bubble at the hole inlet. This coherent unsteadiness is seen for a perpendicular crossflow of CFR equal to 0.1. At a CFR equal to 0.1 all of the coolant leaves the crossflow passage through the cooling holes, and so regions of fluid at near zero velocity are likely to be present in the crossflow passage downstream of the cooling hole inlet.

The numerical model uses a density based solver which is likely to be become unstable for flows with a Mach number of less than 0.03. All of the flows in the experimental investigation are lower than this, and so, as described in Chapter 5, the velocities in the numerical model are scaled by a factor of 52. To keep the Reynolds number constant between the experiment and the numerical model the dynamic viscosity is also scaled. However, the almost stagnant nature of some regions of flow at a CFR of 0.1 means that the scaling required becomes excessive, with the flow elsewhere in the model no longer able to be considered incompressible.

As the case with a perpendicular crossflow of CFR equal to 0.1 cannot be solved by the current numerical model, the counter flowing case of CFR equal to 0.2 is used here to understand the cause of the coherent unsteadiness seen experimentally in Chapter 8. Counter flowing crossflow is chosen as the crossflow is in the opposite direction to the mainstream flow, and so it is likely that this leads to the largest separation bubble at the trailing edge of the hole inlet. For this reason the case of counter flowing crossflow of CFR equal to 0.2, has already been used previously, as described in Chapter 5, to evaluate the grid and temporal sensitivity of the numerical model.

Figure 9.1 shows two instantaneous velocity profiles on the spanwise plane at midspan for the cylindrical hole with a counter flowing crossflow of CFR equal to 0.2. The time difference between the two velocity profiles shown in Fig. 9.1 is 125μs, and the velocity is normalised with respect to the velocity at the edge of the mainstream boundary layer at the domain inlet.

In Fig. 9.1 a high velocity jetting region is seen to form near the leading edge of the hole, whilst a separation bubble forms at the trailing edge. The velocity in the jetting region is seen to be unsteady with alternate bands of high and low velocity being shed towards the hole exit. It was the periodicity of this shedding of high velocity that was used in Chapter 5 for the sensitivity study. With distance along the hole these velocity differences in the jetting region appear to mix out. Downstream of the hole exit the trajectory of the high velocity jet core shows that the jet has separated from the blade surface.

Frequency spectra are also shown in Fig. 9.1, which have been recorded using the pseudo hot wire probes described in Chapter 5. These are located at the same three planes within the cooling hole as measured experimentally in Chapter 8, where S is the distance from the cooling hole exit. The measurement points upon these planes are the same as the three possible locations for the hot wire probe in Chapter 8. It should also be reminded, that to be comparable with the hot wire probe only the velocity component in the spanwise plane (V_{xy}) is taken and processed in the calculations.

In Chapter 8 the amplitude of the in-hole coherent unsteadiness was scaled relative to the local rms velocity. This provided a measure of the coherent unsteadiness compared to the total unsteadiness at a given location. However, in the numerical model, the grid being relatively coarse means that the smaller scales of turbulence are not resolved. So in this chapter it is considered more practical, to scale the amplitude of coherent unsteadiness seen numerically relative to the local-time mean velocity.

Figure 9.1 shows that on the plane closest to the hole inlet at S equal to 4.5D, coherent unsteadiness with a Strouhal number of 0.9 is present on the centreline and 0.25D above and below the centreline. The Strouhal number is calculated based on the bulk velocity through the hole. The relative amplitude of the coherent unsteadiness, is seen to be largest on the hole centreline with an amplitude of greater than 0.4 times the local time-mean velocity. In Chapter 5, when assessing the model sensitivity, it has been noted that the frequency of coherent unsteadiness seen in the frequency spectra, is consistent with the passing of the regions of high velocity in the spanwise velocity profile.

The frequency spectra on the plane at S equal to 2.0D in Fig. 9.1, show that coherent unsteadiness is also present with a Strouhal number of 0.9. However, the coherent unsteadiness reduces in amplitude on the centreline and is less apparent at the point 0.25D

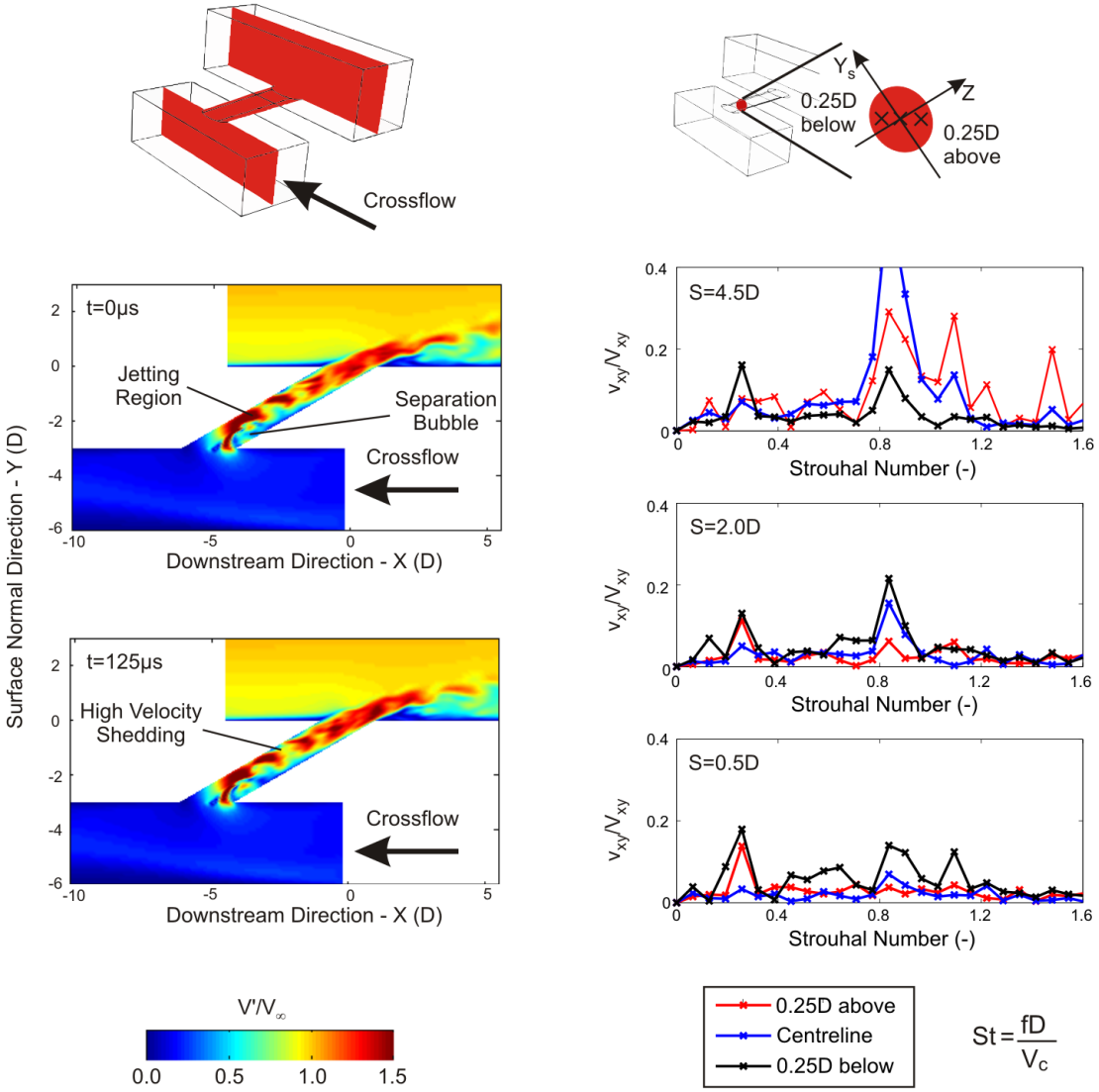

Figure 9.1: Instantaneous velocity profiles in the spanwise plane at midspan and frequency spectra inside the cooling hole. For the cylindrical hole with counter flowing crossflow of CFR equal to 0.2. Obtained using TBLOCK.

below the centreline. At S equal to 0.5D, the amplitude of coherent unsteadiness is reduced further with only a low amplitude peak being seen in the frequency spectrum obtained at the point 0.25D below the centreline.

The coherent unsteadiness shown in Fig. 9.1 has a Strouhal number of 0.9. The coherent unsteadiness shown in Chapter 8 to occur inside the cylindrical hole typically has a Strouhal number in the range 0.6 to 1.0. This level of similarity between the two Strouhal numbers, suggests that it is reasonable to presume that the same in-hole coherent unsteadiness is being seen computationally as experimentally.

The coherent unsteadiness seen experimentally in Chapter 8, on the plane at S equal to 4.5D inside the cylindrical hole (Fig. 8.1), has a coherent unsteadiness intensity in the range of 2% to 5%. In contrast the coherent unsteadiness shown here in Fig. 9.1 at S equal to 4.5D, has an coherent unsteadiness intensity an order of magnitude larger, in the range of 10% to 50%.

Some of this difference may be attributable to the change in the crossflow direction, as the numerical model has a counter flowing crossflow and the experimental setup has a perpendicular crossflow. However, it is perhaps more likely to be due to the small scales of turbulence not being resolved numerically, due to the coarse nature of the grid, or simulated using a turbulence model. Therefore, the mixing out of the coherent unsteadiness occurs at a slower rate in the numerical model than in the experiment.

Shaped Hole

Figure 9.2 is of the same layout as Fig. 9.1, but for a shaped hole with a counter flowing crossflow of CFR equal to 0.2. The instantaneous velocity profiles in Fig. 9.2 on the spanwise plane at midspan, show a similar velocity profile at the hole inlet for the shaped hole to the cylindrical hole shown previously in Fig. 9.1, with a jetting region and a separation bubble at the inlet. In the jetting region the periodic shedding of high velocity is also apparent. The expanding exit of the shaped hole means that close to the hole exit the velocity reduces, and the comparatively low velocity next to the blade surface shows that the downstream jet is attached.

The three frequency spectra in Fig. 9.2 for the planes at S equal to 2.0D and 4.5D, all show that the shedding of high velocity inside the cooling hole is coherent with a Strouhal

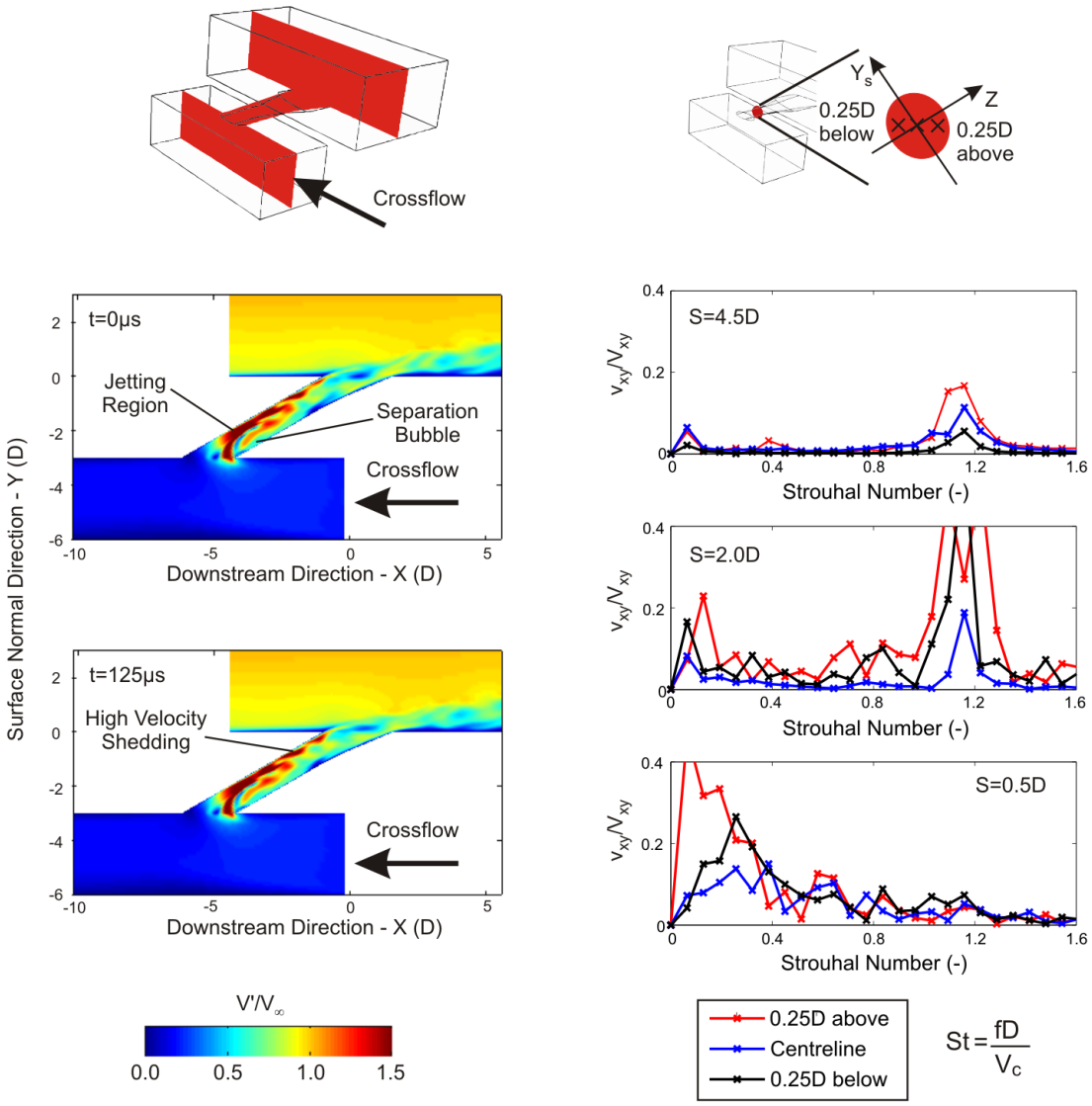

Figure 9.2: Instantaneous velocity profiles in the spanwise plane at midspan and frequency spectra inside the cooling hole. For the shaped hole with counter flowing crossflow of CFR equal to 0.2. Obtained using TBLOCK.

number of 1.1. It is seen that there is a significant increase in the amplitude of coherent unsteadiness between the plane at S equal to 4.5D and that at S equal to 2.0D. However, the frequency spectra of the points on the plane at S equal to 0.5D in Fig. 9.2 show no coherent unsteadiness to be present.

Inside the expanding exit of the shaped hole, as shown previously by Kohli and Thole [47], regions of almost zero velocity are present. Turbulent fluctuations in these regions, therefore require a longer time to average out, than in the main flow through the hole. The measurement planes at S equal to 0.5D and 2.0D, lie inside the expanding exit of the shaped hole, and in the frequency spectra in Fig. 9.2 it is apparent that there are random frequency peaks towards the lower end of the range.

The real time solved in the current numerical model, is relatively short compared to that solved in other unsteady numerical simulations of film cooling. This is likely to be a contributing factor in the occurrence of random low frequency peaks in Fig. 9.2, and it expected that these would average out if a longer solution time were to be solved.

The experimental results of Chapter 8, showed the same frequency of coherent unsteadiness for the cylindrical and the shaped hole with perpendicular crossflow. The frequency spectra shown in this section for the counter flowing cases in Fig. 9.1 and 9.2, show there to be a difference between the frequencies of coherent unsteadiness inside the cylindrical hole and the shaped hole. The sensitivity study in Chapter 5 showed that the numerical model does not have complete convergence in the frequency of coherent unsteadiness. Therefore it is not possible with the current numerical model, to conclude if the difference of 0.2 between the Strouhal number of coherent unsteadiness in the cylindrical hole and that in the shaped hole is a real effect.

9.1.2 In-hole Vortex Shedding

In the discussion of Chapter 8 it was suggested that the coherent unsteadiness inside the cooling hole, is caused by vortex shedding from the separation bubble at the hole inlet. In the previous section it has been shown in Figs. 9.1 and 9.2, that periodic velocity fluctuations occur in the jetting region inside the hole. Here it is confirmed that these velocity fluctuations are due to the shedding of vorticity from the separation bubble.

Figure 9.3 shows iso-surfaces of spanwise vorticity inside the cylindrical hole for a counter

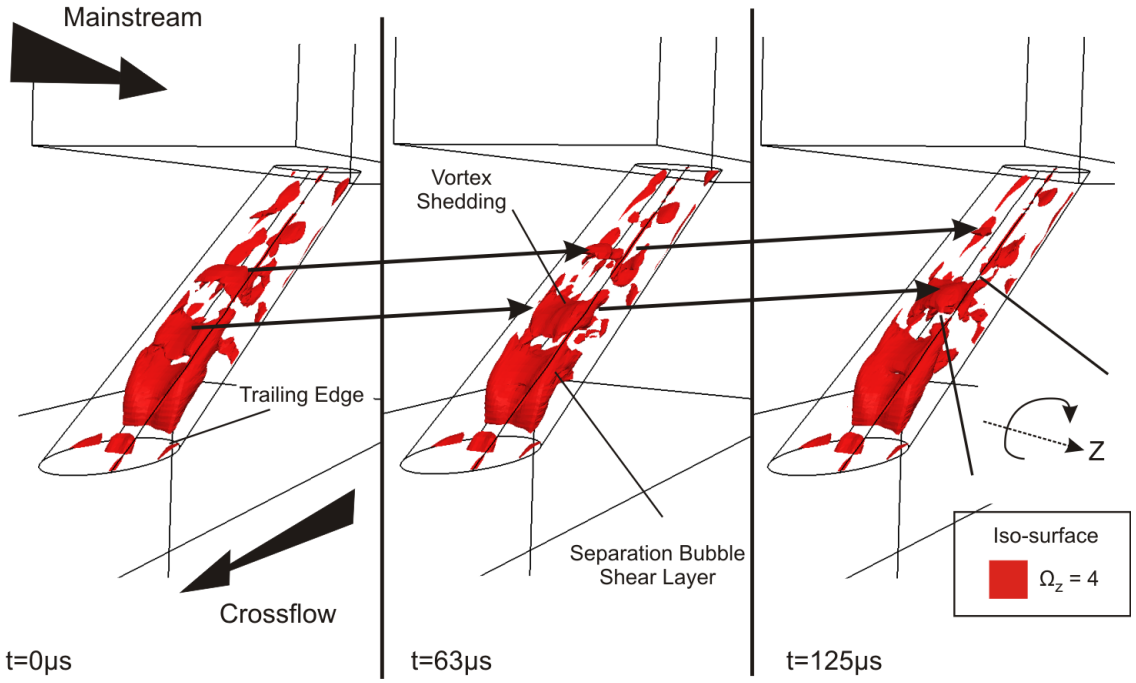

Figure 9.3: Spanwise vorticity inside the cylindrical hole with counter flowing crossflow of CFR equal to 0.2. The timesteps are the same as the instantaneous velocity profiles shown in Fig. 9.1. Obtained using TBLOCK.

flowing crossflow of CFR equal to 0.2. The time in Fig. 9.3 is consistent with that in Fig. 9.1, and so the flowfields at time steps equal to 0μs and 125μs are common to both figures.

The vorticity in Fig. 9.3 is normalised with respect to the bulk velocity through the hole and the cooling hole diameter, according to Eq. 9.1. A value of 4 has been chosen for the spanwise vorticity iso-surface, as this allows the features of interest to be seen. To improve the clarity of Fig. 9.3, the spanwise vorticity in the boundary layer of the cooling hole has been blanked out.

$$\Omega = \frac{\omega D}{V_c} \tag{9.1}$$

A region of high spanwise vorticity is seen in Fig. 9.3 to originate at the trailing edge of the hole inlet. It is reminded that the trailing edge of the hole inlet is defined relative to the direction of the mainstream flow at the hole exit, not the crossflow direction. The region of high spanwise vorticity is that in the shear layer between the jetting region and the separation bubble. With increasing distance along the cooling hole length, the region of high spanwise vorticity is seen to split into discrete patches. These discrete patches

of spanwise vorticity are shed downstream and indicate that vortices are shed from the separation bubble at the hole inlet. The decreasing size of the patches of spanwise vorticity, indicates that the vortex is mixing out with distance along the cooling hole.

The shedding of spanwise vorticity shown in Fig. 9.3 is also seen inside the shaped hole for a counter flowing crossflow of CFR equal to 0.2. In both cases the spatial distance between the shed vortices is comparable with the spacing of the high velocity regions in Fig. 9.1 and 9.2. This furthers the suggestion that the in-hole coherent unsteadiness, shown to occur experimentally in Chapter 8, is due to the shedding of vortices from the cooling hole inlet separation bubble. Consequently, the shedding of high velocity seen in subsequent instantaneous velocity profiles shown in this chapter, will be referred to as vortex shedding.

9.1.3 Increased Crossflow Velocity

Coherent vortex shedding has been seen previously in this chapter to occur with counter flowing crossflow of a CFR equal to 0.2. Fig. 9.4 shows a typical instantaneous velocity profile on the spanwise plane at midspan and frequency spectra on the hole centreline for the cylindrical hole with a CFR equal to 0.6.

The instantaneous velocity profile in Fig. 9.4 shows similar features to those shown to be present in Fig. 9.1 for a counter flowing crossflow of CFR equal to 0.2. In Figure 9.4 there is a separation bubble at the trailing edge of the hole inlet and a jetting region of high velocity close to the leading edge of the hole. However, there does not appear to be any clearly identifiable periodic vortex shedding within the cooling hole downstream of the separation bubble.

Frequency spectra are shown in Fig. 9.4 for the points on the centreline at each of the three in-hole planes. On the plane at S equal to 4.5D the frequency spectra on the centreline shows there to be coherent unsteadiness with a Strouhal number of 0.9. This frequency is the same as that seen with counter flowing crossflow of a lower velocity in Fig. 9.4. However, the frequency spectra closer to the hole exit at S equal to 0.5D and 2.0D show no coherent unsteadiness with a Strouhal number close to 0.9 to be present. The low frequency peaks in all three frequency spectra in Fig. 9.4, like those in Fig. 9.2, are suspected to be due to the relatively short real time from which to take the time trace for the Fourier transform.

Figure 9.5 shows a typical instantaneous velocity profile on the spanwise plane at

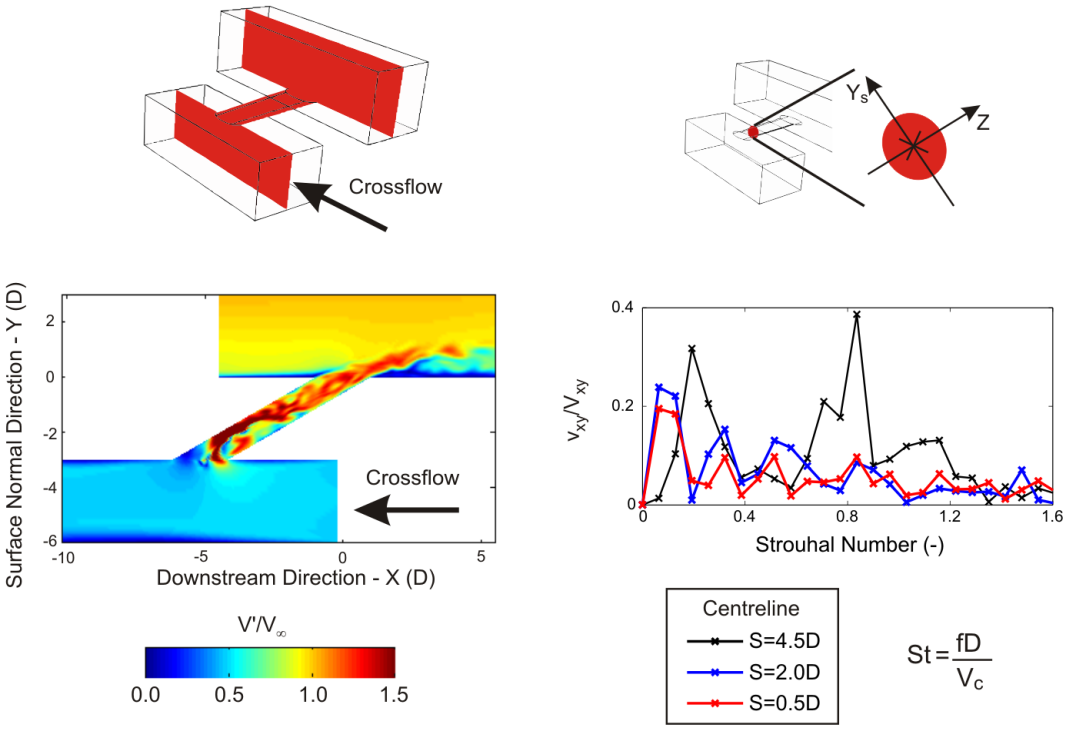

Figure 9.4: Instantaneous velocity profiles in the spanwise plane at midspan and frequency spectra inside the cooling hole. For the cylindrical hole with counter flowing crossflow of CFR equal to 0.6. Obtained using TBLOCK.

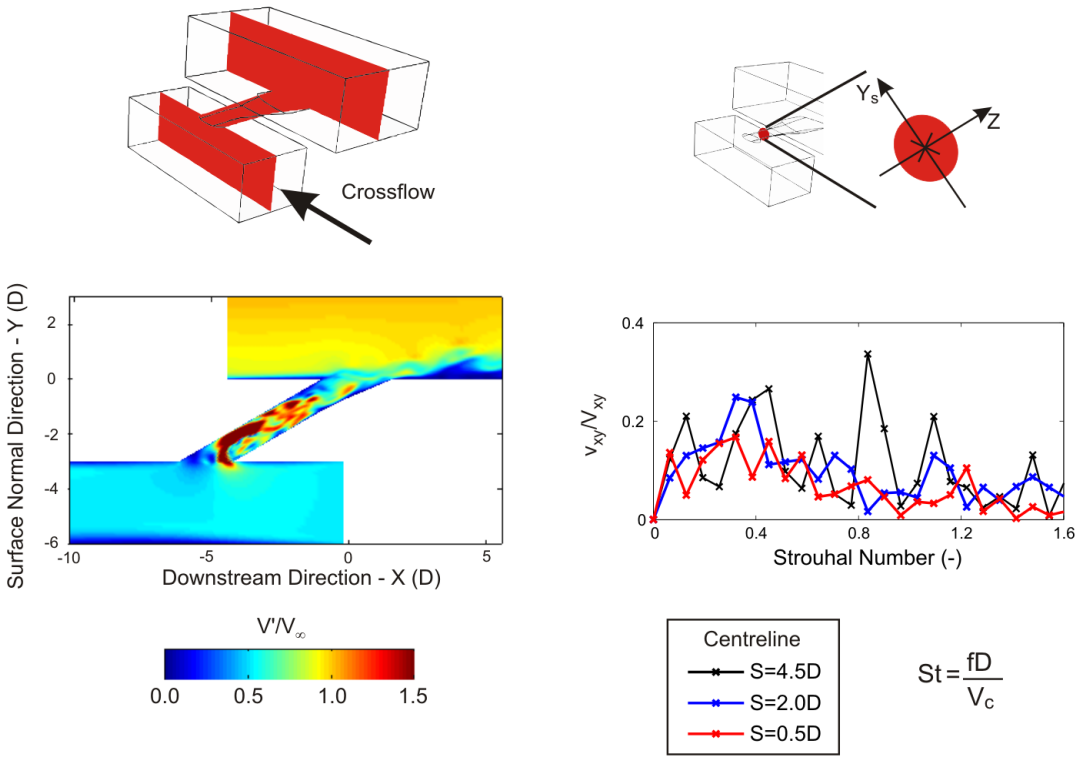

Figure 9.5: Instantaneous velocity profiles in the spanwise plane at midspan and frequency spectra inside the cooling hole. For the shaped hole with counter flowing crossflow of CFR equal to 0.6. Obtained using TBLOCK.

midspan for the shaped hole with counter flowing crossflow of CFR equal to 0.6. The jetting region and the separation bubble at the hole trailing edge, that have been shown to be present at the lower crossflow velocity, can both be seen in the instantaneous velocity profile. However, as for the cylindrical hole shown in Fig. 9.4, no shed vortices are present inside the jetting region in Fig. 9.5.

Frequency spectra are shown in Fig. 9.5 for the points on the centreline of the three in-hole planes. In the plane at S equal to 4.5D coherent unsteadiness is seen on the centreline with a Strouhal number of 0.9. Given the limitations of the numerical model this is the same Strouhal number as at the lower crossflow velocity shown in Fig. 9.2. The wide peak at a Strouhal number close to 0.4, in the frequency spectra of Fig. 9.5 at S equal to 4.5D, may be a lower order harmonic of the coherent unsteadiness with a Strouhal number of 0.9. However, this is suggested very tentatively, as it has previously been highlighted that the short real time of the numerical model could also be a factor.

Closer to hole exit on the planes at S equal to 2.0D and 0.5D the frequency spectra in

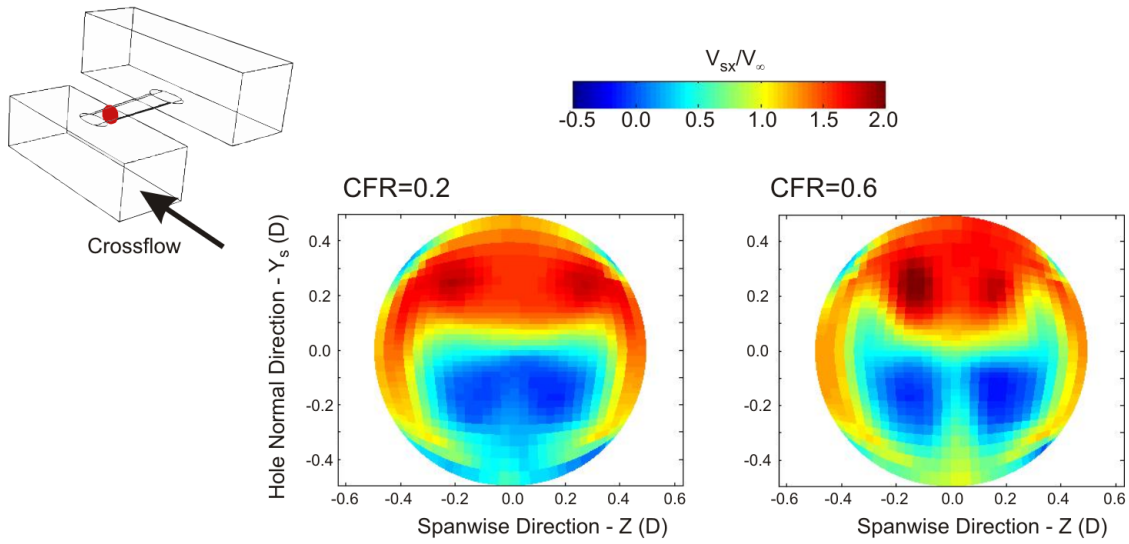

Figure 9.6: Time-mean velocity profile of the V_{sx} component on the hole normal plane at S equal to 4.5D. For the cylindrical hole with counter flowing crossflow of CFR equal to 0.2 and 0.6. Obtained using TBLOCK.

Fig. 9.5 show there to be no coherent unsteadiness with a Strouhal number of 0.9. The wide peaks in the frequency spectra close to a Strouhal number of 0.4, which are also seen in the frequency spectra for the points 0.25D above and below the centreline, have no common frequency. As discussed previously with regard to Fig. 9.2, these are likely to be due to the short real time solved by the numerical model.

It appears for both cooling hole geometries, from the lack of coherent unsteadiness near the exit of the cooling hole in Fig. 9.4 and 9.5, that on increasing the CFR from 0.2 to 0.6 the coherent unsteadiness in the separation bubble does not lead to coherent vortex shedding. This change is also apparent on observing iso-surfaces of spanwise vorticity, similar to that plotted in Fig. 9.3.

The time-mean profile of the velocity parallel to hole axis (V_{sx}), is shown in Fig. 9.6 on the plane at S equal to 4.5D inside the cylindrical hole. The cases of counter flowing crossflow equal to 0.2 and 0.6 are both shown. It is seen that the profile of the shear layer between the jetting region and the separation bubble differs between the two cases. The shear layer at a CFR of 0.2 is shown in Fig. 9.6 to be a 2-D plane with no variation in the hole normal direction, whilst that at a CFR of 0.6 is seen to be highly curved. This distortion of the shear layer at a CFR of 0.6, possibly explains why the vorticity in the shear layer is not able to be shed in a coherent manner.

9.2 Perpendicular Crossflow

9.2.1 Comparison with Experimental Results

Previously in this chapter, the case with counter flowing crossflow has been presented to show that the coherent unsteadiness, seen experimentally inside the cooling hole, is likely to arise due to vortex shedding from the separation bubble at the hole inlet. However, the experimental results in Chapter 8 were for a perpendicular crossflow at the hole inlet.

In Chapter 8 it has been shown that there is no coherent unsteadiness inside either cooling hole geometry with a perpendicular crossflow of CFR equal to 0.6. Although the numerical model is not able to solve the case with a perpendicular crossflow equal to 0.1, it can be used to investigate the in-hole flowfield with higher perpendicular crossflow velocities. Therefore the numerical model can be used to provide a possible explanation for the lack of coherent unsteadiness at a CFR of 0.6.

Figure 9.7 shows typical instantaneous velocity profiles on the spanwise plane at midspan, for the cylindrical hole with perpendicular crossflows of CFR equal to 0.2 and 0.6. At a CFR of 0.2, the instantaneous velocity profile looks similar to those seen previously in this chapter with counter flowing crossflow. Close to the hole inlet a jetting region and a separation bubble are both seen, and downstream of the separation bubble vortex shedding occurs. In contrast, the instantaneous velocity profile in Fig. 9.7 at a CFR of 0.6, does not show a separation bubble to form at the hole inlet or vortices to be shed. Indeed the observed velocity profile is seen to be largely steady, with no significant changes from the instantaneous profile shown in Fig. 9.7.

Frequency spectra are shown in Fig. 9.7 for points on the hole centreline at the three measurement planes within the cooling hole. At a CFR of 0.2, the vortex shedding has a Strouhal number of 1.1 at all three locations, with the maximum amplitude relative to the local time-mean velocity being in the plane at S equal to 2.0D. A Strouhal number of 1.1 is consistent with the frequencies shown previously in this chapter for vortex shedding with counter flowing crossflow.

On increasing the perpendicular crossflow to have a CFR of 0.6, Fig. 9.7 shows negligible unsteadiness on the centreline inside the cylindrical cooling hole. The frequency spectra for the points 0.25D above and below the centreline are also similar, showing only frequency

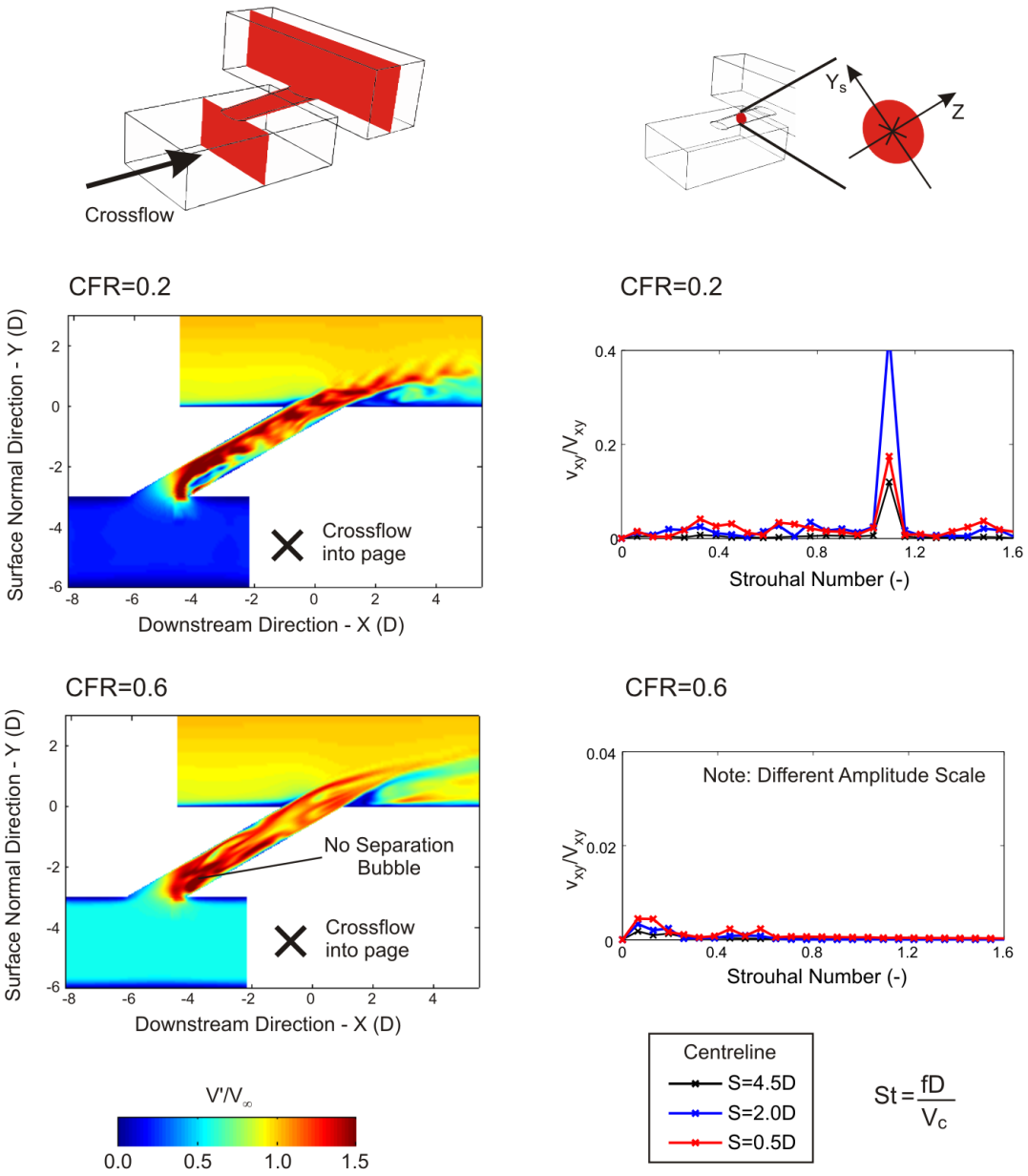

Figure 9.7: Instantaneous velocity profiles in the spanwise plane at midspan and frequency spectra inside the cooling hole. For the cylindrical hole with perpendicular crossflow of CFR equal to 0.2 and 0.6. Obtained using TBLOCK.

peaks with amplitudes of less than 2% of the local time-mean velocity.

Figure. 9.8, which has the same layout as Fig. 9.7, shows the unsteadiness inside the shaped hole with perpendicular crossflow. The instantaneous velocity profile in Fig. 9.8 at a CFR of 0.2 shows that a separation bubble and a jetting region both form at the inlet of the cooling hole. However, unlike for the cylindrical hole with perpendicular crossflow of CFR equal to 0.2, shown in Fig. 9.7, no vortex shedding is seen in the jetting region. At the larger CFR of 0.6 the instantaneous velocity profile in Fig. 9.8 shows that no separation bubble is present at the hole inlet. Within the hole, a large decrease in the velocity seen in the measurement plane of Fig. 9.8 occurs close to beginning of the expanding hole exit.

Frequency spectra are also shown in Fig. 9.8 for points on the centreline of the shaped hole. At both crossflow velocities the frequency spectra are largely the same. In the plane at S equal to 4.5D no unsteadiness is seen for either a CFR of 0.2 or 0.6. Closer to the exit at S equal to 0.5D and 2.0D unsteadiness is seen in the frequency spectra, but at neither CFR does any coherent unsteadiness appear to be present.

In this section it is shown that no coherent unsteadiness occurs in the numerical model for both hole types with a perpendicular crossflow of CFR equal to 0.6. This is consistent with the experimental observations of Chapter 8. The instantaneous velocity profiles included in Fig. 9.7 and 9.8, both show that for a CFR of 0.6 the inlet separation bubble, from which vortices are typically shed, has been altered by the presence of perpendicular crossflow.

9.2.2 Discussion of the Lack of In-hole Coherent Unsteadiness

The case with a perpendicular crossflow of CFR equal to 0.6 has been shown numerically (in this chapter) and experimentally (in Chapter 8) to inhibit the formation of any coherent unsteadiness inside either cooling hole. In contrast coherent vortex shedding is seen to occur inside the cooling hole with counter flowing crossflow at the inlet, as shown in Fig. 9.1 and 9.2. In this section the flowfield inside the cylindrical hole with a counter flowing crossflow of CFR equal to 0.2, is compared to the in-hole flowfield with a perpendicular crossflow equal to 0.6 to obtain a possible explanation for the difference.

Figure 9.9 shows the time-mean velocity normal to the axis of the cooling hole (V_{sx}), upon six planes normal to the hole axis inside the cylindrical hole with counter flowing crossflow of CFR equal to 0.2. The vertical axis in Fig. 9.9 is the hole normal direction

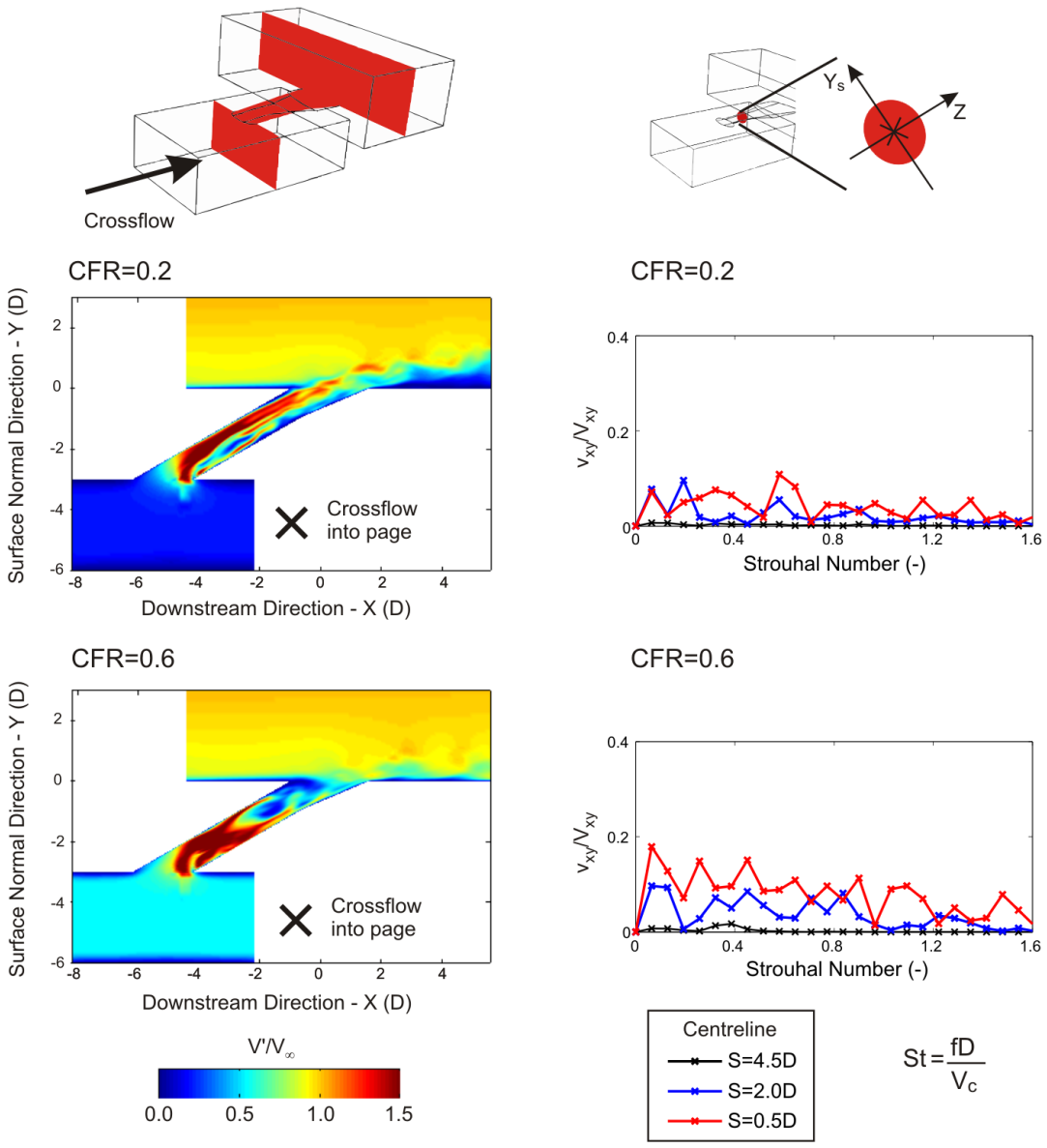

Figure 9.8: Instantaneous velocity profiles in the spanwise plane at midspan and frequency spectra inside the cooling hole. For the shaped hole with perpendicular crossflow of CFR equal to 0.2 and 0.6. Obtained using TBLOCK.

(Y_s), and the region of the hole in the positive Y_s direction will be referred to here as the upper half and that in the negative Y_s direction as the lower half.

The plane at S equal to 5.5D in Fig. 9.9, which is not completely inside the cooling hole, shows the velocity to be largely uniform across the majority of the plane. The jetting region and the separation bubble, seen previously in this chapter, form before the plane at S equal to 4.5D. With increasing distance along the hole, the jetting region in the upper part of the plane, is seen in Fig. 9.9 to move towards the axis of the cylindrical hole. The planes at S

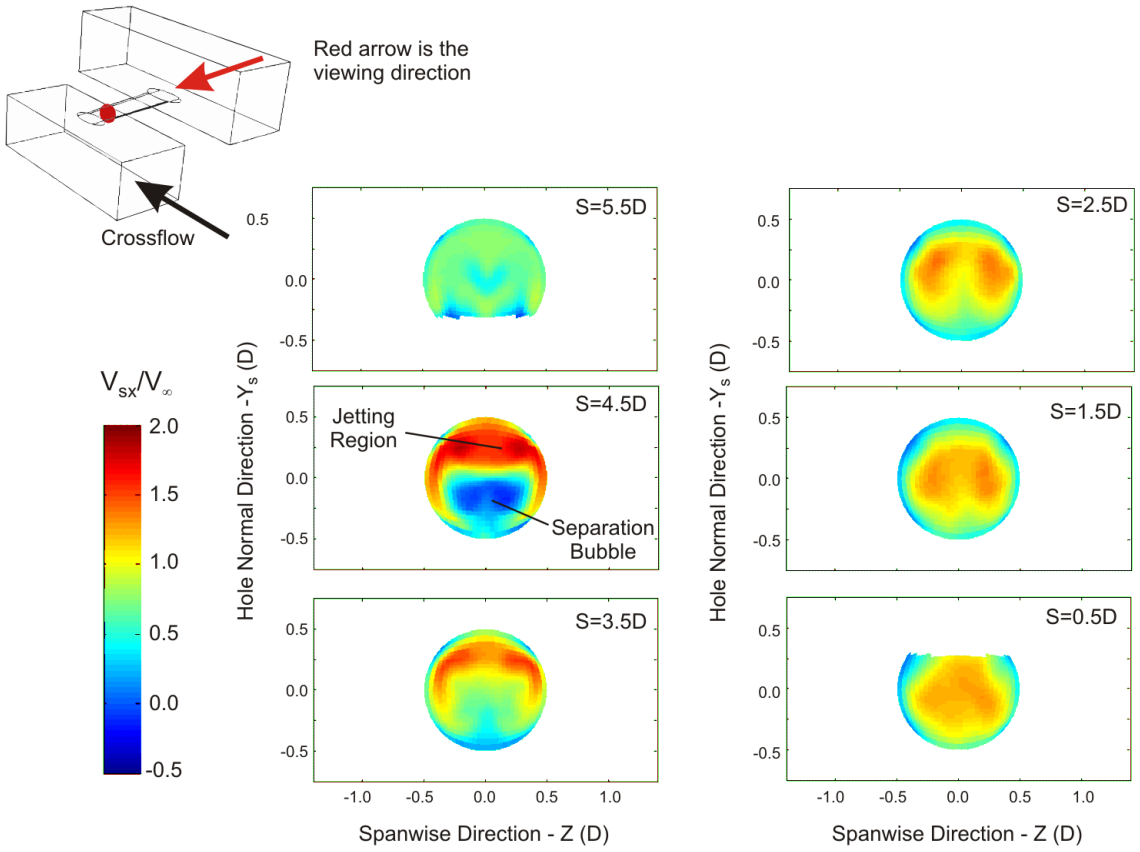

Figure 9.9: Time-mean velocity profile of the V_{sx} component on the hole normal plane at S equal to 0.5D to 5.5D. For the cylindrical hole with counter flowing crossflow of CFR equal to 0.2. Obtained using TBLOCK.

equal to 1.5D and 0.5D show the jetting region to mix out. This leaves a flowfield similar to that expected of pipe flow with high velocity fluid in the mid-pipe region and low velocity fluid in the near wall region.

The in-hole time-mean flowfield is shown in Fig. 9.10 for both the cylindrical and the shaped hole with a perpendicular crossflow of CFR equal to 0.6. As in Fig. 9.9 the V_{sx} component is shown upon six planes normal to the hole axis. It is apparent that the time-mean flowfield in Fig. 9.10 has some discontinuous features, which are perhaps not to be expected of a time-mean flowfield.

The length of time over which the time-mean has been calculated equates to the time for flow traveling at the bulk velocity of the hole to pass through the hole 2.5 times. It is also shown by the velocity profiles in Fig. 9.11 that calculating the time-mean for the shaped hole over a length of time four times longer does not lead to significantly different

velocity profiles from those shown in Fig. 9.10. Computational resource limitations mean that obtaining a time-mean over a longer time period is not practical within the current study, but as discussed later in this section the trends seen in Fig. 9.10 are qualitatively similar to other time-mean results.

Figure 9.10 shows that at the inlet of the cylindrical hole (S equal to 5.5D), a region of higher velocity is present close to Y_s equal to 0D on the side closest to the approaching crossflow. This high velocity region is denoted 'Fluid A' in Fig. 9.10, and on moving downstream inside the hole it rotates in the anti-clockwise direction (on looking into the page) as is shown by its position at S equal to 4.5D. A second patch of high velocity fluid is seen at the lower edge of the plane at S equal to 5.5D. This is labeled 'Fluid B' in Fig. 9.10, and as with Fluid A it is seen to rotate anti-clockwise and mix out with downstream distance. In the plane at S equal to 2.5D, there is no distinction between Fluid A and B.

In the plane at S equal to 5.5D, Fig. 9.10 shows the velocity profile inside the shaped hole to be similar to that in the cylindrical hole, with patches of high velocity fluid equivalent to Fluid A and B. Both these are seen to rotate anti-clockwise with downstream distance and mix into each other before the plane at S equal to 3.5D. Beyond this plane, the patch of higher velocity fluid does not continue to rotate and remains on the side of the hole closest to the approaching crossflow. The exception to this is the fluid closest to the lower edge of the hole, labeled 'Fluid C' in Fig. 9.10, which continues to rotate and expands along the lower edge of the hole. It should also be noted that within the planes in the expanding exit of the shaped hole there are regions with almost a zero velocity component in the X_s direction.

In Fig. 9.10 a separation bubble is seen to be present for both cooling holes on the plane at S equal to 5.5D between Fluid A and B. This separation bubble does rotate to be at the lower edge of the hole by the plane at S equal to 4.5D, as is shown to be the case in Fig. 9.9 with counter flowing crossflow. However the spiraling motion of the in-hole flowfield means that the shear layer of the separation bubble is not a 2-D plane with perpendicular crossflow of CFR equal to 0.6. The separation bubble with perpendicular crossflow equal to 0.6 is shown in Fig. 9.10 to mix out by S equal to 3.5D. The lack of in-hole coherent unsteadiness with perpendicular crossflow of CFR equal to 0.6, therefore appears to be due to the shape of the separation bubble created at the cooling hole inlet.

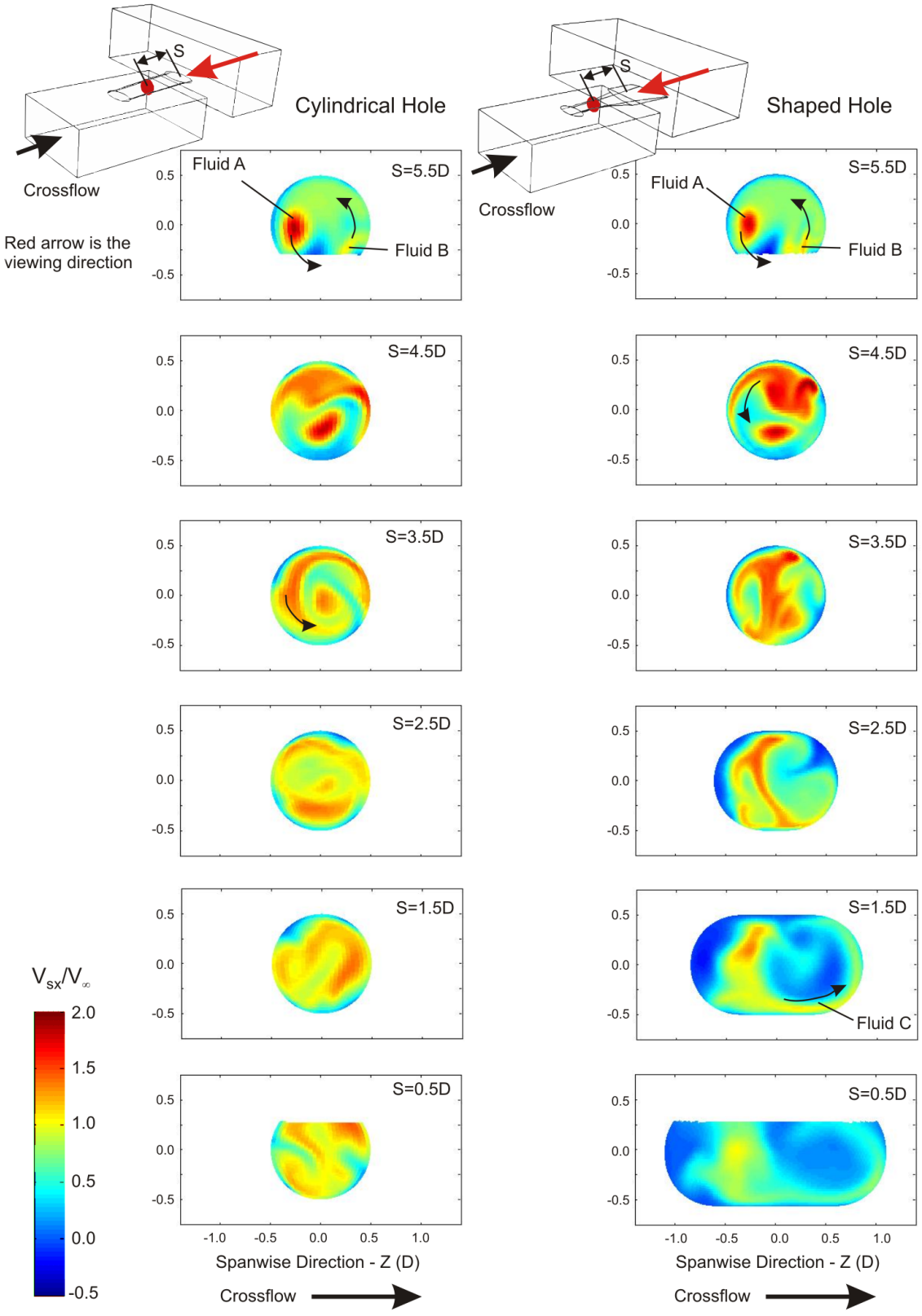

Figure 9.10: Time-mean velocity profile of the V_{sx} component on the hole normal plane at S equal to 0.5D to 5.5D. For the cylindrical hole and the shaped hole with perpendicular crossflow of CFR equal to 0.6. Obtained using TBLOCK.

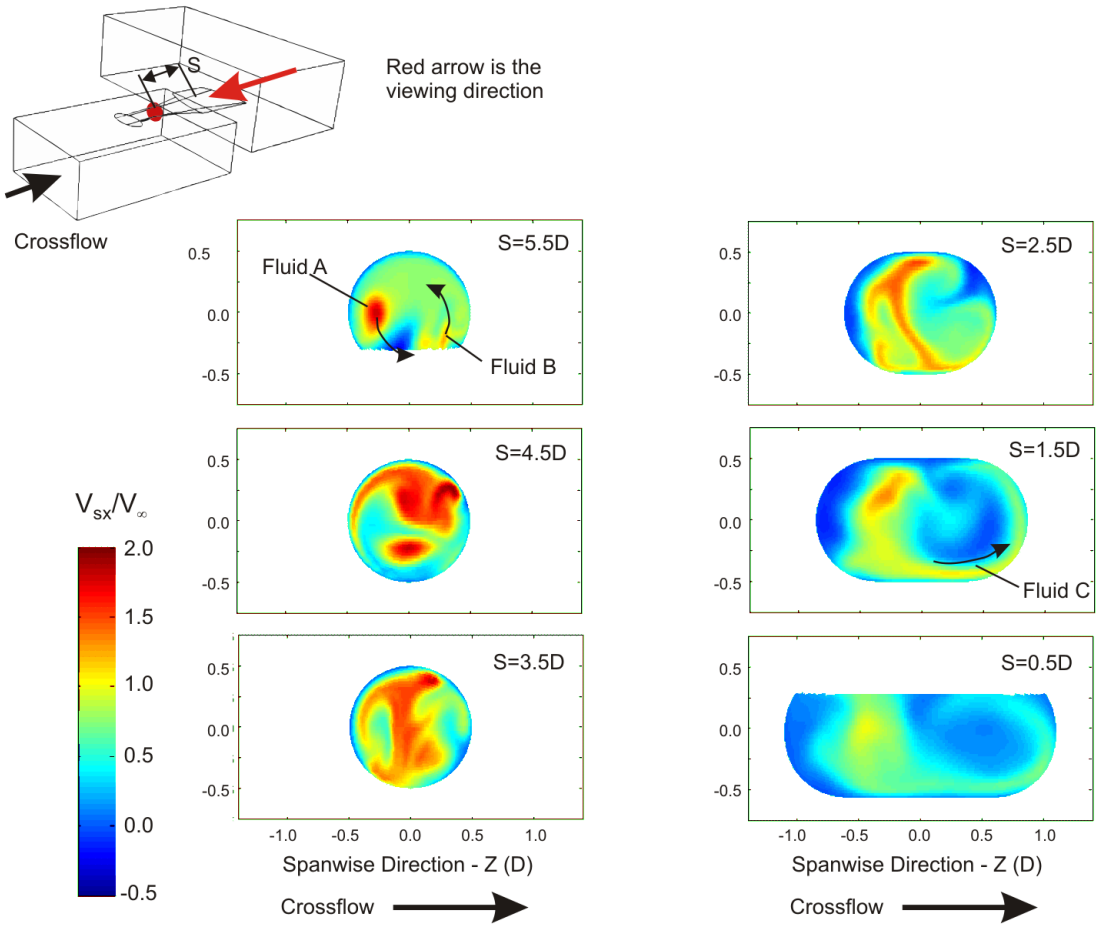

Figure 9.11: Repeat of the time-mean velocity profile of the V_{sx} component on the hole normal plane at S equal to 0.5D to 5.5D. For the shaped hole with perpendicular crossflow of CFR equal to 0.6. Obtained using TBLOCK.

The anti-clockwise rotation shown in Fig. 9.10 is also apparent inside both the cylindrical and shaped holes with a perpendicular crossflow of CFR equal to 0.2, with the jetting region seen to rotate. The anti-clockwise rotation of the jetting region with a CFR of 0.2 does not extend beyond the plane at S equal to 3.5D. A similar spiralling of the fluid inside the hole as shown in this section, has also been alluded to by Kholi and Thole [47] and Saumweber and Schulz [89] based on their steady state computations.

Further evidence that the in-hole velocity profile shown numerically in Fig. 9.10 is comparable with the experimental case, is shown by the position of the jet downstream of the hole exit. In Fig. 9.12 the time-mean temperature contours in the secondary flow plane 2D downstream of the cylindrical hole and 1D downstream of the shaped hole are shown. In each case the jet can be identified as the region of higher temperature fluid.

Figure 9.12 shows the jet to be symmetrical for a perpendicular crossflow of CFR equal to 0.2. On increasing the CFR to 0.6 it can be seen that the jet is not symmetric with a clockwise rotation of approximately 10°. These flowfields show qualitative agreement with the time-mean pixel intensity of the jet shown previously in Fig. 7.2, although the rotation seen numerically is in the opposite direction to that seen experimentally.

The time-mean temperature profiles downstream of the shaped hole in Fig. 9.12, also have qualitative agreement with the time-mean pixel intensity shown in Fig. 7.4. As the jet in Fig. 9.12 is biased to lower spanwise edge of the hole for a CFR equal to 0.2, and splits into two jets at the different edges of the hole with a CFR of 0.6.

9.3 Co-flowing Crossflow

9.3.1 In-hole Coherent Unsteadiness

The third configuration of crossflow, which has been discussed in the literature review, is co-flowing crossflow. Co-flowing crossflow is orientated in the same direction as the mainstream flow. The study of Thole et al [95] (included in the literature review), has shown that for an inclined hole, such as in the current study, the size of the trailing edge separation bubble can be reduced by using co-flowing crossflow. This reduction occurs due to the smaller turning angle required of the flow to enter the cooling hole.

Figure 9.13 shows typical instantaneous velocity profiles on the spanwise plane at midspan

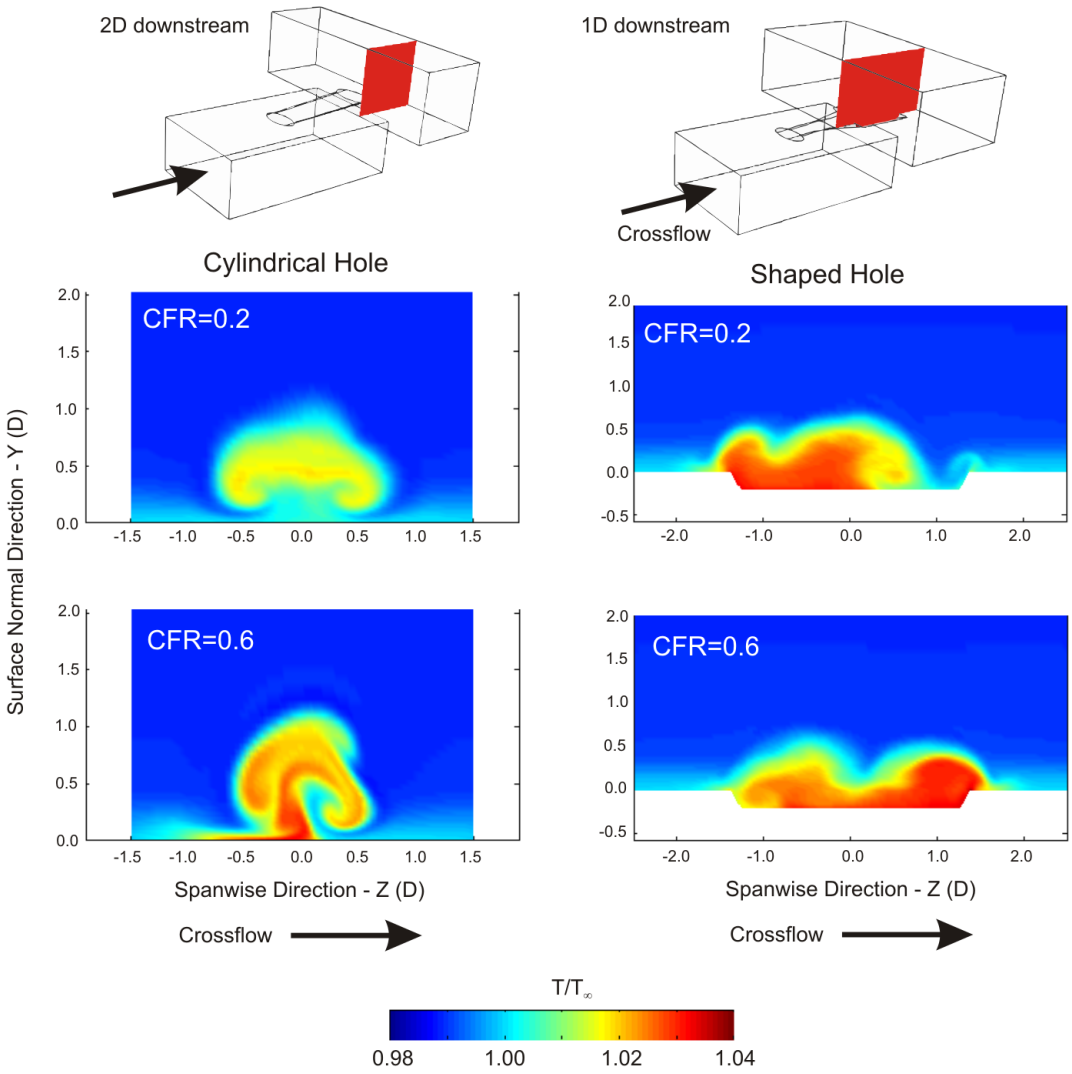

Figure 9.12: Time-mean temperature profile downstream of the exit of the cylindrical hole and the shaped hole with perpendicular crossflow of CFR equal to 0.6. Obtained using TBLOCK.

for the cylindrical hole with co-flowing crossflows of CFR equal to 0.2 and 0.6. At a CFR of 0.2 a separation bubble and jetting region are both present near the hole inlet. Inside the jetting region the shedding of vortices, seen previously in this chapter, is apparent. On increasing the CFR to 0.6, the instantaneous velocity profile in Fig. 9.13, shows the jetting region and separation bubble to remain, but with the shedding of vortices beginning noticeably closer to the hole exit than at a CFR of 0.2.

Frequency spectra are also shown in Fig. 9.13 for the points on the centreline of the three measurement planes. These show the vortex shedding to have a Strouhal number close to 0.9 at both crossflow velocities. At a CFR of 0.6, the initiation of the vortex shedding closer to the hole exit than at a CFR of 0.2, means that no coherent unsteadiness is seen in the frequency spectra on the centreline at S equal to 4.5D.

The instantaneous velocity profiles and frequency spectra in Fig. 9.14 show that coherent vortex shedding also occurs inside the shaped hole with a co-flowing crossflow. The instantaneous velocity profile on the spanwise plane at midspan for a CFR of 0.2, shows there to be vortex shedding in the jetting region. The frequency spectra recorded on the centreline of the S equal to 0.5D and 2.0D planes show the vortex shedding to have a Strouhal number of 0.9. As for the cylindrical hole with a co-flowing crossflow of CFR equal to 0.6, shown previously in Fig. 9.13, the vortex shedding is only observed downstream of the plane at S equal to 4.5D.

On increasing the CFR of the co-flowing crossflow to 0.6, the instantaneous velocity profile in Fig. 9.14 also shows the shedding of vortices. The frequency spectrum at S equal to 2.0D shows the vortex shedding to have a Strouhal number of 0.7. Given the limitations of the numerical model, this frequency is considered to be consistent with the other instances of in-hole vortex shedding. As discussed previously, the short time period over which the numerical model has been solved, is possibly the reason for the apparent random peaks in the frequency spectrum at S equal to 0.5D in Fig. 9.14.

It has been shown in Fig. 9.13 and 9.14, that for both hole geometries a co-flowing crossflow causes a separation bubble to form at the hole inlet. However, the initiation of the vortex shedding from the separation bubble tends to be shifted towards the hole exit compared to the counter flowing case. It is apparent, on viewing the plane normal to the hole axis, that co-flowing crossflow leads to a separation bubble with a relatively 2-D shear

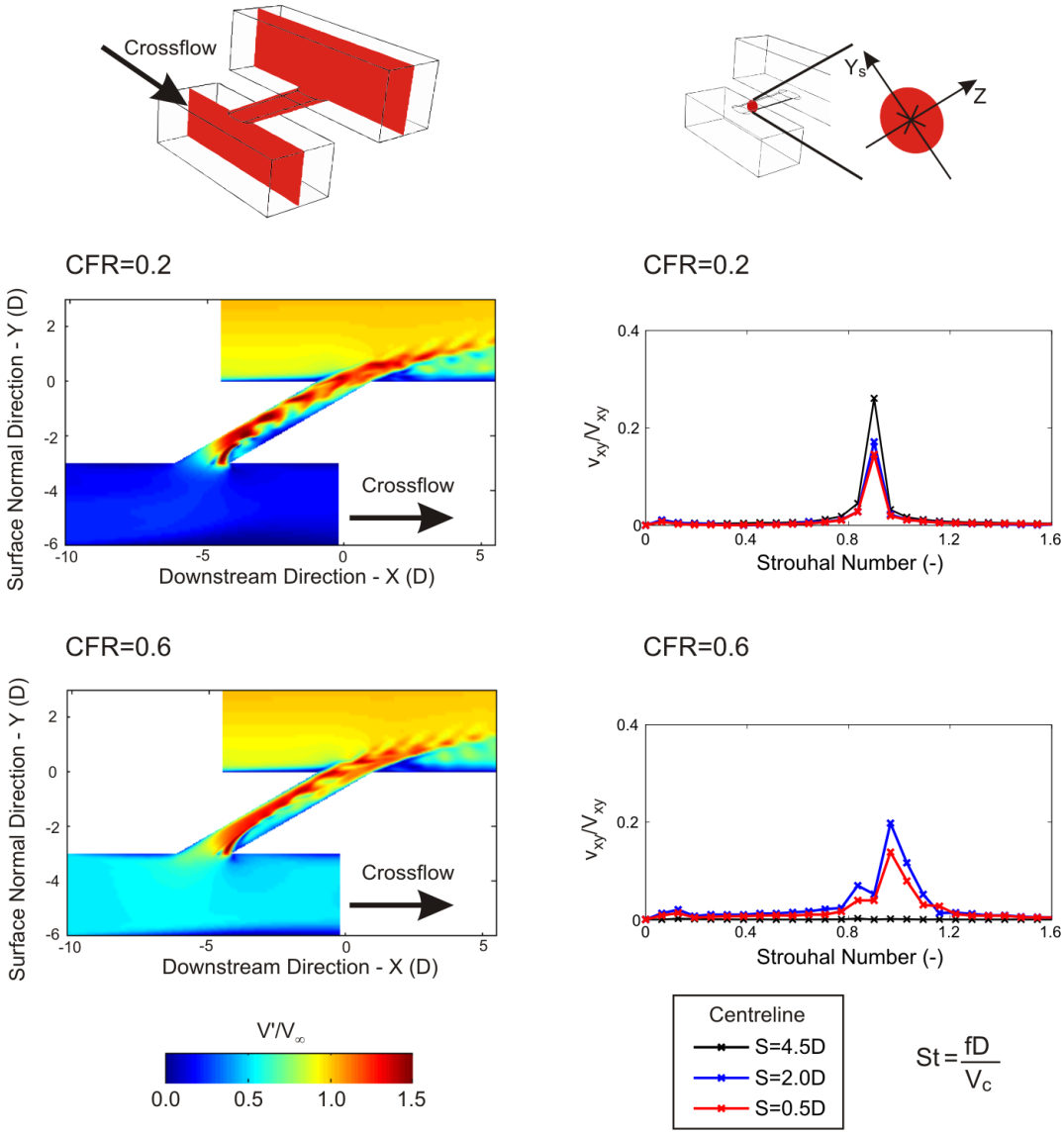

Figure 9.13: Instantaneous velocity profiles on the spanwise plane at midspan and frequency spectra inside the cooling hole. For the cylindrical hole with co-flowing crossflow. Obtained using TBLOCK.

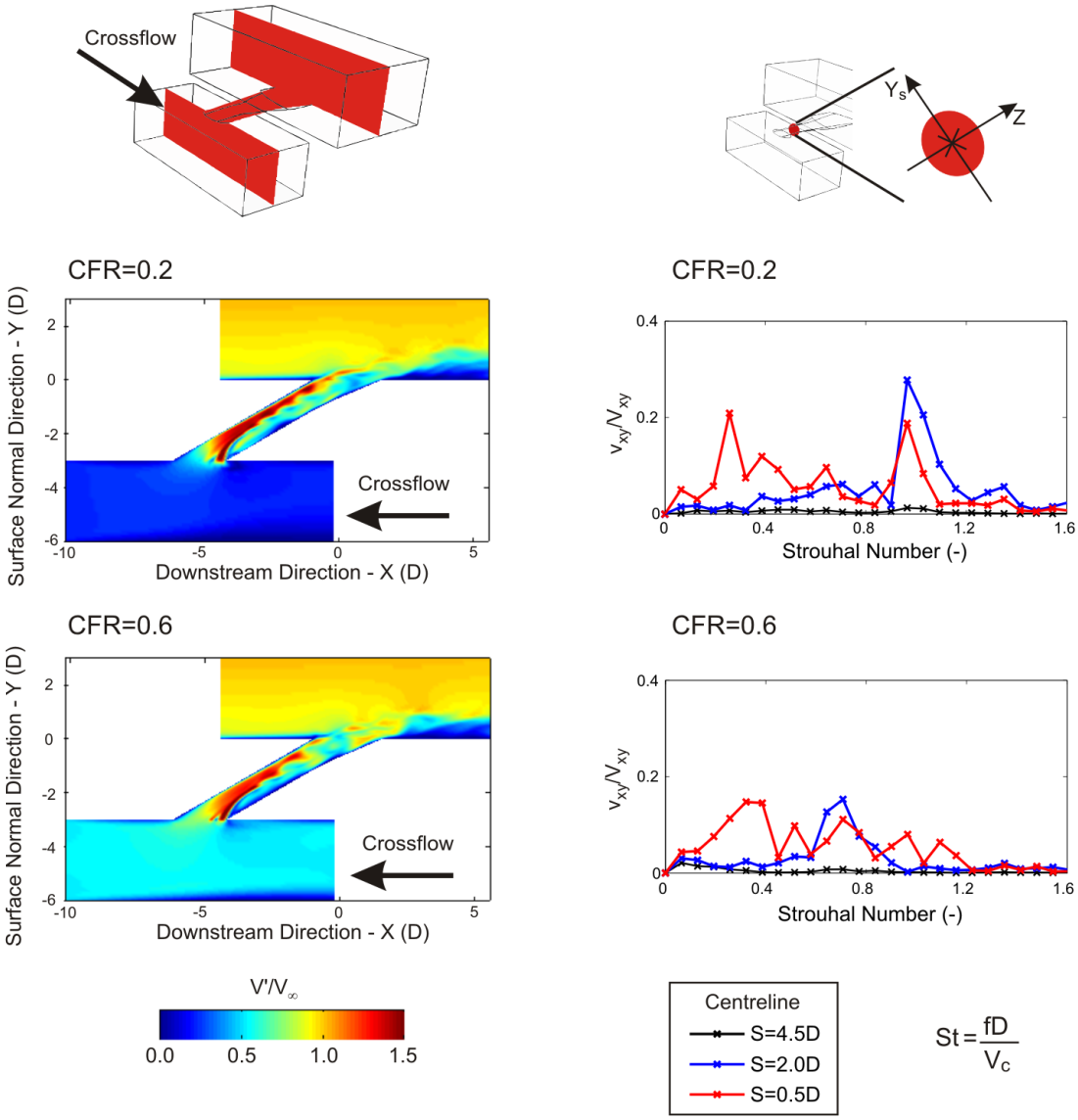

Figure 9.14: Instantaneous velocity profiles on the spanwise plane at midspan and frequency spectra inside the cooling hole. For the shaped hole with co-flowing crossflow. Obtained using TBLOCK.

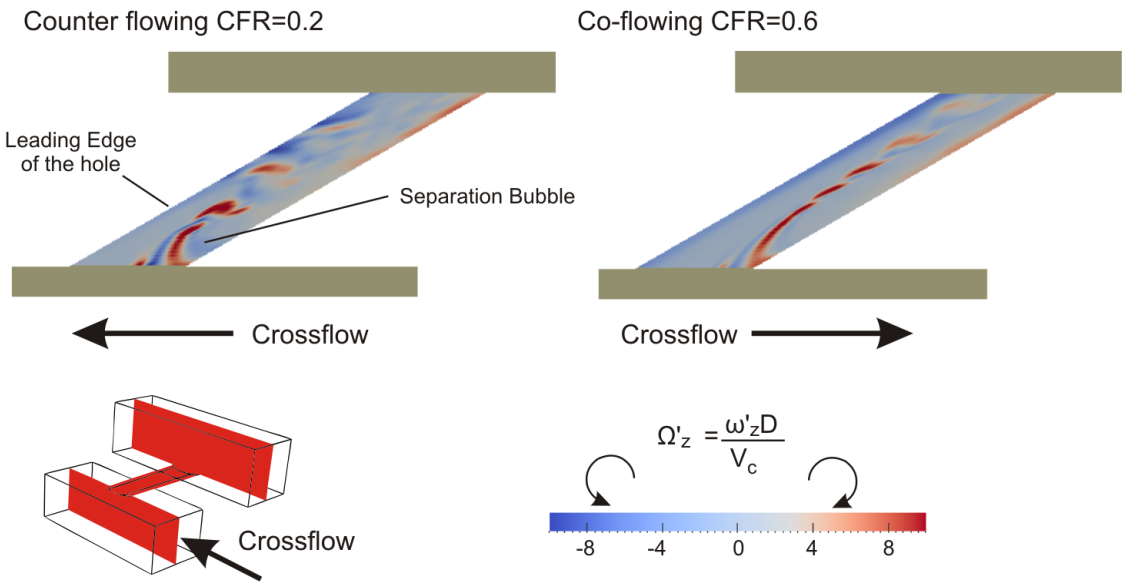

Figure 9.15: Spanwise vorticity inside the cooling hole upon the spanwise plane at midspan. For the cylindrical hole with (left) counter flowing crossflow of CFR equal to 0.2 and (right) co-flowing crossflow of CFR equal to 0.6. Obtained using TBLOCK.

layer and a smaller cross sectional area than counter flowing crossflow. The difference in size is attributed to the lower turning angle required by the flow to enter the cooling hole from a co-flowing crossflow.

9.3.2 In-hole Hairpin Vortices

The spanwise vorticity on the spanwise plane at midspan is compared in Fig. 9.15 for the cylindrical hole with counter flowing crossflow of CFR equal to 0.2 and co-flowing crossflow of CFR equal to 0.6. It is reminded here that the spanwise vorticity in Fig. 9.15 has been normalised according to Eq. 9.1. For the counter flowing case in Fig. 9.15, the vortices shed from the separation bubble move towards the cooling hole leading edge with distance along the cooling hole. In contrast, vortices shed from the smaller separation bubble formed with co-flowing crossflow are seen to remain on the axis of the hole.

Figure 9.16 shows instantaneous iso-surfaces of the spanwise vorticity (ω'_z) and hole normal vorticity (ω'_{sy}), within the cylindrical hole with a co-flowing crossflow of CFR equal to 0.6. A similar vorticity profile is also seen inside the shaped hole for the same crossflow condition. To improve the clarity of Fig 9.16, the vorticity in the boundary layer of the hole has been blanked out.

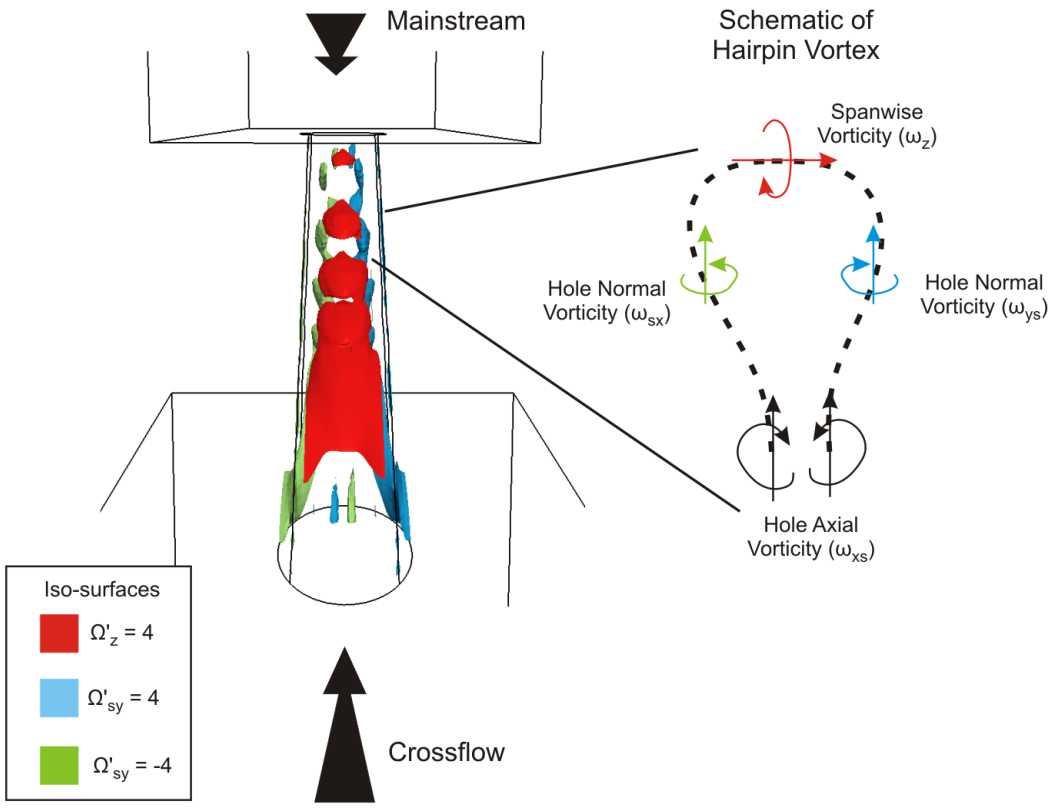

Figure 9.16: Hairpin vortices inside the cylindrical hole with co-flowing crossflow of CFR equal to 0.2. Obtained using TBLOCK.

It is shown in Fig. 9.16 that the spanwise vortex seen in Fig 9.15 appears to be part of a hairpin vortex. A schematic of the shape of the vortex line within a hairpin vortex is included in Fig. 9.16, and it is colour coded to show where the three iso-surfaces of vorticity shown inside the cooling hole apply. Here the hole normal vorticity components, correspond to the hairpin vortex as it turns from being aligned in the spanwise direction into the hole axial direction. The part of the hairpin vortex aligned in the hole axial direction (ω_{sx}) is also seen inside the hole, but is omitted in Fig. 9.16 for clarity.

It has been shown previously in Fig. 9.3 and 9.15, that spanwise vorticity is also shed from the separation bubble at the hole inlet with counter flowing crossflow. A vortex line cannot end in space, and indeed iso-surfaces of vorticity inside the hole show some evidence for the presence of a hairpin vortex. However, the larger size of the inlet separation bubble with counter flowing crossflow, means that more turbulence is formed downstream of the separation bubble than for the co-flowing crossflow case in Fig. 9.16. The increased level of turbulence means that the vorticity components in the hole normal and axial directions,

that form part of the hairpin vortex, mix out over a relatively short distance inside the cooling hole.

In the current study coherent vortex shedding has only been observed for the cases when the separation bubble has a reasonably 2-D shear layer. It is reminded here that the study of Kiya and Sasaki [49], introduced in the discussion of Chapter 8, showed that hairpin vortices also form downstream of a separation bubble on a blunt flat plate. Therefore if there is a 2-D shear layer the in-hole separation bubble appears to act similar to that at the leading edge of a blunt flat plate.

In Chapters 6 and 7 of the current investigation, hairpin vortices have been shown to form in the jet downstream of the cooling hole exit. It has been shown in Chapter 8, that the coherent unsteadiness inside the hole has a similar frequency to that of the passing of the hairpin vortices. This led to the suggestion in Chapter 8, that the in-hole unsteadiness might merge into the hairpin vortices present in the downstream jet.

The decreasing size of the regions enclosed by the iso-surfaces in Figure 9.16, shows that the hairpin vortices are mixing out with distance along the cooling hole. In addition, there is no evidence in the numerical model to suggest the presence of hairpin vortices in the downstream jet.

To better understand if there is a link between the hairpin vortices present in and out of the hole, additional blowing ratios need to be investigated, as hairpin vortices do not appear to form in the downstream jet for a BR equal to 0.9 in the current numerical investigation. However, it should be reminded that in Chapter 5, the sensitivity of the numerical model has only been assessed with respect to resolving the coherent unsteady structures inside the cooling hole.

9.4 Conclusions

In this chapter the numerical model described in Chapter 5 has been used to investigate the cause of the coherent unsteadiness seen inside the cooling hole in Chapter 8. Co-flowing, counter flowing and perpendicular crossflows have been modeled, for crossflow velocities equal to 0.2 and 0.6 times the bulk velocity through the hole.

The discussion of Chapter 8 suggested that the coherent unsteadiness inside the cooling hole is due to vortex shedding from a separation bubble at the cooling hole inlet. The

numerical results presented in this chapter show that a separation bubble does form at the trailing edge of the hole inlet, with either co-flowing or counter flowing crossflow. Vorticity is seen to be shed, with a Strouhal number close to 0.9, from the separation bubble if its shear layer has a largely 2-D profile. It is seen this vorticity orientates into a series of hairpin vortices downstream of the separation bubble.

The distance over which the hairpin vortices mix out, appears to depend on the turning angle of the flow entering the hole. With a large turning angle, the turbulence production is increased and so the hairpin vortices mix out more readily. In contrast a small turning angle means a smaller separation bubble, less turbulence production and the hairpin vortices to be more prevalent.

The numerical model is consistent with the experimental results of Chapter 8 in showing that coherent unsteadiness is not present inside the cooling hole with perpendicular crossflow of 0.6 times the bulk jet velocity. The in-hole velocity profiles obtained numerically, show that with perpendicular crossflow the in-hole velocity profile changes significantly compared to the cases with co-flowing and counter flowing crossflow. The time-mean flow is seen to spiral along the length of the cooling hole. A separation bubble is seen to form at the hole inlet, but this is deformed by the spiralling flowfield and within a short distance along the hole mixes out.

The presence of a separation bubble at the hole inlet, appears to determine whether coherent hairpin vortices are seen inside the hole. Hairpin vortices being seen with counter flowing and co-flowing crossflow, but not with perpendicular crossflow. The presence of hairpin vortices within the hole is interesting, given the occurrence of hairpin vortices within the downstream jet shown in Chapters 6 and 7.

Chapter 10

Conclusions and Recommendations

10.1 Conclusions

Images of the jet downstream of both the cylindrical and shaped cooling holes, recorded with high speed photography, showed that two coherent unsteady structures could occur. These structures were called shear layer vortices and hairpin vortices. Both of these structures have been shown previously in open literature, but are shown here experimentally for flow conditions more typical of film cooling.

The formation of both these coherent unsteady structures appeared to depend on the velocity difference across the shear layer between the jet and the mainstream. Shear layer vortices appeared to form due to a Kelvin-Helmholtz instability in the shear layer at relatively high blowing ratios. Hairpin vortices in contrast were seen to occur at comparatively lower blowing ratios, for which the jet velocity was less than the mainstream velocity. In the intermediate case, when the velocity difference across the shear layer was minimal, no coherent unsteadiness was seen to occur.

Frequency spectra, obtained using Hot Wire Anemometry and from a sequence of high speed images (using the temporal variation in pixel intensity), showed the passing of the shear layer vortices to be of a Strouhal number close to 1.0. Using the same measurement techniques, the passing of the hairpin vortices was seen to be of a Strouhal number in the range of 0.5 to 0.8.

The diffusion of the jet in the expanding exit of the shaped hole, meant that for a given blowing ratio the velocity of the downstream jet was lower than the equivalent jet from

the cylindrical hole. Thus the hairpin vortices were seen to occur at a BR close to 0.9 for the shaped hole, in contrast to 0.7 for the cylindrical hole when a minimal perpendicular crossflow was present at the hole inlet.

Images recorded with high speed photography showed hairpin vortices to also be present when the velocity of the perpendicular crossflow was increased to 0.6 times the bulk jet velocity. However, when the cooling hole inlet was of the idealised case, no hairpin vortices were seen in the jet from the cylindrical hole. Whilst for the shaped hole, hairpin vortices were seen to occur only at a lower BR of 0.5. Therefore, it appears that changing to an idealised hole inlet altered the shear layer velocity gradient for a given BR, and thus decreased the prevalence of hairpin vortices at the blowing ratios of interest.

Frequency spectra obtained using Hot Wire Anemometry and images recorded with high speed photography, showed shear layer vortices to be present in the jet from the cylindrical hole for a BR close to 1.8 for all the hole inlet conditions investigated. In contrast shear layer vortices were only seen in the jet from the shaped hole, at a BR of 1.4, for the case of an idealised hole inlet.

The flow condition at the cooling hole inlet was also important in determining the time-mean position of the jet. Images recorded with high speed photography, showed that for a change in the perpendicular crossflow velocity from 0.1 to 0.6 times the bulk jet velocity, the jet from the cylindrical hole rotated about its axis. A similar variation in the perpendicular crossflow velocity caused the jet from the shaped hole to bias to different edges of the expanding exit. Comparing these changes in the time-mean flowfield to film effectiveness measurements in open literature, suggests that these changes may be advantageous for a cylindrical hole, but detrimental for a shaped hole.

The velocity of the perpendicular crossflow was also seen to determine whether coherent unsteadiness was present inside both the cylindrical and the shaped holes. Frequency spectra obtained using Hot Wire Anemometry, showed that with a minimal perpendicular crossflow, coherent unsteadiness was present close to the hole inlet across a BR range of 0.7 to 1.8. The frequency of the in-hole coherent unsteadiness was either 70Hz, 140Hz or 210Hz, and at which frequencies it occurred varied between blowing ratios.

Frequency spectra obtained closer to the hole exit also showed coherent unsteadiness to be present. However, this was typically only for blowing ratios of 1.0 and less, with the

coherent unsteadiness at BR higher than this appearing to have mixed out. The Strouhal number of the in-hole coherent unsteadiness seen at the lower BR, was consistent with that of the hairpin vortices, that were also seen in the downstream jet for similar blowing ratios. This suggests there may be a link between the in-hole and out of hole coherent unsteadiness.

On increasing the perpendicular crossflow velocity to 0.6 times the bulk jet velocity, it was seen experimentally and numerically that coherent unsteadiness did not occur inside the cooling hole. The existence of hairpin vortices in the downstream jet for the same hole inlet condition therefore suggests that in-hole coherent unsteadiness, whilst maybe a contributor, cannot be the only reason for the formation of hairpin vortices.

Coherent unsteadiness, of a similar Strouhal number as seen experimentally with a minimal perpendicular crossflow, was seen numerically inside both cooling hole types with counter and co-flowing crossflows. It was seen that the coherent unsteadiness was due to the shedding of hairpin vortices inside the cooling hole, from a separation bubble at the trailing edge of the hole inlet. These hairpin vortices arose when the shear layer of the separation bubble was largely 2-D. For the BR equal to 0.9 case, which was tested numerically, the in-hole hairpin vortices mixed out before the hole exit and did not propagate into the downstream jet.

The numerical results suggest that the separation bubble at the trailing edge of the hole inlet is relatively small with large perpendicular crossflow velocities. Additionally this crossflow was shown to cause a steady spiraling of flow along the length of the hole. It appears to be these changes to the in-hole flowfield that inhibit the formation of coherent hairpin vortices inside the cooling hole with a perpendicular crossflow of 0.6 times the bulk jet velocity.

10.2 Recommendations

The impact of crossflow on the coherent unsteadiness inside the hole, as well as the characteristics of the coherent unsteadiness in the downstream jet, presented in this thesis, provide an initial understanding of the coherent unsteadiness occurring in film cooling flows. However, further research is required to take forward the conclusions made here, so as to identify more clearly if there are potential benefits to turbine blade film cooling design. Here recommendations are made to suggest how the current investigation might be continued to

achieve this aim.

The hairpin vortices in the downstream jet, were seen to occur in a jet that was attached to the blade surface. In such a jet high film effectiveness is to be expected, and thus there is a need to establish the impact of the passage of hairpin vortices on the local film effectiveness. If the impact of the hairpin vortices is deemed to be significant then the effect of other factors on their formation, such as the location of the cooling holes on the blade surface or higher Mach number conditions, should then be investigated.

The current results suggest that there may be a link between hairpin vortices in the hole and those in the downstream jet. This is interesting, for it could potentially offer a means to control the hairpin vortices in the downstream jet. A possible next step in confirming such a link, would be to use the current numerical model to investigate a range of blowing ratios for a crossflow direction in which coherent hairpin vortices are seen inside the cooling hole.

Bibliography

[1] *World Airport Traffic Report for 2009.* ACI World, Geneva, 2010.

[2] EN ISO 5167-2:2003. Measurement of fluid flow by means of pressure differential devices inserted in circular-cross section conduits running full - Part 2: Orifice plates., 2003.

[3] R.S. Abhari and A.H. Epstein. An experimental study of film cooling in a rotating transonic turbine. In *Proceedings of the International Gas Turbine and Aeroengine Congress, Cologne*, 1992. 92-GT-201.

[4] J. Andreopoulos. On the structure of jets in a crossflow. *Journal of Fluid Mechanics*, 157:163–197, 1985.

[5] J. Andreopoulos and W. Rodi. Experimental investigation of jets in a crossflow. *Journal of Fluid Mechanics*, 138:93–127, 1984.

[6] G.K. Batchelor. *An Introduction to Fluid Dynamics.* Cambridge University Press, Cambridge, 3rd edition, 2000.

[7] H.A. Becker and T.A. Massaro. Vortex evolution in a round jet. *Journal of Fluid Mechanics*, 31:435–448, 1968.

[8] G. Bergeles, A.D. Gosman, and B.E. Launder. Near-field character of a jet discharging through a wall at 30° to a mainstream. *AIAA Journal*, 15(4):499–504, 1977.

[9] P. Bradshaw and F.Y.F. Wong. The reattaching and relaxation of a turbulent shear layer. *Journal of Fluid Mechanics*, 52:113–135, 1972.

[10] R. Bunker. Film cooling effectiveness due to discrete holes within a transverse surface slot. In *Proceedings of the ASME Turbo Expo, Amsterdam*, 2002. GT2002-30178.

[11] R.S. Bunker. A review of shaped hole turbine film-cooling technology. *Journal of Heat Transfer*, 127(4):441–453, 2005.

[12] S.W. Burd, R.W. Kaszeta, and T.W. Simon. Measurements in film cooling flows: Hole L/D and turbulence intensity effects. *Journal of Turbomachinery*, 120(4):791–798, 1998.

[13] S.W. Burd and T.W. Simon. Measurement of discharge coefficients in film cooling. *Journal of Turbomachinery*, 121(2):243–248, 1999.

[14] N.J. Cherry, R. Hillier, and M.E.M.P. Latour. Unsteady measurements in a separated and reattaching flow. *Journal of Fluid Mechanics*, 144:13–46, 1984.

[15] S.C. Crow and F.H. Champagne. Orderly structure in jet turbulence. *Journal of Fluid Mechanics*, 48:547–591, 1971.

[16] J.D. Denton. An improved time-marching method for turbomachinery flow calculation. *Journal of Turbomachinery*, 105(3):514–524, 1983.

[17] J.D. Denton. The calculation of three dimensional viscous flow through multistage turbomachines. In *Proceedings of the International Gas Turbine and Aeroengine Congress, Brussels*, 1990. 90-GT-19.

[18] A. Dhungel, Y. Lu, W. Phillips, S.V. Ekkad, and J. Heidmann. Film cooling from a row of holes supplemented with anti vortex holes. In *Proceedings of the ASME Turbo Expo, Montreal*, 2007. GT2007-27419.

[19] R.P. Dring, M.F. Blair, and H.D. Joslyn. An experimental investigation of film cooling on a turbine rotor blade. *Journal of Engineering for Power*, 102(1):81–87, 1980.

[20] S.V. Ekkad, D. Zapata, and J.C. Han. Film effectiveness over a flat surface with air and CO_2 injection through compound angle holes using a transient liquid crystal image method. *Journal of Turbomachinery*, 119(3):587–593, 1997.

[21] S.V. Ekkad, D. Zapata, and J.C. Han. Heat trasfer coefficients over a flat surface with air and CO_2 injection through compound angle holes using a transient liquid crystal image method. *Journal of Turbomachinery*, 119(3):580–586, 1997.

[22] V.L. Eriksen and R.J. Goldstein. Heat transfer and film cooling following injection through inclined circular tubes. *Journal of Heat Transfer*, 96(2):239–245, 1974.

[23] T.E. Faber. *Fluid Dynamics for Physicists*. Cambridge University Press, Cambridge, 1st edition, 1997.

[24] T.F. Fric and A. Roshko. Vortical structure in the wake of a transverse jet. *Journal of Fluid Mechanics*, 279:1–47, 1994.

[25] S. Friedrichs, H.P. Hodson, and W.N. Dawes. Distribution of film-cooling effectiveness on a turbine endwall measured using the ammonia and diazo technique. *Journal of Turbomachinery*, 118(4):613–621, 1996.

[26] R.J. Goldstein. Film cooling. *Advances in Heat Transfer*, 7:321–379, 1971.

[27] R.J. Goldstein, E.R.G. Eckert, and F. Burggraf. Effects of hole geometry and density on three-dimensional film cooling. *International Journal of Heat and Mass Transfer*, 17(5):595–607, 1974.

[28] R.J. Goldstein, E.R.G. Eckert, and J.W. Ramsey. Film cooling with injection through holes: Adiabatic wall temperatures downstream of a circular hole. *Journal of Engineering for Power*, 90:384–395, 1968.

[29] R.J. Goldstein and T. Yoshida. The influence of laminar boundary layer and laminar injection on film cooling performance. *Journal of Heat Transfer*, 104:355–362, 1982.

[30] D.G. Gregory-Smith and J.G.E. Cleak. Secondary flow measurements in a turbine cascade with high inlet turbulence. *Journal of Turbomachinery*, 114(1):173–183, 1992.

[31] M. Gritsch, C. Saumweber, A. Schulz, S. Wittig, and E. Sharp. Effect of internal coolant crossflow orientation on the discharge coefficient of shaped film-cooling holes. *Journal of Turbomachinery*, 122(1):146–152, 2000.

[32] M. Gritsch, A. Schulz, and S. Wittig. Adiabatic wall effectiveness measurements of film-cooling holes with expanded exits. *Journal of Turbomachinery*, 120(3):549–556, 1998.

[33] M. Gritsch, A. Schulz, and S. Wittig. Discharge coefficient measurements of film-cooling holes with expanded exits. *Journal of Turbomachinery*, 120(3):557–563, 1998.

[34] M. Gritsch, A. Schulz, and S. Wittig. Effect of internal coolant crossflow the effectiveness of shaped film-cooling holes. *Journal of Turbomachinery*, 125(3):547–554, 2003.

[35] K.L. Harrison and D.G. Bogard. Comparison of RANS turbulence models for prediction of film cooling performance. In *Proceedings of the ASME Turbo Expo, Berlin*, 2008. GT2008-51423.

[36] B.A. Haven and M. Kurosaka. Kidney and anti-kidney vortices in crossflow jets. *Journal of Fluid Mechanics*, 352:27–64, 1997.

[37] N. Hay, S.E. Henshall, and A. Manning. Discharge coefficients of holes angled to the flow direction. *Journal of Turbomachinery*, 116(1):92–96, 1994.

[38] N. Hay, D. Lampard, and S. Benmansour. Effect of crossflows on the discharge coefficient of film cooling holes. *Journal of Engineering for Power*, 105(2):243–248, 1983.

[39] N. Hay, D. Lampard, and C.L. Saluja. Effects of cooling films on the heat transfer coefficient on a flat plate with zero mainstream pressure gradient. *Journal of Engineering for Gas Turbines and Power*, 107(1):105–110, 1985.

[40] N. Hay, D. Lampard, and C.L. Saluja. Effects of the condition of the approach boundary layer and of mainstream pressure gradients on the heat transfer coefficient on film cooled surfaces. *Journal of Engineering for Gas Turbines and Power*, 107(1):99–104, 1985.

[41] J. Heidmann and S.V. Ekkad. A novel anti-vortex turbine film cooling hole concept. In *Proceedings of the ASME Turbo Expo, Montreal*, 2007. GT2007-27528.

[42] D.G. Hyams and J.H. Leylek. A detailed analysis of film cooling physics: Part III-streamwise injection with shaped holes. *Journal of Turbomachonery*, 122(1):122–132, 2000.

[43] W. Jessen, M. Konopka, and W. Schröder. Particle image velocimetry measurements of film cooling in an adverse pressure gradient flow. In *Proceedings of the ASME Turbo Expo, Glasgow*, 2010. GT2010-22411.

[44] K. Kadotani and R.J. Goldstein. On the nature of jets entering a turbulent flow Part A - jet-mainstream interaction. *Journal of Engineering for Power*, 101(3):459–465, 1979.

[45] K. Kadotani and R.J. Goldstein. On the nature of jets entering a turbulent flow Part B - film cooling performance. *Journal of Engineering for Power*, 101(3):466–470, 1979.

[46] R.M. Kelso, T.T. Lim, and A.E. Perry. An experimental study of round jets in cross-flow. *Journal of Fluid Mechanics*, 306:111–144, 1996.

[47] A. Kholi and K. Thole. A CFD investigation on the effects of entrance crossflow directions to film-cooling holes. *Proceedings of ASME Heat Transfer Conference*, 12:223–232, 1997.

[48] M. Kiya and K. Sasaki. Structure of a turbulent separation bubble. *Journal of Fluid Mechanics*, 137:83–113, 1983.

[49] M. Kiya and K. Sasaki. Structure of large-scale vortices and unsteady reverse flow in the reattaching zone of a turbulent separation bubble. *Journal of Fluid Mechanics*, 154:463–491, 1985.

[50] S.J. Kline and F.A. McClintock. Describing uncertainties in single-sample experiments. *Mechanical Engineering*, 75:3–8, 1953.

[51] C. Klostermeier. *Investigation into the capability of large eddy simulation for turbomachinery design.* PhD thesis, University of Cambridge, 2008.

[52] K. Kusterer, D. Bohn, T. Sugimoto, and R. Tanaka. Double-jet ejection of cooling air for improved film cooling. *Journal of Turbomachinery*, 129(4):809–815, 2007.

[53] L.S. Langston. Crossflows in a turbine cascade passage. *Journal of Engineering for Power*, 102:866–874, 1980.

[54] B. Laveau and R.S. Abhari. Influence of flow structure on shaped hole film cooling performance. In *Proceedings of the ASME Turbo Expo, Glasgow*, 2010. GT2010-23032.

[55] S.W. Lee, Y.B. Kim, and J.S. Lee. Flow characteristics and aerodynamic losses of film cooling jets with compound angle orientations. *Journal of Turbomachinery*, 119(2):310–319, 1997.

[56] S.W. Lee, S.W. Park, and J.S. Lee. Flow charateristics inside circular holes injection holes normally oriented to a crossflow: Part 1 - flow visualisations and flow data on the symmetry plane. *Journal of Turbomachinery*, 123(2):266–273, 2001.

[57] C. Leiss. Experimental investigation of film cooling with ejection from a row of holes for the application to gas turbine blades. *Journal of Engineering for Power*, 97(1):21–27, 1975.

[58] J.H. Leylek and R.D. Zerkle. Discrete-jet film cooling: a comparison of computational results with experiments. *Journal of Turbomachinery*, 116(3):358–368, 1994.

[59] H.L. Lim, G. Pullan, and P. Ireland. Influence of film cooling hole angles and geometries on aerodynamic loss and net heat flux reduction. In *Proceedings of the ASME Turbo Expo 2011, Vancouver*, number GT2011-45721, 2011.

[60] T.T. Lim, T.H. New, and S.C. Luo. On the development of large-scale structures of a jet normal to a cross flow. *Physics of Fluids*, 13(3):770–775, 2001.

[61] Y. Lu, A. Dhungel, and S.V. Ekkad. Effect of trench width and depth on film cooling from cylindrical holes embedded in trenches. In *Proceedings of the ASME Turbo Expo, Montreal*, 2007. GT2007-27388.

[62] Y. Lu, A. Dhungel, S.V. Ekkad, and R.S. Bunker. Film cooling measurements for crated cylindrical inclined holes. In *Proceedings of the ASME Turbo Expo, Montreal*, 2007. GT2007-27386.

[63] R.J. Margason. Fifty years of jets in crossflow research. In *AGARD Symposium on a Jet in Crossflow*, 1993. CP-534.

[64] B. Massey. *Mechanics of Fluids*. Taylor and Francis, 8th edition, 2006.

[65] H. Matsuda, S. Lida, and M. Hayakawa. Coherent structures in a 3-dimensional wall jet. *Journal of Fluids Engineering*, 112(4):462–467, 1990.

[66] K.T. McGovern and J.H. Leylek. A detailed analysis of film cooling physics: Part II - compound-angle injection with cylindrical holes. *Journal of Turbomachinery*, 122(1):113–121, 2000.

[67] D.J. Mee, N.C. Baines, and M.L.G. Oldfield. Detailed boundary layer measurements on a transonic turbine cascade. *Journal of Turbomachinery*, 114(1):163–172, 1992.

[68] A.B. Mehendale, J.-C. Han, S. Ou, and C.P. Lee. Unsteady wake over a linear turbine blade cascade with air and CO_2 film injection: Part II - effect on film effectiveness and heat transfer distributions. *Journal of Turbomachinery*, 116(4):730–737, 1994.

[69] C.B. Meher-Homji. The development of the Whittle turbojet. *Journal of Engineering for Gas Turbines and Power*, 120(2):249–256, 1998.

[70] C.B. Meher-Homji and E. Prisell. Pioneering turbojet development of Dr. Hans Von Ohain - from the Hes 1 to the Hes 011. *Journal of Engineering for Gas Turbines and Power*, 122(2):191–201, 2000.

[71] B.R. Morton and A. Ibbetson. Jets deflected in a crossflow. *Experimental Thermal and Fluid Science*, 12(2):112–133, 1996.

[72] T.H. New, T.T. Lim, and S.C. Luo. Elliptic jets in cross-flow. *Journal of Fluid Mechanics*, 494:119–140, 2003.

[73] P. Palafox. *Gas Turbine Tip Leakage flow and Heat Transfer*. PhD thesis, Department of Engineering Science, University of Oxford, 2005.

[74] Y.V. Peet and S.K. Lele. Near field of film cooling jet issued into a flat plate boundary layer: LES study. In *Proceedings of the ASME Turbo Expo, Berlin*, 2008. GT2008-50420.

[75] A.E. Perry. *Hot Wire Anemometry*. Oxford Science Publications, Oxford, 1st edition, 1982.

[76] S.D. Peterson and M.W. Plesniak. Short-hole jet-in-crossflow velocity field and its relationship to film-cooling performance. *Experiments in Fluids*, 33(6):889–898, 2002.

[77] S.D. Peterson and M.W. Plesniak. Evolution of jets emanating from short holes into crossflow. *Journal of Fluid Mechanics*, 503:57–91, 2004.

[78] J.R. Pietrzyk, D.G. Bogard, and M.E. Crawford. Hydrodynamic measurements of jets in crossflow for gas turbine film cooling applications. *Journal of Turbomachinery*, 111(2):139–145, 1989.

[79] J.R. Pietrzyk, D.G. Bogard, and M.E. Crawford. Effects of density ratio on the hydrodynamics of film cooling. *Journal of Turbomachinery*, 112(3):437–443, 1990.

[80] Rolls-Royce Group plc. Annual report, 2009.

[81] J.S. Porter, A.D. Henderson, and Walker G.J. Influence of inlet velocity ratio on the outlet flow uniformity of a fan-shaped film cooling hole. In *Proceedings of the ASME Turbo Expo, Orlando*, 2009. GT2009-59581.

[82] M. Raffel, C.E. Willert, S.T. Wereley, and J. Kompenhans. *Particle Image Velocimetry - A Practical Guide.* Springer, 2nd edition, 2007.

[83] P. Renze, W. Schroder, and M. Meinke. Large-eddy simulation of film cooling flows with variable density jets. *Flow Turbulence and Combustion*, 80:119–132, 2008.

[84] Bernstein Research. Commercial aircraft cycle: Party like it's 1999. White Book, 2007.

[85] Rolls-Royce. *The Jet Engine.* Rolls Royce Technical Publications, 6th edition, 2005.

[86] D.A. Rowbury, M.L.G. Oldfield, and G.D. Lock. Large scale testing to validate the influence of external crossflow on the discharge coefficient of film cooling holes. *Journal of Turbomachinery*, 123(3):593–600, 2001.

[87] J.E. Sargison, S.M. Guo, M.L.G. Oldfield, G.D. Lock, and A.J. Rawlinson. A converging slot-hole film-cooling geometry - Part 1: Low-speed flat-plate heat transfer and loss. *Journal of Turbomachinery*, 124(3):453–460, 2002.

[88] J.E. Sargison, S.M. Guo, M.L.G. Oldfield, G.D. Lock, and A.J. Rawlinson. A converging slot-hole film-cooling geometry - Part 2: Transonic nozzle guide vane heat transfer and loss. *Journal of Turbomachinery*, 124(3):461–471, 2002.

[89] C. Saumweber and A. Schulz. Comparison of the cooling performance of cylindrical and fan-shaped cooling holes with special emphasis on the effect of internal coolant crossflow. In *Proceedings of the ASME Turbo Expo*, 2008. GT2008-51036.

[90] H. Schichting and K. Gersten. *Boundary Layer Theory.* Springer, 8th edition, 2000.

[91] A.K. Sinha, D.G. Bogard, and M.E. Crawford. Film-cooling effectiveness downstream of a single row of holes with variable density ratio. *Journal of Turbomachinery*, 113(3):442–449, 1991.

[92] Dantec Measurement Technology. *FlowMap PIV Instrumentation, Installation and User's Guide*, 4th edition, 1998.

[93] A.J.H. Teekaram, C.J.P. Forth, and T.V. Jones. Film cooling in the presence of mainstream pressure gradients. *Journal of Turbomachinery*, 113(3):484–492, 1991.

[94] K. Thole, M. Gritsch, A. Schulz, and S. Wittig. Flowfield measurements for film-cooling holes with expanded exits. *Journal of Turbomachinery*, 120(2):327–336, 1998.

[95] K.A. Thole, M. Gritsch, A. Schulz, and S. Wittig. Effect of a crossflow at the entrance to a film cooling hole. *Journal of Fluids Engineering*, 119(3):533–540, 1997.

[96] The Times. Air fares 'to double' as Europe votes for green tax. 5th July, 2006.

[97] M. Tyagi and S. Acharya. Large eddy simulation of film cooling flow from an inclinded cylindrical jet. *Journal of Turbomachinery*, 125(4):734–742, 2003.

[98] D.K. Walters and J.H. Leylek. A detailed analysis of film-cooling physics: Part I - streamwise injection with cylindrical holes. *Journal of Turbomachinery*, 122(1):102–112, 2000.

[99] S.K. Waye and D.G. Bogard. High-resolution film cooling effectiveness measurements of axial holes embedded in a transverse trench with various trench configurations. *Journal of Turbomachinery*, 129(2):294–302, 2007.

[100] A. Wheeler. Large eddy simulations of film cooling flows. Technical report, University of Oxford for Rolls-Royce, July 2008.

[101] C.E. Willert and M. Gharib. Digital particle image velocimetry. *Experiments in Fluids*, 10:181–193, 1991.

[102] A. Yamamoto. Interaction mechanisms between tip leakage flow and the passage vortex in a linear rotor cascade. *Journal of Turbomachinery*, 110:329–338, 1988.

[103] L.L. Yuan, R.L. Street, and J.H. Ferziger. Large-eddy simulations of a round jet in crossflow. *Journal of Fluid Mechanics*, 379:71–104, 1999.